Communauté
UNIVERSITÉ Grenoble Alpes

THÈSE

Pour obtenir le grade de

DOCTEUR DE LA COMMUNAUTÉ UNIVERSITÉ GRENOBLE ALPES

Spécialité : **Physique de la matière condensé et du rayonnement**

Arrêté ministériel : 7 Août 2006

Présentée par

Emilie LEFRANÇOIS

Thèse dirigée par **Laurent C. Chapon et Rafik Ballou**
et codirigée par **Virginie Simonet**

préparée au sein **de l'Institut Laue-Langevin et de l'Institut Néel au CNRS**
et de **l'École doctorale de Physique de Grenoble**

Synthesis and study of iridium oxide compounds for entangled spin-orbit physics

Thèse soutenue publiquement le **29 Septembre 2016**,
devant le jury composé de :

Dr. Benjamin Canals
Institut Néel, CNRS & Université Grenoble Alpes, Président
Pr. Desmond McMorrow
London Center for Nanotechnology, University College London, Rapporteur
Dr. Philippe Mendels
Laboratoire de Physique des Solides, Université Paris Sud, Rapporteur
Dr. Pascal Manuel
ISIS, Rutherford Appleton Laboratory, Examinateur
Dr. Laurent C. Chapon
Institut Laue-Langevin, Directeur de thèse
Dr. Rafik Ballou
Institut Néel, CNRS & Université Grenoble Alpes, Directeur de thèse
Dr. Virginie Simonet
Institut Néel, CNRS & Université Grenoble Alpes, Invitée

Acknowledgments

There are several people that I would like to thank for these three years of PhD.

I would like to start by thanking my PhD supervisors: Rafik Ballou, Virginie Simonet and Laurent Chapon, for which I have the greatest respect as physicists and persons. I learned a lot from each of you as you have different but complementary approaches to science. I also spent great time with you during the numerous experiments performed at the ILL, ESRF, ISIS and Diamond. It has been a real pleasure to work with all of you.

I would like then to thank Pascal Lejay and Abdel Hadj-Azzem without whom, this project would not have been possible. I have learned a lot from working with you on the sample synthesis, especially learned that it can be really challenging and that you need a lot of patience and can go through a lot of trials (and failures...) to finally get what you want. Thanks a lot for your hard work and patience with me and my samples.

I would then like to thank all the people I have worked and interact with: Elsa Lhotel, Carley Paulsen, Joël Balay, Julien Robert, Sophie de Brion, Vadim Cathelin, Benjamin Canals, Claire Colin, scientists from the diffraction group at the ILL, people from the technical poles both at Institut Néel: Eric Eyraud, Didier Dufeu, Yves Deschanels, Sébastien Pairis, Pierre Lachkar, Patrick Belmain and at the ILL for their support during experiments and people from the administration: Christine Martinelli, Lilien De-Coster, Elodie Bernard and Brigitte Dubouloz

Thanks to Pr. Desmond McMorrow and Dr. Philippe Mendels for accepting to review my manuscript and to Dr. Pascal Manuel and Dr. Benjamin Canals as examinators for my PhD.

I would like to thank especially all the local contacts I have worked with at the ILL: Jacques Ollivier, Björn Fåk, Gøran Nilsen, Henry Fischer, Claire Colin, Stéphane Rols, Marek Koza and Eric Ressouche, at ISIS: Pascal Manuel and Dmitry Khalyavin, at Diamond: Alessandro Bombardi and at the ESRF: Marco Moretti. Thanks to all of you I had great time during my experiments and learned a lot.

My endless gratitude goes to my friends: those I know for long time and those I met during my PhD. Thanks to all of you I had great times both at work and outside of work. A special thanks to Gabrielle who has always been present for me despite the distance and to my former officemates: Karim, Ioan, Evan, José-Ioan, Lidia, Annalisa and Frédéric.

And I would like to finish by thanking my family for their endless support.

Contents

General introduction

Iridium oxides have attracted a lot of attention in the condensed matter community over the past decade. These compounds were first thought to behave as metals, the electronic correlations being reduced compared to the 3*d* or 4*d* transition metal oxides. However, the first studies evidenced insulating properties. Theoretical studies suggested that these unexpected behaviors could be explained taking into account the strong spin-orbit coupling of the 5*d* electrons. In iridates, spin-orbit coupling is of the same order of magnitude as the electronic correlations inducing strong spin-orbit entanglement and producing unprecedented phases such as topological insulator, Weyl semimetal ... It also acts together with the electronic correlation to generate spin-orbit induced Mott insulators. In a perfect octahedral environment the strong spin-orbit coupling and the large crystal field gives rise to a unique physics of holes in a highly entangled spin-orbit state characterized by an effective isospin $j_{\text{eff}} = 1/2$. This state is predicted to lead to exotic magnetism with in particular highly anisotropic exchange interactions.

In this context, my thesis focused on the magnetic properties of two families of compounds: the chain compounds of formula Sr_3NiMO_6 (M = Pt, Ir) and the pyrochlore iridates $R_2Ir_2O_7$ (R = rare-earth element). These two systems present additional specificities such as the presence of two different magnetic elements with possible magnetocrystalline anisotropy and the possibility to have magnetic frustration. In this manuscript, I present my results on the characterization of the Ir ion state and on the understanding of its role in the very rich physics of these materials.

Besides macroscopic magnetization measurements, their magnetic and electronic properties were probed by two complementary techniques: neutron and resonant X-ray scattering.

The next chapter gives a general overview of the motivation to the study of the iridates and of the physics involved in the iridates and more specifically for the two systems that I have studied. A brief description of the different techniques used to synthesize and characterize the magnetic and electronic properties is provided in Chapter 2. Chapter 3 is dedicated to the study of the two chains compounds Sr_3NiPtO_6 and Sr_3NiIrO_6. Finally the study of the pyrochlore iridates will be described in Chapter 4 before concluding.

Chapter 1

Introduction

Contents

In this chapter, I will first discuss the characteristics of Iridium oxides, and 5*d* transition metal oxides in general, starting with the spin-orbit coupling (SOC) in order to introduce the $j_{\text{eff}} = 1/2$ state. I will then discuss the effects of the SOC on the properties of the Ir oxides compared to the 3*d* ones. In a second part, I will present the additional properties characteristic of the studied compounds: the presence of magnetic frustration, the presence of two different magnetic species and the role of the anisotropy.

1.1 Interest of Ir-based systems

For the past decades, 3*d* transition metal oxides (TMO) have been widely studied as they exhibit a plethora of interesting behaviors such as metal-insulator transition, magnetic spin orders, high-T_C superconductivity, colossal magnetoresistance, quantum criticality ... There is a strong interplay between the charge, spin and orbital degrees of freedom in these systems. Models were developed in order to understand the ingredients at the origin of these behaviors in the strongly correlated regime, among which the well studied Hubbard model.

1.1.1 Mott physics in 3*d* systems

The Hubbard model incorporates hopping processes of the electrons and on-site electron-electron correlations. In its simplest formulation without orbital degeneracy, the Hubbard Hamiltonian writes:

$$\mathcal{H} = -t \sum_{i,j} \sum_{\sigma} (c^{\dagger}_{i\sigma} c_{j\sigma} + c_{i\sigma} c^{\dagger}_{j\sigma}) + U \sum_{i} n_{i\uparrow} n_{i\downarrow} \tag{1.1}$$

The first term corresponds to the tight-binding model, where t represents the hopping integral and is related to the kinetic energy of the electrons hoping from one site to another. $c^{\dagger}_{i\sigma}$ and $c_{i\sigma}$ are respectively the creation and annihilation operators and $\sigma = \uparrow, \downarrow$ corresponds to the spin state of the electron. The second term stands for the onsite repulsion, where U is the energy cost of having two electrons at the same site i and $n_i = c^{\dagger}_{i\sigma} c_{i\sigma}$ is the number counting operator.

In this model there is a competition between the kinetic term that favors a delocalization of the electrons and the repulsion term which on the contrary forces the electron to remain localized at their site.

This model described well the physics of systems presenting electronic band at the Fermi level with a small bandwidth, W, which is related to the hopping parameter t. Considering a half-filled band system, *i.e.* a system with one electron per site, it is in a metallic state for $t \equiv W \gg U$ and in a Mott-insulating state when $t \equiv W \ll U$ (see Fig. 1.1). Therefore a metal-insulator transition (MIT) is observed as function of U/W.

This model allows for a good description of the 3*d* TMO insulating behavior as these materials present narrow bands and strong electronic correlations, *i.e.* they are in the $U/W \gg 1$

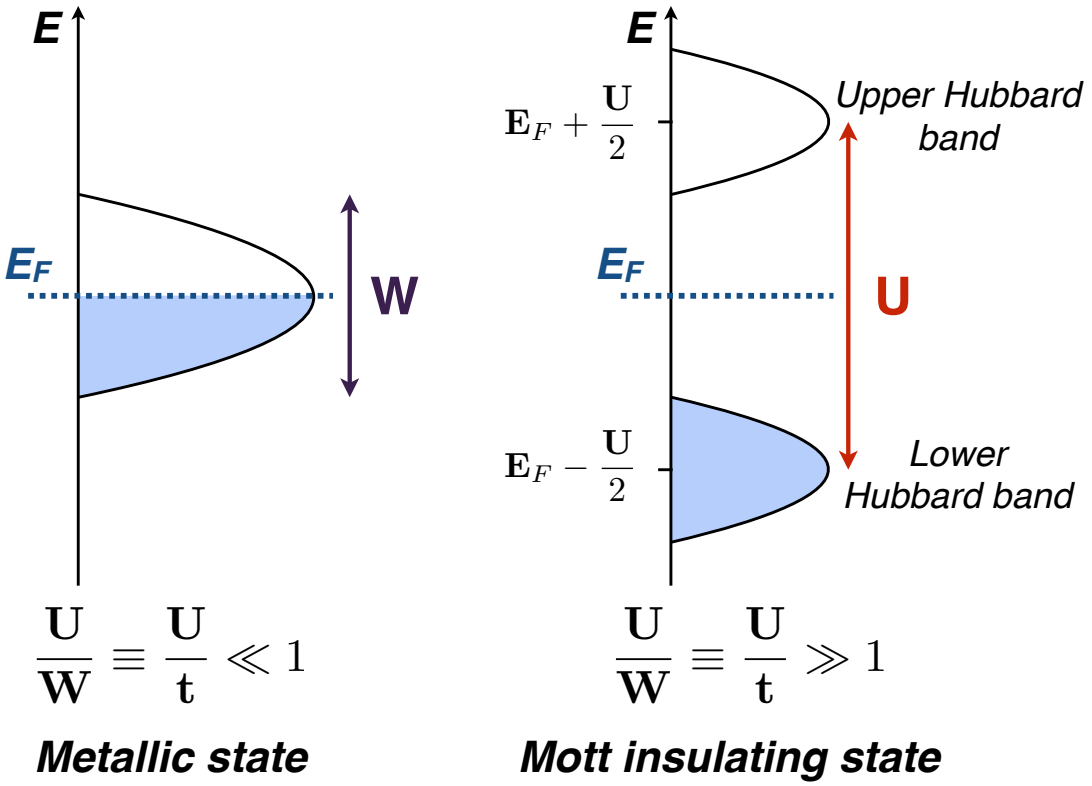

Figure 1.1 – *Representation of the density of states of electrons in the Hubbard model for half filled band.*

limit. However for 4*d* or 5*d* TMO, the width of the band at the Fermi level is larger while the electronic correlations are smaller due to the spacial extension of the electrons. They are getting closer to the $U/W < 1$ limit and a metallic state is in principle expected.

Note that in the strongly localized limit and for exactly half-filled bands, the Hubbard model favors an antiferromagnetic coupling between nearest neighbors. Indeed, because of the Pauli exclusion principle, electrons can hope from one site to the neighboring one only if the spin states are different. This model can thus be translated into an antiferromagnetic Heisenberg model:

$$\mathcal{H} = J \sum_{i,j} \mathbf{S}_i \cdot \mathbf{S}_j \tag{1.2}$$

where in this case, the magnetic exchange between neighboring sites i and j is expressed as $J = 4t^2/U$.

Despite this prediction, some 4*d* and 5*d* transition metal oxides were reported to be insulators [CBM+98]. This unexpected behavior has been understood by taking into account the presence of the spin-orbit interaction, which becomes non negligible for these systems compared to the 3*d* ones.

1.1.2 Origin of the spin-orbit coupling

The spin-orbit interaction originates from a relativistic effect due to the motion of the electrons around a positively charged nucleus. If we consider the system in the rest frame of the electron, there is a magnetic field created by the motion of the nucleus (see Fig. 1.2). This magnetic field obtained by a Lorentz transform is written as:

$$\mathbf{B} = -\frac{\mathbf{v} \times \mathbf{E}}{c^2} \tag{1.3}$$

where $\mathbf{v}$ is the nucleus velocity, $\mathbf{E} = -\boldsymbol{\nabla} V(\mathbf{r}) = -\frac{\mathrm{d}V(r)}{\mathrm{d}r}\frac{1}{r}\mathbf{r}$ represents the electric field produced by the positively charged nucleus, and $V(r)$ is the electrostatic potentiel due to the nucleus. Moreover, the angular momentum of a particle is defined by $\mathbf{L} = \mathbf{r} \times \mathbf{p}$, where $\mathbf{p} = m\mathbf{v}$ corresponds to the particle momentum. The magnetic field can be written as:

$$\mathbf{B} = \frac{1}{c^2}\mathbf{r} \times \mathbf{v}\frac{1}{r}\frac{\mathrm{d}V(r)}{\mathrm{d}r} = \frac{1}{mc^2}\mathbf{L}\frac{1}{r}\frac{\mathrm{d}V(r)}{\mathrm{d}r} \tag{1.4}$$

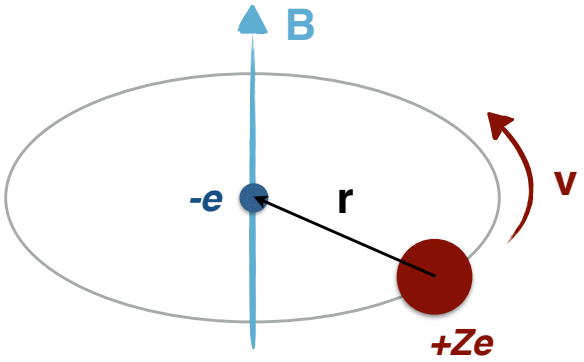

Figure 1.2 – *Sketch of a positively charged nucleus orbiting around an electron seen in the electron rest frame.*

The electron magnetic moment $\boldsymbol{\mu} = -\frac{e}{2m}g\mathbf{S} = -\frac{e}{m}\mathbf{S}$ interacts with this magnetic field according to:

$$\mathcal{H}_{SO} = -\boldsymbol{\mu} \cdot \mathbf{B} = \frac{e}{(mc)^2}\frac{1}{r}\frac{\mathrm{d}V(r)}{\mathrm{d}r}\mathbf{S} \cdot \mathbf{L} \tag{1.5}$$

For a hydrogen-like system, the electrostatic potential is given by $V(r) = \frac{1}{4\pi\epsilon_0}\frac{Ze^2}{r}$, with Z the nucleus charge. This leads to:

$$\mathcal{H}_{SO} = \frac{Ze^3}{8\pi\epsilon_0(mc)^2 r^3}\mathbf{S} \cdot \mathbf{L} \tag{1.6}$$

A $1/2$ factor has been added in order to take into account the Thomas precession. This is a relativistic correction that applies to the spin of an elementary particle or the rotation of a macroscopic gyroscope and relates the angular velocity of the spin of a particle following a curvilinear orbit to the angular velocity of the orbital motion.

Then for an electron characterized by the quantum numbers n and l, we have:

$$\langle r^{-3}\rangle_{n,l} = \frac{2Z^3}{a_0^3 n^3 l(l+1)(2l+1)} \tag{1.7}$$

where a_0 represents the Bohr radius.

Therefore the spin-orbit interaction rewrites:

$$\mathcal{H}_{SO} = \frac{e^3}{4\pi\epsilon_0 (mc)^2 a_0^3} \frac{1}{l(l+1)(2l+1)} \frac{Z^4}{n^3} \mathbf{S}\cdot\mathbf{L} = \lambda \mathbf{S}\cdot\mathbf{L} \tag{1.8}$$

It is important to note that the spin-orbit interaction scales with Z^4/n^3. Thus it increases significantly from $3d$ electrons (n = 3 and $Z \in [22-30] \Rightarrow Z^4/n^3 \in [8\,700 - 30\,000]$) to $5d$ ones (n = 5 and $Z \in [72-80] \Rightarrow Z^4/n^3 \in [215\,000 - 328\,000]$).

The SOC constant, λ, is thus of the same order of magnitude $[0.1 - 0.7$ eV$]$ than the electronic correlations in $5d$ TMO.

In order to understand the effect of the spin orbit coupling, the Ir ions have then to be considered in their charge environment.

1.1.3 The $j_{\text{eff}} = 1/2$ state.

For a free Ir^{4+} ($5d^5$) ion (spherical symmetry), all the $5d$ levels would be degenerate. The d orbitals are linear combination of the $|l, m_l\rangle$ states, where $l = 2$ and $m_l = \{-2,\ -1,\ 0,\ 1,\ 2\}$ and are defined by:

$$\left.\begin{array}{rcl} d_{xy} &=& -\frac{i}{\sqrt{2}}(|2,2\rangle - |2,-2\rangle) \\ d_{xy} &=& \frac{i}{\sqrt{2}}(|2,1\rangle + |2,-1\rangle) \\ d_{zx} &=& -\frac{1}{\sqrt{2}}(|2,1\rangle - |2,-1\rangle) \end{array}\right\} |t_{2g}\rangle \qquad \left.\begin{array}{rcl} d_{x^2-y^2} &=& \frac{1}{\sqrt{2}}(|2,2\rangle + |2,-2\rangle) \\ d_{z^2} &=& |2,0\rangle \end{array}\right\} |e_g\rangle \tag{1.9}$$

According to Hund's rules and Pauli exclusion principle, the Ir $5d$ electrons would fill every d-orbital in such way that they are all singly occupied, resulting in a high spin state $S = 5/2$.

However for most iridates, the Ir ions are located at the center of an octahedron formed by six oxygen ions. This results in the lifting of the $5d$ orbital degeneracy. Indeed the (antibonding) e_g orbitals are pointing in the direction of the oxygen ions and their energy is increased. On the contrary the (bonding) t_{2g} orbitals are pointing between the oxygen ions and their energy is lowered (see Fig. 1.3). This is known as the crystalline electric field splitting. The energy gap between the t_{2g} and e_g levels is denoted by $10D_q$, and is reported about 2-4 eV in the iridates [Mat76]. This results in a lower spin state $S = 1/2$ as only the t_{2g} states are filled.

As this energy gap between the t_{2g} and e_g states is about one order of magnitude above all the other energy scale (U, λ), we will only consider the t_{2g} states in the following parts.

We can now consider the effect of the spin-orbit interactions $\mathcal{H}_{SO} = \lambda \mathbf{S}\cdot\mathbf{L}$ on these levels,

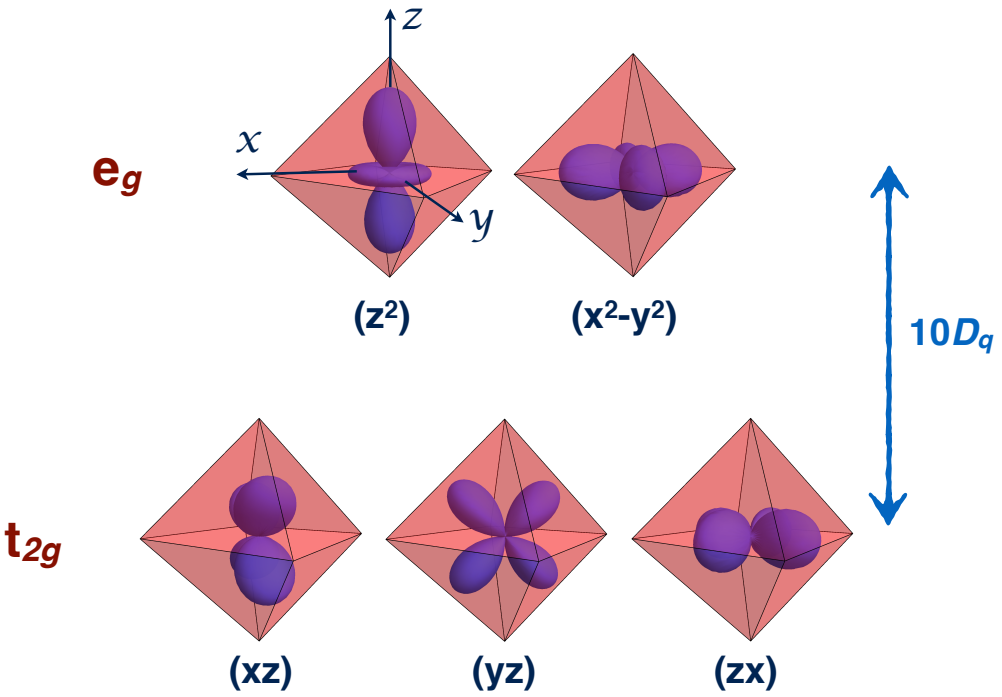

Figure 1.3 – *Schematic view of the 5d orbitals in an octahedral environment splitted by the octahedral crystal field.*

where the angular momentum $\mathbf{L} = (L_x, L_y, L_z)$ and the spin momentum $\mathbf{S}$ act on the $|t_{2g}\rangle$ states.

The orbital momentum operator acts on the $|l, m_l\rangle$ states according to:

$$\begin{array}{rcl} L_z|l,m_l\rangle & = & m_l|l,m_l\rangle \\ L_\pm|l,m_l\rangle & = & \sqrt{l(l+1)-m_l(m_l\pm 1)}|l,m_l\rangle \end{array} \tag{1.10}$$

where $L_\pm = (L_x \pm iL_y)$. The calculated matrix elements of $\langle t_{2g}|\mathbf{L}|t_{2g}\rangle$ in the $|t_{2g}\rangle = (|xy\rangle, |yz\rangle, |xz\rangle)$ basis are:

$$L_x = \begin{pmatrix} 0 & i & 0 \\ -i & 0 & 0 \\ 0 & 0 & 0 \end{pmatrix}, \; L_y = \begin{pmatrix} 0 & 0 & -i \\ 0 & 0 & 0 \\ i & 0 & 0 \end{pmatrix} \text{ and } L_z = \begin{pmatrix} 0 & 0 & 0 \\ 0 & 0 & i \\ 0 & -i & 0 \end{pmatrix} \tag{1.11}$$

These matrix elements are opposite to the ones that would be obtained for the $|p\rangle$ orbitals $(l = 1) : \mathbf{L}(t_{2g}) = -\mathbf{L}(p)$. This means that the t_{2g} subspace is equivalent to the one of an angular momentum $l_{\text{eff}} = -1$. The $|l_{\text{eff}}, m_l\rangle$ can be written in the d orbitals basis as:

$$\begin{cases} |1,0\rangle & = & |d_{xy}\rangle \\ |1,\pm 1\rangle & = & \frac{1}{\sqrt{2}}(i|d_{xz}\rangle \pm |d_{yz}\rangle) \end{cases} \tag{1.12}$$

The spin-orbit eigenstates can be described by an effective total angular momentum, the isospin $j_{\text{eff}} = l_{\text{eff}} \pm S$. The t_{2g} states are thus split into two levels, a quadruply degenerate $j_{\text{eff}} = 3/2$ and a doubly degenerate $j_{\text{eff}} = 1/2$ (see Fig. 3.32), the latter being higher in energy,

thus half occupied.

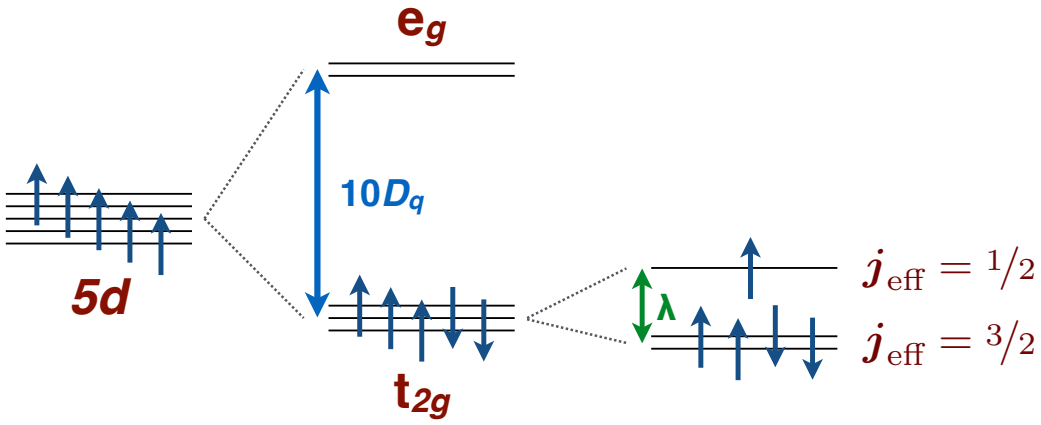

Figure 1.4 – *5d level splittings by the octahedral crystal field and SOC for Ir^{4+} ions.*

As a result of the SOC, the Ir valence electron states are described by j_{eff} states in which the spin and orbital degrees of freedom are entangled. These states can be expressed in the d orbitals basis:

$$\left.\begin{aligned} |\tfrac{1}{2},+\tfrac{1}{2}\rangle &= \frac{|d_{xy},\uparrow\rangle + i|d_{yz},\downarrow\rangle + |d_{xz},\downarrow\rangle}{\sqrt{3}} \\ |\tfrac{1}{2},-\tfrac{1}{2}\rangle &= \frac{|d_{xy},\downarrow\rangle + i|d_{yz},\uparrow\rangle - |d_{xz},\uparrow\rangle}{\sqrt{3}} \end{aligned}\right\} j_{\text{eff}} = 1/2 \tag{1.13}$$

$$\left.\begin{aligned} |\tfrac{3}{2},+\tfrac{3}{2}\rangle &= \frac{i|d_{yz},\uparrow\rangle + |d_{xz},\uparrow\rangle}{\sqrt{2}} \\ |\tfrac{3}{2},-\tfrac{3}{2}\rangle &= \frac{i|d_{yz},\downarrow\rangle - |d_{xz},\downarrow\rangle}{\sqrt{2}} \\ |\tfrac{3}{2},+\tfrac{1}{2}\rangle &= \frac{2|d_{xy},\uparrow\rangle - i|d_{yz},\downarrow\rangle \pm |d_{xz},\downarrow\rangle}{\sqrt{6}} \\ |\tfrac{3}{2},-\tfrac{1}{2}\rangle &= \frac{2|d_{xy},\downarrow\rangle - i|d_{yz},\uparrow\rangle \pm |d_{xz},\uparrow\rangle}{\sqrt{6}} \end{aligned}\right\} j_{\text{eff}} = 3/2 \tag{1.14}$$

Figure 1.5 shows the density profile of a hole in the isospin up $|\frac{1}{2},\frac{1}{2}\rangle$ state.

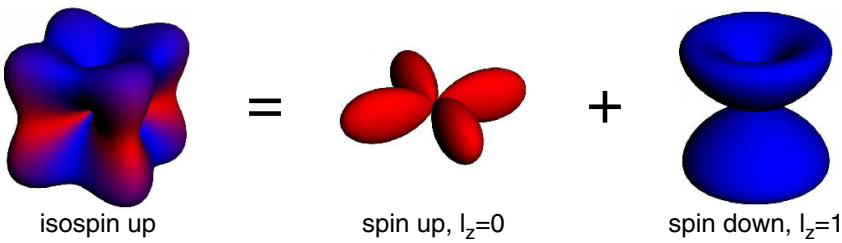

Figure 1.5 – *Density profile of a hole in the isospin up state. It is a superposition of a spin up hole density in $|xy\rangle$-orbital, $l_z = 0$ (middle), and spin down one in $(|yz\rangle + i|xz\rangle)$ state, $l_z = 1$ (right). From [JK09].*

1.1.4 New physics in iridates

Resulting from the octahedral CEF and the SOC in iridium oxides, the band at the Fermi level is no longer a wide band that cannot be split by the weak electronic correlations but is a $j_{\text{eff}} = 1/2$ band whose effective bandwidth is largely reduced. Therefore even relatively weak electronic correlations can open a gap and create a SOC induced Mott insulating state (see Fig. 1.6). This allows to explain qualitatively the insulating properties reported in some iridates.

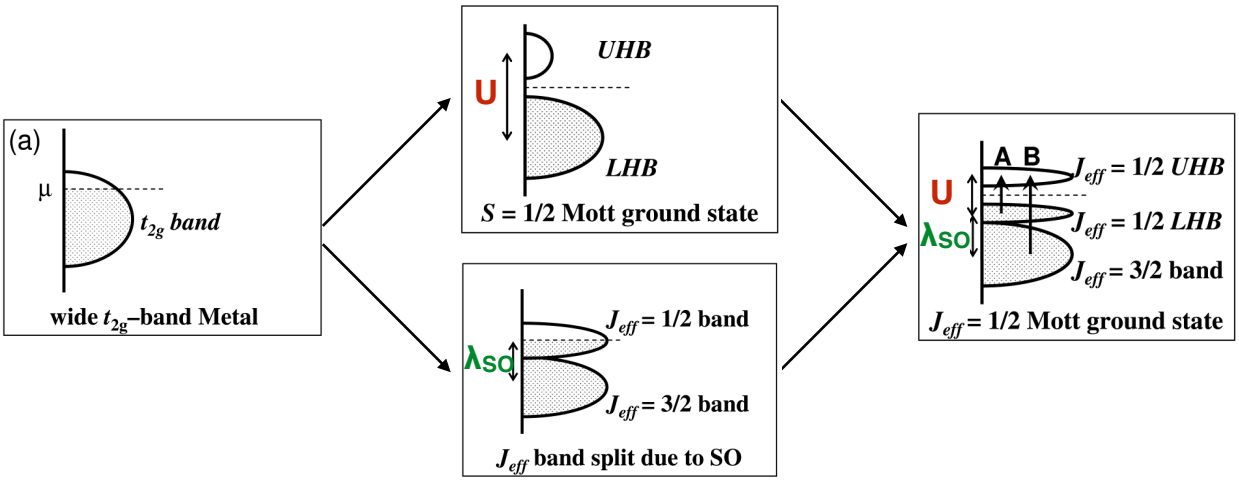

Figure 1.6 – *Schematic energy diagrams for the $5d^5$ ($t_{2g}{}^5$) configuration without SOC and U (left), with an unrealistically large U but no SOC (middle - top), with SOC but no U (middle - bottom), and (d) with SOC and U (right). Possible optical transitions A and B are indicated by the arrows. Adapted from [KJM+08]*

The Hubbard model described in the section 1.1.1 must be completed in order to take into account the SOC for the iridates. The Hamiltonian becomes:

$$\mathcal{H} = -t \sum_{i,j} \sum_{\sigma} (c^{\dagger}_{i\sigma} c_{j\sigma} + c_{i\sigma} c^{\dagger}_{j\sigma}) + \lambda \sum_{i} \mathbf{S}_i \cdot \mathbf{L}_i + U \sum_{i} n_{i\uparrow} n_{i\downarrow} \tag{1.15}$$

This model is not exactly solvable, but a schematic phase diagram can be drawn in terms of relative strength of the interaction U/t and SOC λ/t. The left part of Figure 1.7 corresponds to the conventional TMO (weak SOC), for which a metal insulator transition is observed upon increasing electronic correlations. The right part is related to materials with stronger SOC. In the weakly correlated regime, $U/t \ll 1$, topological insulator and semimetal phases are expected. With increasing electronic correlations, *i.e.* for comparable electronic correlations and SOC energy scales, the systems are entering a spin-orbit induced Mott insulating phase.

It is also interesting to look at the magnetism in this regime. Indeed, the magnetic properties are no longer described with pure spin but with an admixture of spatially anisotropic orbitals. Therefore the magnetic interactions are predicted to strongly depend on the lattice and bonding geometries [JK09]. Two cases can be distinguished: the corner sharing octahedra

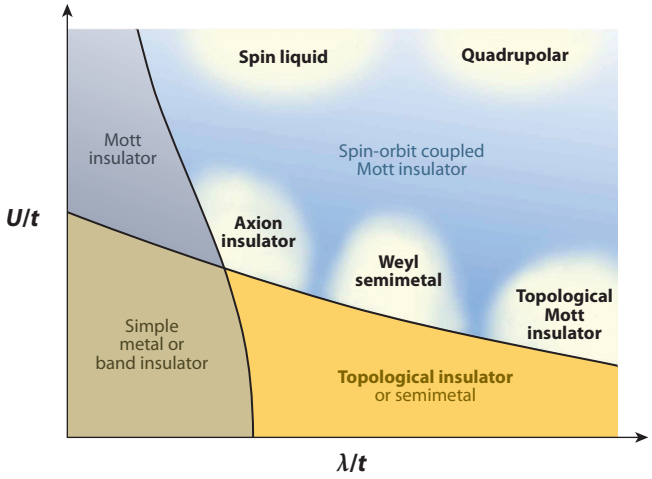

Figure 1.7 – *Sketch of a generic phase diagram for electronic materials in terms of the interaction strength U/t and spin-orbit coupling λ/t. From [WKCKB14]*

leading to 180° Ir-O-Ir bonds and the edge sharing tetrahedra resulting in 90° Ir-O-Ir bonds (see Fig. 1.8).

In the 180° geometry, only two orbitals are active on a given bond. The exchange Hamiltonian interaction (reported in [Kha05]) is expressed as:

$$\mathcal{H} = \sum_{i,j} \left(J_1 \mathbf{S}_i \cdot \mathbf{S}_j + J_2 (\mathbf{S}_i \cdot \mathbf{r}_{ij})(\mathbf{r}_{ij} \cdot \mathbf{S}_j) \right) \tag{1.16}$$

where $\mathbf{S}$ denotes the isospin $1/2$ operator and $\mathbf{r}_{ij}$ is the unit vector along the ij bond. The first term corresponds to an Heisenberg interaction while the second is a dipolar-like interaction and is anisotropic. Its magnitude depends on the ratio of the Hund's exchange and the Coulomb repulsion, J_H/U.

In the 90° geometry, there are also only two orbitals active on a bond in a given plane. However, two possible exchange paths are possible, via the upper or lower oxygen. As a result, the exchange interaction is given by:

$$\mathcal{H}_{ij}^{(\gamma)} = -J \sum_i S_i^\gamma \cdot S_j^\gamma \tag{1.17}$$

where $\gamma = (x, y, z)$ is defined as the vector perpendicular to the Ir-O-Ir plane. This model is a quantum analog of the compass model, that describes the physical properties of materials with orbital degrees of freedom. It was first encountered in 1982 by Kugel and Khomskii [KK82] but received a lot of attention only in the last decades [TN00, vdB04, Kha05, NvdB15]. Moreover, for a honeycomb lattice, it corresponds to the Kitaev model [Kit06, JK09]. This is a model of spin $1/2$ on a honeycomb lattice with highly anisotropic magnetic couplings between nearest neighbors which is completely solvable and leads to a spin liquid ground state. It presents two main characteristics: it can be reduced to a problem of non-interacting Majorana fermions and it has a topological order. Schematic representation of the realization of this

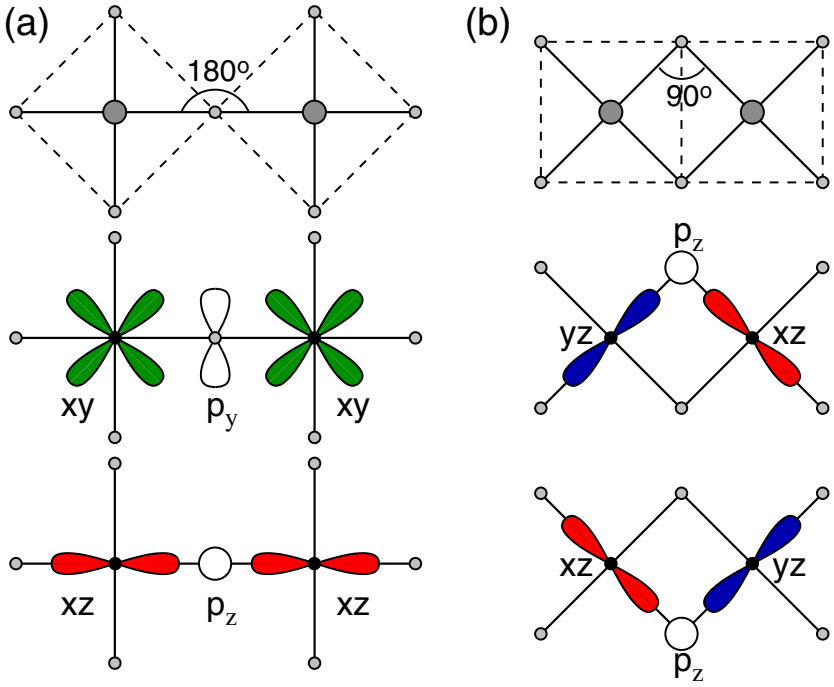

Figure 1.8 – *Two possible geometries of a TM-O-TM bond with corresponding orbitals active along these bonds. The large (small) dots stand for the transition metal (oxygen) ions. (a) A 180°-bond formed by corner shared octahedra and (b) a 90°-bond formed by edge-shared octahedra. From [JK09].*

model are drawn Figure 1.9.

The realization of such exotic electronic and magnetic phases was reported or predicted in several iridate compounds.

As an illustration, I will briefly recall the properties of the perovskite iridate Sr_2IrO_4. Its structure is made of corner-sharing IrO_6 octahedra sandwiched between layers of Sr. A behavior similar to its 4*d* analogue Sr_2RuO_4, which is a Fermi liquid [KYK+06], was expected. However, transport properties evidenced an insulating behavior [CBM+98] and susceptibility measurements showed the presence of a ferromagnetic (FM) transition at 240 K [CSH+94]. Its magnetic structure is a (***ab***)-plane canted antiferromagnetic (AFM) structure [KOK+09]. A puzzling result is that the expected "weak" ferromagnetism is actually found to be related to a quite large FM moment [CBM+98].

The insulating behavior was explained by the presence of the large SOC of the Ir ions which allows the relatively weak electronic correlations to open a gap in the $j_{\text{eff}} = 1/2$ band and to create a SOC induced Mott insulating phase. The presence of anisotropic magnetic interactions induced by the $j_{\text{eff}} = 1/2$ state of the Ir ions explained the unusual magnetic properties. It was found that the system can be modeled by Heisenberg interactions and Ising-like Kitaev interactions [JK09]:

$$\mathcal{H}_{ij}^{(\gamma)} = J_1 \mathbf{S}_i \cdot \mathbf{S}_j - J_K S_i^\gamma \cdot S_j^\gamma \tag{1.18}$$

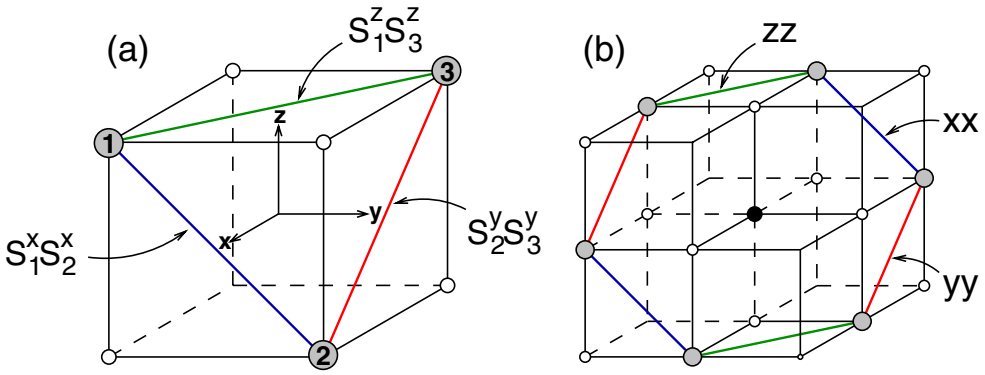

Figure 1.9 – *Examples of structural units formed by 90° Ir-O-Ir bonds and corresponding spin-coupling patterns. Gray circles stand for the Ir ions and small open circles for the oxygen sites. (a) Realization of a quantum compass model on a triangular lattice. (b) Realization of the Kitaev model on a honeycomb lattice. From [JK09].*

Moreover, it was recently predicted that electron- and hole-doped Sr_2IrO_4 could exhibit superconducting properties [SKYK15].

Another interesting family of compounds are the three-dimensional honeycomb iridates Li_2IrO_3. It was first thought that the 2D-Li_2IrO_3 could realize the Kitaev model and its spin liquid ground state. However it was found to order [LBY+11, YCC+12, CCK+12, GCS+13] due to crystal distortions and further neighbor interactions [KY11, RK14, KNY+14, YNK+14, SPWP14]. Nevertheless, in 2013, 3-dimensional phases of these compounds were discovered: the hyperhoneycomb β-Li_2IrO_3 and the stripyhoneycomb γ-Li_2IrO_3. There were first thought to be an experimental realization of the Kitaev model. However it has been later shown that these two compounds exhibits long range order [BJC+14, BJK+14].

Finally, another interesting family of compounds that I have been studying during this PhD, is the pyrochlore iridates $R_2Ir_2O_7$ with R a rare-earth element. These compounds exhibit a metal-insulator transition upon cooling. The temperature of this transition has been found to depend on the rare-earth element. It decreases for increasing rare-earth ionic radius [MWHT11]. Theoretical works predict that this is due to the rare-earth ionic size that affects the effective bandwidth of the $j_{\text{eff}} = 1/2$ conduction band and thus the metal-insulator transition [PB10]. Resulting from the strong SOC and moderate electronic correlations, novel correlated topological phases have been predicted at the condition that the Ir sublattice orders in the so-called all-in/all-out magnetic configuration (on each tetrahedra, all the spin are either pointing inward or outward its center): $\mathbb{Z}_2$ topological insulator [PB10], Weyl semimetal [Bal11, WKK12, WKGK13, MCU+15], axion insulator [WTVS11, GWKJ+12] and topological Mott insulator [WKCK10, KWF11, KYI11, IYK14].

1.2 The $R_2Ir_2O_7$ and Sr_3NiIrO_6 systems

I will now briefly introduce the two systems that I have been studying during my PhD (a more developed introduction can be found in the introduction of chapters 3 and 4) and the specificities related to these systems.

1.2.1 Magnetic frustration

The $R_2Ir_2O_7$ and Sr_3NiIrO_6 compounds both present lattices with geometry that can induce magnetic frustration.

Frustration in condensed matter physics can be defined as ***the impossibility to simultaneously satisfy all the interactions***.

This concept was first introduced in spin glasses by G. Toulouse in 1977 [Tou77]. Usually two origins for magnetic frustration can be distinguished:

– the presence of *competing interactions*. As an example, we consider a square lattice with Ising spins interactions with ferromagnetic nearest neighbor interaction and antiferromagnetic next nearest neighbor interaction, respectively designated by J_1 and J_2, of same magnitude. In this case, all the interactions cannot be satisfied at once. Figure 1.10 shows two different configurations satisfying 4 interactions out of 6. In all cases, a minimum of two interactions cannot be satisfied.

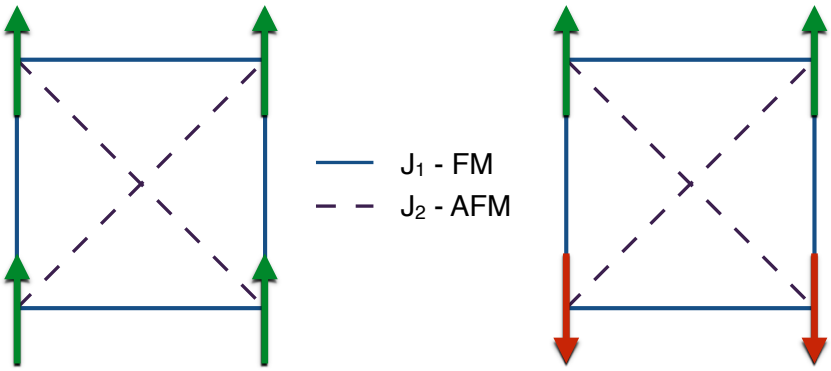

Figure 1.10 – *Example of frustration due to competing interactions: Ising spins on a square lattice with FM and AFM first (continuous blue line) and second (purple dashed line) nearest neighbor interactions.*

– the *geometry* of the lattice. As a typical example, considering antiferromagnetically coupled Ising spins on a triangular lattice (see left part of Fig. 1.11), only two interactions out of three can be satisfied at once. However if XY or Heisenberg spins are considered, a solution can be found, with spins at 120° (see right part of Fig. 1.11). For XY spins, the ground state is then doubly degenerated (in addition to a global rotation). In the case of an extended triangular lattice, the arrangement on one triangle will determine the spin arrangements on the whole lattice and a non-colinear magnetic order is reached at T = 0.

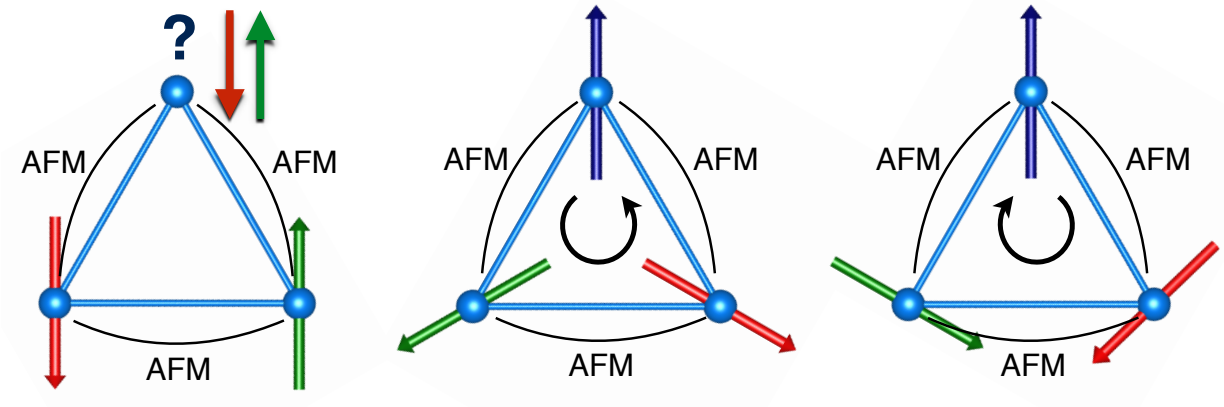

Figure 1.11 – *Example of frustration due to the lattice geometry: Ising (left) and XY or Heisenberg (middle and right) spins on a triangular lattice with AFM nearest neighbor interactions.*

These examples allow to underline two particularities related to magnetic frustration. First, the influence of the frustrated magnetic interactions and lattice geometry on the ground state properties also depends on the spin interaction symmetry (Ising, XY or Heisenberg). The second particularity is that magnetic frustration usually leads to a degeneracy of the ground state. Indeed, as seen from the previous examples, there are several possibilities to satisfy most interactions, leading to multiple spin configurations with the same energy.

Coming back to our compounds, Sr_3NiIrO_6 presents chains of alternating magnetic ions (Ni^{2+} and Ir^{4+}) arranged on a triangular lattice. Thus depending on the magnetic interaction and on the spin dimensionality, it can be prone to magnetic frustration as discussed above.

The $R_2Ir_2O_7$ compounds present two interpenetrating pyrochlore lattices, *i.e.* lattices made of corner sharing tetrahedra. Similarly to the triangular lattice, depending on both the spin dimensionality and the magnetic interactions, magnetic frustration can be at play.

A famous example is the case of Ising spins (spin with an easy axis parallel to their local $\langle 111 \rangle$ direction) with ferromagnetic nearest neighbor interactions. This leads to the spin-ice state [BG01], in which two spins are pointing inward and two spin are pointing outward the center of each tetrahedra (see left part of Fig. 1.12).

On the contrary, for antiferromagnetic interactions, the system is less frustrated and an all-in/all-out magnetic order, *i.e.* all the spins pointing either inward or outward from the center of each tetrahedra, will be stabilized (see right part of Fig. 1.12).

Now considering XY spins (spin with an easy plane anisotropy perpendicular to their local $\langle 111 \rangle$ direction), ferromagnetic interactions are predicted to lead to a long range ordered phase while antiferromagnetic ones should enhance frustration and lead to a disordered phase or an exotic order stabilized by additional mechanisms (dipolar interactions, order-by-disorder, ...).

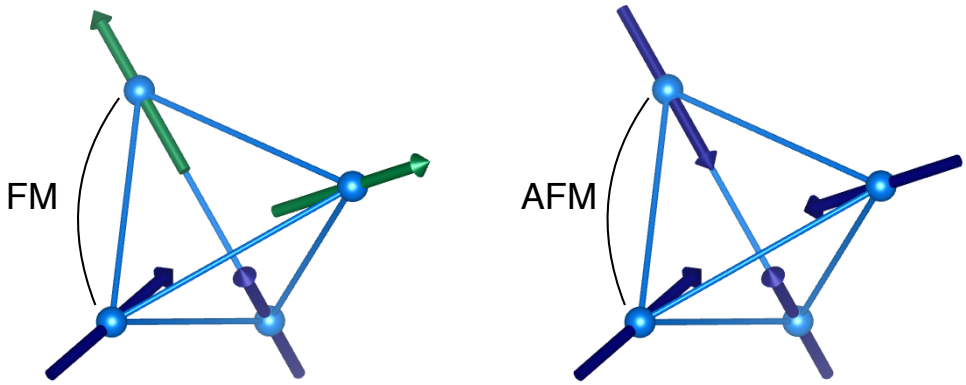

Figure 1.12 – *Examples of magnetic configuration for Ising spins on a tetrahedron for ferromagnetic (left) and antiferromagnetic (right) nearest neighbors interactions.*

1.2.2 Anisotropy: a key ingredient

In the previous section, the dimensionality of the spin system was mentioned. This is a direct consequence of the magnetocrystalline anisotropy, *i.e.* the effect of the local charge environment on the valence electrons of the considered ions.

This has been rapidly mentioned in the first part, where we discussed the effect of the octahedral oxygen environment of the Ir^{4+} ions. In this case, we saw that an octahedral environment lifts the d levels into two group called the e_g and t_{2g} orbitals. The shape of the orbitals involved in the different levels being different, this will induce anisotropic properties.

In order to understand the properties of a compound it will then be important to properly characterize its local magnetocrystalline anisotropy, as well as the valence electron wavefunctions.

Moreover, in the case of the Ir^{4+} ions, we saw that the $j_{\text{eff}} = 1/2$ state consists of an admixture of different orbital and spin states. Therefore strongly anisotropic behaviors are also to be expected for the magnetic interactions.

1.2.3 Systems of mixed spin

Both these compounds present two magnetic sites occupied by two distinct ions: Ni^{2+} and Ir^{4+} for Sr_3NiIrO_6 and rare-earth R^{3+} and Ir^{4+} for the pyrochlore iridates. The interplay between these magnetic ions, which display different properties, increases the richness of the physics in these compounds.

However, this will also complicate the interpretation of their bulk physical properties as it requires to understand the role played by each magnetic element individually and to understand the coupling between them.

A way of probing the properties of each element is to use complementary techniques which are mainly sensitive to only one of the elements. This is developed in the following

section.

1.3 Probing iridates with complementary techniques

The two systems have been studied using different techniques: macroscopic measurements (magnetometry), neutron scattering and resonant X-ray scattering. Each one of these techniques provide complementary information on the physical properties. Details on the different techniques are given in chapter 2.

The magnetization measurements give very useful information at the macroscopic level (phase transition, spin dynamics, ...). It is impossible to separate the contributions of the different ions from these measurements. However, if single crystals are measured, invaluable information on the magnetocrystalline anisotropy can be obtained.

Neutron scattering is a powerful tool in order to study the static and dynamical properties of condensed matter, especially the magnetic properties. However, iridium ions displaying weak magnetic moments in most iridates, it might be difficult to probe the Ir magnetism alone using neutron scattering experiments. This is especially the case for the pyrochlore iridates. Nevertheless the magnetism of the other magnetic ions as well as the effects of the Iridium magnetism on these elements can be probed. Thus neutron scattering will provide information on the Ni^{2+} and Ir^{4+} in the chains and on the R^{3+} ions in the pyrochlores, as well as on the coupling between these two ions and the Ir^{4+} ions.

Resonant X-ray scattering allows to choose the chemical element that will be probed depending on the incoming X-ray energy. The latter will be fixed at a resonance edge of the chosen element. In this study, we have worked at the Ir L_3 resonance edge, therefore the measurements were only sensitive to the Ir ions. Using this technique, we were able to go further in the understanding of the Ir properties and to achieve a coherent picture of the whole system in agreement with the neutron results.

In summary, using the combination of these three techniques, we were able to probe the physical properties of the whole system and also the properties of each magnetic elements together with its coupling with the other element. This study is therefore a nice example of the complementary of different techniques which are often put in competition with each other.

In this chapter, I gave an overview of the motivations for studying iridium oxides and I briefly described the physical properties related to the iridates and to the two compounds that will be presented in this manuscript.

Bibliography

[Bal11] L. Balents. Viewpoint: Weyl electrons kiss. *Physics*, 4, 2011.

[BG01] Steven T. Bramwell and Michel J. P. Gingras. Spin ice state in frustrated magnetic pyrochlore materials. *Science*, 294(5546):1495–1501, 2001.

[BJC+14] A. Biffin, R. D. Johnson, Sungkyun Choi, F. Freund, S. Manni, A. Bombardi, P. Manuel, P. Gegenwart, and R. Coldea. Unconventional magnetic order on the hyperhoneycomb Kitaev lattice in β-Li_2IrO_3: Full solution via magnetic resonant x-ray diffraction. *Phys. Rev. B*, 90:205116, Nov 2014.

[BJK+14] A. Biffin, R. D. Johnson, I. Kimchi, R. Morris, A. Bombardi, J. G. Analytis, A. Vishwanath, and R. Coldea. Noncoplanar and Counterrotating Incommensurate Magnetic Order Stabilized by Kitaev Interactions in γ-Li_2IrO_3. *Phys. Rev. Lett.*, 113:197201, Nov 2014.

[CBM+98] G. Cao, J. Bolivar, S. McCall, J. E. Crow, and R. P. Guertin. Weak ferromagnetism, metal-to-nonmetal transition, and negative differential resistivity in single-crystal Sr_2IrO_4. *Phys. Rev. B*, 57:R11039–R11042, May 1998.

[CCK+12] S. K. Choi, R. Coldea, A. N. Kolmogorov, T. Lancaster, I. I. Mazin, S. J. Blundell, P. G. Radaelli, Yogesh Singh, P. Gegenwart, K. R. Choi, S.-W. Cheong, P. J. Baker, C. Stock, and J. Taylor. Spin Waves and Revised Crystal Structure of Honeycomb Iridate Na_2IrO_3. *Phys. Rev. Lett.*, 108:127204, Mar 2012.

[CSH+94] M. K. Crawford, M. A. Subramanian, R. L. Harlow, J. A. Fernandez-Baca, Z. R. Wang, and D. C. Johnston. Structural and magnetic studies of Sr_2IrO_4. *Phys. Rev. B*, 49:9198–9201, Apr 1994.

[GCS+13] H. Gretarsson, J. P. Clancy, Yogesh Singh, P. Gegenwart, J. P. Hill, Jungho Kim, M. H. Upton, A. H. Said, D. Casa, T. Gog, and Young-June Kim. Magnetic excitation spectrum of Na_2IrO_3 probed with resonant inelastic x-ray scattering. *Phys. Rev. B*, 87:220407, Jun 2013.

[GWKJ+12] Ara Go, William Witczak-Krempa, Gun Sang Jeon, Kwon Park, and Yong Baek Kim. Correlation effects on 3d topological phases: From bulk to boundary. *Phys. Rev. Lett.*, 109:066401, Aug 2012.

[IYK14] Masatoshi Imada, Youhei Yamaji, and Moyuru Kurita. Electron correlation effects on topological phases. *Journal of the Physical Society of Japan*, 83(6):061017, 2014.

[JK09] G. Jackeli and G. Khaliullin. Mott Insulators in the Strong Spin-Orbit Coupling Limit: From Heisenberg to a Quantum Compass and Kitaev Models. *Phys. Rev. Lett.*, 102:017205, 2009.

[Kha05] Giniyat Khaliullin. Orbital order and fluctuations in mott insulators. *Progress of Theoretical Physics Supplement*, 160:155–202, 2005.

[Kit06] Alexei Kitaev. Anyons in an exactly solved model and beyond. *Annals of Physics*, 321(1):2 – 111, 2006. January Special Issue.

[KJM+08] B. J. Kim, Hosub Jin, S. J. Moon, J.-Y. Kim, B.-G. Park, C. S. Leem, Jaejun Yu, T. W. Noh, C. Kim, S.-J. Oh, J.-H. Park, V. Durairaj, G. Cao, and E. Rotenberg. Novel $J_{\text{eff}} = 1/2$ Mott State Induced by Relativistic Spin-Orbit Coupling in Sr_2IrO_4. *Phys. Rev. Lett.*, 101:076402, 2008.

[KK82] K. I. Kugel and D. I. Khomskii. The jahn-teller effect and magnetism: transition metal compounds. *Sov. Phys. Uspekhi*, 25:231–256, 1982.

[KNY+14] Vamshi M Katukuri, S Nishimoto, V Yushankhai, A Stoyanova, H Kandpal, Sungkyun Choi, R Coldea, I Rousochatzakis, L Hozoi, and Jeroen van den Brink. Kitaev interactions between j = 1/2 moments in honeycomb Na_2IrO_3 are large and ferromagnetic: insights from *ab initio* quantum chemistry calculations. *New Journal of Physics*, 16(1):013056, 2014.

[KOK+09] B. J. Kim, H. Ohsumi, T. Komesu, S. Sakai, T. Morita, H. Takagi, and T. Arima. Phase-Sensitive Observation of a Spin-Orbital Mott State in Sr_2IrO_4. *Science*, 323(5919):1329–1332, 2009.

[KWF11] Mehdi Kargarian, Jun Wen, and Gregory A. Fiete. Competing exotic topological insulator phases in transition-metal oxides on the pyrochlore lattice with distortion. *Phys. Rev. B*, 83:165112, Apr 2011.

[KY11] Itamar Kimchi and Yi-Zhuang You. Kitaev-Heisenberg-J_2-J_3 model for the iridates A_2IrO_3. *Phys. Rev. B*, 84:180407, Nov 2011.

[KYI11] Moyuru Kurita, Youhei Yamaji, and Masatoshi Imada. Topological insulators from spontaneous symmetry breaking induced by electron correlation on pyrochlore lattices. *Journal of the Physical Society of Japan*, 80(4):044708, 2011.

[KYK+06] B. J. Kim, Jaejun Yu, H. Koh, I. Nagai, S. I. Ikeda, S.-J. Oh, and C. Kim. Missing xy-Band Fermi Surface in 4d Transition-Metal Oxide Sr_2RhO_4: Effect of the Octahedra Rotation on the Electronic Structure. *Phys. Rev. Lett.*, 97:106401, Sep 2006.

[LBY+11] X. Liu, T. Berlijn, W.-G. Yin, W. Ku, A. Tsvelik, Young-June Kim, H. Gretarsson, Yogesh Singh, P. Gegenwart, and J. P. Hill. Long-range magnetic ordering in Na_2IrO_3. *Phys. Rev. B*, 83:220403, Jun 2011.

[Mat76] L. F. Mattheiss. Electronic structure of RuO_2, OsO_2, and IrO_2. *Phys. Rev. B*, 13:2433–2450, Mar 1976.

[MCU+15] Eric Yue Ma, Yong-Tao Cui, Kentaro Ueda, Shujie Tang, Kai Chen, Nobumichi Tamura, Phillip M. Wu, Jun Fujioka, Yoshinori Tokura, and Zhi-Xun Shen. Mobile metallic domain walls in an all-in-all-out magnetic insulator. *Science*, 350(6260):538–541, 2015.

[MWHT11] Kazuyuki Matsuhira, Makoto Wakeshima, Yukio Hinatsu, and Seishi Takagi. Metal-Insulator Transitions in Pyrochlore Oxides $Ln_2Ir_2O_7$. *J. Phys. Soc. Jpn*, 80(9):094701, 2011.

[NvdB15] Zohar Nussinov and Jeroen van den Brink. Compass models: Theory and physical motivations. *Rev. Mod. Phys.*, 87:1–59, Jan 2015.

[PB10] Dmytro Pesin and Leon Balents. Mott physics and band topology in materials with strong spin-orbit interaction. *Nature Physics*, 6:376–381, 2010.

[RK14] J. G. Rau and H.-Y. Kee. Trigonal distortion in the honeycomb iridates: Proximity of zigzag and spiral phases in Na_2IrO_3. *ArXiv e-prints*, August 2014.

[SKYK15] R. Schaffer, E. Kin-Ho Lee, B.-J. Yang, and Y. B. Kim. Recent progress on correlated electron systems with strong spin-orbit coupling. *ArXiv e-prints*, December 2015.

[SPWP14] Yuriy Sizyuk, Craig Price, Peter Wölfle, and Natalia B. Perkins. Importance of anisotropic exchange interactions in honeycomb iridates: Minimal model for zigzag antiferromagnetic order in Na_2IrO_3. *Phys. Rev. B*, 90:155126, Oct 2014.

[TN00] Y. Tokura and N. Nagaosa. Orbital physics in transition-metal oxides. *Science*, 288(5465):462–468, 2000.

[Tou77] G. Toulouse. Theory on the frustration effect in spin glasses : I. *Communications on Physics*, 2:115, 1977.

[vdB04] Jeroen van den Brink. Orbital-only models: ordering and excitations. *New Journal of Physics*, 6(1):201, 2004.

[WKCK10] William Witczak-Krempa, Ting Pong Choy, and Yong Baek Kim. Gauge field fluctuations in three-dimensional topological mott insulators. *Phys. Rev. B*, 82:165122, Oct 2010.

[WKCKB14] William Witczak-Krempa, Gang Chen, Yong Baek Kim, and Leon Balents. Correlated quantum phenomena in the strong spin-orbit regime. *Annu. Rev. Condens. Matter Phys.*, 5(1):57–82, 2014.

[WKGK13] William Witczak-Krempa, Ara Go, and Yong Baek Kim. Pyrochlore electrons under pressure, heat, and field: Shedding light on the iridates. *Phys. Rev. B*, 87:155101, Apr 2013.

[WKK12] William Witczak-Krempa and Yong Baek Kim. Topological and magnetic phases of interacting electrons in the pyrochlore iridates. *Phys. Rev. B*, 85:045124, 2012.

[WTVS11] Xiangang Wan, Ari M. Turner, Ashvin Vishwanath, and Sergey Y. Savrasov. Topological semimetal and fermi-arc surface states in the electronic structure of pyrochlore iridates. *Phys. Rev. B*, 83:205101, May 2011.

[YCC+12] Feng Ye, Songxue Chi, Huibo Cao, Bryan C. Chakoumakos, Jaime A. Fernandez-Baca, Radu Custelcean, T. F. Qi, O. B. Korneta, and G. Cao. Direct evidence of a zigzag spin-chain structure in the honeycomb lattice: A neutron and x-ray diffraction investigation of single-crystal Na_2IrO_3. *Phys. Rev. B*, 85:180403, May 2012.

[YNK+14] Youhei Yamaji, Yusuke Nomura, Moyuru Kurita, Ryotaro Arita, and Masatoshi Imada. First-Principles Study of the Honeycomb-Lattice Iridates Na_2IrO_3 in the Presence of Strong Spin-Orbit Interaction and Electron Correlations. *Phys. Rev. Lett.*, 113:107201, Sep 2014.

Chapter 2

Experimental techniques

Contents

In this chapter I will give details on the different experimental techniques used during my PhD. I will start with sample preparation. Then I will describe the magnetometry measurements that were used to determine the magnetic properties of the compounds. I will finish by experiments performed at large scale facilities: neutron and synchrotron X-ray scattering, beginning by a general reminder on both neutron and X-ray scattering and then going into the details of the specific techniques and instruments I have used during my PhD work.

2.1 Sample synthesis

Two families of compounds have been studied as part of this work: Sr_3NiMO_6 with M = Pt or Ir and $R_2Ir_2O_7$ with R = Y, Tb, Er, Dy, Ho, Yb, Gd. For the first family, both polycrystalline and single crystals have been synthesized. The solid state reaction and flux method have been used to synthesize respectively the powder samples and the single crystals. Concerning the second family of compounds: all measurements have been performed on polycrystalline samples. I will describe the different techniques used in order to produce high quality samples. We have also tried to synthesized single crystal of the pyrochlore but did not succeed to grow large enough sample for measurements. I will give some details on the technique used and the challenge that represents the synthesis of this compounds.

All the synthesis were performed with the collaboration of Pascal Lejay, Abdel Hadj-Azzem and Joël Balay at the Institut Néel

2.1.1 Synthesis techniques

2.1.1.1 Solid state reaction

The solid state reaction is the most widely used method to prepare polycrystalline samples. For this method, the solid materials are mixed in an agate mortier and pestle until a homogeneous mix is obtained. The mixed reagents are then pressed into a pellet using a hydrostatic press. This pellet is placed into a crucible to be heated in a furnace up to high temperature. The heat treatment is usually performed in several stages with intermediate grinding in order to ensure the homogeneity of the mix.

Several parameters need to be carefully considered for a successful solid state reaction:

- the starting reagents need to be very pure and put in the exact stoichiometric proportion otherwise parasite phases could be synthesized at the same time
- the reagents need to be well ground into a fine powder and well mixed in order to maximize the surface area and thus insure an efficient reaction
- depending on the reagents, specific crucibles and/or environment are required. Indeed the crucible has to be chemically inert to the reactants under the heating conditions used. The most used materials for crucibles are ceramic (silica, alumina, zirconia, ...) and precious metals (Pt, Au, Ag, ...). The atmosphere will also affect the reaction. In order to form compounds with an element having an higher oxidation state, oxidizing gas (air, O_2) might be used. On the contrary to form a low oxidation state, reducing gas (H_2/Air, CO/CO_2) will be used and finally noble gases (usually Ar) are used to prevent a change of the oxidation state.
- the temperature at which the reagents are heated needs to be carefully chosen depending on the phase stability diagram of the desired phase.

2.1.1.2 Flux method

The flux method is a technique which is mostly used to produce single crystal of materials presenting an incongruent melting. This corresponds to the situation when cooling the desired liquid phase will give two different solid phases with stoichiometry differing from the melt (see Fig. 2.1).

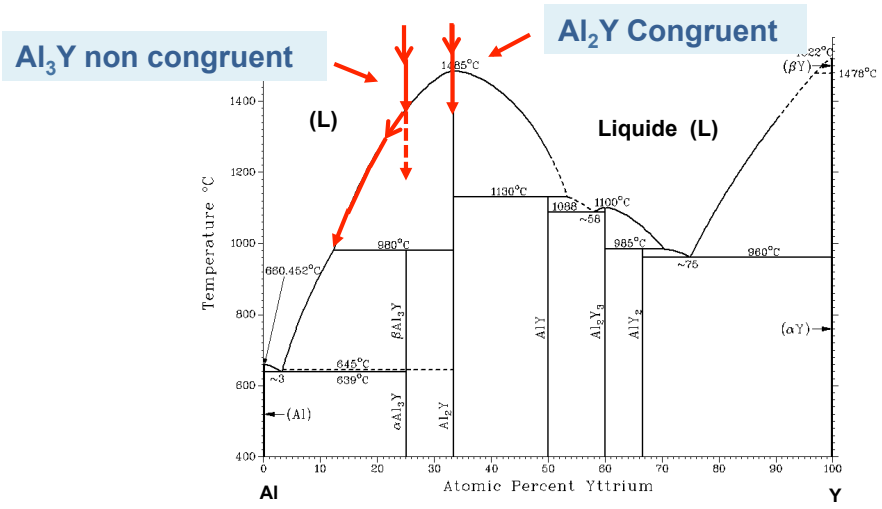

Figure 2.1 – *Binary phase diagram of the Al-Y mix. The red arrows show what happens when cooling the non-congruent Al_3Y and the congruent Al_2Y alloys*

For this method the solid materials are dissolved in a flux reagent, which is solid at room temperature but presents a melting point below the one of the desired phase. Upon heating the mix above the flux melting point, the materials dissolve into the liquid flux. At this point the flux-solid solution is supersaturated and a nucleation process of the desired material begins. Then, the solution is slowly cooled down, leading to a slow increase of the supersaturation of the flux-solid solution and thus to an increase of the nucleated crystal size. The choice of the maximum temperature and the speed at which the temperature is cooled down will strongly affect the efficiency of this method and thus the size of the single crystals.

The flux has to be carefully chosen depending on its melting temperature and on the desired phase melting temperature. The flux can either be a different material or one of the starting material itself. In the second case the method is called the *self-flux* method.

Also one can choose to start with the desired phase which has been previously synthesized as a powder or to start directly with the different reagents mixed in the correct stoichiometry similarly to the solid state reaction.

At the end of the reaction, the main difficulty is to separate the crystals from the flux. Usually the solution is mixed into a base or acid solution which dissolves only the flux. For some fluxes, water or alcohol can also simply be used.

2.1.1.3 Mineralization process

The mineralization process is another method to synthesize polycrystalline samples. This method can be seen as an intermediate technique between the solid state reaction and the flux method.

The solid starting reagents are first ground and mixed together, then a small amount of a flux material is added to the mix. This final preparation is then pressed into a pellet and placed into a

crucible to be heated up to a temperature just above the flux melting point. The temperature treatment is then similar to the one used for solid state reaction. In this case the flux will enhance the reaction as it will favor the diffusion of the reagents inside the pellet. Besides, the amount of flux agent used being very small compared to the one used for the flux method, it is much easier to clean the solution in order to obtain the desired phase.

2.1.2 Synthesis of the Sr_3NiMO_6 compounds

Powder samples

The polycrystalline samples of Sr_3NiPtO_6 and Sr_3NiIrO_6 have been synthesized using the solid state reaction method based on the following reaction:

$$3\ SrCO_3 + NiO + Pt/Ir \longrightarrow Sr_3Ni(Pt/Ir)O_6 \tag{2.1}$$

The synthesis were performed inside an alumina crucible in the air atmosphere environment, with the following heat treatment:

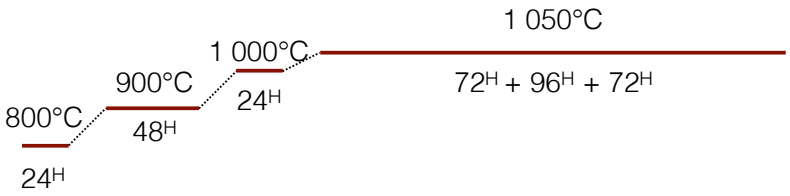

At each of these steps the pellets were ground and X-ray diffraction performed to check the evolution of the synthesis.

Single crystals

The single crystals were grown using the flux method. The starting reagents were mixed together with a K_2CO_3 flux. The mixture was then put into an alumina (Al_2O_3) crucible. The heat treatment, illustrated in Fig. 2.2, was then applied in air.

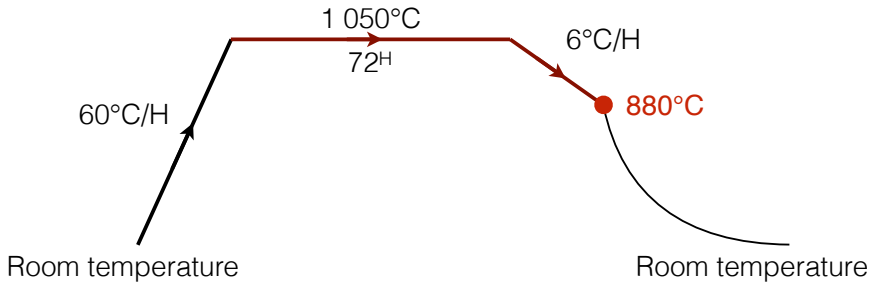

Figure 2.2 – *Heat treatment applied for the synthesis of the Sr_3NiMO_6 compounds using the flux process.*

Single crystals with sizes up to 1 mm in width and 0.3 mm of height were obtained (see Fig. 2.3). These were first characterized using X-ray diffraction on powder made of crushed single crystals. This allows to check that the right phase was produced without the presence of impurities. Then Energy

Dispersive X-ray (EDX) spectroscopy using a Scanning Electron Miscroscope (SEM) was performed on several single crystals. This technique allows to quantify the relative amount of the different chemical species in the sample. Last, Laue diffraction measurements were made in order to ensure that the crystals present a unique crystalline domain (see Fig. 2.4).

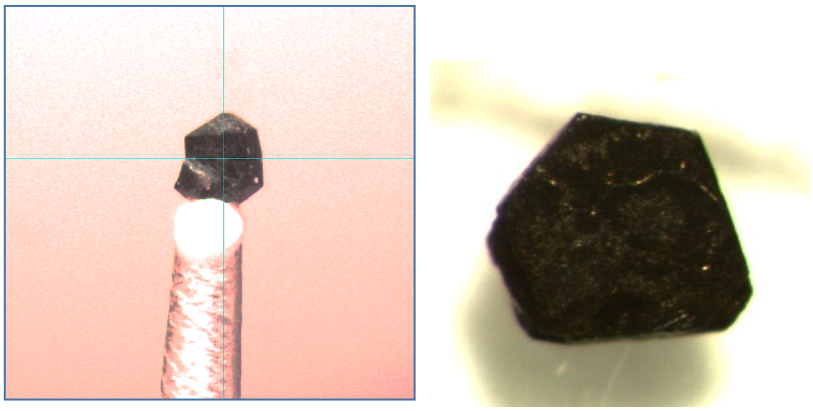

Figure 2.3 – *Single crystals of Sr_3NiPtO_6 (left) and Sr_3NiIrO_6 (right).*

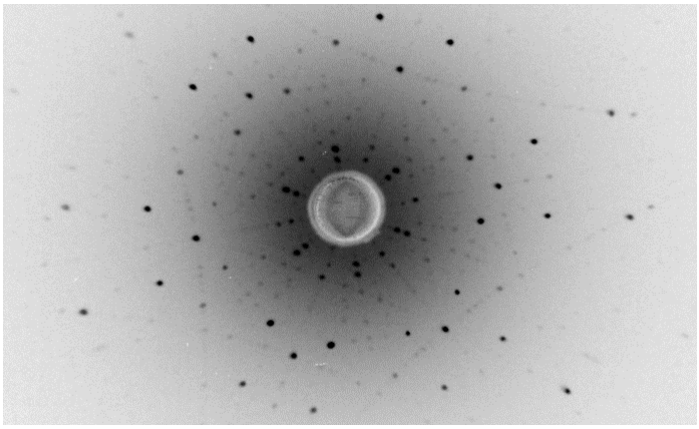

Figure 2.4 – *Laue diffraction pattern of Sr_3NiPtO_6 realized with the incident X-ray beam aligned along the chain axis (**c** axis).*

2.1.3 Synthesis of the $R_2Ir_2O_7$ compounds

Powder samples

For the pyrochlore iridates several methods have been used to synthesize the polycrystalline samples.

1. *Solid state reaction*

   This is the first method used for the synthesis of the pyrochlore compounds with the following rare-earth elements: Y, Er and Tb. The chemical reaction is:

   $$R_2O_3 + 2\ IrO_2 \longrightarrow R_2Ir_2O_7 \tag{2.2}$$

   The synthesis were performed into an alumina crucible in the atmosphere environment, with the following heat treatment:

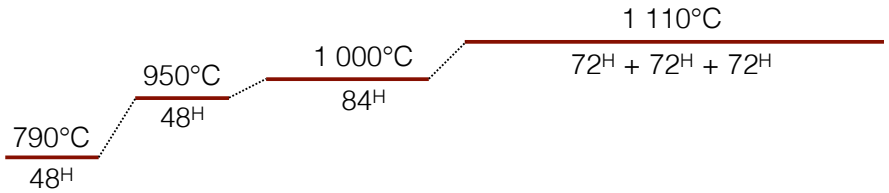

This method was efficient for the synthesis of $Y_2Ir_2O_7$. However, we were unable to synthesize the pure phase of the other pyrochlore compounds. A large weight fraction of rare-earth oxide impurities (between 30 and 40 %) was present in the final product. This is related to the fact that the iridium oxide evaporates during the reaction, thus the reaction stoichiometry was changed. We have tried to change the reaction stoichiometry by increasing the amount of iridium oxide, up to 2:2.2:7 instead of 2:2:7, in order to overcome its evaporation. This allowed to decrease the proportion of rare earth oxide impurities only down to $\approx$ 10 %.

2. *Flux method*

Polycrystalline sample were also synthesized using the flux method. The starting reagents were mixed together with a KF flux. KF reacts with water to produce HF which is an extremely corrosive acid. Therefore KF had to be manipulated into a glove box with a purged environment dedicated to the preparation of KF-based samples. The mixture was then put into an sealed Platinum crucible in order to avoid the presence of air inside the crucible. The heat treatment illustrated in Fig. 2.5 was then applied.

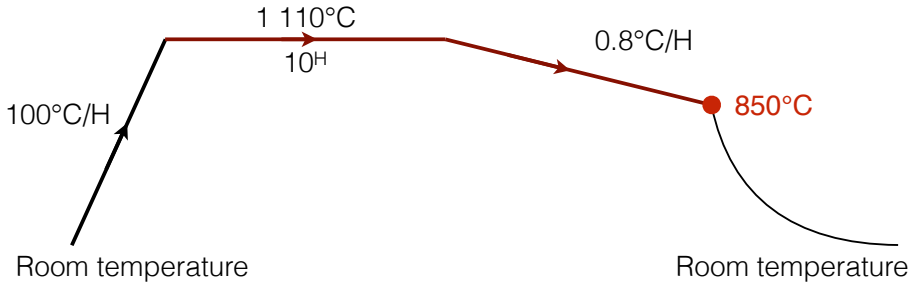

Figure 2.5 – *Heat treatment applied for the synthesis of the $R_2Ir_2O_7$ compounds using the flux process.*

Using this method, we were able to produce much better quality polycrystalline samples than using the solid state reaction method with only 1-2 % of rare-earth oxides impurities.

However, this technique presents a few drawbacks:

- KF is extremely unstable in air and form a highly corrosive acid.
- The volume of the sealed Pt crucible was relatively small, allowing to synthesize only up to 0.5 g of sample per synthesis.
- The synthesis is slow as the heat treatment is long ($\approx$ 14 days)

Taking into account that the amount of sample needed for neutron scattering experiment is around 3 g, 84 days are necessary to produce the desired quantity for only one $R_2Ir_2O_7$ compound.

This method was used to produce the pyrochlore compounds with Er and Tb.

3. *Mineralization process*

   The mineralization process was finally used to synthesize the polycrystalline $R_2Ir_2O_7$ compounds. The flux used for this reaction was KF, similarly to the flux method described previously. The starting reagents were mixed together with a small amount of KF inside the glove box described previously. Then, the mixture was pressed into a pellet and placed into an open Pt crucible. The heat treatment detailed in Fig.2.6 was then applied under air atmosphere.

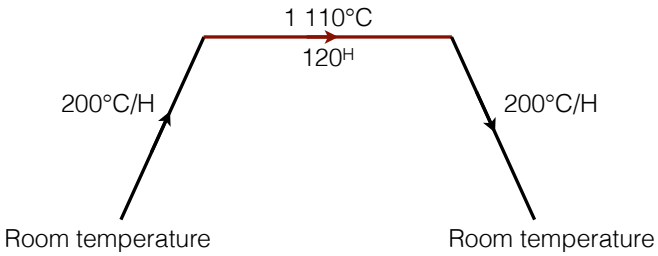

Figure 2.6 – *(Heat treatment applied for the synthesis of the $R_2Ir_2O_7$ compounds using the mineralization process.*

Using this process, very high quality polycrystalline samples were obtained with less than 1 % of magnetic impurities.

Moreover this technique requires considerably less times than the flux method. Indeed the amount of produced sample is no longer limited and the heat treatment is only 6 days long. Therefore it requires 14 times less time to synthesize the same amount of sample. This method was used to produce the pyrochlore compounds with Ho, Dy, Yb and Gd.

Single crystals

We have tried to grow single single crystals of the pyrochlore compound studied during my PhD project (with R = Y, Tb, Er, Ho, Dy, Yb and Gd) but have been unsuccessful so far. Note that we have been successful in growing small single crystals of $Pr_2Ir_2O_7$. These were obtained using a KF flux, starting from the Pr oxide and Ir oxides powders mixed together and following the same heat treatment as for the polycrystalline sample synthesized using the flux method (Fig. 2.5). Small bipyramidal $Pr_2Ir_2O_7$ single crystals of about 200 µm of width were obtained using this method (see Fig. 2.7).

In the literature, only single crystals of $Eu_2Ir_2O_7$, $Nd_2Ir_2O_7$ and $Pr_2Ir_2O_7$ are reported so far [CGL+15, TKT+15]. These rare-earths correspond to the light rare-earths while all our studied pyrochlores are based on heavy rare-earths. Therefore we believe that depending of the rare-earth element the synthesis process should be adapted in some way.

P. Lejay and A. Hadj-Azzem have started to investigate on this matter by trying different fluxes and different heat treatments. However, this remains an ongoing work at this stage.

Figure 2.7 – *$Pr_2Ir_2O_7$ single crystal.*

2.2 SQUID magnetometers

The magnetometers allow to probe the static (DC) and dynamic (AC) magnetic properties of a sample at the macroscopic level. Two types of measurement are generally performed:

- magnetic field dependence of the magnetization at fixed temperature. This allows to observe possible hysteresis behavior or magnetic field induced transitions.
- temperature dependence of the magnetization. This allows to see the presence of magnetic transitions, which are characterized by a deviation of the magnetic susceptibility, $\chi = \frac{\partial M}{\partial H}$, from the Curie-Weiss law:

$$\chi(T) = \frac{C}{T - \theta} \tag{2.3}$$

  where C is the material-specific Curie constant and θ is the Curie-Weiss temperature. This law describes the evolution of a paramagnet magnetization as function of the temperature. The value of the Curie temperature depends on the magnetic interactions: $\theta = 0$ if there is no interactions and $\theta > 0$ (resp. $\theta < 0$) for ferromagnetic (resp. antiferromagnetic) interactions. The magnetic susceptibility can also be measured following the Zero field cooled (ZFC) - Field cooled (FC) procedure. This allows to probe phenomena such as magnetic viscosity or the presence of magnetic domains. In such cases, a difference between the ZFC and FC curves will be observed.

The magnetization measurements have been performed using different SQUID (Superconducting QUantum Interference Device) magnetometers: two commercial devices, the MPMS-XL® and MPMS®3 Quantum devices and a magnetometer built at the Institut Néel by C. Paulsen.

The measurement is based on the extraction method using the displacement of the sample inside a set a detection coils. The sample displacement creates a variation of the magnetic flux:

$$\delta\phi = \frac{1}{\mu_0} \iiint \frac{B}{I} M \mathrm{d}V \tag{2.4}$$

where μ_0 is the vacuum permeability, B is the magnetic field created by the current I flowing into the detection coils and M is the sample magnetization. This detections coils are then coupled to a SQUID device, whose current depends on the magnetic flux flowing through it (see Fig. 2.8). The SQUID is sensitive to flux quanta and can measure magnetization with a very good precision of 10^{-10} A $\cdot$ m^2

Quantum Design MPMS-XL® magnetometer

This magnetometer is a commercial device that can produce magnetic field up to 5 T and reach temperature down to 2 K.

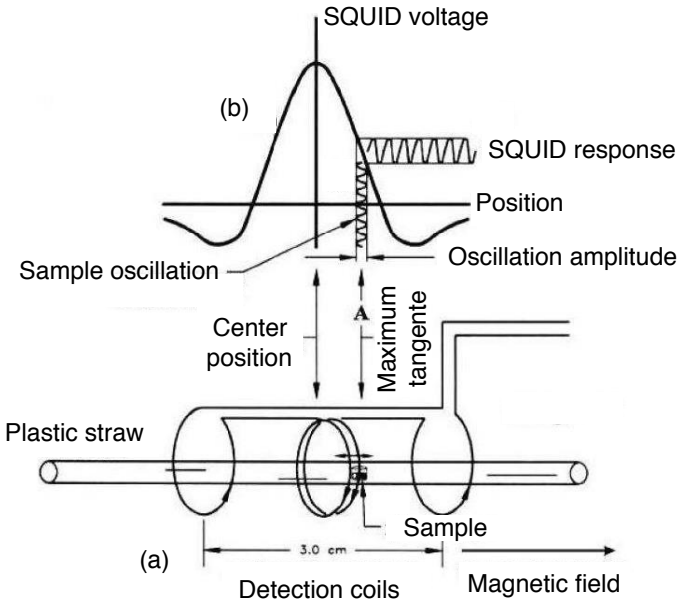

Figure 2.8 – *Detection system of a commercial Quantum Design MPMS-XL® SQUID magnetometer: (a) superconducting coils used for the detection, (b) variation of the SQUID voltage as function of the sample position*

The measurements can be performed using two different modes:

- the DC mode where the sample is moved along the full length of the detection coils.
- the Reciprocating Sample Option (RSO) where the sample is placed in such a way that the measure will be sensitive to a very small displacement as illustrated in Fig. 2.8. The sample is rapidly oscillating around this position and the SQUID response is recorded.

Quantum Design MPMS®3 magnetometer

This magnetometer is a commercial device using the Vibrating Sample mode. It allows to reach magnetic field up to 7 T and temperature down to 2 K. For the measurement, the sample is positioned in such a way that the SQUID voltage is maximum and oscillates at a fixed frequency around this position. The produced signal is then a sinusoidal signal whose frequency is the one fixed for the sample vibration and that is detected using a synchronous detection. This detection system gives a precision of 10^{-11} A $\cdot$ m^2

Very low temperature magnetometer

This magnetometer has been developed at the Institut Néel by C. Paulsen and presents characteristics which makes it unique worldwide. Indeed, it can reach magnetic field up to 8 T and is equipped with a ^{3}He - ^{4}He dilution refrigerator allowing it to reach temperatures down to 80 mK. The measurement system is similar to the DC mode with the sample moving between the two detection coils.

2.3 Neutron scattering

2.3.1 Generalities

2.3.1.1 General properties

Neutrons are elementary particles whose existence was first predicted by E. Rutherford in 1920 and discovered in 1932 by J. Chadwick [Cha32]. The neutron has a mass $m_n = 1.67493 \times 10^{-27}$ kg, it carries a zero electric charge, a nuclear spin $S = 1/2$ and a magnetic moment $\mu_n = -\gamma\mu_N\sigma = -1.913\ \mu_N$, where $\mu_N = \frac{e\hbar}{2m_p}$ is the nuclear magneton and m_p is the proton mass. It has been used as a tool for scattering experiments for the first time by C. Schull in 1946. Indeed its unique properties make it a very powerful tool to probe condensed matter systems.

1. The neutron has no charge thus is not subject to Coulomb interaction and can interact directly with the nuclei by penetrating deeply in matter.
2. Neutrons are particles but can also be considered as waves. The particle energy is related to the temperature: $E = k_B T$, where k_B is the Boltzmann constant. The wave is characterized by the wavevector $\vec{k} = \frac{m}{\hbar}\vec{v}$. The associated wavelength is given by the de Broglie formula $\lambda = \frac{2\pi}{k} = \frac{h}{m_n v}$, where h is the Planck constant and v the neutron velocity. Thermal neutrons ($T = 300$ K) have a velocity $v \approx 2200\ \mathrm{m \cdot s^{-1}}$ which gives a wavelength $\lambda \approx 1.8\ \mathrm{\AA^{-1}}$. This wavelength is of the order of interatomic distances in condensed matter, making thermal neutrons a tool well suited to probe condensed matter structures.
3. Neutrons have a spin angular momentum and can thus interact with magnetic fields, in particular induced by unpaired electrons. Neutrons are therefore also an ideal probe for the study of magnetism.
4. The neutron energy is given by its kinetic energy $E = \frac{(\hbar k)^2}{2m}$. For thermal neutrons $v \approx 2200\ \mathrm{m \cdot s^{-1}}$ which gives $E \approx 25$ meV. Their energy is therefore of the same order of magnitude than the nuclear lattice vibrations and the magnetic excitations, making them also useful to probe the dynamical properties.

2.3.1.2 Production of neutrons

There exists two methods which are commonly used to produce neutrons.

Fission process

Neutron can be produced as the results of a nuclear reaction: the fission of an enriched Uranium nucleus ${}^{235}_{92}U$ into fissile isotopes by thermal neutrons (see Fig. 2.9). The production is a self-sustaining nuclear chain reaction.

$$ {}^{235}_{92}U\ +\ {}^{1}_{0}n\ \rightarrow\ {}^{236}_{92}U\ \rightarrow\ X\ + Y + k\,{}^{1}_{0}n \tag{2.5} $$

X and Y are the fission products and k is the number of produced neutrons. k can vary between 2 and 5 from one fission process to another and the average value is $k = 2.5$. The energy of the produced neutrons is $E \approx 2$ MeV. The probability for a neutron to hit an Uranium nucleus is larger for thermal neutrons, the produced neutrons thus need to be slowed down in order to be used in the fission process and to sustain the chain reaction. This is performed using the collision of the neutrons with a moderator nuclei. As the loss energy process is more efficient for small nuclei, the following elements are mostly used as moderators: hydrogen (water), deuterium (heavy water), beryllium and graphite. After a dozen collisions, the neutrons are in a thermal equilibrium with the moderator and the speed

distribution is described by a Maxwell-Boltzmann distribution:

$$\phi(v) \propto v^3 \exp[-(\frac{v}{v_0})^2] \tag{2.6}$$

centered on a mean value v_0 given by $E = \frac{1}{2}mv_0^2 \sim k_B T$. Depending on the moderator, neutrons with different energies can be obtained:

- For a very low temperature moderator (liquid hydrogen or deuterium, $T = 20$ K), cold neutrons are obtained with $E \approx 1.5$ meV and $\lambda \approx 3.5$ Å.
- For a room temperature moderator (water, $T = 300$ K), thermal neutrons are obtained with $E \approx 25$ meV and $\lambda \approx 1.8$ Å.
- Using a hot moderator (graphite heated at 2000 K), hot neutrons are obtained with $E > 100$ meV and $\lambda > 0.5$ Å.

Once slowed down, a fraction of the neutrons produced are used in the chain reaction, the other part being used for the experiments.

There are several nuclear reactors among which we can name: the Institut Laue-Langevin in Grenoble, that is the brightest source in the world (flux: 1.5×10^{15} n/s/cm^2, thermal power: 58 MW), Orphée at the Laboratoire Léon Brillouin in Saclay (thermal power: 14 MW), the High Flux Isotope Reactor in Oak Ridge (TN), USA (thermal power: 85 MW), ...

Spallation process

A target made of a heavy metal (U, W, Hg, ...) is hit by high energy protons ($E \approx$ 1GeV) produced by a particle accelerator. Several high energy ($\sim$ MeV) particles are ejected in the process (neutrons, protons, neutrinos, ... - see Fig. 2.9). The neutrons need to be moderated using a process similar to the one described previously. In general, spallation sources are using pulsed proton jets that produce intense neutrons wave packets with a frequency of 50 Hz. In the past few years, the spallation sources underwent a strong interest as they produce less nuclear wastes than nuclear sources.

Examples of spallation sources: ISIS in England (pulsed source), SINQ at PSI in Switzerland (continuous source), ESS in Sweden (pulsed source, currently in construction), ...

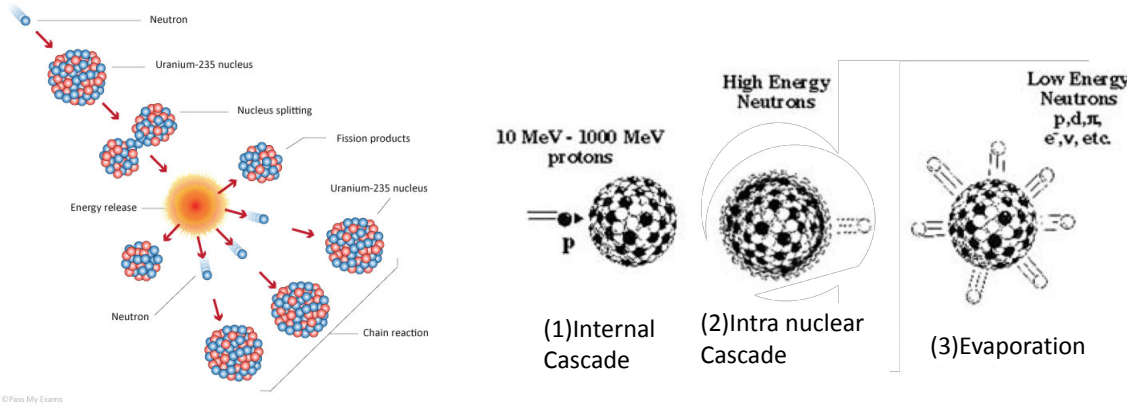

Figure 2.9 – *Sketches of the fission (left) and spallation (right) processes.*

2.3.1.3 Scattering cross section

In this paragraph, I will briefly present the formalism of the interaction between neutrons and the matter happening during a scattering experiment. More details on this formalism can be found in

[Squ78, Lov84a, Lov84b].

During a scattering process, an incident neutron, characterized by its wavevector $\vec{k}_i$, its energy E_i and its spin σ_i, is scattered by the sample into a small solid angle $d\Omega$ with a final wavevector $\vec{k}_f$, a final energy E_f and a spin σ_f (see Fig. 2.10). During this process, the sample change from an initial state $|\lambda_i\rangle$ to a final state $|\lambda_f\rangle$. The neutron gives the sample an impulsion $\hbar\vec{Q}$, where $\vec{Q} = \vec{k}_i - \vec{k}_f$ and an energy $\hbar\omega = E_i - E_f = E_{\lambda_i} - E_{\lambda_f}$, where E_{λ_i} and E_{λ_f} are the initial and final energies of the sample.

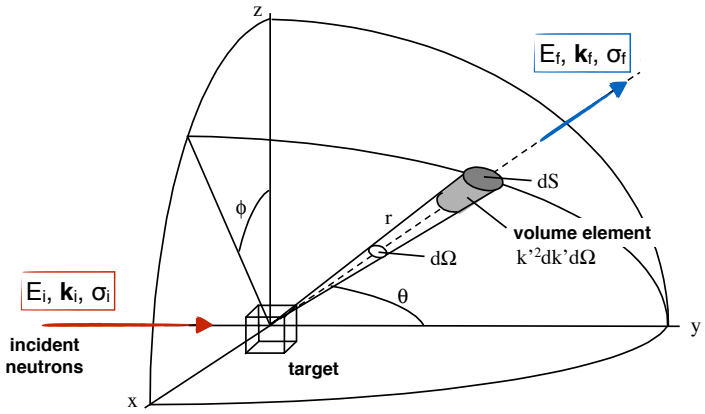

Figure 2.10 – *Sketch of a scattering process.*

The detectors will measure the number of neutrons scattered into the solid angle $d\Omega$ with energies between E_f and $E_f + dE$, this intensity is directly proportional to the partial differential scattering cross section $\frac{d^2\sigma}{d\Omega dE}$:

$$I_{scattered} = I_0 \, F_{scale} \, f_{corr} \, \frac{d^2\sigma}{d\Omega dE}, \tag{2.7}$$

where I_0 is the incident intensity, F_{scale}, a scaling factor characteristic of the number of scatterers in the sample and f_{corr} a correction term taking into account experimental artifacts.

The expression of this cross section is obtained from the Fermi golden rule and writes:

$$\left(\frac{d^2\sigma}{d\Omega dE}\right)_{\lambda_i \to \lambda_f, \vec{k}_i \to \vec{k}_f, \sigma_i \to \sigma_f} = \frac{k_f}{k_i}\left(\frac{m}{2\pi\hbar^2}\right)^2 |\langle \lambda_f, \vec{k}_f, \sigma_f | V | \lambda_i, \vec{k}_i, \sigma_i \rangle|^2 \delta(E_i - E_f + E_{\lambda_i} - E_{\lambda_f}), \tag{2.8}$$

where V is the scattering potential. This potential depends on the nature of the interactions which can be of two types: nuclear and magnetic.

Nuclear contribution

There are nuclear forces, that are mediated by the strong force, between the neutron and the nuclei of the scattering system. These are short distance forces, much smaller than the nucleus dimension, *i.e.* 10^{-5} to 10^{-4} Å. For a scattering center j, the potential can be written as the Fermi pseudo-potential:

$$V_j(\vec{r}) = \frac{2\pi\hbar^2}{m} b_j \delta(\vec{r} - \vec{R}_j), \tag{2.9}$$

where $\vec{r}$ corresponds to the neutron position, $\vec{R}_j$ to the position of the scattering center j, and b_j to its the scattering length. From Eq. 2.8, we can easily show that the nuclear partial differential cross section

can be written as:

$$\left(\frac{d^2\sigma}{d\Omega dE}\right)_N = \frac{1}{2\pi\hbar}\frac{k_f}{k_i}\sum_{j,j'}\langle b_j b_j^*\rangle \int_{-\infty}^{\infty}\langle e^{-i\vec{Q}\cdot\vec{R}_j(0)}e^{-i\vec{Q}\cdot\vec{R}'_j(t)}\rangle e^{-i\omega t}\mathrm{d}t \tag{2.10}$$

where $\langle\cdots\rangle$ represents the thermal average (average on the initial states λ_i).

The scattering length b_j is characteristic of the interaction force between the neutron and the scattering center. It depends on the chemical element considered, on the isotope and on the nucleus spin state. It is purely real for non absorbing elements and presents an imaginary part in the other cases. For each atom, b_j can be written as:

$$b_j = \bar{b} + \Delta b_j \tag{2.11}$$

where $\bar{b}$ is the scattering length of the nucleus j averaged onto the isotopes and the spins and Δb_j is the deviation from the mean value. As a result, the nuclear cross section can be separated into two terms, the coherent $\left(\frac{d^2\sigma}{d\Omega dE}\right)_N^{coh}$ and the incoherent cross section $\left(\frac{d^2\sigma}{d\Omega dE}\right)_N^{inc}$:

$$\left(\tfrac{d^2\sigma}{d\Omega dE}\right)_N^{coh} = \tfrac{1}{2\pi\hbar}\tfrac{k_f}{k_i}\textstyle\sum_{j,j'}\bar{b_j}\bar{b'_j}\int_{-\infty}^{\infty}\langle e^{-i\vec{Q}\cdot\vec{R}_j(0)}e^{-i\vec{Q}\cdot\vec{R}'_j(t)}\rangle e^{-i\omega t}\mathrm{d}t \tag{2.12}$$

$$\left(\tfrac{d^2\sigma}{d\Omega dE}\right)_N^{inc} = \tfrac{1}{2\pi\hbar}\tfrac{k_f}{k_i}\textstyle\sum_j(\bar{b^2}_j - (\bar{b}_j)^2)\int_{-\infty}^{\infty}\langle e^{-i\vec{Q}\cdot\vec{R}_j(0)}e^{-i\vec{Q}\cdot\vec{R}_j(t)}\rangle e^{-i\omega t}\mathrm{d}t \tag{2.13}$$

The coherent cross section is related to correlations between the scattering center and corresponds to the scattering obtained if the sample was made of identical scattering centers with an averaged scattering length. This term gives rise to interference phenomena and is interesting to probe the static properties of the system such as the crystalline structure. The incoherent cross section gives information on the correlations on a scattering center and itself (autocorrelations). This term is useful to probe the dynamic of the system as it gives information on the time evolution of a particle.

The total nuclear scattering cross section is the sum of these two contributions:

$$\left(\frac{d^2\sigma}{d\Omega dE}\right)_N = \left(\frac{d^2\sigma}{d\Omega dE}\right)_N^{coh} + \left(\frac{d^2\sigma}{d\Omega dE}\right)_N^{inc} \tag{2.14}$$

The scattering cross section can also be written as function of the scattering function $S(\vec{Q},\omega)$:

$$\left(\frac{d^2\sigma}{d\Omega dE}\right)_N = \frac{\sigma_{coh}}{4\pi}\frac{k_f}{k_i}N_{at}S_{coh}(\vec{Q},\omega) + \frac{\sigma_{inc}}{4\pi}\frac{k_f}{k_i}N_{at}S_{inc}(\vec{Q},\omega) \tag{2.15}$$

where N_{at} is the number of atoms in the system, $\sigma_{coh} = 4\pi(\bar{b})^2$ and $\sigma_{inc} = 4\pi(\bar{b^2} - (\bar{b})^2)$.

$S_{coh}(\vec{Q},\omega)$ is proportional to the double Fourier transform in space and time of the pair correlation function: $\langle\rho_j(\vec{r'}+\vec{r},t)\cdot(\rho_{j'}(\vec{r'},0))\rangle$. This corresponds to the nucleus density function correlation and gives the probability to have an atom j' at the position $\vec{r'}$ at $t = 0$ and to find another atom j in $\vec{r}$, after a time t. $S_{inc}(\vec{Q},\omega)$ is proportional to the double Fourier transform in space and time of the time-dependent pair autocorrelation function: $\langle\rho_j(\vec{r'}+\vec{r},t)\cdot(\rho_j(\vec{r'},0))\rangle$.

Finally, the total nuclear scattering cross section can be expressed using a condensed expression:

$$\left(\frac{d^2\sigma}{d\Omega dE}\right)_N = \frac{k_f}{k_i}\frac{1}{2\pi\hbar}\int_{-\infty}^{\infty}\langle N^\dagger(\vec{Q},0)\cdot N(\vec{Q},t)\rangle e^{-i\omega t}\mathrm{d}t \tag{2.16}$$

Or using reduced notation:

$$\left(\frac{d^2\sigma}{d\Omega dE}\right)_N = \langle N^\dagger(\vec{Q},0)\cdot N(\vec{Q},t)\rangle_\omega \tag{2.17}$$

where $N(\vec{Q},t) = \sum_j b_j e^{i\vec{Q}\cdot\vec{R}_j(t)}$ is the nuclear structure factor, the † symbol representing the complex conjugate.

Magnetic contribution

As stated before, the neutron is also sensitive to magnetic field produced by unpaired electrons. In this case, the scattering potential can be written as:

$$V_m = -\vec{\mu_n}\cdot\vec{B}_e \tag{2.18}$$

where $\vec{B}_e = \sum_i \frac{\mu_0}{4\pi}\left(\vec{rot}\left(\frac{\vec{\mu}_e\times R_i}{R_i^3}\right) - \frac{2\mu_B}{\hbar}\frac{\vec{p}_e\times\vec{R}_i}{R_i^3}\right)$ and corresponds to the sum of the magnetic fields produced by unpaired electrons. It results from the contribution of the electron spin ($\vec{\mu}_e = -g\mu_B\vec{s}_e$: spin angular momentum of the electron, with $g \approx 2$) and from an orbital contribution ($\vec{p}_e$: electron momentum). $\vec{R}_i$ corresponds to the neutron position, the origin being the electron position and $\vec{\mu}_n = -\gamma\mu_N\sigma_n$ is the neutron magnetic moment with $\gamma \approx 1.91$, the gyromagnetic ratio of the neutron.

Using Eq. 2.8, the magnetic cross section writes:

$$\left(\frac{d^2\sigma}{d\Omega dE}\right)_M = \frac{p^2}{2\pi\hbar}\frac{k_f}{k_i}\sum_{j,j'} f_j(\vec{Q})f_j'(\vec{Q})\int_{-\infty}^{\infty}\langle\vec{m}_\perp^{j'}(0)m_\perp^j(t)e^{i\vec{Q}\cdot(\vec{R}_j(t)-\vec{R}_{j'}(t))}\rangle e^{-i\omega t}\mathrm{d}t \tag{2.19}$$

where $p = \gamma\frac{e^2}{2m_e}$ is the equivalent scattering length for 1 μ_B and $f_j(\vec{Q})$ is the magnetic form factor. The magnetic form factor takes into account the spatial extension of the electron density, which cannot be considered as a delta function, contrary to the nuclear potential. This quantity decreases for increasing $\vec{Q}$, hence neutrons are more sensitive to the magnetism for small scattering vector. $m_\perp^j$ is the magnetic moment of the atom j projected onto the plane perpendicular to the scattering vector $\vec{Q}$.

This cross section is proportional to the double Fourier transform in space and time of the correlation function associated to the magnetization density $\vec{m}^j(t)$: $\langle\vec{m}_\perp^j(\vec{r'}+\vec{r},t)\cdot\vec{m}_\perp^{j'}(\vec{r'},0)\rangle$.

It can be written in a more condensed way as:

$$\left(\frac{d^2\sigma}{d\Omega dE}\right)_M = \frac{k_f}{k_i}\frac{1}{2\pi\hbar}\int_{-\infty}^{\infty}\langle\vec{M}_\perp^\dagger(\vec{Q},0)\cdot M_\perp(\vec{Q},t)\rangle e^{-i\omega t}\mathrm{d}t \tag{2.20}$$

Or using reduced notation:

$$\left(\frac{d^2\sigma}{d\Omega dE}\right)_M = \langle\vec{M}_\perp^\dagger(\vec{Q},0)\cdot\vec{M}_\perp(\vec{Q},t)\rangle_\omega \tag{2.21}$$

where $\vec{M}_\perp(\vec{Q},t) = \frac{\gamma r_0}{g}\sum_j f_j(\vec{Q})\langle\vec{m}_\perp^j(t)\rangle e^{i\vec{Q}\cdot\vec{R}_j(t)}$, the magnetic interaction vector corresponding to the projection of the magnetic structure factor $\vec{M}(\vec{Q},t)$ on the plane perpendicular to the scattering vector.

Total cross section

The total cross section is the sum of the nuclear and of the magnetic cross sections:

$$\left(\frac{d^2\sigma}{d\Omega dE}\right) = \left(\frac{d^2\sigma}{d\Omega dE}\right)_N + \left(\frac{d^2\sigma}{d\Omega dE}\right)_M \tag{2.22}$$

$$\left(\frac{d^2\sigma}{d\Omega dE}\right) = \frac{k_f}{k_i}\frac{1}{2\pi\hbar}\left(\int_{-\infty}^{\infty}\langle N^\dagger(\vec{Q},0)\cdot N(\vec{Q},t)\rangle e^{-i\omega t}\mathrm{d}t + \int_{-\infty}^{\infty}\langle \vec{M}_\perp^\dagger(\vec{Q},0)\cdot M_\perp(\vec{Q},t)\rangle e^{-i\omega t}\mathrm{d}t\right) \quad (2.23)$$

$$\left(\frac{d^2\sigma}{d\Omega dE}\right) = \langle N^\dagger(\vec{Q},0)\cdot N(\vec{Q},t)\rangle_\omega + \langle \vec{M}_\perp^\dagger(\vec{Q},0)\cdot \vec{M}_\perp(\vec{Q},t)\rangle_\omega \quad (2.24)$$

2.3.2 Elastic coherent neutron scattering

In this section, we will now focus on the formalism associated to elastic neutron scattering from a crystal, *i.e.* diffraction. In this case, there is no transferred energy: $\hbar\omega = E_i - E_f = E_{\lambda_f} - E_{\lambda_i} = 0$ and the cross section becomes:

$$\left(\frac{d^2\sigma}{d\Omega dE}\right)_{el}^{coh} = \langle N^\dagger(\vec{Q},0)\cdot N(\vec{Q},t)\rangle_{\omega=0} + \langle \vec{M}_\perp^\dagger(\vec{Q},0)\cdot \vec{M}_\perp(\vec{Q},t)\rangle_{\omega=0} \quad (2.25)$$

Nuclear contribution

The nuclear cross section is now expressed as :

$$\left(\frac{d^2\sigma}{d\Omega dE}\right)_{N,el}^{coh} = \frac{(2\pi)^3}{V}N_{cell}\sum_{\vec{H}}|N(\vec{Q})|^2\delta(\vec{Q}-\vec{H}) \quad (2.26)$$

where $\frac{(2\pi)^3}{V}$ is the unit cell volume in the reciprocal space, N_{cell} is the number of cell in the crystal and $\vec{H} = h\vec{a^*} + k\vec{b^*} + l\vec{c^*}$ is the position in the reciprocal space. The δ-function, $\delta(\vec{Q}-\vec{H})$, corresponds to the Bragg condition. In a perfect crystal, this condition is satisfied when the scattering vector coincides with a vector of the reciprocal space and gives rise to the nuclear Bragg peaks.
For elastic scattering, the expression of the nuclear structure factor, $N(\vec{Q})$ is:

$$N(\vec{Q}) = \sum_\nu b_\nu e^{i\vec{Q}\cdot\vec{r}_\nu}e^{-W_\nu} \quad (2.27)$$

where ν is the ν^{th} atom of the unit cell, $\vec{r}_\nu$ is the position of the atom ν in the unit cell and
$W = \langle U^2\rangle = \langle(\vec{Q}\cdot\vec{u}_0(0))^2\rangle$ is the Debye-Waller factor, that takes into account the thermal agitation.

Magnetic contribution

The magnetic cross section becomes:

$$\left(\frac{d^2\sigma}{d\Omega dE}\right)_{M,el}^{coh} = \frac{(2\pi)^3}{V}N_{cell}\sum_{\vec{H}}\sum_{\vec{\tau}}|M_\perp(\vec{Q})|^2\delta(\vec{Q}-\vec{H}-\vec{\tau}) \quad (2.28)$$

where the magnetic structure factor is expressed as:

$$\vec{M}(\vec{Q}=\vec{H}+\vec{\tau}) = \sum_{|nu}f_\nu(\vec{Q})\vec{m}_{\nu\vec{\tau}}e^{i\vec{Q}\cdot\vec{r}_\nu}e^{-W_\nu} \quad (2.29)$$

where $\vec{m}_{\nu\vec{\tau}}$ is the Fourier transform of the magnetization distribution associated to the propagation vector τ. This propagation vector characterizes the periodicity of the magnetic structure in the crystallographic structure:

- for $\vec{\tau} = \vec{0}$, the magnetic and nuclear unit cells are identical

– for $\vec{\tau} = (\tau, 0, 0)$, the magnetic unit cell length along the $\vec{a}$ direction is $1/\tau$ ($\tau < 1$) times the ones of the nuclear unit cell

The magnetic contibution will give rise to magnetic Bragg peaks at positions $\vec{H} \pm \vec{\tau}$, *i.e.* shifted by $\pm\vec{\tau}$ from the nuclear Bragg peak positions.

2.3.3 Inelastic coherent neutron scattering

For inelastic scattering, energy transfers between the neutrons and the system are now considered. In this case, the cross section writes:

$$\left(\frac{d^2\sigma}{d\Omega dE}\right)^{coh}_{inel} = \langle N^\dagger(\vec{Q},0)\cdot N(\vec{Q},t)\rangle_\omega + \langle \vec{M}^\dagger_\perp(\vec{Q},0)\cdot \vec{M}_\perp(\vec{Q},t)\rangle_\omega \tag{2.30}$$

Nuclear contribution

The nuclear part of the cross section takes into account the creation or annihilation process of the lattice excitations, called phonons. For the creation of one phonon, the cross section writes:

$$\left(\frac{d^2\sigma}{d\Omega dE}\right)^{coh}_{N,inel} = \frac{\sigma_{coh}}{4\pi}\frac{k_f}{k_i}\frac{(2\pi)^3}{V}\frac{1}{2M_{at}}e^{-W}\sum_s\sum_{\vec{H}}\frac{(\vec{Q}\cdot\vec{e}_s)^2}{\omega_s^p}\langle n_s+1\rangle\delta(\omega-\omega_s)\delta(\vec{Q}-\vec{H}-\vec{q}) \tag{2.31}$$

where ω_s^p is the phonon energy, $\delta(\omega-\omega_s^p)$ corresponds to the creation of a phonon ($\delta(\omega+\omega_s^p)$ for the annihilation), M_{at} is the atom mass and n_s is the Bose factor. This term gives the population of phonons as function of temperature, which is described by the Bose-Einstein statistic:

$$n_s = \frac{1}{\exp(E_s/k_BT)-1} \tag{2.32}$$

$\vec{e}_s$ in Eq.2.31 corresponds to the polarization of phonon mode, thus the inelastic scattering is maximum when $\vec{Q} \parallel \vec{e}_s$ due to the term $(\vec{Q}\cdot\vec{e}_s)^2$. Moreover this term implies that the measured intensity is proportional to Q^2.

Magnetic contribution

The magnetic part takes into account the creation or annihilation process of magnetic excitations, often magnons. For the creation of one magnon, the cross section writes:

$$\left(\frac{d^2\sigma}{d\Omega dE}\right)^{coh}_{M,inel} = (\gamma r_0)^2\frac{k_f}{k_i}\frac{(2\pi)^3}{V}\frac{S}{2}\left(1+\frac{\vec{u}^2_{Q_\perp}}{\vec{u}^2_Q}\right)e^{-W}|f(\vec{Q})|^2\sum_s\sum_{\vec{\tau}}\langle n_s+1\rangle\delta(\omega-\omega_s^m)\delta(\vec{Q}-\vec{\tau}-\vec{q}) \tag{2.33}$$

where ω_s^m is the magnon energy. The term $\left(1+\frac{\vec{u}^2_{Q_\perp}}{\vec{u}^2_Q}\right)$, where $u_{\vec{Q}} = \frac{\vec{Q}}{\|\vec{Q}\|^2}$, shows that neutrons are only sensitive to the dynamics of the spin components perpendicular to the scattering vector. The intensity is proportional to $|f(\vec{Q})|^2$, so magnons will be visible only for small Q values.

2.3.4 Polarized neutron scattering

So far, only unpolarized neutron scattering was mentioned, for which all contributions add together (incoherent and coherent nuclear scattering, magnetic scattering). It allows to get useful information

but in some cases it may reveal difficult to extract quantitative information. Using polarized neutrons, the different contributions can be separated and additional information can then be extracted from the scattering data.

Principle

First the neutron beam is prepared in a certain spin state, $|\uparrow\rangle$ or $|\downarrow\rangle$ by means of either Bragg reflection from a magnetized ferromagnetic crystal or transmission through a neutron spin-filter. When the neutron interacts with the sample, there can be two different processes:

- Non spin-flip (NSF) : the neutron state is unchanged after the interaction with the sample ($|\uparrow\rangle \Rightarrow |\uparrow\rangle$)
- Spin-flip (SF) : the interaction with the sample changes the spin state ($|\uparrow\rangle \Rightarrow |\downarrow\rangle$)

The SF process are purely magnetic, while the NSF process are more complex and are due to both magnetic and nuclear contributions.

The final state of the neutron is then determined using an analyzer placed in front of the detector.

The XYZ neutron polarization analysis method

In order to analyze the neutron beam polarization, a three-directional neutron polarization analysis method is used. This method allows to unambiguously separate the magnetic, nuclear and spin-incoherent cross sections on a multidetector instrument.

For that, a (x, y, z) coordinate system is defined in such a way that the scattering vector $\vec{Q}$ is in the (xy) plane (see Fig. 2.11). The measurements are then performed with the incident polarization alternately in the x, y and z directions and selecting the SF or NSF intensity, leading to the measure of six different cross sections. The main contribution for the six configurations are listed in Table 2.1.

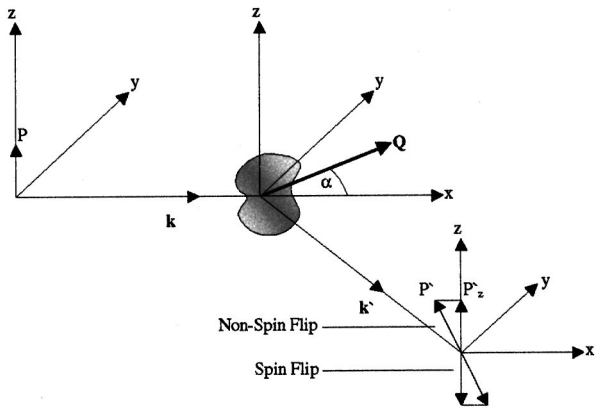

Figure 2.11 – *The geometry of an XYZ neutron polarization analysis experiment with initial polarization along z. $\vec{Q}$ is the scattering vector and $\vec{P}$ and $\vec{P}'$ are the polarization vector of respectively the incident and final neutron beam. From [SACM00]*

The NSF processes contain information on the nuclear correlations and on correlation between the spin component parallel to the polarization direction. For the SF processes, information on correlation between the spin component perpendicular to the polarization direction are obtained. Moreover note that neutrons are only sensitive to the spins components perpendicular to the scattering vector.

Polarization direction	NSF	SF
x	N	$M_y + M_z$
y	$N + M_y$	M_z
z	$N + M_z$	M_y

Table 2.1 – *Contributions for the different polarization setup for a scattering vector along x. M_y and M_z correspond to the correlations functions $\langle S_y \cdot S_y \rangle$ and $\langle S_z \cdot S_z \rangle$*

At the end, the magnetic, spin incoherent and nuclear cross sections are calculated using the different NSF and SF contributions:

$$\left(\frac{d^2\sigma}{d\Omega dE}\right)_M = 2\left[\left(\frac{d^2\sigma}{d\Omega dE}\right)^x_{\uparrow\downarrow} + \left(\frac{d^2\sigma}{d\Omega dE}\right)^y_{\uparrow\downarrow} - 2\left(\frac{d^2\sigma}{d\Omega dE}\right)^z_{\uparrow\downarrow}\right] \tag{2.34}$$

$$= -2\left[\left(\frac{d^2\sigma}{d\Omega dE}\right)^x_{\uparrow\uparrow} + \left(\frac{d^2\sigma}{d\Omega dE}\right)^y_{\uparrow\uparrow} - 2\left(\frac{d^2\sigma}{d\Omega dE}\right)^z_{\uparrow\uparrow}\right] \tag{2.35}$$

$$\left(\frac{d^2\sigma}{d\Omega dE}\right)_{SI} = \frac{1}{2}\left(\frac{d^2\sigma}{d\Omega dE}\right)_{TSF} - \left(\frac{d^2\sigma}{d\Omega dE}\right)_M \tag{2.36}$$

$$\left(\frac{d^2\sigma}{d\Omega dE}\right)_N + \left(\frac{d^2\sigma}{d\Omega dE}\right)_{II} = \frac{1}{6}\left[2\left(\frac{d^2\sigma}{d\Omega dE}\right)_{TNSF} - \left(\frac{d^2\sigma}{d\Omega dE}\right)_{TSF}\right] \tag{2.37}$$

In order to get better statistics, the magnetic (M) cross section is calculated as the average of the SF(2.34) and NSF (2.35) cross sections. The spin incoherent (SI), nuclear (N) and isotope incoherent (II) cross sections are calculated using the total spin-flip (TSF) and total non spin-flip (TNSF) cross sections defined as:

$$\left(\frac{d^2\sigma}{d\Omega dE}\right)_{TSF} = \left(\frac{d^2\sigma}{d\Omega dE}\right)^x_{\uparrow\downarrow} + \left(\frac{d^2\sigma}{d\Omega dE}\right)^y_{\uparrow\downarrow} + \left(\frac{d^2\sigma}{d\Omega dE}\right)^z_{\uparrow\downarrow} \tag{2.38}$$

$$\left(\frac{d^2\sigma}{d\Omega dE}\right)_{NTSF} = \left(\frac{d^2\sigma}{d\Omega dE}\right)^x_{\uparrow\uparrow} + \left(\frac{d^2\sigma}{d\Omega dE}\right)^y_{\uparrow\uparrow} + \left(\frac{d^2\sigma}{d\Omega dE}\right)^z_{\uparrow\uparrow} \tag{2.39}$$

$$\tag{2.40}$$

2.3.5 Instruments for neutron scattering experiments

Two types of instruments have been used: powder diffractometers using monochromatic incident neutrons (D1B, D4c and D7) at the Institut Laue-Langevin (ILL), a Time-of-Flight (TOF) diffractometer (WISH) at the ISIS Facility and TOF spectrometers (IN4, IN5 and IN6) at the ILL. These instruments are briefly described in this section.

2.3.5.1 Powder diffractometers

During diffraction experiments, we are interested only into the crystalline and magnetic structures corresponding to the elastic part ($\hbar\omega = E_f - E_i = 0$) of the scattering cross section. In practice, there is no analysis of the neutron energy after the interactions with the sample. Therefore, in the measured intensity, the signal is integrated over all transferred energy range.

The diffraction process happens when the Bragg condition is realized. This condition is expressed

by:

$$2d \sin\theta = \lambda_i \Leftrightarrow Q = 2k_i \sin\theta \tag{2.41}$$

where $\lambda_i = {}^{2\pi}/_{k_i}$ is the incident wavelength, $d = {}^{2\pi}/_{Q}$ is the inter-reticular distance for a family of reticular planes and 2θ corresponds to the angle between the incident and the scattered neutron beam (see Fig. 2.12).

The powder diffractometers are also called 2-axes diffractometers because they present two vertical axes, the first axis being the monochromator axis and the second axis being the one of the sample.

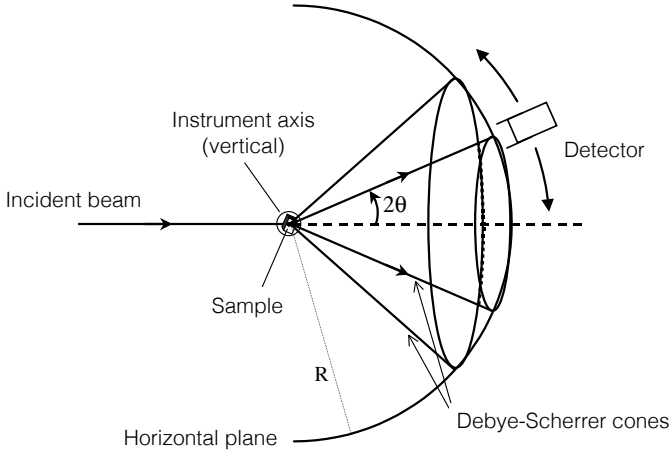

Figure 2.12 – *Sketch of a 2-axes diffractometers*

The diffractometers used at the ILL work with a constant incident wavelength λ_i. The Q dependence is obtained by varying 2θ. The incident wavelength is selected using a monochromator. Indeed by using the Bragg condition on a single crystal, a particular wavelength can be selected out of a polychromatic beam, for a chosen inter-reticular distance d and angle θ. The monochromatic neutron beam is then scattered by the sample in different space directions and collected by one or multiple detectors (see Fig. 2.13).

The sample being a polycrystalline sample, there are always some microcrystals for which the Bragg condition is observed. Therefore, a cone of diffraction of half angle 2θ, called the Debye-Scherrer cone, is obtained.

The difference between the D1B and D4c diffractometers at the ILL is in the incoming wavelength. Indeed for D1B, thermal neutrons are used ($\lambda_i = 2.52$ Å) while hot neutrons are used for D4c ($\lambda_i = [0.35 - 0.7]$ Å). The latter is more suited for studying liquid and amorphous materials for which we want to know the structure factor over a large Q-range. It is also useful in the case of strongly absorbing materials for which high energy neutrons are needed in order to minimize absorption through the sample.

In the case of the D7 diffractometer, polarized neutrons are used associated to XYZ polarization analysis in order to separate the different contributions.

The powder diffractometer used at ISIS is a TOF diffractometer. The Q-dependence of the scattered intensity is obtained by varying the incident wavelength λ_i for a fixed angle 2θ.

A polychromatic neutron beam is sent on the sample and the TOF method is used in order to determine the wavelength of the scattered neutrons. The TOF method is based on the determination

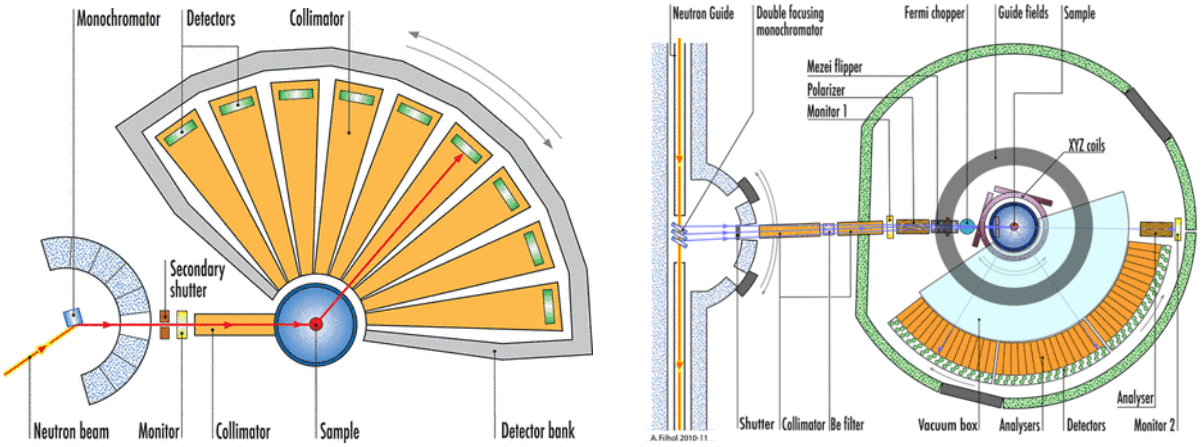

Figure 2.13 – *2-axes diffractometer used at the ILL: D4c and D7*

of the time needed for a neutron to "fly" other a given distance (see Fig. 2.14). When a neutron hits the detector at an angle 2θ, its time of flight from the pulsed source to the detector, τ, is recorded. Its velocity v is then given by:

$$v = \frac{\tau}{L_1 + L_2} \tag{2.42}$$

where L_1 and L_2 correspond respectively to the distances from the source to the sample and from the sample to the detector.

The neutron wavelength is then obtained by:

$$\lambda = \frac{h}{mv} \tag{2.43}$$

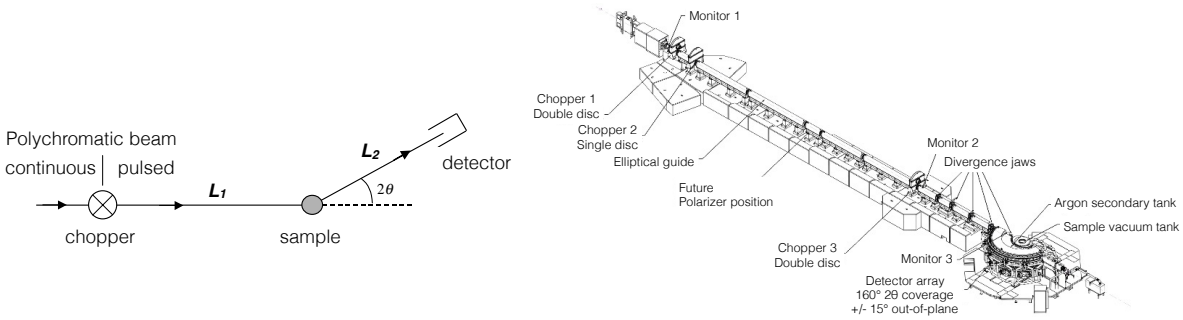

Figure 2.14 – *(top) Sketch of the working principle of a TOF diffractometer. (bottom) Schematic view of the WISH TOF powder diffractometer.*

2.3.5.2 Time-of-flight spectrometers

The TOF spectrometers allow to detect neutrons simultaneously for different scattering vector $\vec{Q}$ and different energies $\hbar\omega$. Pulses of neutron with fixed wavelength and thus fixed velocity, v_i, are send onto the sample and both the position 2θ and the time of flight from the sample to the detector, τ, are recorded. The final velocity is calculated by: $v_f = {}^{d}/_{\tau}$, where d is the travelled distance.

The energy difference is related to the difference between the square of the initial and final velocity:

$$\hbar\omega = E_f - E_i = \frac{1}{2}m(v_f^2 - v_i^2) \tag{2.44}$$

and the scattering vector is expressed by:

$$\frac{\hbar^2 Q^2}{2m} = E_f + E_{-i} - 2\sqrt{E_f E_i}\cos(2\theta) \tag{2.45}$$

Usually cold neutrons are used as it allows to get a good precision on the time-of-flight and thus a good energy resolution.

There are two ways to produce the monochromatic incident beam:

- using a single crystal as monochromator (IN4 and IN6). The beam is then cut into pulses using choppers.
- using several choppers (IN5). The phase difference between the choppers allows to select a chosen velocity

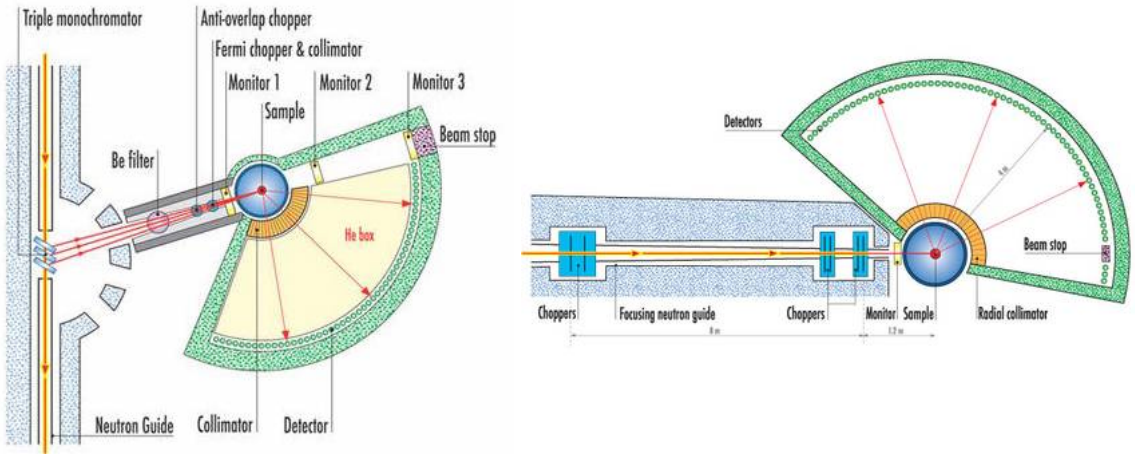

Figure 2.15 – *Sketches of two TOF spectrometers: IN6 (left) and IN5 (right)*

2.4 Resonant X-ray Scattering

2.4.1 Generalities on synchrotron X-ray

Synchrotron X-rays are a specific electromagnetic radiation emitted by relativistic charged particles (deviated from their trajectory by a magnetic field). This has been first demonstrated theoretically in 1898 by A. Liénard [Lie98] and observed for the first time using a synchrotron in the General Electrics laboratory [EGLP47, ELP48]. Nowadays, synchrotron radiation has become a powerful tool to probe the matter and many synchrotron sources have been developed among which there are the European Synchrotron Radiation Facility (ESRF) in Grenoble and the Diamond Light Source synchrotron in Didcot, Oxfordshire. These sources are third generation sources, *i.e.* X-ray radiations are produced along the whole storage ring circumference using both bending magnets and insertion devices such as undulators (see Fig. 2.16).

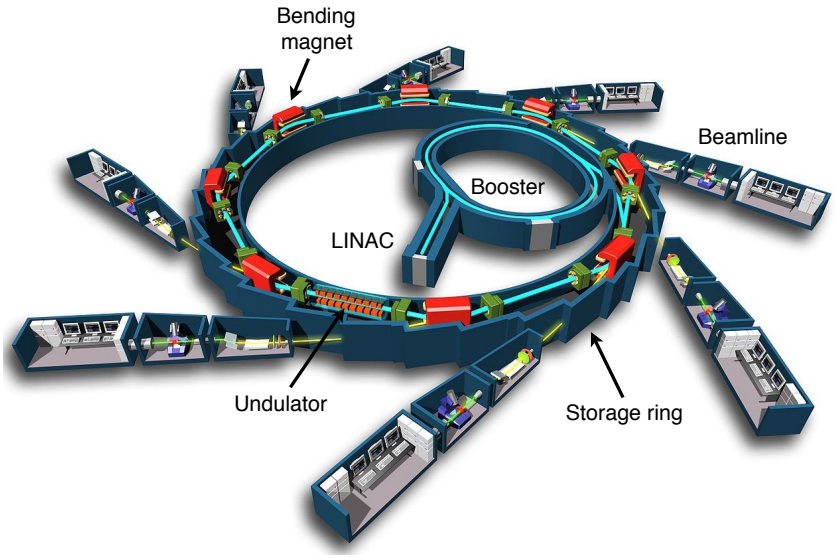

Figure 2.16 – *Schematic view a third generation synchrotron source. From [San]*

The electrons are produced by a electron gun and fired out into the LINear ACcelerator (LINAC) then into the circular accelerator (Booster) where they are accelerated until a given energy (3 GeV at the Diamond Light Soure and 6 GeV at the ESRF). Then they are sent to the storage ring which is made of small linear portions to form a polygon (circumference of the polygon: 844 m for the ESRF and 738 m for Diamond). In the storage ring, the electrons produce synchrotron radiation thanks to the magnetic devices, the bending magnets and the undulators, that send intense beam of light from the UV to hard X-ray regime to the beam lines.

Until 10-15 years ago, mostly neutron scattering experiments were used to probe the magnetic properties of condensed matter systems. In particular, the fact that the scattering of X-ray by magnetic moments of the electrons in a solid is very weak compared to the charge scattering ($\sim$ 5 orders of magnitude below) has made the study of the magnetic properties very challenging. With the development of third generation synchrotron sources, which provide a high brilliance radiation as well as the development of new techniques, X-ray scattering have now become also a powerful tool in this area. Indeed, in 1988, Hannon *et al.* predicted a large enhancement of the magnetic scattering when the X-ray energy is tuned at an absorption edge of an element [HTBG88], *i.e.* using resonant scattering. X-ray scattering has become complementary to neutron scattering, in particular when only small amount of sample is available, when chemical selectivity is needed, or for studying strong neutron absorbers.

2.4.2 Resonant X-ray scattering

2.4.2.1 What is Resonant X-ray scattering ?

Resonant X-ray scattering is a second order, "photon in $-$ photon out" process as illustrated in Figure 2.17.

An incident photon of well defined energy $\hbar\omega_i$ and momentum $\vec{k_i}$ is absorbed by the sample leading to the excitation of a core electron into the valence band. The excited electron immediately ($\sim 10^{-15}$ s) decays back into the initial core level and emits a new photon of energy $\hbar\omega_f$ and momentum $\vec{k_f}$. This process can either be elastic ($\hbar\omega_i = \hbar\omega_f$) and we will talk of Resonant Elastic X-ray scattering (REXS)

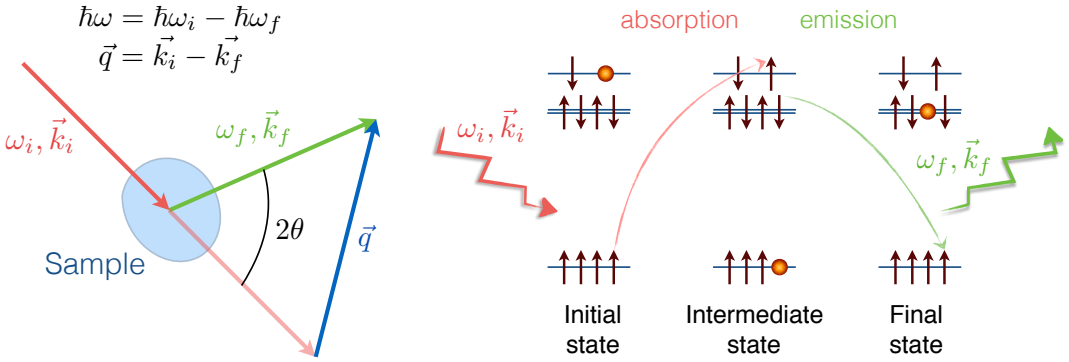

Figure 2.17 – *(left) Schematic diagram of the "photon in − photon out" process. (right) Schematic representation of the Resonant X-ray scattering process.*

or inelastic ($\hbar\omega_i \neq \hbar\omega_f$) leading to Resonant Inelastic X-ray scattering (RIXS). An excitation of energy $\hbar\omega = \hbar\omega_i - \hbar\omega_f$ and of momentum $\vec{q} = \vec{k_i} - \vec{k_f}$ is created during this process.

RIXS allows to measure both the energy and momentum dependence of low energy valence electron excitations in crystals. These excitations can be phonons, magnons, *dd* or charge transfer in nature (see Fig. 2.18).

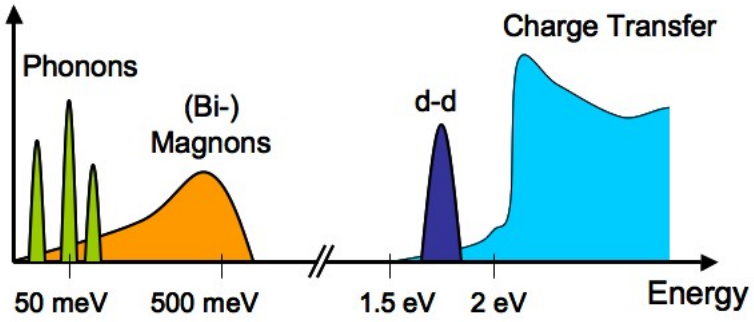

Figure 2.18 – *Elementary excitations in condensed matter systems that can be measured by RIXS. The indicated energy scales are the ones relevant for transition metal oxides. From [AvVD+11].*

2.4.2.2 Features and limitations of Resonant X-ray scattering

RIXS presents a number of features that makes this spectroscopy technique particular:

1. In the case of hard x-rays, it can probe the *energy and momentum dependence* of excitations in a large part of the Brillouin zone. This is due to the fact that the momentum transfer during the scattering process is $|\vec{q}| = \frac{4\pi}{\lambda}\sin\theta$, where 2θ is the scattering angle and λ is the wavelength of the incoming photon and that hard X-rays are used ($\hbar\omega_i \sim 10$ keV $\Rightarrow \lambda \sim 1$ Å).
2. *Polarization sensitivity*. It is possible to polarize the incoming photon beam and to measure the polarization of the outgoing photon beam. This allows to characterize the symmetry and the nature of the measured signal.
3. *Chemical selectivity*. As the incident photon energy is tuned to a specific resonance edge, one can choose it, in order to probe the properties related to a specific element of the material.

4. *Bulk sensitivity*. The penetration depth of X-rays strongly depends on their incident energy. In the hard X-ray regime, this depth is of the order of a few μm.
5. *Small sample volume*. Compared to neutron scattering, X-ray scattering require a tiny amount of sample. This difference is related to the difference of flux. The typical beam size is of a few hundreds of microns on the Resonant X-ray Scattering beam lines

However, there are also some limitations to this technique:

1. In order to get high energy and momentum resolutions, the experiments require a lot of incident photons and thus *longer measurement times* than other standard X-ray experiments.
2. *Energy resolution*. As there is a huge difference between the energy of the photons and the energy of the probed excitations, a large resolving power is needed. RIXS has long been limited to an energy resolution of 1 eV. Recent progress in the RIXS instrumentation has helped a lot to improve this resolution which is now of the order of 25 meV in this hard X-ray regime such as ID20 at the ESRF. The resolution is expected to go down to 10-15 meV in the upcoming years.

2.4.2.3 Resonant X-ray scattering cross section

In this section, the REXS and RIXS cross section is derived. The complete derivation can be found in [Blu85]. Let's consider electrons interacting with a quantized electromagnetic field described by a vector potential $A(\vec{r},t)$. The Hamiltonian is given by:

$$\mathcal{H} = \mathcal{H}_{el} + \mathcal{H}_{ph} + \mathcal{H}' \tag{2.46}$$

where $\mathcal{H}_{el}$ is the Hamiltonian corresponding to the non interacting electrons and $\mathcal{H}_{ph}$ the Hamiltonian corresponding to the non interacting photons. Therefore $\mathcal{H}_{el} + \mathcal{H}_{ph}$ corresponds to the Hamiltonian of the unperturbed system. Then $\mathcal{H}'$ represents the photon-electron interactions term. These Hamiltonians are expressed by:

$$\mathcal{H}_{el} = \sum_j \frac{1}{2m}\mathbf{p}^2 + \sum_{ij} V(\mathbf{r}_{ij}) + \frac{e\hbar}{2(mc)^2}\sum_j \mathbf{s}_j \cdot (\nabla\Phi_j \times \mathbf{p}_j) \tag{2.47}$$

$$\mathcal{H}_{ph} = \sum_{\mathbf{k}\epsilon} \hbar\omega \left(c^\dagger(\mathbf{k},\epsilon)c(\mathbf{k},\epsilon) + \frac{1}{2}\right) \tag{2.48}$$

$$\mathcal{H}' = \mathcal{H}'_2 + \mathcal{H}'_3 + \mathcal{H}'_4 + \mathcal{H}'_1 \tag{2.49}$$

$$= \frac{e^2}{2mc^2}\sum_j \mathbf{A}^2(\mathbf{r}_j) - \frac{e}{mc}\sum_j \mathbf{A}(\mathbf{r}_j)\cdot\mathbf{p}_j - \frac{e\hbar}{mc}\sum_j \mathbf{s}_j \cdot [\nabla \times \mathbf{A}(\mathbf{r}_j)] - \frac{e\hbar}{2(mc)^2}\frac{e}{c^2}\sum_j \mathbf{s}_j \cdot \left[\frac{\partial \mathbf{A}(\mathbf{r}_j)}{\partial t} \times \mathbf{A}(\mathbf{r}_j)\right] \tag{2.50}$$

where $\mathbf{s}_j$ and $\mathbf{p}_j$ represents the spin and momemtum operator of the electron j at a position $\mathbf{r}_j$ and $c^\dagger(\mathbf{k},\epsilon)$ and $c(\mathbf{k},\epsilon)$ are the creation and annihilation operators of a photon characterized by the quantum numbers ($\mathbf{k}$, ϵ). In $\mathcal{H}_{el}$, the first term corresponds to the kinetic energy, the second term is the interaction potential with the background of lattice of nuclei and the other electrons in the sample and the last term describes the spin-orbit interaction. Note that the expression of $\mathcal{H}'$ is obtained using the Coulomb gauge: $\nabla\cdot\mathbf{A} = 0$, *i.e.* $\mathbf{p}\cdot\mathbf{A} = \mathbf{A}\cdot\mathbf{p}$.

As the operator $\mathbf{A}$ is linear in $c^\dagger(\mathbf{k},\epsilon)$ and $c(\mathbf{k},\epsilon)$, the $\mathcal{H}'_1$ and $\mathcal{H}'_4$ term will contribute to the first order perturbation while $\mathcal{H}'_2$ and $\mathcal{H}'_3$ will contribute to the second order.

The scattering process corresponds to transition between the eigenstates of $\mathcal{H}_{el}$ and $\mathcal{H}_{ph}$ due to the perturbation $\mathcal{H}'$. In the perturbation term, $\mathcal{H}'_1$ and $\mathcal{H}'_4$ are quadratic in $\mathbf{A}$, while $\mathcal{H}'_2$ and $\mathcal{H}'_3$ are linear.

We can express the probability of the transition from an initial state $|i\rangle = |a;\mathbf{k},\epsilon\rangle$ to a final state $|f\rangle = |b;\mathbf{k}',\epsilon'\rangle$ using the Fermi's golden rule up to the second order ($|i\rangle$ and $|f\rangle$ are eigenstates of the unperturbed Hamiltonian whose energies are $E_i = E_a + \hbar\omega_{\mathbf{k}}$ and $E_f = E_b + \hbar\omega_{\mathbf{k}'}$) :

$$W = \frac{2\pi}{\hbar}\left|\langle f|\mathcal{H}'|i\rangle + \sum_n \frac{\langle f|\mathcal{H}'|n\rangle\langle n|\mathcal{H}'|i\rangle}{E_i - E_n}\right|^2 \delta(E_i - E_f) \tag{2.51}$$

$$= \frac{2\pi}{\hbar}\left|\langle b;\mathbf{k}',\epsilon'|\mathcal{H}'_1 + \mathcal{H}'_4|a;\mathbf{k},\epsilon\rangle + \sum_n \frac{\langle b;\mathbf{k}',\epsilon'|\mathcal{H}'_2 + \mathcal{H}'_3|n\rangle\langle n|\mathcal{H}'_2 + \mathcal{H}'_3|a;\mathbf{k},\epsilon\rangle}{E_a + \hbar\omega_{\mathbf{k}} - E_n}\right|^2 \times \delta(E_a - E_b + \hbar\omega_{\mathbf{k}} - \hbar\omega_{\mathbf{k}'}) \tag{2.52}$$

The total cross section is then given by:

$$\frac{\mathrm{d}^2\sigma}{\mathrm{d}\Omega'\mathrm{d}E'} = W\frac{\rho(E_f)}{I_0} \tag{2.53}$$

where $\rho(E_f) = \frac{\Omega}{(2\pi)^3}\frac{\omega^2_{\mathbf{k}'}}{\hbar c^3}$ represents the density of final states and I_0 is the incident flux.

After some calculations, the total cross section can then be written as:

$$\frac{\mathrm{d}^2\sigma}{\mathrm{d}\Omega'\mathrm{d}E'} = \left(\frac{e^2}{mc^2}\right)\frac{\omega_{\mathbf{k}'}}{\omega_{\mathbf{k}}}\left|\mathcal{A}_0 + \mathcal{A}_{nonres} + \mathcal{A}_{res}\right|^2 \delta(E_a - E_b + \hbar\omega_{\mathbf{k}} - \hbar\omega_{\mathbf{k}'}) \tag{2.54}$$

The first term $\mathcal{A}_0$ is given by:

$$\mathcal{A}_0 = \left\langle b\left|\sum_j e^{i\mathbf{Q}\cdot\mathbf{r}_j}\right|a\right\rangle \hat{\epsilon}'\cdot\hat{\epsilon} \tag{2.55}$$

where $\mathbf{Q} = \mathbf{k} - \mathbf{k}'$ is the scattering vector. This term corresponds to the Thomson scattering when $|b\rangle = |a\rangle$ and the crystal periodicity is accounted for. It contains the Fourier transform of the electron density and gives rise to the Bragg peaks.

The second term $\mathcal{A}_{nonres}$ is written as:

$$\mathcal{A}_{nonres} = -i\frac{\hbar\omega_{\mathbf{k}}}{mc^2}\left\langle b\left|\sum_j e^{i\mathbf{Q}\cdot\mathbf{r}_j}\left(i\frac{\mathbf{Q}\times\mathbf{p}_j}{\hbar k^2}\cdot\mathbf{A}' + \mathbf{s}_j\cdot\mathbf{B}'\right)\right|a\right\rangle$$

$$= -i\frac{\hbar\omega_{\mathbf{k}}}{mc^2}\left(\frac{1}{2}\mathbf{L}(\mathbf{Q})\cdot\mathbf{A}'' + \mathbf{S}(\mathbf{Q})\cdot\mathbf{B}'\right) \tag{2.56}$$

where $\mathbf{A}'$, $\mathbf{A}''$ and $\mathbf{B}'$ are polarization dependent terms and $\mathbf{L}(\mathbf{Q})$ and $\mathbf{S}(\mathbf{Q})$ are the Fourier transform of the orbital and spin magnetization density. This term represents the non resonant magnetic scattering and is reduced by a factor $\hbar\omega_{\mathbf{k}}/mc^2$ compared to the Thomson scattering.

Finally the expression of the third term $\mathcal{A}_{res}$ is:

$$\begin{aligned}\mathcal{A}_{res} =& \frac{1}{m}\sum_c\sum_{ij}\frac{E_a-E_c}{\hbar\omega_{\mathbf{k}}} \\ & \left(\frac{\langle b|(\hat{\epsilon}'\cdot\mathbf{p}_i - i\hbar(\mathbf{k}'\times\hat{\epsilon}')\cdot\mathbf{s}_i)e^{-i\mathbf{k}'\cdot\mathbf{r}_i}|c\rangle\langle c|(\hat{\epsilon}\cdot\mathbf{p}_j + i\hbar(\mathbf{k}\times\hat{\epsilon})\cdot\mathbf{s}_j)e^{i\mathbf{k}\cdot\mathbf{r}_j}|a\rangle}{E_a - E_c + \hbar\omega_{\mathbf{k}} - i\Gamma_c/2}\right) \\ =& \frac{1}{m}\sum_c\sum_{ij}\frac{E_a-E_c}{\hbar\omega_{\mathbf{k}}}\left(\frac{\langle b|(\hat{\epsilon}'\cdot\mathbf{p}_i)e^{-i\mathbf{k}'\cdot\mathbf{r}_i}|c\rangle\langle c|(\hat{\epsilon}\cdot\mathbf{p}_j)e^{i\mathbf{k}\cdot\mathbf{r}_j}|a\rangle}{E_a - E_c + \hbar\omega_{\mathbf{k}} - i\Gamma_c/2}\right)\end{aligned} \tag{2.57}$$

where the term $i\Gamma/2$ takes into account the lifetime of the intermediate state $|c\rangle$. $\mathcal{A}_{res}$ comes from second order perturbation theory. It corresponds to the pure resonant scattering cross section and is called the Kramers-Heisenberg formula. When $|b\rangle = |a\rangle$, this term gives the REXS cross section while it gives the RIXS one when $|b\rangle \neq |a\rangle$.

The RIXS process in iridium oxides involves electric dipole transition (optical transition from the $2p_{3/2}$ to the $5d$ states). This allows to use the following approximation: $e^{i\mathbf{k}\cdot\mathbf{r}} \sim 1 + i\mathbf{k}\cdot\mathbf{r} + ...$ by keeping only the first term in the expansion. And using the commutator:

$$[\mathcal{H}_{el}, \mathbf{r}] = \frac{\hbar}{i}\frac{\mathbf{p}}{m} \tag{2.58}$$

we obtain:

$$\begin{aligned}\langle c|(\hat{\epsilon}\cdot\mathbf{p}e^{i\mathbf{k}\cdot\mathbf{r}})|a\rangle =& \langle c|\epsilon\cdot\hat{\mathbf{p}}|a\rangle \\ =& i\frac{m}{\hbar}\langle\epsilon\cdot[\hat{\mathcal{H}}_{el},\mathbf{r}]|a\rangle \\ =& -i\frac{m}{\hbar}(E_a-E_c)\langle c|\mathcal{D}_\epsilon|a\rangle\end{aligned} \tag{2.59}$$

where $\mathcal{D}_\epsilon = \hat{\epsilon}\cdot\mathbf{r}$ is the electric dipole operator. Eqution 2.57 can then be written as:

$$\mathcal{A}_{res} = m\sum_c\sum_{ij}\frac{(E_a-E_c)^3}{\hbar^3\omega_{\mathbf{k}}}\left(\frac{\langle b|(\hat{\epsilon}'\cdot\mathbf{r}_i)|c\rangle\langle c|(\hat{\epsilon}\cdot\mathbf{r}_j)|a\rangle}{E_a - E_c + \hbar\omega_{\mathbf{k}} - i\Gamma_c/2}\right) \tag{2.60}$$

2.4.3 Instrument for Resonant X-ray scattering

2.4.3.1 REXS

The REXS experiments have been performed on the I16 beam line of the Diamond Light Source (UK). This beam line provides incident photons with an energy tunable between 3.3 and 15 keV using a channel-cut Si(111). After the monochromator, a set of mirrors, slits and attenuators allows to control the size, divergence and intensity of the beam (see Fig. 2.19).

The sample is mounted on a 6-circle kappa goniometer (see Fig. 2.20) allowing to probe a large area of the reciprocal space. Several sample environments are available in order to control the sample temperature. During the experiment, we used a closed cycle Displex cryocooler giving access to temperature from 10 K to 300 K.

The detector arm is equipped with a large number of X-ray detectors: four of these are point detectors (an avalanche photodiode, a Vortex Si drift detector, a scintillator and a PIN diode). A 2-

dimensional detector is also available, the Pilatus.

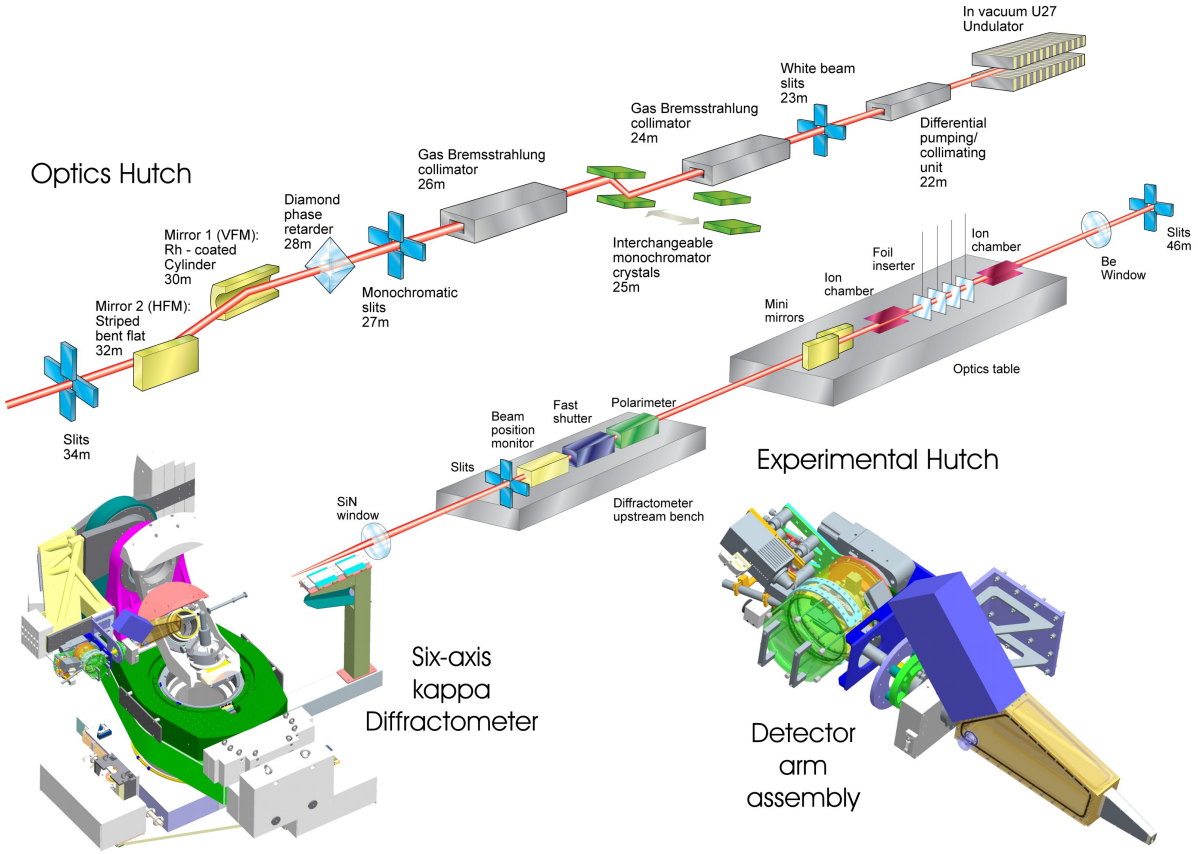

Figure 2.19 – *Schematic view of the Optics and experimental hutch of the I16 beam line at the Diamond Light Source. From [CBM+10]*

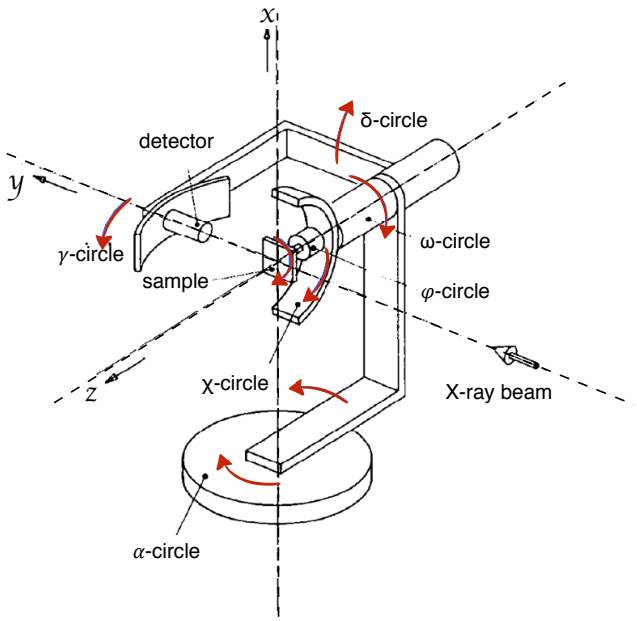

Figure 2.20 – *Schematic view of a 6-circle kappa goniometer. Adapted from [LV93].*

2.4.3.2 RIXS

The RIXS measurements have been performed at the ID20 beam line of the European Synchrotron Radiation Facility (see Fig. 2.21). The beam is monochromatized using a combination of the Si(111) double-crystal monochromator with a Si(844) channel-cut allowing for a flexible choice of the energy-resolution down to 25 meV at the Ir L_3 edge [SHS+13].

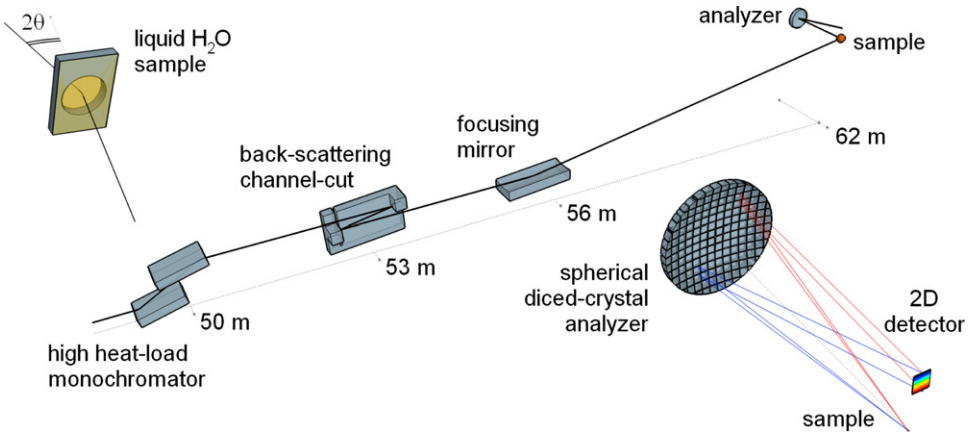

Figure 2.21 – *Schematic view of the optical layout of the ID20 beam line setup for RIXS experiments. From [SHS+13]*

The beam is then focused to reach a size of about 25×120 µm^2 at the sample position. The scattered radiation is then collected by a spherical Si(844) diced crystal analyzer fixed on a 2 m long arm and detected using a 2D detector (see Fig. 2.22).

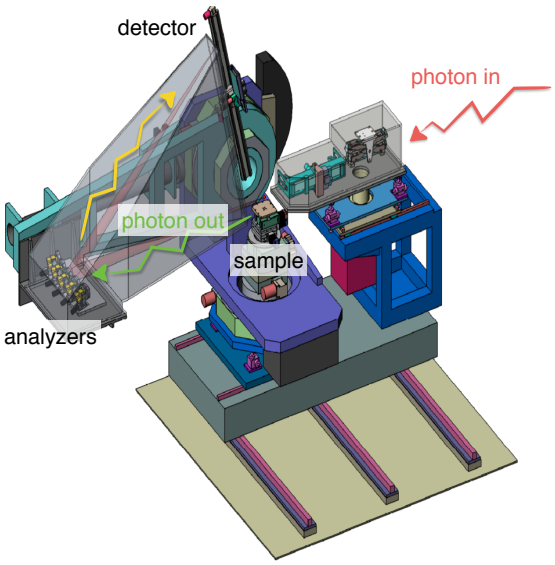

Figure 2.22 – *Schematic view of the ID20 spectrometer*

Bibliography

[AvVD+11] Luuk J. P. Ament, Michel van Veenendaal, Thomas P. Devereaux, John P. Hill, and Jeroen van den Brink. Resonant inelastic x-ray scattering studies of elementary excitations. *Rev. Mod. Phys.*, 83:705–767, Jun 2011.

[Blu85] M. Blume. Magnetic scattering of x rays (invited). *Journal of Applied Physics*, 57(8):3615–3618, 1985.

[CBM+10] S. P. Collins, A. Bombardi, A. R. Marshall, J. H. Williams, G. Barlow, A. G. Day, M. R. Pearson, R. J. Woolliscroft, R. D. Walton, G. Beutier, and G. Nisbet. Diamond beamline i16 (materials & magnetism). *AIP Conference Proceedings*, 1234(1):303–306, 2010.

[CGL+15] J. P. Clancy, H. Gretarsson, E. K. H. Lee, D. Tian, J. Kim, M. H. Upton, D. Casa, T. Gog, Z. Islam, B.-G. Jeon, K. H. Kim, S. Desgreniers, Y. B. Kim, S. J. Julian, and Y.-J. Kim. X-ray scattering study of pyrochlore iridates: crystal structure, electronic and magnetic excitations. *ArXiv e-prints*, October 2015.

[Cha32] James Chadwick. Possible existence of a neutron. *Nature*, 129:312, 1932.

[EGLP47] F. R. Elder, A. M. Gurewitsch, R. V. Langmuir, and H. C. Pollock. Radiation from electrons in a synchrotron. *Phys. Rev.*, 71:829–830, Jun 1947.

[ELP48] F. R. Elder, R. V. Langmuir, and H. C. Pollock. Radiation from electrons accelerated in a synchrotron. *Phys. Rev.*, 74:52–56, Jul 1948.

[HTBG88] J. P. Hannon, G. T. Trammell, M. Blume, and Doon Gibbs. X-ray resonance exchange scattering. *Phys. Rev. Lett.*, 61:1245–1248, Sep 1988.

[Lie98] A.-M. Liénard. Champ électrique et magnétique. *L'Éclairage électrique*, 16, Jul 1898.

[Lov84a] Stephen W. Lovesey. *Theory of neutron scattering from condensed matter, volume I*. Oxford Science Publications, 1984.

[Lov84b] Stephen W. Lovesey. *Theory of neutron scattering from condensed matter, volume II*. Oxford Science Publications, 1984.

[LV93] M. Lohmeier and E. Vlieg. Angle calculations for a six-circle surface X-ray diffractometer. *Journal of Applied Crystallography*, 26(5):706–716, Oct 1993.

[SACM00] J. R. Stewart, K. H. Andersen, R. Cywinski, and A. P. Murani. Magnetic diffuse scattering in disordered systems studied by neutron polarization analysis (invited). *Journal of Applied Physics*, 87(9):5425–5430, 2000.

[San] EPSIM 3D/JF Santarelli. Schéma de principe du synchrotron.

[SHS+13] M. Moretti Sala, C. Henriquet, L. Simonelli, R. Verbeni, and G. Monaco. High energy-resolution set-up for ir l_3 edge rixs experiments. *Journal of Electron Spectroscopy and Related Phenomena*, 188:150 – 154, 2013.

[Squ78] G.L Squires. *Introduction to the theory of thermal neutron scattering*. Cambridge University Press, 1978.

[TKT+15] Zhaoming Tian, Yoshimitsu Kohama, Takahiro Tomita, Hiroaki Ishizuka, Timothy H. Hsieh, Jun J. Ishikawa, Koichi Kindo, Leon Balents, and Satoru Nakatsuji. Field-induced quantum metal-insulator transition in the pyrochlore iridate $nd_2ir_2o_7$. *Nat. Phys.*, 12:134–138, 2015.

Chapter 3

The chain compounds

Contents

3.1 Introduction to the $A_3MM'O_6$ family

Oxides of the family $A_3MM'O_6$, where A is an alkaline-earth metal and M, M' are transition metals have attracted a lot of attention in the past decades because of their unconventional magnetic properties. These properties mainly come from the peculiar crystallographic structure of these compounds, described in the hexagonal $R\bar{3}c$ space group, that consists of chains aligned along the **c** direction. These chains are formed by alternating face-sharing MO_6 trigonal prisms and $M'O_6$ octahedra and are arranged on a triangular lattice in the (**ab**) plane (see Fig. 3.1).

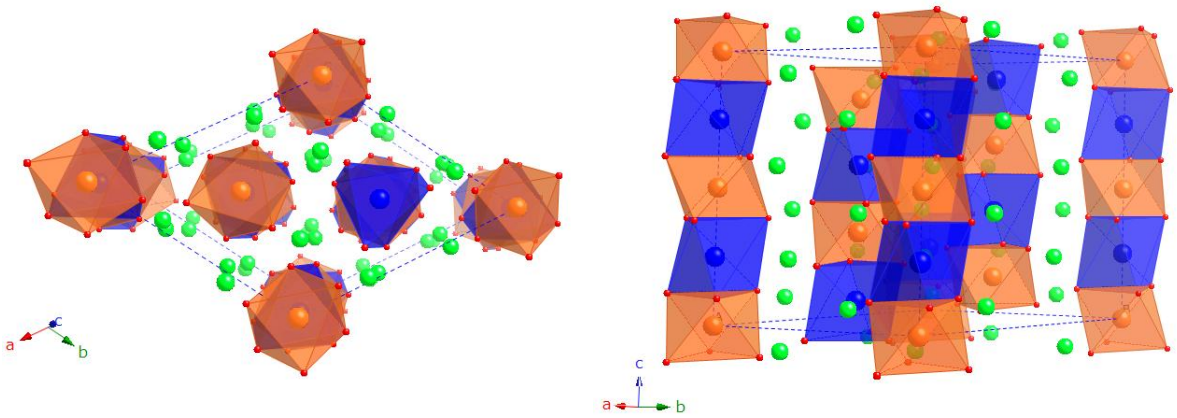

Figure 3.1 – *Structure of the $A_3MM'O_6$ compounds shown projected on the (**ab**) plane (left) and in a perspective view (right). M atoms are represented in blue, M' in orange, A in green and O^{2-} in red. The MO_6 trigonal prisms and NiO_6 octahedra are represented in blue and orange respectively. The conventional hexagonal unit-cell is shown with dotted blue lines.*

The positions of the atoms are described in Table. 3.1. Behaviors induced by low dimensionality and magnetic frustration are to be expected in these compounds due to the geometry of the lattice and competing interactions. In addition, the presence of two different transition metal ions (M and M'), which can either be magnetic or not, complicate the picture, due to the numerous possible exchange paths that exist (see Fig. 3.2). The magnetocrystalline anisotropy conferring their dimensionality to the magnetic moments is also an important ingredient in order to predict the properties of these compounds.

Atoms	Wyckoff sites	Site symmetry	Coordinates
M	6*a*	3 2	(0, 0, 0)
M'	6*b*	$\bar{3}$.	(0, 0, 1/4)
A	18*e*	. 2	(x, 0, 1/4)
O	36*f*	1	(x, y, z)

Table 3.1 – *Details of the symmetry and coordinates of the Wyckoff sites for $A_3MM'O_6$.*

In the Heisenberg classical limit, the magnetic ground state for nearest neighbor antiferromagnetic interchain interactions on a triangular lattice is the 120° spin configuration. In the Ising limit however it is impossible to order all magnetic moments simultaneously and magnetic structures with amplitude modulated moments may be stabilized at finite temperature. In particular, it is interesting to consider

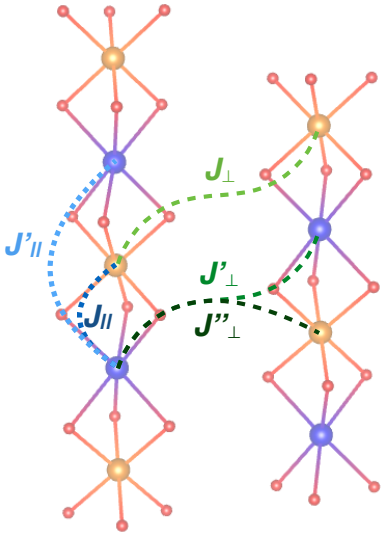

Figure 3.2 – *Structure of the $A_3MM'O_6$ compounds showing the possible magnetic exchange paths. M atoms are represented in blue, M' in orange and O in red. The main intrachain ($J_{\parallel}$) and interchain ($J_{\perp}$) exchange path are shown respectively in blue and green.*

the model with Ising spins interacting with the nearest and second nearest neighbors on a triangular lattice. In this model the triangular lattice is divided into 3 sublattices (see Fig. 3.3-left). Each spin is surrounded by 6 nearest neighbors of different sublattices and by 6 second neighbors of the same sublattice. The magnetic exchange terms are denoted by J_1 and J_2 for the nearest and second neighbors respectively. For $J_1 < 0$ (AFM) and $J_2 > 0$ (FM), a partially disordered magnetic configuration has been predicted [Mek77]. This configuration is characterized by only two thirds of the chains that order whereas the remaining chain keeps fluctuating at low temperature (see Fig. 3.3-right). It has been observed experimentally for the first time in $CsCoCl_3$ [MA78].

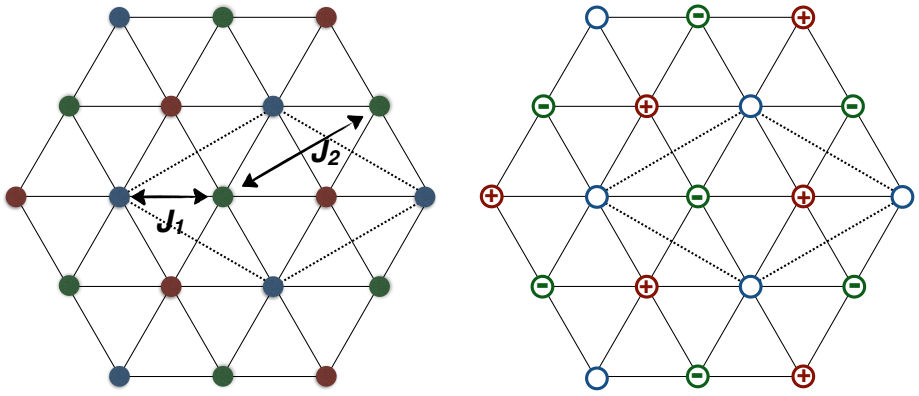

Figure 3.3 – *(left) Sketch of the three sublattices (shown in red, blue and green) in the triangular Ising lattice (right) and of the partially disordered antiferromagnetic structure. The dotted lines show the unit cell.*

Among this family, the most studied compound is $Ca_3Co_2O_6$. It presents a strong easy-axis anisotropy which confines the magnetic moments along the chain axis. This compound displays two magnetic anomalies in the susceptibility measurements:

- the first one at T_1 = 24 K, is evidenced by a deviation of the susceptibility from the Curie-Weiss law and is followed by a steep increase as the temperature is lowered. The onset of strong spin dynamics is also observed below this first anomaly,
- the second one at T_2 = 12 K is where the ZFC and FC susceptibilities get separated and the spin

dynamics freezes.

Below T_1, $Ca_3Co_2O_6$ presents a 1/3 magnetization plateau, followed below T_2 by additional steps in the magnetization corresponding to the progressive flipping of the spins on the triangular lattice until all spins are aligned in the same direction. Moreover there exists two competing magnetic states at low temperature: an amplitude modulated phase with an incommensurate magnetic propagation vector $\mathbf{k}$ = (0, 0, 1.01) determined by Resonant Elastic X-ray Scattering and a commensurate antiferromagnetic phase with $\mathbf{k}$ = (1/2, -1/2, 1) that was observed by neutron powder diffraction experiments [AFC+11].

Most recent studies in this family focus on compounds with transition metal ions belonging to the 4*d* or 5*d* series with the purpose of investigating the influence of the strong SOC on their electronic and magnetic properties. The presence of SOC is expected to affect both the electronic and the magnetic properties of the system and induce for instance strong anisotropy of the magnetic interactions.

Despite the stronger SOC and weaker electronic correlations than their 3*d* counterparts, some of the 4*d* or 5*d* compounds display magnetic behaviors typical of localized magnetism and close to that of $Ca_3Co_2O_6$ with, in particular, the presence of the two magnetic anomalies in the susceptibility measurements. This the case for the following compounds: Ca_3CoRhO_6 [NKK+99], Sr_3CoIrO_6 [MSS+12], Sr_3NiRhO_6 [MIRS07] and Sr_3NiIrO_6 [NzL95, FHM+03, MSS+12]. This is rather surprising since a magnetic behavior characteristics of metals would rather be expected in the 4*d* or 5*d* based compounds, due to weaker electronic correlations. Actually, for Sr_3NiIrO_6, it has been shown by *ab initio* electronic calculations that the SOC opens a gap in the electronic spectrum [ZZJ+10, SKSD10, OW14] leading to an insulating state standardly called a spin-orbit driven Mott insulator. We can also note that the presence of the two magnetic anomalies of $M(T)$ observed in this family seems to be independent not only on the nature of the transition metal ion (3*d*, 4*d* and 5*d*) but also on the number of magnetic species in the system. Indeed in $Ca_3Co_2O_6$, only one out of two Co ions along the chains is magnetic [SFR+04, TMH+05], contrary to the other compounds which present two different magnetic ions alternating along the chain axis. Neutron powder diffraction experiments performed on Ca_3CoRhO_6 and Sr_3CoIrO_6 also support the similarity with the $Ca_3Co_2O_6$ magnetic properties. A long range order is evidenced for both compounds with a magnetic propagation vector $\mathbf{k}$ = (0, 0, 1). The diffractograms are compatible with different magnetic structures including the partially disordered antiferromagnetic state for which only 2/3 of the chains are ordered while the remaining 1/3 remains disordered. The precise role of SOC in the complex magnetic behavior of these systems therefore remains an open question.

In this chapter, I present the study of two compounds belonging to the $A_3MM'O_6$ family: Sr_3NiPtO_6 and Sr_3NiIrO_6.

We have focused on the magnetic properties and the electronic spectrum of the 5*d* electrons in Sr_3NiIrO_6. This material had already been studied by magnetization measurements on a polycrystalline sample [NzL95, FHM+03, MSS+12]. We have been able to synthesized single crystals of Sr_3NiIrO_6 for the first time and we present single crystal magnetization measurements, neutron powder diffraction experiment and single-crystal Resonant Elastic and Inelastic X-ray Scattering experiments. Part of the results have been published in [LCS+14] and [LPMS+16].

To refine our understanding of the magnetic properties of Sr_3NiIrO_6, we also studied the isostructural compound Sr_3NiPtO_6 which allows to probe separately the magnetism of the Ni^{2+} ions. It has already been studied by means of single crystal magnetization and neutron powder diffraction [NGzL94, CLHzL99, CJG+10]. From the magnetization measurements, the Ni^{2+} single ion magne-

tocrystalline anisotropy was found to be strongly easy-plane. The neutron diffraction experiment did not show any long-range ordered phase down to 2 K. This compound was thus proposed to stabilize a "large-*D*" phase [CLHzL99, CJG+10]. We performed additional single crystal magnetization measurements, neutron powder diffraction down to 60 mK and inelastic neutron scattering down to 2 K in order to get direct evidence of this large-*D* phase of Sr_3NiPtO_6.

3.2 Sr_3NiPtO_6

I will first present the study performed on Sr_3NiPtO_6. In this compound the Pt^{4+} ions are non magnetic so only the Ni^{2+} ions contribute to the magnetism. I will first discuss the magnetization measurements then I will present the Time-of-Flight (TOF) inelastic neutron scattering (INS) results and finish by the polarized neutron powder diffraction measurements.

3.2.1 Magnetization measurements

We have measured the magnetization of Sr_3NiPtO_6 using standard Quantum Design MPMS® SQUID magnetometer using magnetic fields up to 5 T and for temperatures between 2 and 300 K. Additional measurements using a SQUID magnetometer equipped with a dilution refrigerator developed by C. Paulsen at Institut Néel were also performed, allowing to go to very low temperature (80 mK). All measurements were performed on single crystals by applying the magnetic field perpendicular or parallel to the chain axis, *i. e.* the c axis. The single crystals have the shape of hexagonal plates, the c axis being perpendicular to the plate, and have been aligned using faces as references with a 5° precision in the two directions.

Figure 3.4 shows the magnetic field dependence of the magnetization for different temperatures. Sr_3NiPtO_6 exhibits a much higher magnetization when the magnetic field is applied perpendicular to the **c** axis than parallel to it, evidencing an easy plane anisotropy perpendicular to this direction.

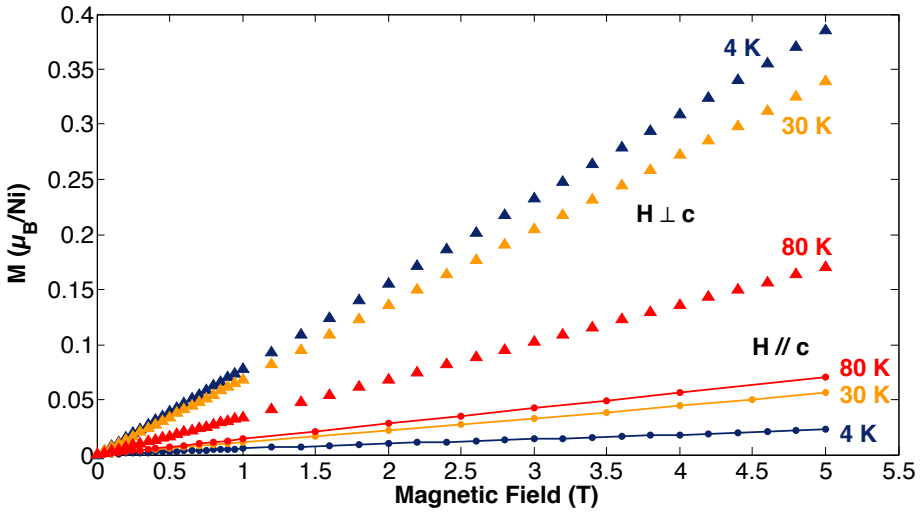

Figure 3.4 – *Magnetic field dependence of the magnetization measured with magnetic fields applied parallel (dots and continuous lines) and perpendicular (triangles) to the* **c** *axis at 4* K *(in blue), 30* K *(in orange) and 80* K *(in red).*

The hysteresis curves (see Fig. 3.5) show no opening in zero field but there is a non linearity of the magnetization for small value of the applied magnetic field, whose signification is discussed latter in this section.

The anisotropy of Sr_3NiPtO_6 is confirmed by the temperature dependence of the magnetization (see Figs. 3.6 and 3.7). The magnetization was measured after a zero-field cooling in 0.01 T and after

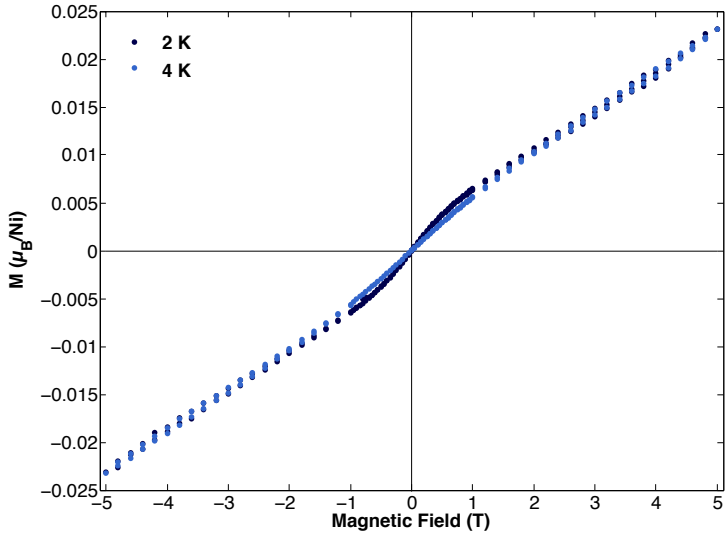

Figure 3.5 – *Magnetization curves measured at 2* K *and 4.2* K *with the magnetic field applied perpendicular to the* **c** *axis.*

field-cooling processes in different magnetic fields. No difference is observed between the ZFC (not shown) and FC curves. The measurements of the FC susceptibility M/H shows very little dependence upon the magnetic field applied during the FC processes. Moreover, the magnetization measurements are in good agreement with the previous studies [CLHzL99, CJG+10].

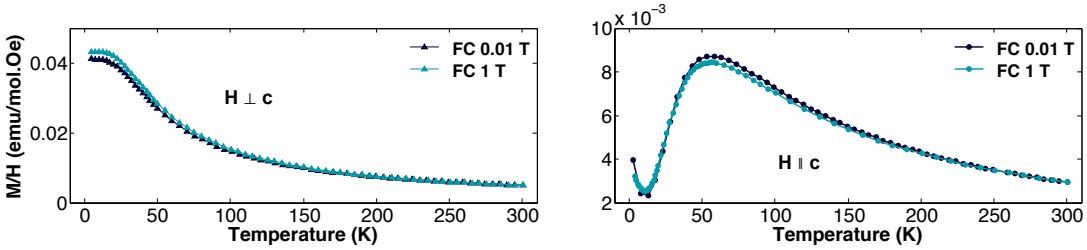

Figure 3.6 – *Temperature dependence of the magnetic susceptibility measured after FC in 0.01* T *(dark blue) and in 1* T *(light blue) with the magnetic field applied perpendicular (left) and parallel (right) to the* **c** *axis.*

At low temperature, an increase of the magnetic susceptibility is observed for decreasing temperature. This is better seen when the magnetic field is applied perpendicular to **c**. This is characteristic of the presence of paramagnetic impurities and could also explain the non linearity of the field dependence of the magnetization measured at 2 K.

The magnetism of Sr_3NiPtO_6 can be modeled by a system of non interacting $S = 1$ Ni^{2+} ions with a large single ion easy plane magnetocrystalline anisotropy D. Fixing the z axis as the quantification axis, the Hamiltonian describing the magnetism of each Ni^{2+} ion can be written as:

$$\mathcal{H} = DS_z^2 - g_\alpha \mu_B \vec{S} \cdot \vec{H} \tag{3.1}$$

the first term corresponds to the single ion magnetocrystalline anisotropy. The second term is due to the Zeemann energy created when a magnetic field $\vec{H}$ is applied, g_α being the Landé factor ($\alpha = \parallel$ or

$\perp$), μ_B the Bohr magneton and $\vec{S}$ the spin operator.

From this Hamiltonian we can compute the theoretical magnetic susceptibility χ for a magnetic field parallel or perpendicular to the **c** (z) axis using the following relation:

$$\chi = -\frac{\mathcal{N}_A}{H}\frac{\partial F}{\partial H}$$

where $\mathcal{N}_A$ is the Avogadro number, F is the free energy of the system and is calculated from the partition function Z using $F = -\frac{1}{\beta} ln(Z)$ and $Z = \exp(-\beta\mathcal{H})$ where $\beta = \frac{1}{k_B T}$.

For a magnetic field applied parallel to the z axis, in the $(|S_z = +1\rangle, |S_z = 0\rangle, |S_z = -1\rangle)$ basis, the Hamiltonian becomes:

$$\mathcal{H} = \begin{pmatrix} D - g_{\parallel}\mu_B H & 0 & 0 \\ 0 & 0 & 0 \\ 0 & 0 & D + g_{\parallel}\mu_B H \end{pmatrix}$$

We can then compute the partition function:

$$Z = 1 + e^{-\beta(D - g_{\parallel}\mu_B H)} + e^{-\beta(D + g_{\parallel}\mu_B H)}$$

and the magnetic susceptibility $\chi_{\parallel}$:

$$\chi_{\parallel} = \mathcal{N}_A g_{\parallel}\mu_B \frac{e^{-\beta D}\left(e^{\beta g_{\parallel}\mu_B H} - e^{-\beta g_{\parallel}\mu_B H}\right)}{1 + e^{-\beta D}\left(e^{\beta g_{\parallel}\mu_B H} + e^{-\beta g_{\parallel}\mu_B H}\right)}$$

Assuming that $\beta g_{\parallel}\mu_B H \ll 1$, the former result rewrites:

$$\chi_{\parallel} = \frac{2\mathcal{N}_A g_{\parallel}^2 \mu_B^2}{k_B T}\frac{e^{-D/k_B T}}{1 + 2e^{-D/k_B T}} \tag{3.2}$$

In the case where the magnetic field is applied perpendicular to the z axis, the Hamiltonian becomes:

$$\mathcal{H} = \begin{pmatrix} D & -\frac{1}{\sqrt{2}}g_{\perp}\mu_B H & 0 \\ -\frac{1}{\sqrt{2}}g_{\perp}\mu_B H & 0 & -\frac{1}{\sqrt{2}}g_{\perp}\mu_B H \\ 0 & -\frac{1}{\sqrt{2}}g_{\perp}\mu_B H & D \end{pmatrix}$$

The eigenvalues of this Hamiltonian are $\left\{D, \frac{1}{2}(D - \sqrt{D^2 + 4g_{\perp}^2\mu_B^2 H^2}), \frac{1}{2}(D + \sqrt{D^2 + 4g_{\perp}^2\mu_B^2 H^2})\right\}$. As $\frac{4g_{\perp}^2\mu_B^2}{D^2} \ll 1$, they can be simplified as $\left\{D, -\frac{g_{\perp}^2\mu_B^2 H^2}{D}, D + \frac{g_{\perp}^2\mu_B^2 H^2}{D}\right\}$.

The magnetic susceptibility $\chi_{\perp}$ is then expressed by:

$$\chi_{\perp} = \frac{2\mathcal{N}_A g_{\perp}^2 \mu_B^2}{D}\left(\frac{1 - e^{-D/k_B T}}{1 + 2e^{-D/k_B T}}\right) \tag{3.3}$$

A fit of the temperature dependence of the magnetization using the relations 3.2 and 3.3 has been performed in order to get the values of $g_{/\!/}$, $g_{\perp}$ and D (see table 3.2 and figure 3.6).

A better agreement between the fitted curves and the experimental data at low temperature is achieved when a contribution from paramagnetic impurities is added using a Curie-Weiss law:

$$\chi = \frac{C}{T - \Theta}$$

where C is the Curie constant which depends on the material and Θ is the Curie-Weiss temperature.

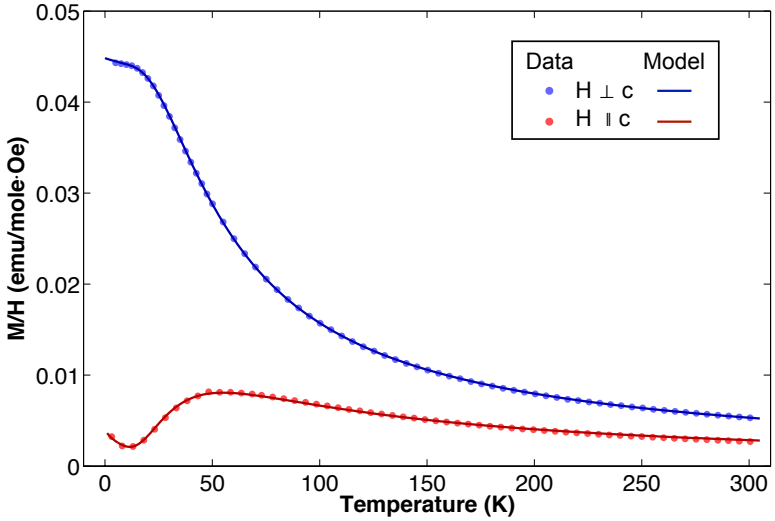

Figure 3.7 – *Experimental data (dots) and model (continuous lines) of the temperature dependence of the magnetic susceptibility with the magnetic field of 0.01* T *applied perpendicular (in blue) and parallel (in red) to the* **c** *axis.*

$g_{\parallel}$	$g_{\perp}$	D (K)	$C_{\parallel}$ (K)	$C_{\perp}$ (K)	$\Theta_{\parallel}$ (K)	$\Theta_{\perp}$ (K)
2.07	2.31	96.63	0.04	0.008	-6.46	-2.03

Table 3.2 – *Parameters obtained from the fit of the susceptibility measurement with the models of Eq. 3.2 and 3.3. $C_{\parallel,\perp}$ and $\Theta_{\parallel,\perp}$ correspond to the Curie constants and Curie temperatures refined for the data measured with the magnetic field parallel and perpendicular to the* **c** *axis.*

The values of the anisotropy constants extracted from the fit are consistent with the ones from previous studies (see table 3.3).

Claridge *et al.* [CLHzL99]	Chattopadhyay *et al.* [CJG+10]	
D	$D_{\parallel}$	$D_{\perp}$
93.7	88.65	107.47

Table 3.3 – *Values of the anisotropy constant obtained in previous studies.*

Claridge [CLHzL99] fitted the data using a unique value of the anisotropy constant, whereas Chattopdhyay [CJG+10] fitted its data independently for the two directions along which the magnetic field was applied. Theoretically the anisotropy constant must be the same in the two directions so we fitted a unique value of D.

Additional magnetization measurements using a SQUID magnetometer equipped with a dilution fridge were performed. No additional anomalies were observed suggesting that Sr_3NiPtO_6 does not order down to 60 mK.

From the magnetization measurements we were able to evidence that Sr_3NiPtO_6 exhibits a large easy plane anisotropy D = 90 K and that it seems to remain disordered down to very low temperature. This suggests that the system may be an experimental realization of a "large-D" phase. This phase exists in quantum spin chains where the anisotropy is much higher than the magnetic interactions, *i.e.* $D/J \gg 1$. The ground state is a collective state of singlet, $S_z = 0$, therefore non-magnetic. In the extreme limit of vanishing intersite interactions, the ground state is separated from the excited states, $S_z = \pm 1$, by an energy barrier corresponding to the anisotropy gap D.

In order to ascertain this hypothesis, INS and polarized neutron diffraction experiments have also been performed. From the INS spectra, a single magnetic excitation at an energy D should be observed.

3.2.2 Inelastic neutron scattering

In order to probe the magnetic excitations in Sr_3NiPtO_6, experiments were performed with J. Ollivier on both the IN6 cold neutron time-of-flight (TOF) spectrometer with incoming neutrons of wavelength 5.1 Å and on the IN4 high-flux thermal neutron TOF spectrometer with incoming neutrons of wavelength 1.1 and 1.6 Å. These measurements were performed on a polycrystalline sample of Sr_3NiPtO_6.

Figures 3.8 and 3.9 show the neutron scattering intensity as function of the wavevector transfer Q and the energy transfer ω for temperatures between 1.5 and 300 K.

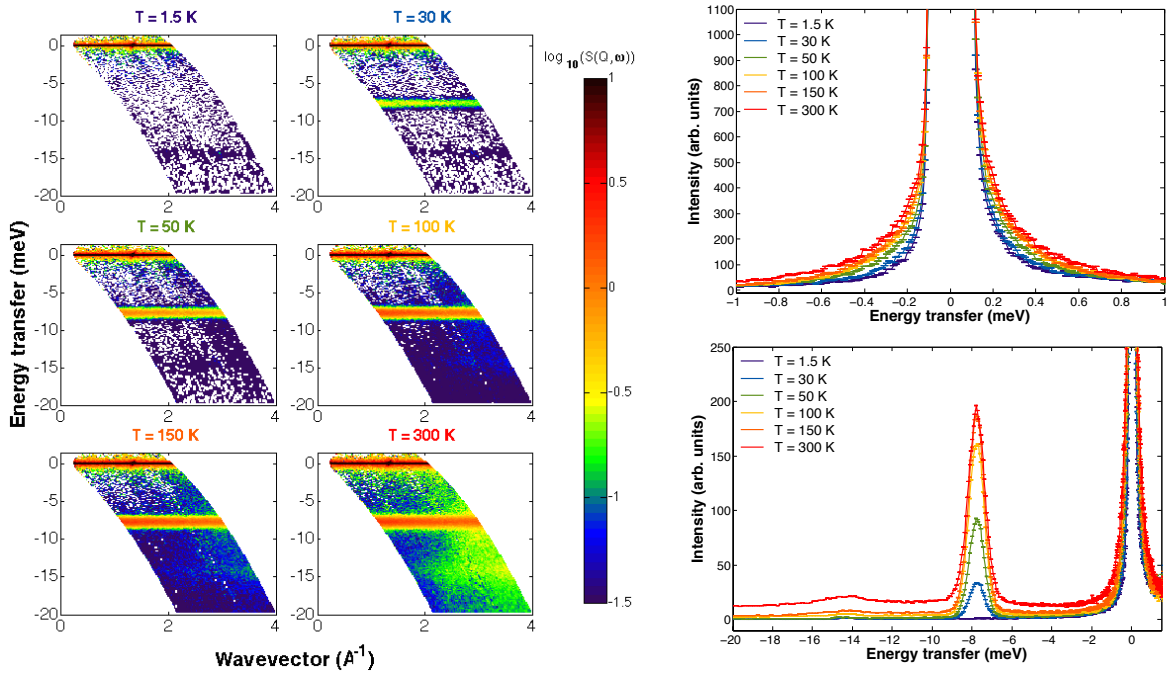

Figure 3.8 – *Neutron intensity S(Q,ω) as function of the wavevector Q and the energy transfer ω (left) and summed over Q (right) measured on IN6 with incoming neutrons of wavelength λ = 5.1 Å for temperatures from 1.5 to 300* K.

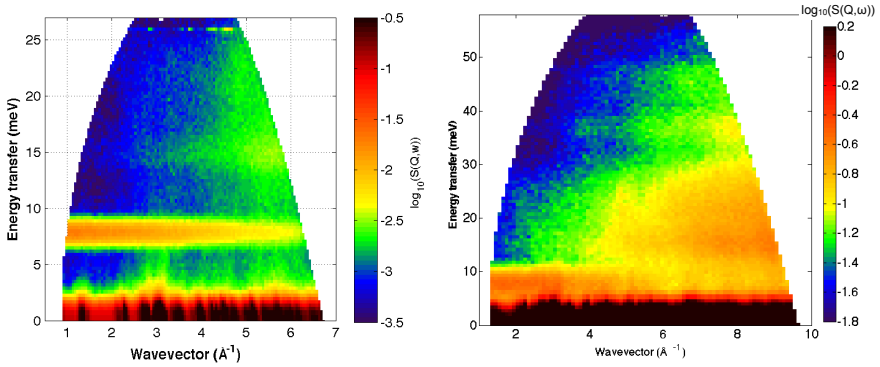

Figure 3.9 – *Observed neutron intensity S(Q,ω) as function of the wavevector transfer Q and the energy transfer ω measured on IN4 with incoming neutrons of wavelengths* 1.6 *Å (left) and* 1.1 *Å (right).*

Both experiments show the presence of two excitations at 7.8 and 14.5 meV respectively. Looking at the Q dependence of these excitations, the one at 7.8 meV is of magnetic origin as its intensity decreases with increasing Q and scales with the square of the Ni^{2+} magnetic form factor. On the other hand, the intensity of the second one increases with Q, it is thereby mainly assigned to phonon contributions. No additional excitations is observed up to 27 meV. The energy of the magnetic excitation is consistent with the anisotropy gap D of 90 K = 7.8 meV. Hence, it can be understood as the excitation of the $S_z = 0$ spin state towards the excited states $S_z = \pm 1$. From the IN4 experiment, for which energies up to 60 meV were probed, no other magnetic excitation was observed (see right part of Fig. 3.9).

From the neutron intensity summed over all wavevectors Q (see right part of Fig. 3.8) we can observe the presence of an additional quasi-elastic signal appearing as the temperature increases that can be assigned to the presence of multi phonons or be a signature of the paramagnetic spin dynamics above the energy gap. The temperature dependence of the 7.8 meV excitations is in agreement with our previous explanation. As the temperature increases, the population of the excited levels and therefore the scattering intensity increases on the anti-Stockes side (neutron energy gain).

3.2.3 Polarized neutron scattering

In order to complete this study, polarized neutron diffraction experiment with XYZ polarization analysis have been performed on the D7 instrument with G. Nilsen at the ILL using a polycrystalline sample of Sr_3NiPtO_6. The nuclear and magnetic scattering cross sections were measured as function of the temperature. A dilution fridge allowed to cool the sample down to 50 mK.

Figure 3.10 shows the magnetic scattering cross section extracted from the neutron intensity. The magnetic Bragg peak observed at $Q = 1.35$ Å^{-1} is due to the presence of a magnetic impurity, NiO, which orders antiferromagnetically below its Néel temperature of 525 K.

At room temperature, a paramagnetic signal scaling with the square of the magnetic form factor is observed. As the temperature is lowered, the magnetic signal intensity decreases to reach a zero value at the lowest temperature. This confirms that the system does not show any evidence of long range order but rather is in a non magnetic singlet state. This is consistent with the low temperature magnetization measurements and with the assumption of a large-D non-magnetic phase.

Note that the intensity measured on D7 is integrated over the energy, therefore a non zero magnetic

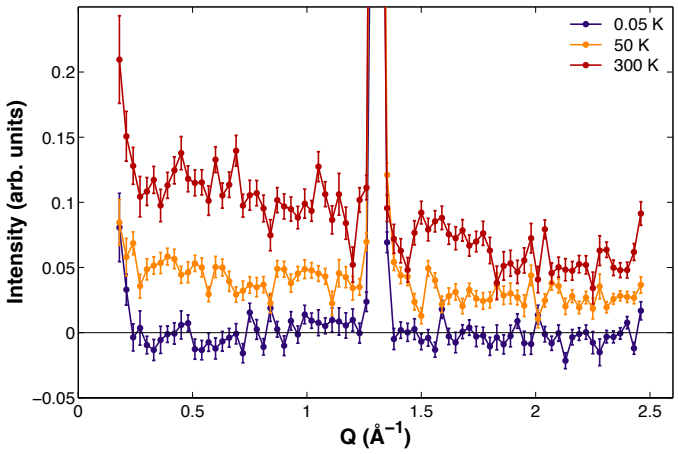

Figure 3.10 – *Magnetic scattering cross section of Sr_3NiPtO_6 measured on D7 at 300* K, *50* K *and 50* mK.

signal could have been observed if the incoming neutron energy was high enough to excite the system. Using incoming neutrons with a wavelength of 5.7 Å (E_i = 1.6 meV), the neutrons cannot fill the excited states and a zero magnetic signal was observed.

In conclusion, Sr_3NiPtO_6 exhibits a large easy-plane of anisotropy D of 90 K$\approx$ 7.8 meV, which has been probed experimentally by magnetic measurements and by inelastic neutron scattering. Moreover no evidence of long-range order is seen but on the contrary the stabilization of a non magnetic state at low temperature is observed. These results suggest that Sr_3NiPtO_6 is an experimental realization of the so-called large-D phase. This phase is predicted for quantum spin chains where the magnetocrystalline anisotropy, D, is much stronger than the magnetic exchange interactions J. The ground state of this system can then be described as non-magnetic singlet ($S_z = 0$) separated from the excited states ($S_z = \pm 1$) by the energy of the anisotropy gap. Excitations of the system correspond to transition from the non magnetic ground state to these excited states for which, in a classical picture, the spins get tilted from the easy plane anisotropy. Although this is not the only compound stabilizing a large-D phase, this work shows the first experimental evidences of such a phase using polarized neutron scattering experiments with XYZ polarization analysis.

3.3 Sr_3NiIrO_6

In this section, we will now present my study performed on the isostructural compound: Sr_3NiIrO_6. The non magnetic Pt^{4+} ions are replaced by Ir^{4+} ions, which are magnetic with a strong SOC. I will first focus on the static magnetic properties with the magnetization measurements and the determination of the magnetic structure. Then the electronic spectra of the Ir 5*d* electrons measured by Resonant Inelastic X-ray Scattering (RISX) will be analyzed and the dynamical properties will be discussed.

3.3.1 Magnetic properties

3.3.1.1 DC Magnetization measurements

Magnetization measurements were performed on a single crystal of Sr_3NiIrO_6 with the magnetic field **H** applied parallel ($\parallel$) and perpendicular ($\perp$) to the **c** axis.

Figure 3.11 shows the temperature dependence of the magnetic susceptibility measured in both directions after a ZFC and a FC in 0.01 T. Two characteristic temperatures are observed:

- $T_1 \approx 75$ K, where the magnetization curves deviate from the Curie-Weiss law
- $T_2 \approx 17$ K, for which a difference between the ZFC and FC curves is observed in both directions. The ZFC curves suddenly drop to small values while the FC curves keep increasing until they reach plateaus.

A crossing of the perpendicular and parallel magnetic susceptibility is observed around 200 K for both the ZFC and FC curves. The magnetization measured along the **c** axis becomes smaller than the one measured perpendicular to the **c** axis above this temperature suggesting an easy plane anisotropy perpendicular to the **c** axis. Below 200 K, the magnetization is much higher when the magnetic field is applied parallel to **c** than perpendicular to it. This evidences an orientation of the magnetic moments preferentially along the **c** axis below this temperature.

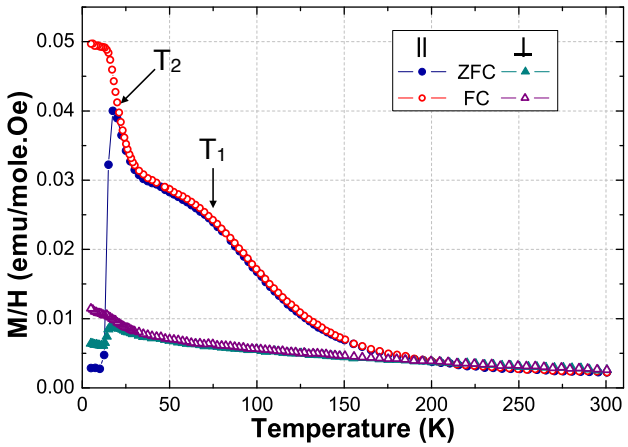

Figure 3.11 – *Temperature dependence of the magnetic susceptibility measured after a ZFC (filled symbols) and a FC in 0.01* T *(open symbols) with the magnetic field applied parallel (circles) and perpendicular (triangles) to the* **c** *axis.*

This observation is confirmed by the magnetic field dependence of the magnetization (see Fig. 3.12). At 300 K, the magnetization measured within the plane perpendicular to the **c** axis is clearly larger than the magnetization measured along the **c** axis, while the reverse is true at 150 K. The high temperature behavior is actually consistent with the one of the previous compound Sr_3NiPtO_6 for which a large

easy-plane anisotropy is evidenced. For Sr_3NiIrO_6, other ingredients have to be taken into account in order to understand the change of anisotropy occurring around 200 K.

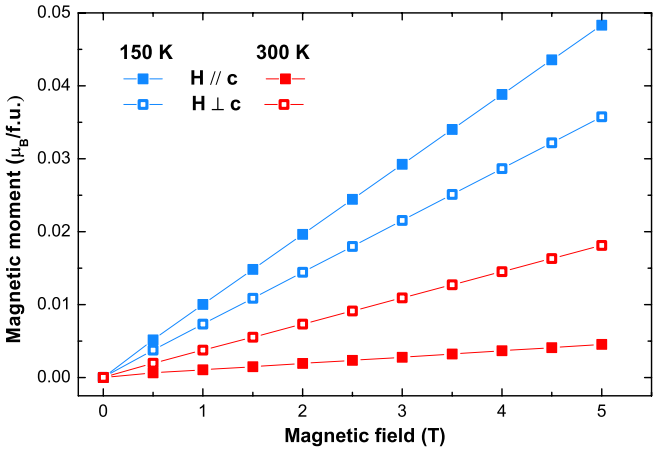

Figure 3.12 – *Temperature dependence of the magnetization measured with the magnetic field applied parallel (filled symbol), a perpendicular (empty symbol) to the* **c** *axis at 300* K *(in red) and 150* K *(in blue).*

The magnetization measurements also reveal the presence of a weak ferromagnetic component along the **c** axis below 17 K (see Fig. 3.13), temperature at which a separation between the FC and ZFC magnetic susceptibility measurements is observed.

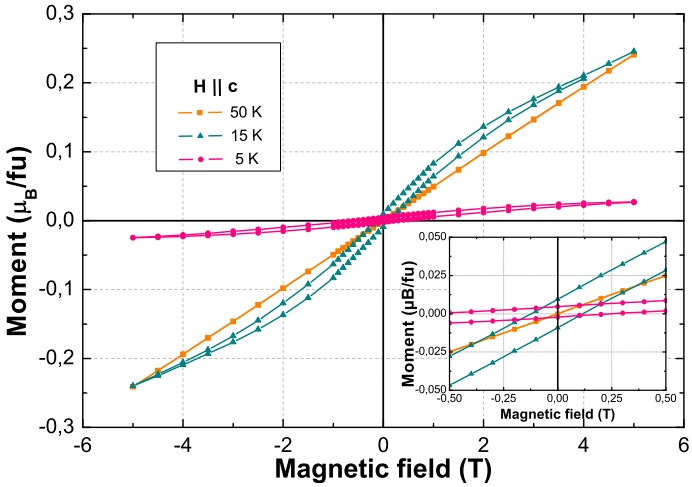

Figure 3.13 – *Magnetization hysteresis curves measured at 5, 15 and 50* K *with the magnetic field applied parallel to* **c**. *Inset: zoom around zero field of the hysteresis curves opening with the temperature.*

Note that the magnetization measured at 5 K is much weaker than the ones measured at higher temperatures indicating a change in the magnetic behavior at T_2. In the ordered phase above T_2=17 K, a two-step reversible magnetization was measured using pulsed magnetic field up to 35 T by Flahaut *et al.* [FHM+03] on a polycrystalline sample. A first plateau reaching $\approx$ 0.2 μ_B/f.u. is stabilized until 7 T, where the increase of the magnetization with the field accelerates. Below 17 K, this two step magnetization is replaced by a hysteresis cycle opening with a coercive field increasing while

decreasing the temperature [FHM+03, SKT+14] (see Fig. 3.14).

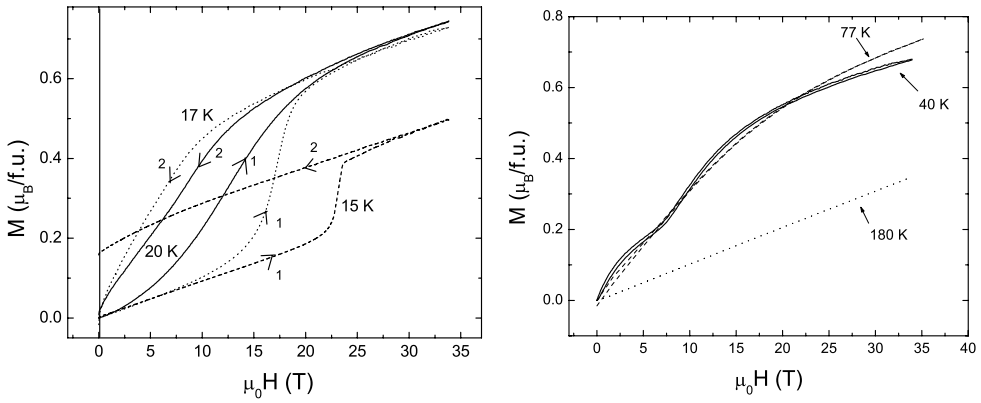

Figure 3.14 – *Magnetization hysteresis curves measured on a polycrystalline sample of Sr_3NiIrO_6 for $T < T_2$ (left) and $T_2 < T < T_1$ (right) using pulsed magnetic field. From [FHM+03]*

The presence of a ferromagnetic component along the **c** axis has been confirmed using magnetization measurements with pulsed magnetic field up to 60 T by Singleton *et al.* (see Fig. 3.16) [SKT+14]. The measurements of Singleton *et al.* confirm that the ferromagnetic component is only present when the magnetic field is applied parallel to the **c** axis and below 20 K, temperature corresponding to the lowest characteristic temperature T_2. Besides, a huge coercive magnetic field, up to 55 T (see Fig. 3.15), was evidenced in this work.

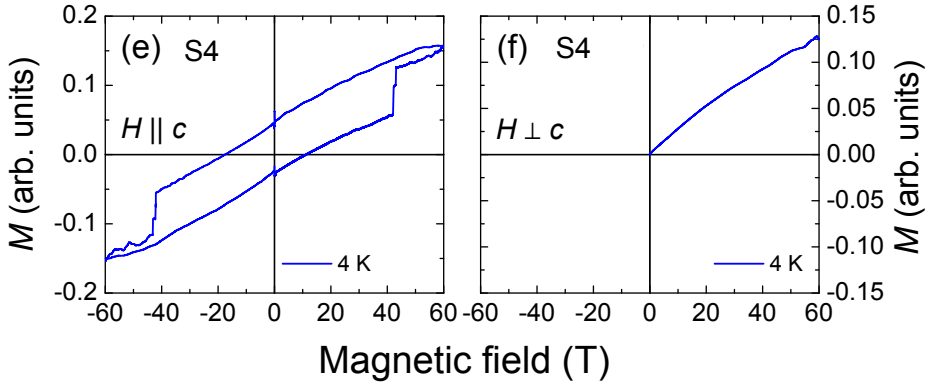

Figure 3.15 – *Magnetization M as a function of magnetic field measured in a series of magnetic pulses using a capacitor-bank-driven 65 T pulsed magnet. An hysteresis is seen in the H ∥ c configuration (left) while no hysteresis is observed in the H ⊥ c configuration (right).* From Singleton *et al* [SKT+14]

3.3.1.2 AC Magnetization measurements

The temperature dependence of the AC susceptibility was measured by Adroja *et al.* in a magnetic field of 6×10^{-3}mT with frequencies ranging from 11 to 2000 Hz on a polycrystalline sample of Sr_3NiIrO_6. I analyzed these data and the left part of Figure 3.17 shows the temperature dependence of the in-phase (M') and out-of-phase (M'') magnetization for different frequencies.

The onset of spin dynamics is observed in the magnetization below 70 K and it gets frozen below $T_2 = 17$ K. The out-of-phase magnetization exhibits a maximum when the in-phase magnetization

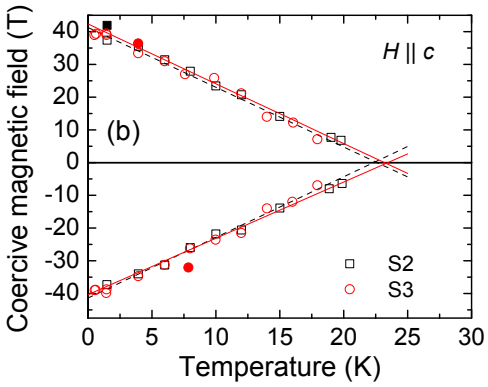

Figure 3.16 – *T-dependence of the coercive field deduced for two different single crystals (called S2 and S3 in the figure) magnetization measurements in pulsed fields. Filled symbols indicate the result obtained after the initial pulse in zero-field cooling from room temperature; these show slightly larger coercive fields values compared to those measured in subsequent pulses (empty symbols). Lines are linear fits to the data.* From Singleton *et al* [SKT+14]

drops. The temperature at which the maximum is observed shifts towards higher temperature as the frequency increases. Assuming that the dynamics is governed by a single relaxation time τ, $M''(T)$ is maximum when the measurement time ($= 1/2\pi f$) is equal to τ. We used a simple model to analyze the measurements although it may be too crude to capture the whole physics of our system. Usually in thermal activated process over an energy barrier E, τ follows an Arrhenius law $\tau = \tau_0.\exp(E/k_BT)$ where τ_0 is the characteristic relaxation time. The refinement of the experimental data (see right part of Fig. 3.17) gives an energy barrier of 422(13) K and a characteristic relaxation time of $2(1) \times 10^{-11}$s.

This activated behavior is characteristic of single-chain magnets with significant anisotropy [CMC06]. It reveals the presence of an energy barrier necessary to create a domain within a chain. For perfect Ising chains, the spin dynamics is well described by the Glauber theory [Gla63] and the energy barrier is equal to $2JS^2$ with J the first neighbor intrachain interaction. For anisotropic Heisenberg spin chains, the energy barrier involves both the exchange interaction and the single-ion anisotropy. Our case, with two atomic species and anisotropic interactions, is more complex but the energy barrier of 422 K mainly reflects the influence of the strongly anisotropic exchange interactions on the spin dynamics of Sr_3NiIrO_6 and is in agreement with the values of the exchange interactions derived from the spin wave analysis (see section 3.3.4.1).

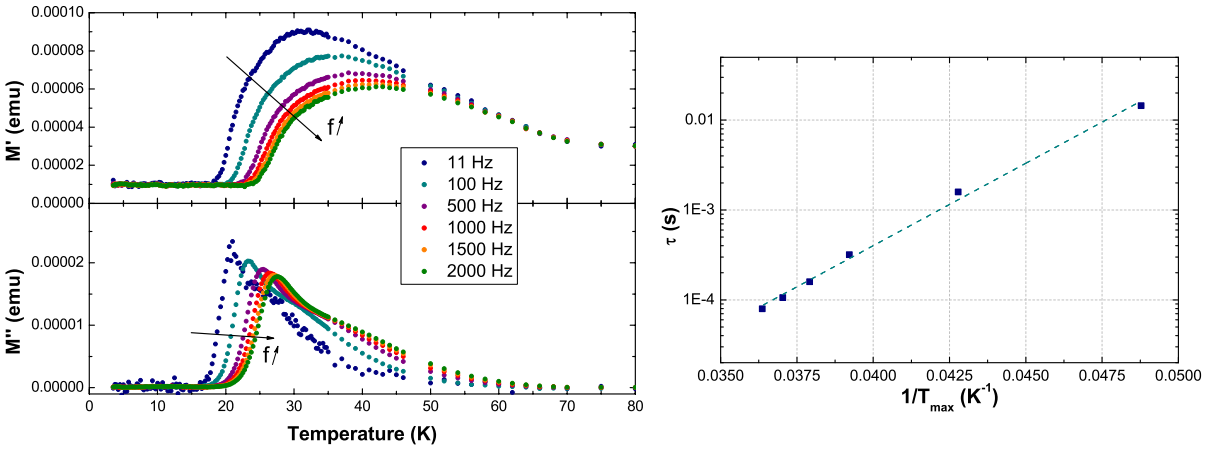

Figure 3.17 – *(left) Temperature dependence of the in-phase (M' - top) and out-of-phase (M'' - bottom) magnetization measured at different frequencies. (right) Temperature dependence of the relaxation time τ. The blue squares are the experimental values and the blue dashed line corresponds to the refinement of the data by an Arrhenius law, with $E = 422 \pm 13$ K and $\tau_0 = 2(1) \times 10^{-11}$ s.*

3.3.1.3 Powder neutron diffraction

In order to determine the magnetic order in Sr_3NiIrO_6, neutron powder diffraction measurements have been performed on polycrystalline sample on the WISH diffractometer at the ISIS Facility. These measurements have been performed by Adroja *et al.* and I analyzed the data.

The inset of Fig. 3.18 shows the diffraction data measured at 2 and 100 K. Additional Bragg peaks are observed rising below 70 K, indicating the presence of a magnetic long range order. From the position of these magnetic Bragg peaks, we can determine the magnetic propagation vector, $\mathbf{k} \approx (0, 0, 1)$. In the primitive rhombohedral description of the lattice, this corresponds to a (1/3, 1/3, 1/3) propagation vector, *i.e.* an antiferromagnetic structure (see details in Appendix A).

In order to guide the refinement of the magnetic Bragg peaks at 2 K, a symmetry analysis was first performed. The possible magnetic structures, compatible with the space group of this compound and the (0, 0, 1) propagation vector in the case of a 2^{nd} order phase transition, were determined using the method of representation analysis [Ber68]. Three irreducible representations are obtained (see Table 3.4):

- τ_1 and τ_2, of dimension 1, corresponding to respectively an AFM and a FM arrangement within each magnetic sublattice (Ni and Ir) with the magnetic moments aligned along the **c** axis
- τ_3 of dimension 2, corresponding to an in-plane magnetic order

τ_2 is the only irreducible representation allowing to refine the data (see Fig. 3.18). The magnetic structure consists of ferromagnetically coupled magnetic moments from the same sublattice while the Ni^{2+} and Ir^{4+} magnetic moments are antiferromagnetically coupled along the chains. The intensity of the refined magnetic moments are $M_{Ni} = 1.5(1)\mu_B$ and $M_{Ir} = 0.5(1)\mu_B$ at 2 K (see Fig. 3.19). These values are smaller than the expected ones: 2 μ_B for S = 1 spin and 1 μ_B for S=1/2 spin. Besides, the intensities of the magnetic peaks saturate below 35 K without any evolution of the peaks shape in particular at 17 K, temperature at which the ZFC and FC magnetic susceptibility get separated.

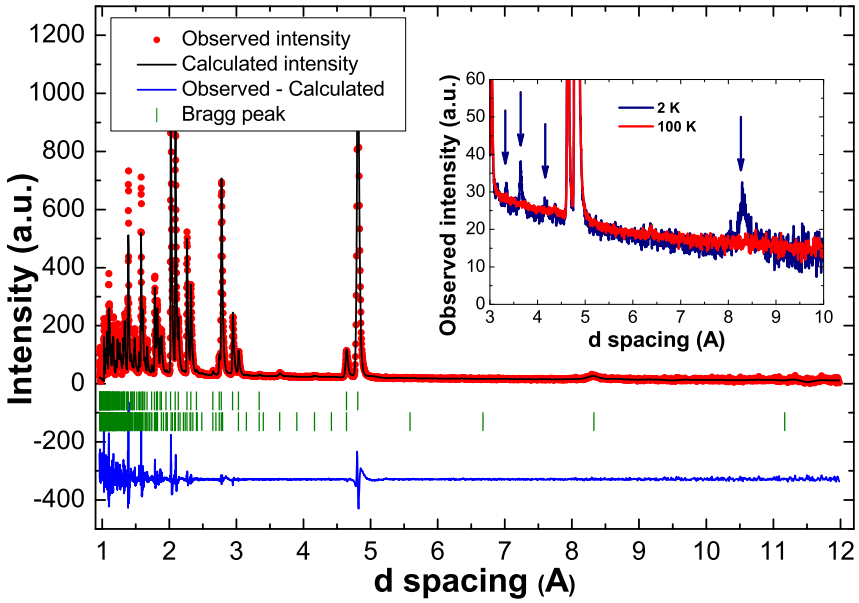

Figure 3.18 – *Neutron powder diffraction of Sr_3NiIrO_6 recorded at 2* K*. The observed and calculated intensities are shown as well as the difference. Inset: zoom of the neutron powder diffraction at 2 and 100* K *showing the onset of magnetic Bragg peaks.*

Using neutron diffraction experiments, we get information about the modulus of the magnetic structure factor, which is defined by

$$F_M = \sum \frac{1}{2} g\langle S\rangle \sigma F(Q) e^{-W} e^{i\varphi}, \tag{3.4}$$

where $g\langle S\rangle$ corresponds to the ordered moment, $F(Q)$ to the magnetic form factor, e^{-W} to the Debye-Waller factor and φ is the global phase related to the magnetic modulation. Therefore we cannot have access to parameters such as the global phase and have to rely on indirect symmetry arguments and bulk properties to propose a unique model for the magnetic structure. Different magnetic structures corresponding to different values of φ are compatible with the neutron integrated intensities (see Fig. 3.20), considering a commensurate or a slightly incommensurate propagation vector, as the instrumental resolution does not allow us to clearly state on that matter.

For a slightly incommensurate propagation vector, an incommensurate amplitude modulated structure ($R\bar{3}c1'$) would be observed, similarly to the case of $Ca_3Co_2O_6$. For a commensurate propagation vector and an arbitrary value of φ, the magnetic structure can be described as a commensurate amplitude modulation of the magnetic moments on the three chains. Two specific values of φ lead to peculiar magnetic arrangements:

- for $\varphi = 0 + n \cdot \frac{2\pi}{3}$ (n: integer), we get (+M, $-\frac{1}{2}M$, $-\frac{1}{2}M$) for the moments at atomic positions $\left[(0,0,z),(\frac{1}{3},\frac{2}{3},\frac{2}{3}+z),(\frac{2}{3},\frac{1}{3},\frac{1}{3}+z)\right]$ ($P\bar{3}c'1$)
- for $\varphi = \frac{\pi}{6} + n \cdot \frac{2\pi}{3}$ (n: integer), we get a partially disordered antiferromagnetic state where 2/3 of the chains are fully ordered and antiferromagnetically coupled and the remaining 1/3 stays disordered ($P\bar{3}'c'1$)

The structure obtained for $\varphi = 0$ is the most symmetric arrangement whose magnetic space group ($P\bar{3}c'1$) allows the coexistence of the antiferromagnetic mode as the primary order parameter and of a

Magnetic sites	Ni_1 $(0,\ 0,\ \frac{1}{4})$	Ni_2 $(0,\ 0,\ \frac{3}{4})$	Ir_1 $(0,\ 0,\ 0)$	Ir_2 $(0,\ 0,\ \frac{1}{2})$
τ_1	$\begin{pmatrix}0\\0\\u_1\end{pmatrix}$	$\begin{pmatrix}0\\0\\-u_1\end{pmatrix}$	$\begin{pmatrix}0\\0\\u_2\end{pmatrix}$	$\begin{pmatrix}0\\0\\-u_2\end{pmatrix}$
τ_2	$\begin{pmatrix}0\\0\\u_1\end{pmatrix}$	$\begin{pmatrix}0\\0\\u_1\end{pmatrix}$	$\begin{pmatrix}0\\0\\u_2\end{pmatrix}$	$\begin{pmatrix}0\\0\\u_2\end{pmatrix}$
τ_3	$\frac{3}{2}\begin{pmatrix}u_1+p_1\\0\\0\end{pmatrix}+ i\sqrt{3}\begin{pmatrix}\frac{1}{2}(-u_1+p_1)\\-u_1+p_1\\0\end{pmatrix}$	$\frac{3}{2}\begin{pmatrix}0\\v_1+w_1\\0\end{pmatrix}+ i\sqrt{3}\begin{pmatrix}v_1-w_1\\\frac{1}{2}(v_1-w_1)\\0\end{pmatrix}$	$\frac{3}{2}\begin{pmatrix}u_2+p_2\\0\\0\end{pmatrix}+ i\sqrt{3}\begin{pmatrix}\frac{1}{2}(-u_2+p_2)\\-u_2+p_2\\0\end{pmatrix}$	$\frac{3}{2}\begin{pmatrix}0\\v_2+w_2\\0\end{pmatrix}+ i\sqrt{3}\begin{pmatrix}v_2-w_2\\\frac{1}{2}(v_2-w_2)\\0\end{pmatrix}$

Table 3.4 – *Magnetic configurations associated with the three irreducible representations of the group of the propagation vector* $\mathbf{k}$ *= (0, 0, 1) for* Sr_3NiIrO_6*.* $u_{1,2}$*,* $p_{1,2}$*,* $v_{1,2}$ *and* $w_{1,2}$ *are refinable parameters of the Fourier coefficients of the spin* S_k*.*

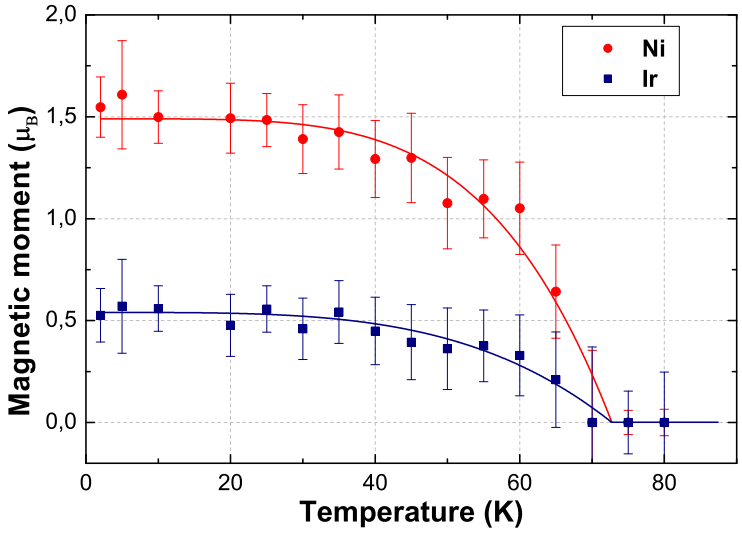

Figure 3.19 – *Temperature dependence of the magnetic moments of Ni and Ir in absolute value from the refinement of the diffractograms. The plain line are guides for the eyes.*

ferromagnetic mode along the c axis, which would then be the secondary (induced) order parameter.

Indeed in the Landau theory, a phenomenological expression for the free energy can be given in the vicinity of the transition temperature T_c, as a Taylor expansion in the order parameter:

$$F = F_0 + a\frac{1}{2}(T - T_c)\psi^2 + b\psi^4 + \cdots,$$

where ψ is the primary order parameter corresponding to the antiferromagnetic mode. The ferromagnetic component observed at low temperature should correspond to a secondary order parameter, i.e. a parameter which becomes non zero as the same time as the primary one but does not drive the transition. Coupling terms of the form $\psi^n M_z^m$, where M_z represents the ferromagnetic component, *i.e.* the secondary order parameter, can then be added in the expression of the Free energy at the condition that they are invariant under the symmetry of the paramagnetic group. In order to see which coupling terms are authorized, one can look at the effects of the different symmetry operations of the space group $R\bar{3}c1'$ on both the primary and secondary order parameters (see Table 3.5). The main term

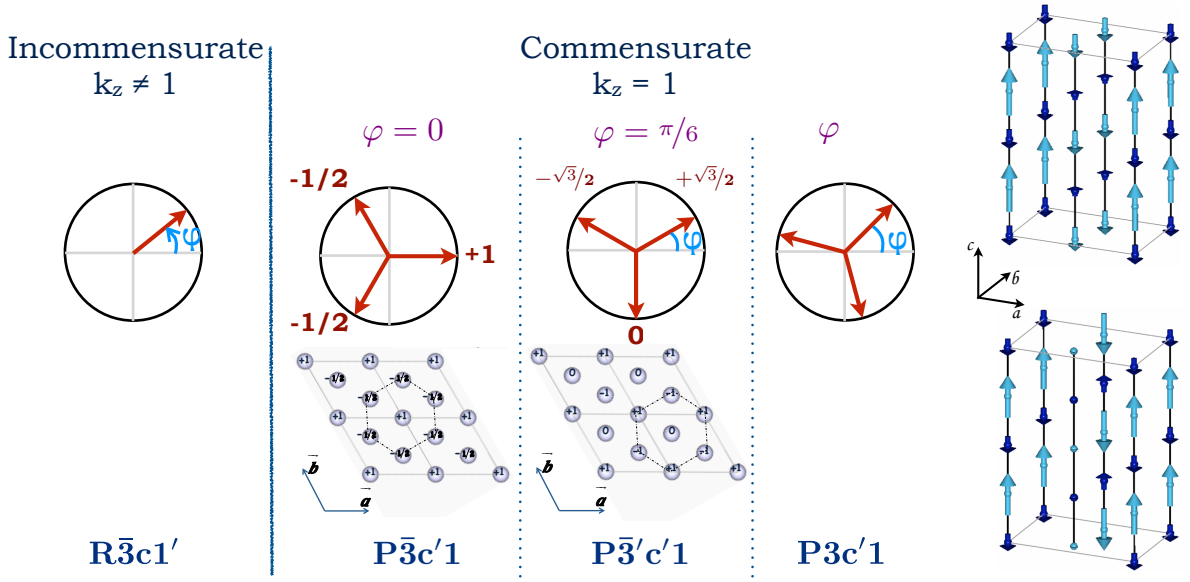

Figure 3.20 – *Magnetic structure compatible with the neutron powder diffraction measurement for a slightly incommensurate propagation vector (left) and for a commensurate propagation vector (right) considering different values of the global phase. The perspective views on the right represent the magnetic structures for $\varphi = 0$ (top) and $\pi/6$. (bottom).*

IR	Symmetry generators of space group $R\bar{3}c1'$					
	$3^+(0,0,z)$	$2(x,x,0)$	$\bar{1}$	$\mathbf{t}_1$	$\mathbf{t}_2$	$1'$
LD1	$\begin{pmatrix} 1 & 0 \\ 0 & 1 \end{pmatrix}$	$\begin{pmatrix} 0 & 1 \\ 1 & 0 \end{pmatrix}$	$\begin{pmatrix} 0 & e^{i\pi k} \\ e^{-i\pi k} & 0 \end{pmatrix}$	$\begin{pmatrix} e^{i\frac{2\pi k}{3}} & 0 \\ 0 & e^{-i\frac{2\pi k}{3}} \end{pmatrix}$	$\begin{pmatrix} e^{i\frac{4\pi k}{3}} & 0 \\ 0 & e^{-i\frac{4\pi k}{3}} \end{pmatrix}$	$\begin{pmatrix} -1 & 0 \\ 0 & -1 \end{pmatrix}$
M_z	M_z	$-M_z$	M_z	M_z	M_z	$-M_z$

Table 3.5 – *Matrix representatives [AKC+06] of the LD1 irreducible representation for generators of the space group $R\bar{3}c1'$ (Miller and Love notation [CDML79]) and wave-vector $\mathbf{k}$ =(0, 0, k). $\mathbf{t}_1$ and $\mathbf{t}_2$ represents the respective R-lattice translations (2/3, 1/3, 1/3) and (1/3, 2/3, 2/3). The 1′ symbol represents time-reversal symmetry. The bottom line shows how the M_z secondary ferromagnetic mode at k=0 transforms under the various symmetries.*

would then be of the form $|\psi|^3 \cdot M_z$

If the ferromagnetic component observed in the magnetization measurement versus H is intrinsic to the long range ordered phase, then the magnetic structure of Sr_3NiIrO_6 at 2 K would be the amplitude modulated antiferromagnetic one corresponding to $P\bar{3}c'1$. The transition observed at 17 K could either be a transition from a low temperature commensurate to a high temperature incommensurate structure or, if the propagation vector remains commensurate, an abrupt change of the phase φ from 0 at low temperature to $\pi/6$ at high temperature, thus from an amplitude modulated to a partially disordered structure. Note that the two-step magnetization observed above T_2 [FHM+03] might indeed be a signature of the partially disordered arrangement. The freezing of the paramagnetic chain in the field direction should give rise to a plateau at 1/3 of the magnetization of the ferromagnetically aligned ferrimagnetic chains. Its disappearance below T_2, as well as the freezing of the spin dynamics, are compatible with the emergence of an alternating magnetic structure with no disordered chains.

On the other hand, if the ferromagnetic component is extrinsic, then all the magnetic structures proposed in Fig. 3.20 would be possible. This extrinsic contribution could be a non-equilibrium configuration induced by the applied magnetic field and pinned by the defects and the strong anisotropy of the system. Alternatively, it could reflect the presence of a competing ferromagnetic phase signaled by ferromagnetic clusters like in $Ca_3Co_2O_6$ [PLM+14].

3.3.2 Nature of the magnetic transitions

Having determine the nature of the magnetic structure below T_2 = 17 K, we then attempted to investigate the nature of the high temperature magnetic structure based on the assumptions made in the previous section. I will first describe the Resonant Elastic X-ray Scattering (REXS) experiments performed on I16 which allowed us to probe the commensurability of the magnetic propagation vector **k** and also measurements performed on ID20 during the Resonant Inelastic X-ray Scattering (RIXS) experiment.

3.3.2.1 Resonant Elastic X-ray Scattering

Resonant Elastic X-ray Scattering (REXS) experiments were performed on the I16 beamline at Diamond with A. Bombardi. We studied the evolution of the magnetic propagation vector with the temperature as well as the magnetic correlations in the ordered phases. The instrumental setup of I16 provides a really good resolution in the **Q** space allowing to probe very small incommensurability of the magnetic wavevector.

Figure 3.21 shows the azimuthal scan performed on the (6 6 4) magnetic reflection.

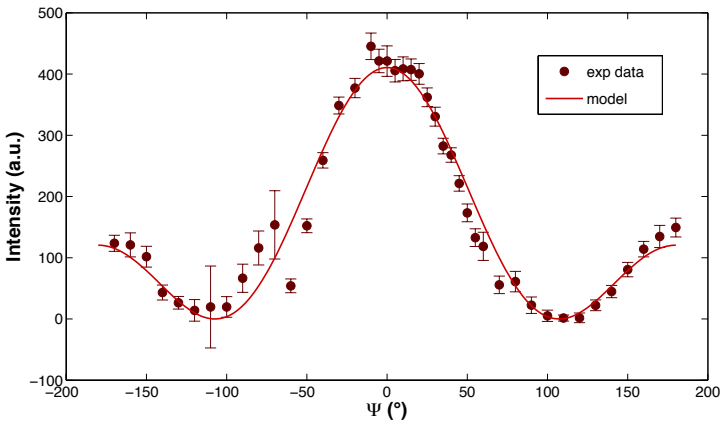

Figure 3.21 – *Azimuthal dependence of the (6 6 4) magnetic reflection intensity. The line is a fit to the data of the scattering amplitude.*

This measurement allows a precise determination of the orientation of the magnetic moments. The expected observed intensity can be calculated using a model taking into account the magnetic moment orientations. In this case, the calculation agrees very well with the experiment for magnetic moments fully confined along the chain axis, confirming the absence of in-plane magnetic moment components.

Moreover, as the measurements are performed at the Ir L_3 resonance edge, only the Ir magnetism is probed. Therefore, this gives a nice confirmation of the direction of the Ir magnetic moments as the Ir contributes weakly to the neutron scattering intensities.

To probe the commensurability of the magnetic propagation vector, scans of the reciprocal space along the L direction were performed. Selecting several magnetic peaks amongst the most intense ones, these scans were made through the magnetic peak and through its two nearest neighbor charge peaks. This allowed to account for possible changes of the lattice parameters with the temperature or misalignment occurring during the experiment. Three different magnetic peaks were measured: (6 6 2), (6 6 4) and (7 5 0). Measurements show identical behavior for the three peaks. I will therefore only present the measurements and analysis performed on the (7 5 0) magnetic peak.

Figure 3.22 shows the temperature dependence of the scans of magnetic and charge peaks performed along the (7 5 **L**) direction.

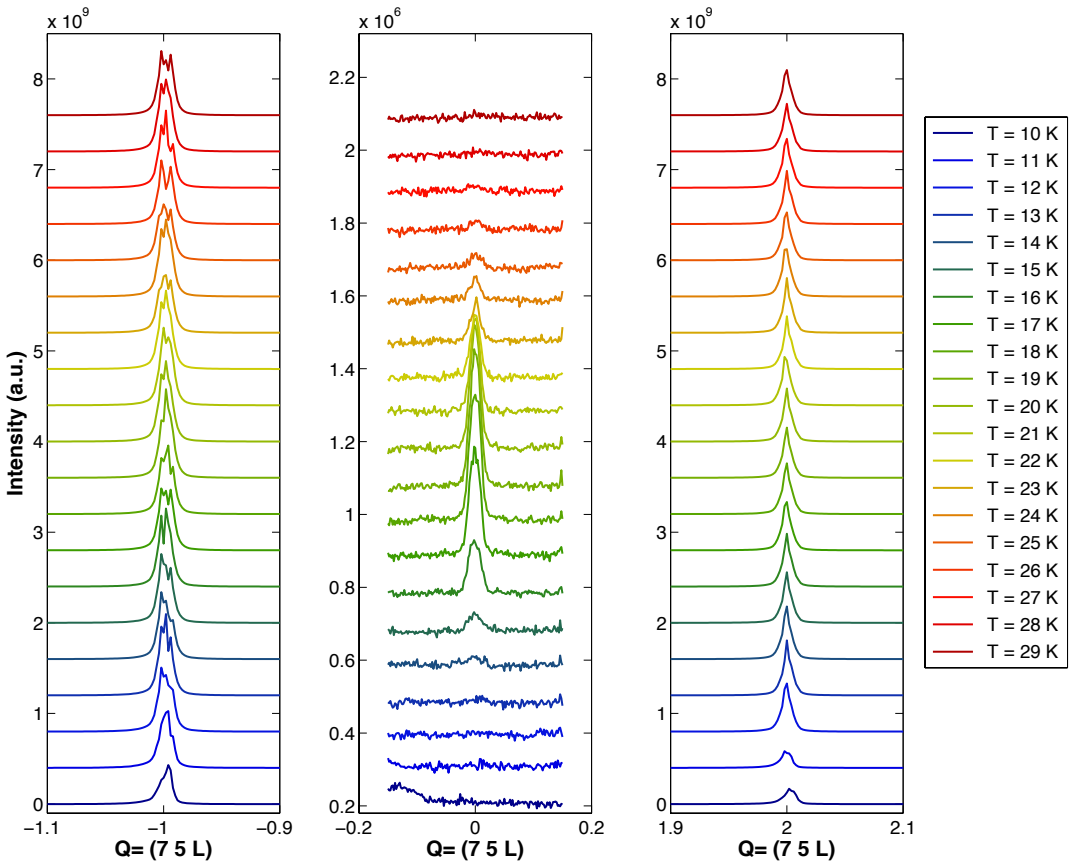

Figure 3.22 – *Scans along the L direction of the reciprocal space for the (7 5 0) magnetic peak [middle] and its two nearest neighbor charge peaks (7 5 -1) and (7 5 2) [left and right].*

By fitting the peaks at all temperature using a Lorentzian distribution (see Appendix B), the positions of the maximum are extracted. In reflection geometry that we have used, it has been difficult to obtain a reliable orientation matrix for all temperatures. Indeed, the position of the charge peaks are slightly shifted of a few per thousand from their expected position (L=-1 and L=2). Thus, in order to minimize offsets when determining the position of the magnetic peaks, the following procedure has been used:

– for the charge peaks, reciprocal space positions were corrected taking into account that the Miller indices should remain fixed at all temperatures and fixed to their expected values

– for the magnetic peak, the value was corrected considering that the ratio r between the distance to one charge peak and the distance to the other should be the same before and after the correction of the charge peaks.

$$r = \frac{x_{C2} - x_M}{x_M - x_{C1}} = \frac{x'_{C2} - x'_M}{x'_M - x'_{C1}}$$

where $x_{C1(2)}$ and $x'_{C1(2)}$ correspond to the position of the first (second) charge peak before and after the corrections and x_M and x'_M are the magnetic peak positions before and after correction. Then the corrected position of the magnetic peak writes:

$$x'_M = \frac{x'_{C2} + r x'_{C1}}{r + 1}$$

Figure 3.23 shows the position of the peaks after correction. Looking at the refined position for the magnetic peak, we can note that there is no change in its position from the L = 0 value within the error bars as the temperature increases from 10 K up to 30 K through the magnetic transition temperature of 17 K.

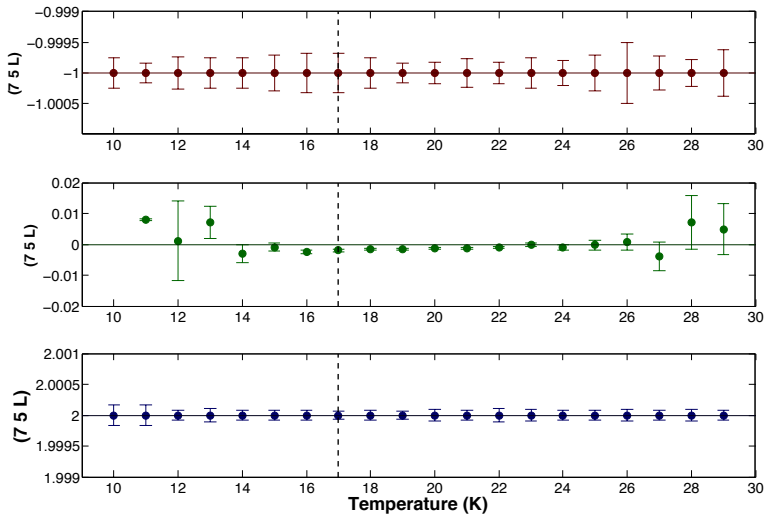

Figure 3.23 – *Temperature dependence of the peak position along the (7 5* **L***) direction after correction for the magnetic Bragg peak (middle) and the two charge peaks (top and bottom). Plain lines are guide to the eyes and the dotted line denote the transition temperature T_2 = 17* K.

This experiment shows that the magnetic propagation vector **k** remains commensurate and is equal to (0 0 1.000(2)), in the two ordered magnetic phases.

In the previous section, different scenarios were described in order to explain the transition observed at T_2. From these REXS measurements, the magnetic propagation is shown to remain commensurate in the two ordered phases. Thus assuming an intrinsic ferromagnetic component below T_2, the transition should be a change of the global phase φ from 0 at low temperature to $\pi/6$ at high temperature, corresponding to a change from an amplitude modulated to a partially disordered structure.

Now looking at the integrated intensity of the magnetic peak extracted from the fits (see Fig. 3.24), we note that the magnetic intensity increases from zero at 30 K to reach a maximum around 18 K ($\approx T_2$) and then quickly decreases as the temperature is decreased. At T_2, the peak width is around 0.02 $Å^{-1}$, leading to a correlation length $\xi \approx 314$ Å.

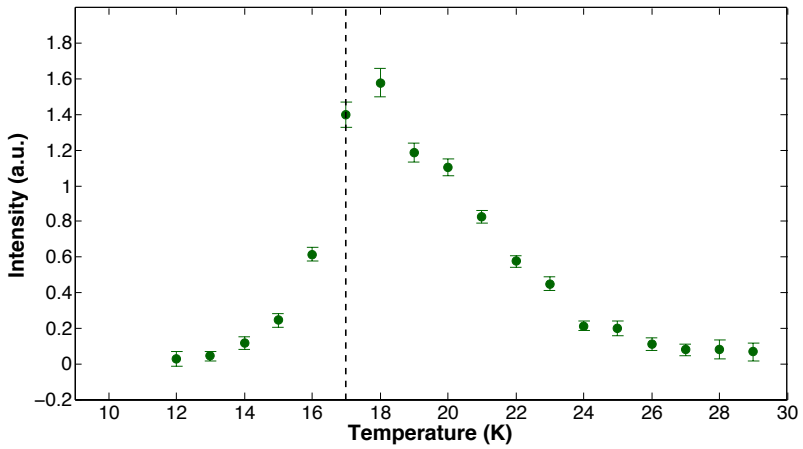

Figure 3.24 – *Temperature dependence of the (7 5 0) magnetic peak integrated intensity extracted from the fits. The dotted line denotes the transition temperature T_2 = 17* K.

We have also performed scans of the reciprocal space to probe the potential presence of a second magnetic phase, as it was reported for $Ca_3Co_2O_6$ [AFC+11]. Nevertheless, no other magnetic peaks were detected. Note however that, in the case of $Ca_3Co_2O_6$, the lower temperature ordered phase was observed only during a neutron powder diffraction experiment. The measurements on single crystals were unable to confirm its presence [private communication with L. Chapon]. This transition from the incommensurate phase with **k** = (0, 0, 1.01) to the commensurate one with **k** = ($^1/_2$, -$^1/_2$, 0) was observed over a quite long time scale of a few hours. This was the time needed for the volume of material exhibiting the short range order to entropically increase as the spin density wave phase become unstable. The reason for which it was not observed on the single crystal could be that the material is subjected to less internal stress in its polycrystalline form.

In summary, from the REXS measurements, we showed that the magnetic propagation vector is commensurate in the two ordered phases. A peculiar behavior is evidenced as function of the temperature with a magnetic intensity and correlation length being maximum at $T_2 \approx 17$ K, both decreasing as the temperature is further lowered or increased. However the very good resolution in the reciprocal space of the instrumental setup made the analysis of the magnetic peak quite difficult as soon as it starts to loose coherence.

3.3.2.2 Resonant Inelastic X ray Scattering

Resonant Inelastic X ray Scattering (RIXS) experiment providing a quite low resolution in **Q** space, it does not allow to obtain precise reciprocal space information but is very useful for signals not well correlated as it was observed by REXS in Sr_3NiIrO_6. During the RIXS experiment we followed the evolution of two magnetic peaks in elastic conditions: (10 -1 6) and (10 0 8) as a function of temperature, scanning the peaks along different directions of reciprocal space. Only the analysis performed on the (10 -1 6) magnetic Bragg peak is shown in this section, but identical results were obtained on the second magnetic peak.

Figure 3.25 shows the scans of the (10 -1 6) magnetic Bragg peak along (10 K 6) and (10 -1 L), for temperatures from 6 K up to 300 K. As the temperature is decreased, the intensity of the magnetic

peak is rising and reaches a maximum value at 22.5 K. Then if the temperature is further lowered, the intensity of this magnetic Bragg peak drops suddenly until 12 K. At this temperature the intensity starts to slowly increase again. This behavior is rather unexpected, indeed the intensity of the magnetic Bragg peaks was expected to continue to increase until it reaches the saturation at low temperature as it was observed in the neutron powder diffraction experiment (see Fig. 3.19).

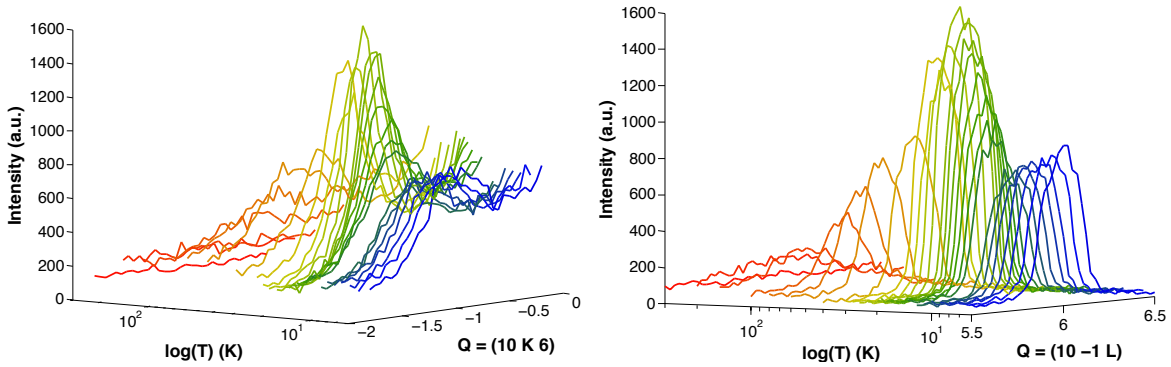

Figure 3.25 – *Scans of the (10 -1 6) magnetic Bragg peak along the (10 K 6) (top) and the (10 -1 L) (bottom) directions for temperature from 6* K *(in blue) to 300* K *(in red).*

Moreover, a drastic change of the shape of the magnetic peak is also observed depending on the scan direction (see Fig. 3.26).

Fits of the peaks were performed to better follow and understand their temperature evolution. This allows extracting the peak area as well as its width.

For the fit along the K and L directions respectively, the following functions were used:

$$f_K(x, a_0, a_1, x_0, \sigma, m) = a_0 + \frac{a_1}{\sigma\sqrt{2\pi}}\left(\exp(-\frac{(x-x_0)^2}{2\sigma^2}) + m\exp(-\frac{x^2}{2\sigma^2})\right) \tag{3.5}$$

$$f_L(x, a_0, a_1, x_0, \sigma, e) = a_0 + \frac{a_1}{2^{1+\frac{1}{e}}(\sigma^2)^{-\frac{1}{e}}\Gamma(1+\frac{1}{e})}\exp\left(-\frac{|x-x_0|^e}{2\sigma^2}\right) \tag{3.6}$$

where a_0 is the constant background, a_1 is the area of the peak, x_0 corresponds to the position of the peak and σ is the width of the peak.

For scans along the (10 K 6) direction, this corresponds to a standard Gaussian distribution (see Eq. 3.5). A second Gaussian distribution is added at **Q** = (10 0 6) taking into account the additional contribution that we can see in the background. The intensity of the second magnetic peak is assumed to follow the same temperature evolution than the (10 -1 6) one, so that only a proportionality coefficient, m, is refined for the intensity of the second peak. This parameter has been fitted at 22.5 K to the value $m = 1.1$ and was then fixed for all the other temperatures as it is assumed to be constant.

For the (10 -1 L) direction, a modified Gaussian distribution has been used with an additional parameter, e, allowing to account for the sharp steepness of the peak. Similarly to the proportionality constant m, this parameter has also been fitted for the scan performed at 22.5 K and then fixed to the value $e = 2.62$ for data at other temperatures.

Fits of the experimental data in the (10 K 6) and (10 -1 L) directions between 6 and 150 K can be found in Appendix C.

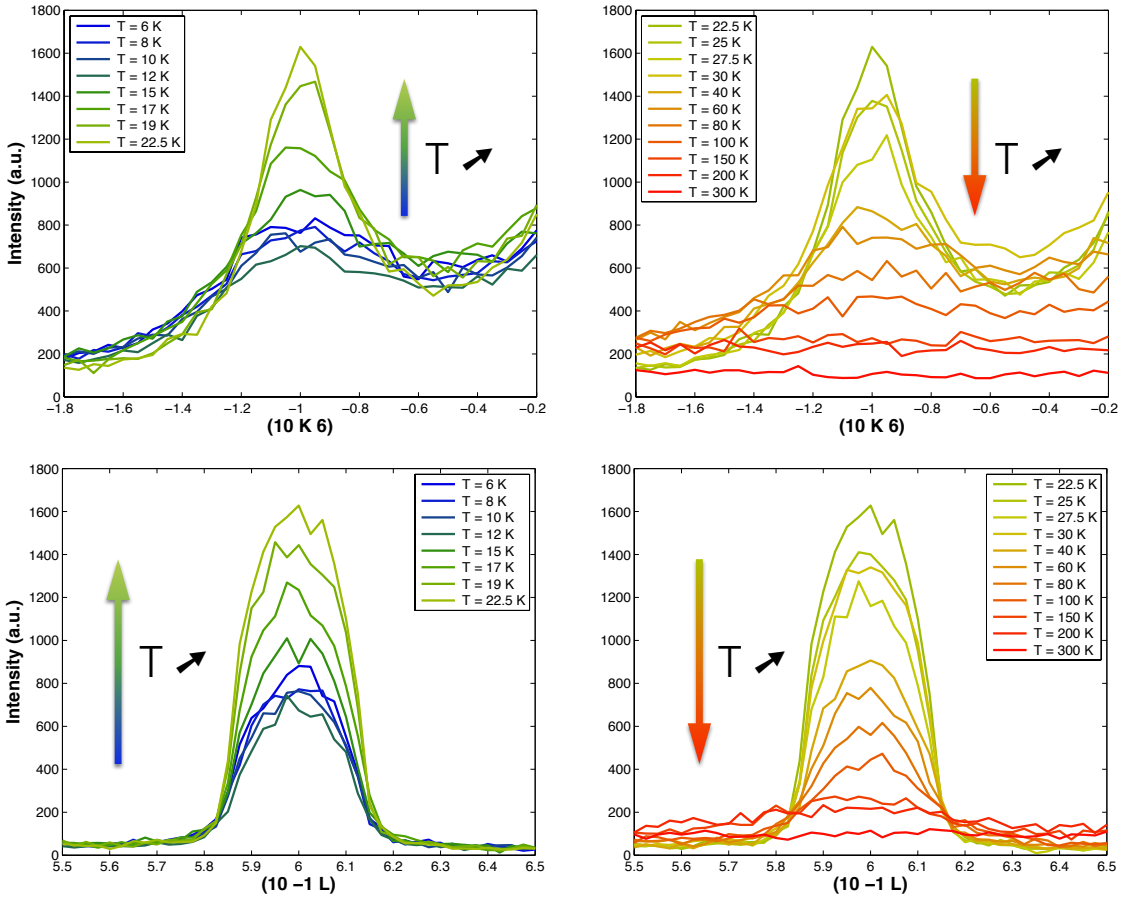

Figure 3.26 – *Scans of the (10 -1 6) magnetic Bragg peak along the (10 K 6) (top) and the (10 -1 L) (bottom) directions for temperature from 6* K *to 22.5* K *(left) and from 22.5* K *to 300* K *(right).*

The peak area can be calculated using a trapezoidal numerical integration of the data after removing the fitted background. Its temperature dependence is similar in the two directions (see Fig. 3.27). It reaches a maximum around 22.5 K followed by a quite abrupt drop as the temperature decreases. This is connected to the ZFC-FC separation which is observed around 17 K in the temperature dependence of the magnetic susceptibility (see Section 3.3.1.1) where a maximum of the magnetic susceptibility is observed before a sudden drop as the temperature is lowered. Below 12 K, the RIXS intensity slowly starts to increase again.

Another drop in the intensity is also observed around 27 K although there is no other evidences of a magnetic transition at this temperature. It could thus not be related to the physics of the system.

Figure 3.28 shows the temperature evolution of the peak position extracted from the fits. The experimental resolution of ID20 in **Q** space being quite low, $\Delta \approx \pm 0.28$ Å^{-1}, it does not really provide quantitative information. We can still note that there seems to be no change in the position of the Bragg peaks as the sample is cooled down from the high temperature through the second magnetic transition observed at 17 K. This is thus consistent with the REXS experiment.

The temperature dependence of the peak width, shown Fig. 3.29, gives useful information as it is inversely proportional to the magnetic correlation lengths.

The first thing to be noted is that the peak is much narrower in the (10 -1 L) direction than in

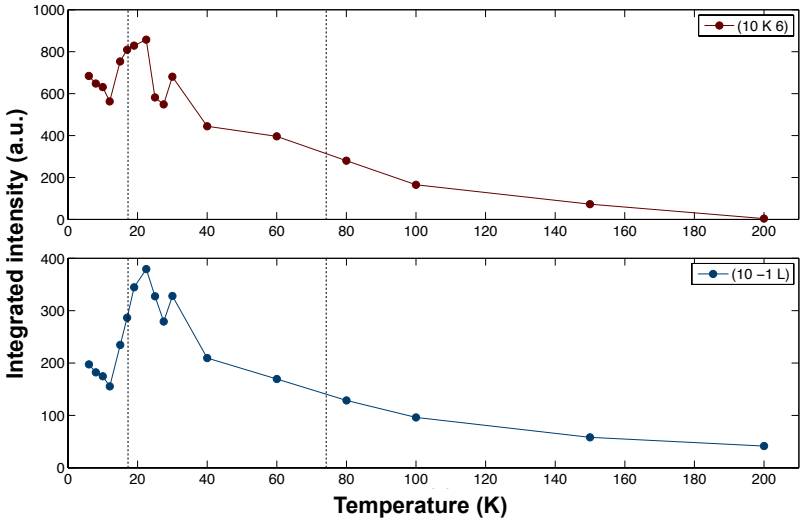

Figure 3.27 – *Evolution of the integrated intensity of the peak along the (10 K 6) (top) and (10 -1 L) (bottom) directions. The dotted lines indicate the two transition temperatures determined from magnetization measurements.*

the (10 K 6) one. At T_2 = 17 K the correlations in the L and K directions are respectively ξ_L = 120 Å and ξ_K = 33 Å. This means that the correlations are much stronger along the chains than between the chains, suggesting a low dimensional behavior. Then, looking at the evolution in both directions, the peak width along the (10 -1 L) direction remains constant below 60 K meaning that, below this temperature, there is no evolution in the length of the magnetic correlations along the chain directions. However looking at the other direction, we can clearly observe a minimum of the peak width at 22.5 K, temperature at which the intensity of the magnetic peak is maximum. At this temperature the interchain correlations are thus strongest and then start to weaken as the temperature is lowered. This behavior is quite peculiar as the peak width in a standard ordered phase would rather be expected to lower and remain constant as the temperature is lowered.

The RIXS measurements performed using elastic condition allowed us to follow the evolution of the magnetic signal on a broad temperature range. The analysis of the temperature dependence of the magnetic Bragg peaks is consistent with the results obtained by REXS. The magnetic signal reaches a maximum in intensity around the lower transition temperature T_2 = 17 K. At this point, the in-plane magnetic correlations are also reaching a maximum value. Below this temperature, the magnetic intensity drops and the in-plane correlations decrease. We do not have yet a clear understanding in order to explain this peculiar behavior. One possibility is the presence of a competing magnetic phase below T_2 although we do not have any evidence of such phase so far.

Nevertheless, these measurements allowed us to get additional information on the nature of the two ordered phases by studying the commensurability of the magnetic propagation vector. Thus Sr_3NiIrO_6 orders below $T_1 \approx 75$ K with a commensurate magnetic propagation vector $\mathbf{k}$ = (0, 0, 1) which remains unaltered down to 2 K. A possible scenario is that from T_1 to T_2 = 17 K, the system orders in a partially disordered antiferromagnetic configuration. Then at T_2, a change of the global phase corresponds to a modification of the structure to an amplitude modulated antiferromagnetic configuration compatible with the presence of a ferromagnetic component along the chain axis.

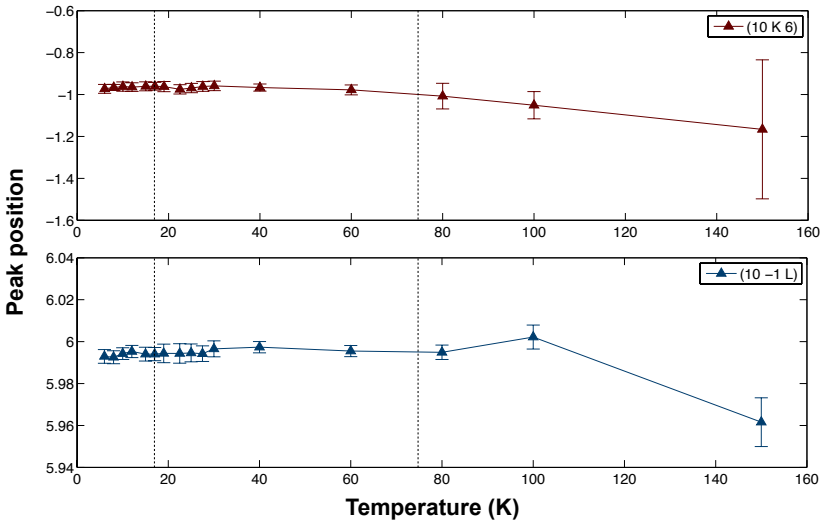

Figure 3.28 – *Evolution of the position of the peak maximum along the (10 K 6) (top) and (10 -1 L) (bottom) directions. The dotted lines indicate the two transition temperatures determined from magnetization measurements.*

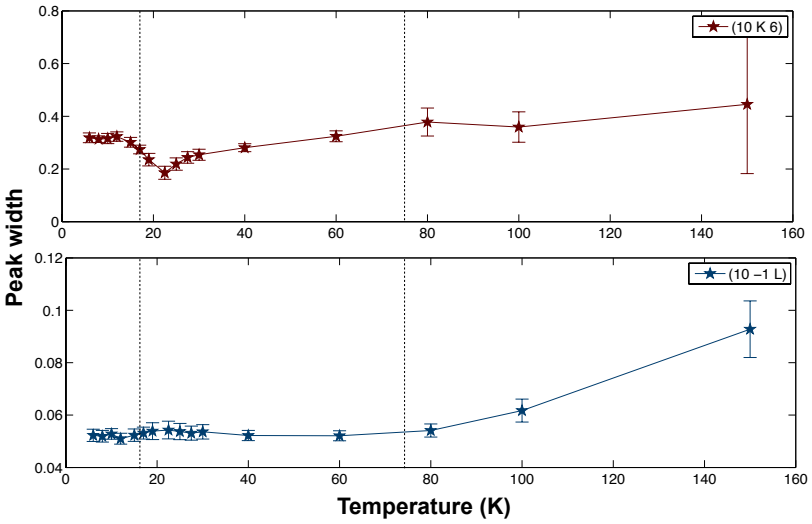

Figure 3.29 – *Evolution of the width of the peak along the (10 K 6) (top) and (10 -1 L) (bottom) directions. The dotted lines indicate the two transition temperatures determined from magnetization measurements.*

3.3.3 Measurements of the inelastic response

We then studied the inelastic spectra of the Ir 5*d* electrons using RIXS experiments. This technique allows to probe simultaneously the electronic and magnetic excitations of Sr_3NiIrO_6. The RIXS measurements were performed at the ID20 beam line of the European Synchrotron Radiation Facility (ESRF) with M. Moretti. The measurements were performed between 10 and 300 K and at different **Q** points of the reciprocal space on a single crystal of Sr_3NiIrO_6.

3.3.3.1 Room temperature measurements

Fig. 3.30 shows a RIXS map obtained from inelastic scans at different incident photon energies. Two features are observed besides the elastic line. The resonance of the t_{2g} Ir^{4+} electronic levels is measured at 11.214 keV, whereas that of the e_g levels is at 11.218 keV. As we are more interested in probing the excitations whithin the t_{2g} manifold, the incident photon energy was then fixed at 11.214 keV in order to enhance the intensity of these excitations.

The intensity of the gap induced by the local octahedral environment, standardly denoted $10Dq$, can also be deduced from the map shown Fig. 3.30. This energy corresponds to the difference between the resonance energy of the e_g states and the one of the t_{2g} states. We obtain a value of $10Dq \approx 4$ eV.

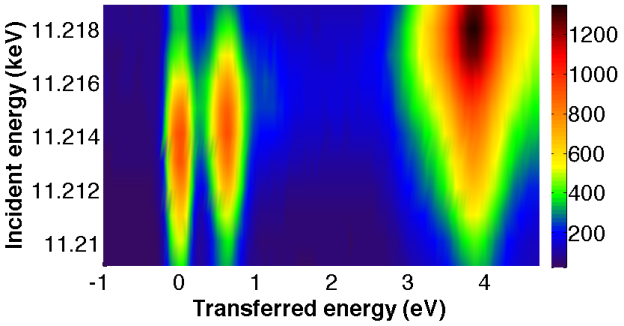

Figure 3.30 – *Incident energy dependence of the Sr_3NiIrO_6 RIXS spectra at the L_3 Ir edge measured at 300* K*, showing the resonance of the t_{2g} and e_g levels at 11.214 and 11.218* keV *respectively.*

In Sr_3NiIrO_6, the IrO_6 octahedra are slightly elongated along the **c** axis (corresponding to the trigonal axis). The Ir-O distances are all equal but there are two different angles: $\alpha = 84.31°$ and $\beta = 95.69°$ (see Fig. 3.31).

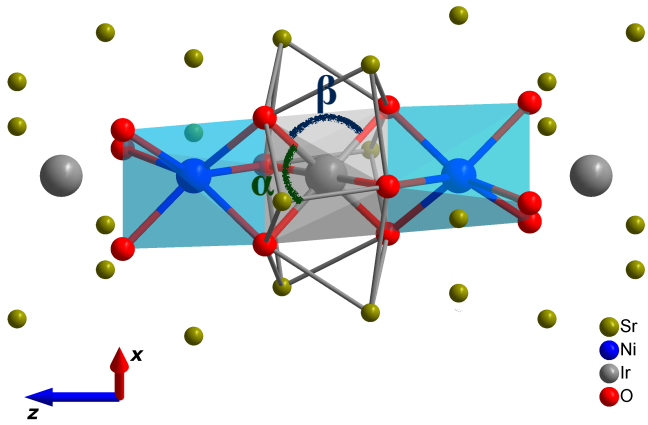

Figure 3.31 – *Detail of the Sr_3NiIrO_6 structure: the central distorted IrO_6 octahedron, its neighboring trigonal prismatic NiO_6 along the chain axis, and the adjacent Sr atoms.*

This trigonal distortion induces a splitting of the t_{2g} levels in addition to the splitting induced by the SOC. Thus taking into account both the trigonal splitting and the SOC, three non degenerated doublets are obtained corresponding to an admixture of the initial t_{2g} states. This admixture differs from what would be obtained in the case of a pure octahedral environment with SOC, which would be a degenerated quadruplet characterized by a $j_{\text{eff}} = \frac{3}{2}$ and a doublet with $j_{\text{eff}} = \frac{1}{2}$ (see scheme Fig. 3.32).

As a result of this trigonal distortion and SOC, we expect to observe two excitations within the t_{2g}

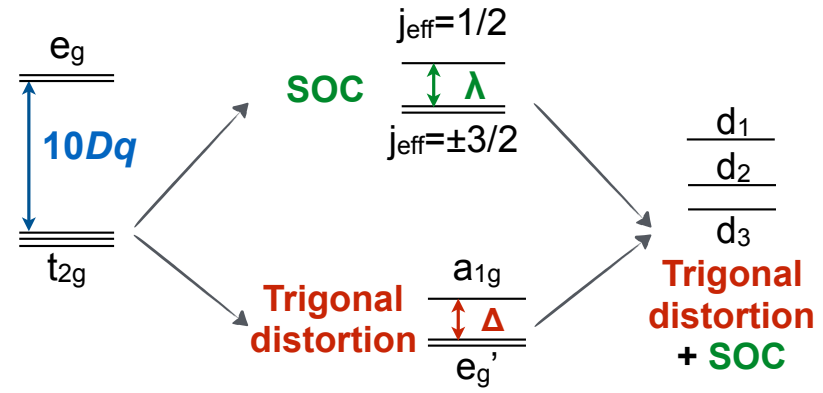

Figure 3.32 – *Splitting of the 5d levels due to the octahedral environment (10Dq), to its trigonal distortion (Δ) and to SOC.*

manifold corresponding to the transition of a hole from the d_1 level to either the d_2 or the d_3 levels. This is indeed confirmed by the RIXS measurements at room temperature (see Fig. 3.33).

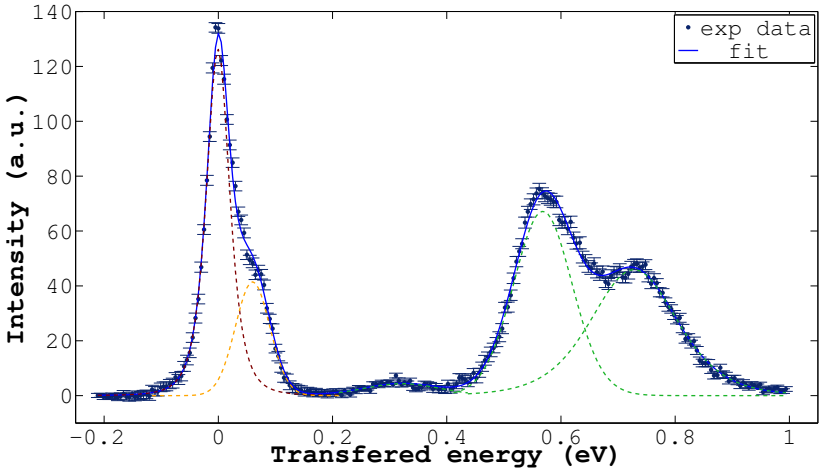

Figure 3.33 – *RIXS spectra of Sr_3NiIrO_6 at reciprocal space position $\mathbf{Q}$ = (10 -1 7) at 300* K. *The dashed curves correspond to the least-square refinements of the different excitations using Pearson-VII functions.*

Four features can be observed, beside the elastic peak, at energies of 50(5), 322(20), 568(2) and 728(5) meV. None of them shows any detectable dispersion (see Fig. 3.34). The most intense at 568(2) and 728(5) meV are interpreted as *d-d* excitations within the t_{2g} levels. The existence of two peaks can be only explained by a sizable contribution from a trigonal crystal field (Δ) in addition to the SOC. This effect can be quantified by considering a local atomic model for the single hole occupying the t_{2g} states with the following Hamiltonian:

$$\mathcal{H} = \Delta\left(\frac{2}{3}|a_{1g}\rangle\langle a_{1g}| - \frac{1}{3}|e_g'^{\pm}\rangle\langle e_g'^{\pm}|\right) + \lambda \mathbf{L}\cdot\mathbf{S} \tag{3.7}$$

where Δ describes the splitting of the t_{2g} orbitals due to the trigonal distortion of the IrO_6 octahedron (Δ >0 for an axial elongation) and λ is the SOC parameter.

The symmetry-adapted $|a_{1g}\rangle$ and $|e_g'^{\pm}\rangle$ wavefunctions for trigonal symmetry are defined below:

$$\begin{cases} |a_{1g}\rangle &= (z^2) \\ |e_g'^{+}\rangle &= \sqrt{\frac{2}{3}}(x^2-y^2) - \sqrt{\frac{1}{3}}(zx) \\ |e_g'^{-}\rangle &= \sqrt{\frac{2}{3}}(xy) + \sqrt{\frac{1}{3}}(yz) \\ |e_g^{+}\rangle &= \sqrt{\frac{1}{3}}(x^2-y^2) + \sqrt{\frac{2}{3}}(zx) \\ |e_g^{-}\rangle &= \sqrt{\frac{1}{3}}(xy) - \sqrt{\frac{2}{3}}(yz) \end{cases} \tag{3.8}$$

with

$$\begin{cases} (xy) &= -\frac{\imath}{\sqrt{2}}(|2,2\rangle - |2,-2\rangle) \\ (yz) &= \frac{\imath}{\sqrt{2}}(|2,1\rangle + |2,-1\rangle) \\ (zx) &= -\frac{1}{\sqrt{2}}(|2,1\rangle - |2,-1\rangle) \\ (x^2-y^2) &= \frac{1}{\sqrt{2}}(|2,2\rangle + |2,-2\rangle) \\ (z^2) &= |2,0\rangle \end{cases} \tag{3.9}$$

Within this model, excitations can be seen as transitions of the hole from the ground state to the lower lying electronic states. We will note that, in contrast to the case of tetragonal distortion, the admixture of the t_{2g} with e_g levels is authorized by symmetry in the case of trigonal distortion of interest here. However the $10Dq$ splitting between t_{2g} and e_g levels being of the order of 4 eV, i.e. much larger than λ and Δ, it means that the e_g levels can be ignored in first approximation.

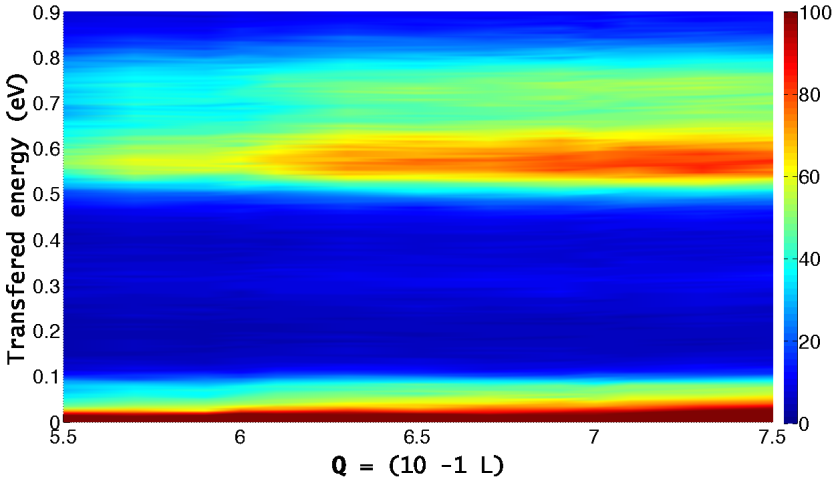

Figure 3.34 – *Out of plane wavevector dependence of the RIXS response of Sr_3NiIrO_6 in the* 0 − 900 meV *range in the high-symmetry direction* $\mathbf{Q}$ *= (10, -1, L) at 300* K.

The values of λ and Δ can be obtained by constraining the eigenvalues of $\mathcal{H}$ to the energies of the excitations within the t_{2g} manifold determined from the experiment. Two solutions exist, depending on the sign of Δ: λ=396(1) meV and Δ=294(7) meV for the first one (trigonal elongation of the octahedron) and λ=417(4) meV and Δ=-218(8) meV for the second one (trigonal compression of the octahedron). Wave-functions (shown in Fig. 3.35) for the highest doublet in the t_{2g} subspace (occupied by the hole) can be written as:

$$\begin{cases} |0,\uparrow\rangle = \frac{ip|a_{1g},\uparrow\rangle + i|e_g'^{+},\downarrow\rangle + |e_g'^{-},\downarrow\rangle}{\sqrt{p^2+2}} \\ |0,\downarrow\rangle = \frac{p|a_{1g},\downarrow\rangle - |e_g'^{+},\uparrow\rangle - i|e_g'^{-},\uparrow\rangle}{\sqrt{p^2+2}} \end{cases} \tag{3.10}$$

where the parameter p depends on the ratio λ/Δ as shown Fig. 3.35.

RIXS analysis alone does not allow determining the sign of Δ. However additional arguments can be used to conclude on that matter. First ab-initio quantum chemistry calculations performed by A.-M. Pradipto and S. Picozzi [LPMS+16] showed that the a_{1g} singlet lies higher in energy than the e'_g doublet in the absence of SOC. This corresponds to a positive value of Δ. Second, for a positive Δ, the calculated value of the z component of the total magnetic moment $\langle L_z + 2S_z \rangle$ is reduced compared to the value of 1 μ_B expected for a perfect octahedron (see Fig. 3.35). This is in better agreement with the value refined from neutron diffraction experiment which is equal to 0.5 μ_B.

Note that the excitation at 50(5) meV is not accounted for by the electronic level scheme derived previously and we will discuss its origin hereafter. The origin of the weak signal observed around 322 meV is unclear, but very similar (energy and spectral weight) to that observed in almost all iridate compounds [LKH+12, HGC+14, CGL+15], which suggests that it might be an intrinsic characteristic of this class of materials.

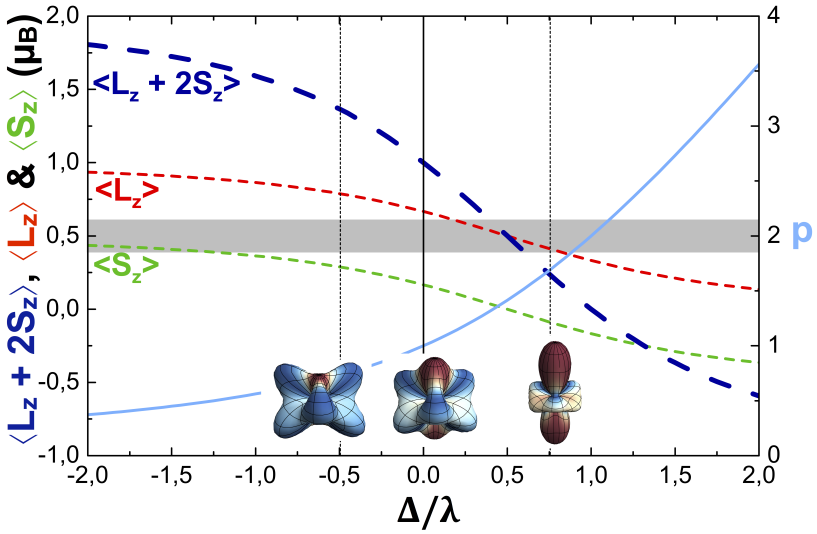

Figure 3.35 – *Evolution of the z components of the orbital <L_z>, spin <S_z>, total magnetic moment $< L_z + 2S_z >$ and of p as a function of $\frac{\Delta}{\lambda}$. The grey stripe shows the Ir magnetic moment refined from neutron diffraction. The amplitudes of the probability of presence of the t_{2g} hole are shown at the bottom: for a perfect octahedral environment ($\frac{\Delta}{\lambda} = 0$), for a trigonal compression ($\frac{\Delta}{\lambda} = -0.52$) and for a trigonal elongation ($\frac{\Delta}{\lambda} = 0.73$) of the octahedron. The latter two are in agreement with the RIXS results but only the positive $\frac{\Delta}{\lambda}$ is compatible with quantum chemistry calculations. The surfaces of constant amplitude of probability are colored from red for pure $|a_{1g}, \uparrow\rangle$ state, to blue for pure $(i|e'^{+}_g, \downarrow\rangle + |e'^{-}_g, \downarrow\rangle)$ state, through white for an equal mix of these states.*

3.3.3.2 Temperature dependence of the RIXS measurements

Fig. 3.36 shows the RIXS spectra of Sr_3NiIrO_6 between 10 and 300 K, at the same momentum transfer **Q** = (10 -1 7). As the temperature decreases, a more complex structure with additional features of the electronic excited states associated to the intra t_{2g} transitions is observed (see Fig. 3.36). This change of shape is attributed to the influence of the Ni-Ir nearest neighbor magnetic exchange interactions, which become relevant in the magnetically ordered phase.

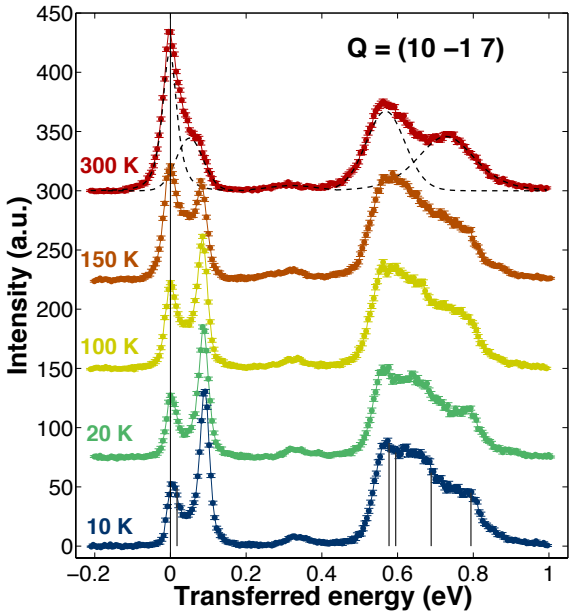

Figure 3.36 – *RIXS spectra of Sr_3NiIrO_6 at the reciprocal space position **Q** = (10 -1 7) between 10 and 300 K. The dashed curves for the 300 K scan correspond to the least-square refinements of the different excitations using a Pearson-VII function. The vertical lines on the 10 K curve correspond to the eigenvalues of $\mathcal{H}$ calculated for $\lambda = 396$ meV $\Delta = 294$ meV, $\alpha_{x,y} = 0$ and $\alpha_z = 0.1$ eV.*

Indeed, the local Hamiltonian can be completed in order to take into account this additional perturbation on the Ir electronic states and rewrites:

$$\mathcal{H} = \Delta\left(\frac{2}{3}|a_{1g}\rangle\langle a_{1g}| - \frac{1}{3}|e_g'^{\pm}\rangle\langle e_g'^{\pm}|\right) + \lambda \mathbf{L}\cdot\mathbf{S} - \alpha_{xy}(S_x + S_y) - \alpha_z S_z \tag{3.11}$$

The last terms $\alpha_i S_i = -2J_{ii}\langle S_i^{Ni}\rangle S_i$, $(i = x, y, z)$ represents the molecular field components produced on the Ir spin by its two Ni^{2+} nearest neighbors.

Although the complex features observed above 500 meV do not allow to unequivocally determine the values of $\alpha_{x,y,z}$, a solution is shown in Fig. 3.36 on the 10 K curve. The energies of the split peaks were obtained using $\alpha_{x,y} = 0$ and $\alpha_z = 0.1$ eV and are in agreement with the experimental data. Moreover the values of $\alpha_{x,y,z}$ are compatible with the strong uniaxial character of the magnetic structure and with the values of the anisotropic exchange interactions deduced from the spin wave calculations (see section 3.3.4.1) .

Inspecting the temperature evolution of the lowest energy excitation, we observed a change in the shape (peak width and intensity) as well as in its position. At 300 K, the position of the maximum is around 50 meV and the peak is quite broad. Its intensity increases as the temperature is lowered and its position in energy shifts to 90 meV from 300 K to $\approx$ 100 K where it remains constant for lower temperatures. This excitation cannot be accounted for by the electronic level scheme. Its temperature dependence is compatible with a magnetic excitation, whose observation by RIXS is allowed (see Appendix D).

This magnetic excitation does not show any detectable dispersion along the (10 -1 L) direction within the instrumental resolution of 25 meV(see Fig. 3.37). Besides the persistence of the magnetic excitation far above the ordering temperature is consistent with another magnetic excitation observed

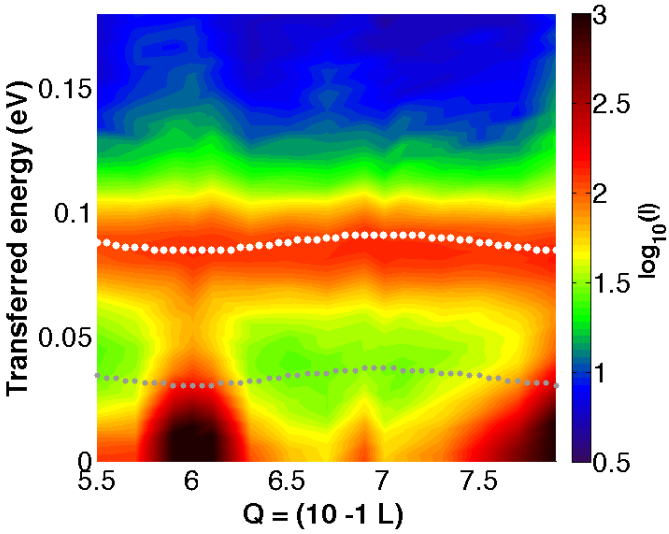

Figure 3.37 – *RIXS map measured at 10 K along the (10 -1 L) direction. The dotted lines show the spin-wave excitations calculated with $J_{xx} = J_{yy} = 20$ meV, $J_{zz} = 46$ meV and $D = 9$ meV. The Ir and Ni main contributions are in white and gray respectively.*

at 35 meV using Inelastic Neutron Scattering on a polycrystalline sample of Sr_3NiIrO_6 (see Fig. 3.38) [WAT+15, TWA+16]. This behavior can be attributed to the presence of strong spin correlations associated with the low dimensionality of the magnetic structure.

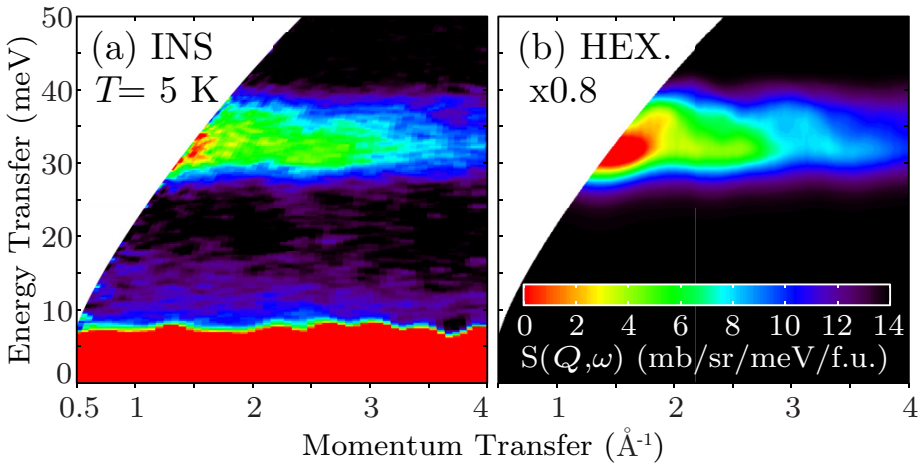

Figure 3.38 – *(a) The magnetic scattering at 5 K obtained from powder neutron diffraction after subtracting the phonon contribution using the 300 K data. The strong scattering below 10 meV is due to the incoherent background. (b) The simulated spin wave scattering at 5* K. *From [TWA+16]*

3.3.4 A model describing the magnetic properties of Sr_3NiIrO_6

3.3.4.1 Spin wave calculations

To understand the two excitations reported in Sr_3NiIrO_6 using RIXS and INS, we performed spin wave calculations using the Holstein-Primakov formalism within the linear approximation with the *Spinwave* software developed by S. Petit (LLB-CEA Saclay) for INS experiments.

The initial spin configuration is obtained from the mean field solution of the following Hamiltonian:

$$\mathcal{H} = \sum_i J_{xx}(S_i^x S_{i+1}^x + S_i^y S_{i+1}^y) + J_{zz} S_i^z S_{i+1}^z + \sum_{i \epsilon Ni} D(S_i^z)^2 \tag{3.12}$$

It consists in starting from a random configuration for the spin observables $\langle \vec{S}_i \rangle$. The mean-field contribution to the Hamiltonian at site i is then calculated. This yields the energies $E_{i,n}$ and the wave functions $|\phi_{i,n}\rangle$. The updated expectation values, $\langle \vec{S}_i \rangle'$, at each step of the iteration procedure, are given by:

$$\langle \vec{S}_i \rangle' = \sum_n \frac{e^{-E_{i,n}/k_B T}}{Z} \langle \phi_{i,n} | \vec{S}_i | \phi_{i,n} \rangle$$

with

$$Z = \sum_n \exp\left(-E_{i,n}/k_B T\right).$$

These are finally used to proceed to site j, and this is repeated until convergence.

The model given by equation 3.12 describes isolated chains with alternating spin 1 (Ni) and pseudo-spin $\frac{1}{2}$ (Ir) antiferromagnetically coupled along the chains. We treat here the ideal $j_{\text{eff}} = \frac{1}{2}$ state as isospin operators. The Hamiltonian also includes the magnetocrystalline anisotropy of the Ni ions modeled by $D(S_i^z)^2$. It corresponds to an easy plane anisotropy perpendicular to the z-axis for positive D values. The symmetric exchange tensor J is constrained by the symmetry of the Ni-Ir bond, allowing only the diagonal term with $J_{xx} = J_{yy}$ and J_{zz} (see Appendix E). Dzyaloshinskii-Moriya (DM) interaction is not taken into account here. It will be shown latter that including this effect does not influence significantly the results.

We were able to reproduce the two magnetic excitations observed by INS and RIXS with the following set of parameters: $J_{xx} = 20(2)$ meV, $J_{zz} = 46(2)$ meV and $D = 9$ meV (see Fig. 3.37). The calculations were performed considering the dispersion spectrum of a single crystal along the $(10\ -1\ L)$ reciprocal space direction and the excitations as function of $|Q|$ for a powder in order to compare them with the RIXS and neutron experiment (see Fig. 3.39) respectively. The parameters of the model are quite constrained by experimental evidences. Indeed the position of the maxima of the two modes are equal to $J_{zz} - D$ and to $2J_{zz}$ whereas the dispersion is related to J_{xx}/J_{zz}. Besides, the value obtained for the single ion magnetocrystalline anisotropy is in very good agreement with the value of 7.8 meV found in the iso-structural compound Sr_3NiPtO_6.

Moreover, the contributions from the different magnetic species can be extracted from the calculations (see Fig. 3.40). The 90 meV excitation is essentially due to the Ir contribution, while the lower one arises mainly from the Ni. This explains why we were unable to observe the low-energy excitation in the RIXS experiment, the energy being fixed to the Ir L_3 resonance edge.

One main result is that the spin wave simulations show that the nearest neighbor interactions are highly anisotropic. This is at the origin of the magnetic quasi-Ising behavior of the Ni and Ir along the z-axis. This occurs despite the strong single ion magnetocrystalline easy-plane anisotropy of the Ni^{2+}

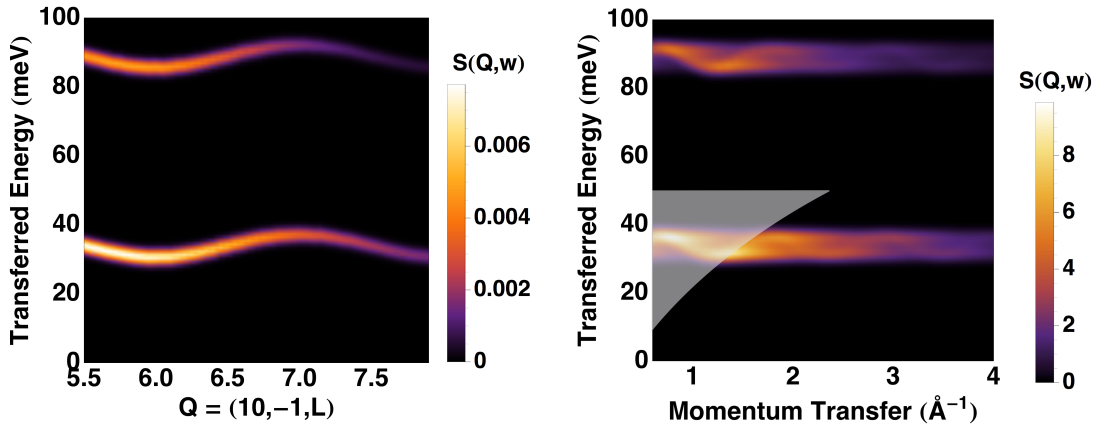

Figure 3.39 – *Calculated spin waves with exchange interactions* $J_{xx} = J_{yy} = 20$ meV, $J_{zz} = 46$ *meV and single ion magnetocrystalline anisotropy* $D = 9$ *meV for a single crystal (left) and for a polycrystalline sample (right). The white zone represents the region which was not accessible in the INS experiment from Fig. 3.38 up to 50* meV.

ion perpendicular to this direction.

Using the same spin wave software, we also examined the influence of the interchain interactions on the spin wave spectrum by calculating the response of three chains on a triangular lattice: two of them are antiferromagnetically coupled by a mean interchain interaction, $J_\perp$, while the third one is allowed to fluctuate. This spin configuration is one of the two that are compatible with the neutron diffraction experiment. The other one, involving a modulation of the amplitude of the magnetic moments, cannot be implemented in the *Spinwave* software. Note that these two magnetic structures are equivalent up to a global phase. The inclusion of the interchain interactions modifies slightly the energy of the two branches (see Fig. 3.41) by increasing (decreasing) their energy for ferromagnetic (antiferromagnetic) interchain coupling without affecting the amplitude of the dispersion.

The interchain exchange interaction might be estimated from the ordering temperature, but this is not straightforward for mixed-spin quantum chains where the intrachain exchange anisotropy competes with single-ion anisotropy so that the spin dimensionality evolves from almost XY to almost Ising by decreasing the temperature. An upper bound can nevertheless be derived through analytical and numerical estimates from different models [Ogu64, SIP75, VL77, BdJK81, YTH+05]. In the case of classical spin-S chains without anisotropy, by treating exactly the effects of the intrachain exchange $J_\parallel$ and in mean field those of the interchain exchange $J_\perp$, the ordering temperature is analytically computed in the form:

$$T_N \approx J_\parallel S(S+1)\left((8/3)z_\perp \frac{J_\perp}{J_\parallel}\right)^{1/2}$$

where $z_\perp$ is the number of chains with which each chain interacts. With $S = 1/2$, $J_\parallel = J_{xx} = J_{yy} = 20$ meV and $T_N \approx 80$ K ≈ 6.9 meV, this leads to the exchange ratio $\eta = J_\perp/J_\parallel \approx 0.02$ and an interchain exchange $J_\perp \approx 0.4$ meV. With the larger exchange, $J_\parallel = J_{zz} = 46$ meV, a smaller exchange ratio η is obtained hence a smaller $J_\perp$. Néel ordering is inhibited by interchain correlations and quantum fluctuations, which would suggest that $J_\perp$ is larger. A numerical approximation of these effects in the case of the extreme limit of S=1/2 quantum spins shows that they lead indeed to an increase of the exchange ratio up to $\eta \approx 0.1$ and therefore of interchain exchange up to $J_\perp \approx 2$ meV. These values decrease to $\eta \approx 0.075$ and $J_\perp \approx 1.5$ meV for larger quantum spins S=3/2. Néel ordering on the other hand should

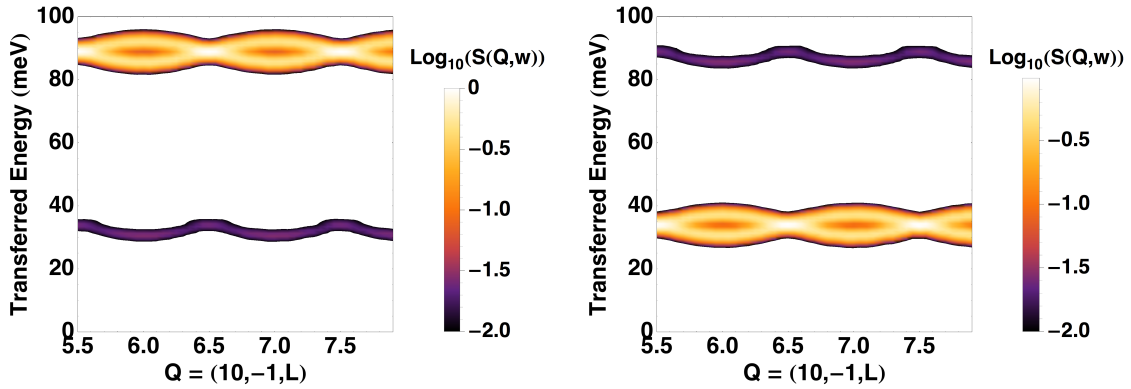

Figure 3.40 – *Individual contributions from the different magnetic species to the simulated spin wave scattering. The calculations were performed for a single crystal along the (10,-1,L) direction using the program developed by S. Petit. The exchange parameters were fixed to* $J_{zz} = 46$ *meV and* $J_{xx} = 20$ *meV and the single ion anisotropy to* $D = 9$ *meV. Note that the figure shows two interlaced branches around 25 and 90 meV. This is due to the fact that the unit cell contains two Ir and two Ni atoms. Only one branch actually carries significant physical intensity as shown in Fig. 3.39.*

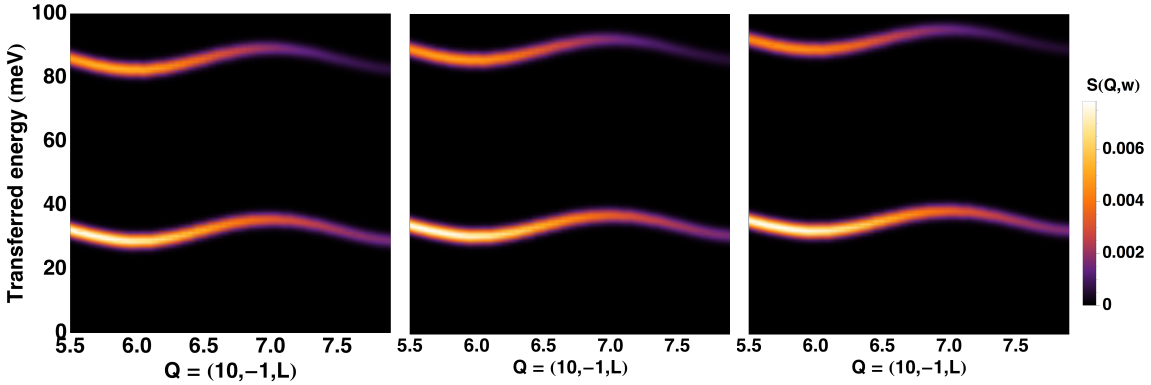

Figure 3.41 – *Calculated spin waves with intrachain interactions* $J_{xx} = 20$ meV, $J_{zz} = 46$ meV, *magnetocrystalline anisotropy* $D = 9$ meV, *and interchain interaction* $J_\perp$ = *-1* meV *(left), 0* meV *(middle) and +1* meV *(right).*

be favored by the reduction of the spin dimensionality caused by the single ion and intrachain exchange anisotropies that should lead to much lower values of the interchain exchange $J_\perp$, as suggested by the exchange ratio $\eta \approx 0.009$ obtained in the Ising limit. It follows that the $J_\perp \approx 0.4$ meV estimated from the classical spin-S chains without anisotropy can be considered safely as an upper bound.

As a matter of fact, another independent estimate of $J_\perp$ can be obtained from the coercive field H_c. We assume that this coercive field corresponds to the minimum field of coherent reversal of spin chains. In case of the frustrated magnetic structure with two out of three chains frozen with antiparallel moments and the third chain being paramagnetic, there is a degeneracy of the possible configurations. Each frozen chain can be surrounded by (3 + n) chains of opposite moment orientation and 6-(3+n) chains of same moment orientation, with n = 0, 1, 2, 3. On the other hand, each unfrozen chain is always surrounded by 3 chains of opposite moment orientation and 3 chains of same moment orientation (see Fig. 3.42).

We can write $(3 + \langle n \rangle /3) J_\perp \approx C\ H_c$ with $C \approx 0.058$ for H_c given in Tesla and $J_\perp$ in meV, which leads to values of $J_\perp$ (≈ 1.06 meV for $\langle n \rangle = 0$, ≈ 0.80 meV for $\langle n \rangle = 1$, ≈ 0.64 meV for $\langle n \rangle = 2$

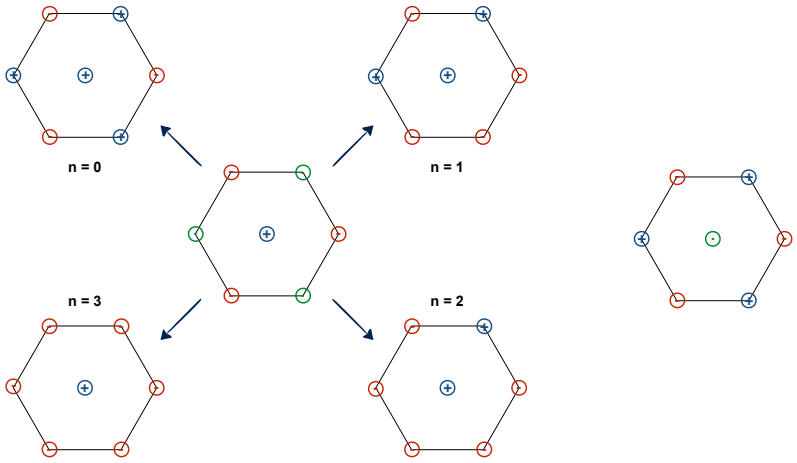

Figure 3.42 – *Sketch of the partially disordered antiferromagnetic state projected on the (**ab**) plane. (left) A frozen chain surrounded by (3 + n) chains of opposite moment orientation and 6-(3+n) chains of same moment orientation, with n = 0, 1, 2, 3. (right) An unfrozen chain surrounded by 3 chains of opposite moment orientation and 3 chains of same moment orientation. The red and blue colors correspond respectively to magnetic moments frozen in one direction and its opposite. The green color corresponds to the unfrozen magnetic moment.*

and ≈ 0.53 meV for $\langle n \rangle = 3$) of the order of the upper bound extracted from the Néel temperature. Accordingly, the interchain exchange is expected to have a minor effect on the spin wave spectrum and confirms the quasi-one dimensional character of Sr_3NiIrO_6.

The point symmetry between Ni and Ir site is 3 (3-fold axis), thus allowing for antisymmetric exchange interactions with a Dzyaloshinskii-Moriya $\vec{D}$ vector pointing along the **c** axis (see Appendix E for details), the Dzyaloshinskii-Moriya interaction being expressed by:

$$\mathcal{H}_{\text{DMI}} = \vec{D} \cdot (\vec{S}_i \times \vec{S}_j).$$

We found that the small changes produced by this term in the energy position and the dispersion of the spin waves cannot be seen in the RIXS and INS experiments, up to values of 5 meV. It has also no effect on the magnetic configuration.

Using spin wave calculations, we are now able to reproduce the two magnetic excitations observed at 90 meV in RIXS and at 37 meV with INS. These two excitations show similar behavior as they exhibit little dispersion in the reciprocal space and persist well above the ordering temperature of 75 K. The small dispersion is found to come from the highly anisotropic Ni-Ir nearest neighbor magnetic interaction: J_{xx} = 20 meV and J_{zz} = 46 meV. The fact that these excitations remain until quite high temperature is related to the low dimensionality of the system. Indeed the mean interchain interaction is estimated to be approximately ten times smaller than the intrachain ones. The calculations also allowed determining the Ni^{2+} ions magnetocrystalline anisotropy, D = 9 meV. This corresponds to an easy plane anisotropy and its value is consistent with the one reported in the isostructural compound Sr_3NiPtO_6.

Having determined the magnetic exchange interactions for Sr_3NiIrO_6, we then performed Monte Carlo calculations with these parameters in order to see if we could reproduce the experimental ob-

servation, in particular the change of magnetic anisotropy observed around 200 K in the magnetic susceptibility measurements.

3.3.4.2 Monte Carlo simulations

Monte-Carlo simulations have been performed by considering a system of chains of antiferromagnetically coupled alternating classical spin 1/2 and spin 1, the interchain interactions being neglected for simplicity. The intrachain anisotropic exchange interactions and the single ion anisotropy have been fixed to the values provided by the spin-waves analysis. The simulations have been performed using a conventional Metropolis algorithm, cooling the system from 2000 K down to 1 K. The temperature was decreased exponentially (0.95 times the previous temperature). At each step in temperature, 10^4 spin flips per spin were conducted for equilibration and a further 10^4 steps for data taking. The magnetic susceptibility was calculated using the fluctuation-dissipation theorem:

$$\chi_\alpha = \frac{\langle m_\alpha^2 \rangle - \langle m_\alpha \rangle^2}{NT} \tag{3.13}$$

where N is the number of spins in the simulations and α=x,y,z is the direction. Simulations using supercells of 3x3x200 up to 3x3x800 have been used. The results presented correspond to the largest supercell with 20000 spins. The extracted magnetic susceptibility in the direction along and perpendicular to the **c** axis (see Fig. 3.43) is in very good agreement with the measured magnetic susceptibility shown in Fig. 3.11.

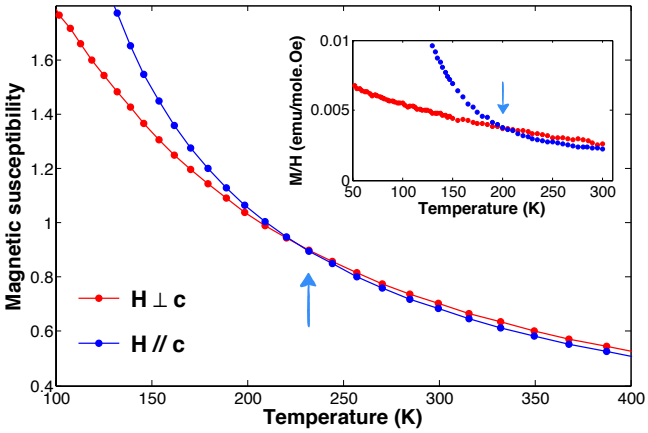

Figure 3.43 – *Magnetic susceptibility for a magnetic field applied along the* **c** *axis (in blue) and perpendicular to the* **c** *axis (in red) extracted from Monte Carlo simulations performed with exchange parameters* $J_{zz} = 46$ meV *and* $J_{xx} = 20$ meV *and with a single ion anisotropy* $D = 9$ *meV. The arrows indicate the crossing of the curves.*

From the determined magnetic exchange interactions, we can nicely reproduce the observed magnetic behavior of Sr_3NiIrO_6. The change of anisotropy can be explained by the presence of both an Ni^{2+} easy plane anisotropy and strong anisotropic intrachain Ni-Ir magnetic exchange interactions due to the Ir^{4+} SOC. At low temperature, the system is governed by the magnetic interactions and a magnetic structure with moments aligned along the **c** axis is observed. As the temperature increases, magnetic interactions decrease and a change of effective anisotropy is observed when the Ni easy plane anisotropy becomes predominant.

An interesting issue concerns the strength of the exchange anisotropy which is driven by p in equation 3.10, and is related to the relative weight of the $|a_{1g}\rangle$ and $|e'_g\rangle$ electronic wave functions. Those are respectively contributing to the isotropic (resp. anisotropic) part of the interactions [YLT+13]. The parameter p then varies with the octahedral distortion Δ and might be tunable by a chemical or external pressure.

3.3.5 Conclusion on Sr_3NiIrO_6

Our study on Sr_3NiIrO_6 allowed to evidence a very complex magnetic behavior in this system. Single crystal magnetization measurements show the existence of an easy axis anisotropy along the chain axis below 200 K as well as the presence of two magnetic anomalies at $T_1 = 70$ K and around $T_2 = 17$ K. T_1 is associated with the deviation of the magnetic susceptibility from the Curie-Weiss law, with the magnetic ordering of the system and with the onset of spin dynamics observed by AC magnetic susceptibility. Around T_2, a separation of the ZFC and FC magnetic susceptibilities is observed and the spin dynamics get "frozen". Below this temperature, the presence of a ferromagnetic component along the chain axis is also evidenced in the magnetic hysteresis, giving rise to record value for the coercive field. Indeed coercive fields up to 55 T have been observed at 2 K on single crystal specimens.

Neutron powder diffraction experiments confirmed the magnetic ordering of Sr_3NiIrO_6 below T_1 with a propagation vector $\mathbf{k}$= (0, 0, 1). The refined magnetic structure is composed of antiferromagnetically coupled Ni and Ir magnetic moments along the chain axis, the spins being aligned along this axis. The value of the ordered moments are modulated from one chain to the others. The modulation compatible with the presence of the ferromagnetic component along the chain axis leads to an amplitude modulated antiferromagnetic configuration where only one chain presents fully ordered moments. For the other two chains, the ordered moment is reduced to half and they are antiferromagnetically coupled to the first chain.

With RIXS experiments, we determined the energy level scheme of the 5d electrons of the Ir^{4+} ions and extracted the values of the Ir spin orbit coupling and of the trigonal distortion intensity using a simple model. We also evidenced the presence of a quasi dispersionless magnetic excitation at 90 meV. A spin wave model able to reproduce this mode, as well as the 35 meV mode reported by Wu *et al.* using inelastic neutron scattering experiments [TWA+16], has been found. It includes highly anisotropic magnetic exchange interactions between Ni and Ir along the chain due to Ir^{4+} SOC and an easy plane magnetocrystalline anisotropy of the Ni^{2+} ions. The latter is in agreement with the anisotropy energy observed for Sr_3NiPtO_6. In summary in Sr_3NiIrO_6, the magnetocrystalline anisotropy of the Ni ions is overcome at low temperature by the highly anisotropic magnetic exchange interactions leading to a magnetic order with moments confined perpendicular to the easy plane anisotropy of the Ni.

Moreover, a peculiar behavior is also observed concerning the temperature dependence of the magnetic correlations. Indeed the RIXS and REXS measurements show that the intensity of the Bragg peaks associated with the magnetic ordered phase reaches a maximum around T_2 before decreasing as the temperature is lowered. The in-plane correlation lengths seem also to follow the same behavior, contrary to the out-of-plane correlations which appear to remain constant below T_2. However, no evidence of a second magnetic phase, competing with the observed one and which would explain its decorrelation when decreasing the temperature, was observed during these experiments.

In conclusion we have gained detailed insights into the physics of Sr_3NiIrO_6 and evidenced some crucial consequence of the SOC of the iridium on the magnetic properties. Nevertheless, several experimental observations remain to be explained, in particular those related to the nature of the 17 K magnetic transition.

3.4 Conclusion

In this chapter, we discussed the physics of two compounds: Sr_3NiPtO_6 and Sr_3NiIrO_6. Although isostructural, the substitution of the non magnetic ion Pt^{4+} by the magnetic Ir^{4+} changes drastically the magnetic properties.

The Pt compound stabilizes a large-*D* phase due to a large easy plane single magnetocrystalline anisotropy of the Ni^{2+} perpendicular to the chain axis compared to the magnetic exchange interactions, leading to a non-magnetic ground state.

On the other hand, in Sr_3NiIrO_6, the same Ni^{2+} anisotropy competes with the highly anisotropic magnetic interactions. This forces the spins to align along the **c** direction leading to a peculiar modulated spin arrangement induced by the frustration. Actually, SOC is a key ingredient in the understanding of the magnetic properties of this system as it is responsible for the peculiar ground state of the Ir ions with a strong entanglement of the spin and orbital degrees of freedom, leading to anisotropic magnetic interactions.

Bibliography

[AFC+11] S. Agrestini, C. L. Fleck, L. C. Chapon, C. Mazzoli, A. Bombardi, M. R. Lees, and O. A. Petrenko. Slow magnetic order-order transition in the spin chain antiferromagnet $Ca_3Co_2O_6$. *Phys. Rev. Lett.*, 106:197204, May 2011.

[AKC+06] Mois I. Aroyo, Asen Kirov, Cesar Capillas, J. M. Perez-Mato, and Hans Wondratschek. Bilbao Crystallographic Server. II. Representations of crystallographic point groups and space groups. *Acta Crystallographica Section A*, 62(2):115–128, Mar 2006.

[BdJK81] F. Boersma, W. J. M. de Jonge, and K. Kopinga. Anisotropic classical chain: Numerical calculations of thermodynamic properties. *Phys. Rev. B*, 23:186–197, Jan 1981.

[Ber68] E. F. Bertaut. Representation analysis of magnetic structures. *Acta Crystallogr. A.*, 24(1):217–231, 1968.

[CDML79] A.P. Cracknell, B.L. Davies, S.C. Miller, and W.F. Love. *Kronecker product tables. General introduction and tables of irreducible representations of space groups.*, volume 1. IFI/Plenum, 1979.

[CGL+15] J. P. Clancy, H. Gretarsson, E. K. H. Lee, D. Tian, J. Kim, M. H. Upton, D. Casa, T. Gog, Z. Islam, B.-G. Jeon, K. H. Kim, S. Desgreniers, Y. B. Kim, S. J. Julian, and Y.-J. Kim. X-ray scattering study of pyrochlore iridates: crystal structure, electronic and magnetic excitations. *ArXiv e-prints*, October 2015.

[CJG+10] S. Chattopadhyay, Deepti Jain, V. Ganesan, S. Giri, and S. Majumdar. Observation of large-*d* magnetic phase in Sr_3NiPtO_6. *Phys. Rev. B*, 82:094431, Sep 2010.

[CLHzL99] John B. Claridge, Ralph C. Layland, W. Hampton Henley, and Hans-Conrad zur Loye. Crystal growth and magnetic measurements on aligned single crystals of the oxides Sr_3NiPtO_6 and Sr_3CuPtO_6. *Chemistry of Materials*, 11(5):1376–1380, 1999.

[CMC06] Claude Coulon, Hitoshi Miyasaka, and Rodolphe Clérac. *Single-Chain Magnets:Theoretical Approach and Experimental Systems*, pages 163–206. Springer Berlin Heidelberg, Berlin, Heidelberg, 2006.

[FHM+03] D. Flahaut, S. Hébert, A. Maignan, V. Hardy, C. Martin, M. Hervieu, M. Costes, B. Raquet, and J. M. Broto. A magnetic study of the one dimensional Sr_3NiIrO_6 compound. *Eur. Phys. J. B - Condens. Matter*, 35(3):317–323, October 2003.

[Gla63] Roy J. Glauber. Time-dependent statistics of the ising model. *Journal of Mathematical Physics*, 4(2):294–307, 1963.

[HGC+14] L. Hozoi, H. Gretarsson, J. P. Clancy, B.-G. Jeon, B. Lee, K. H. Kim, V. Yushankhai, Peter Fulde, D. Casa, T. Gog, Jungho Kim, A. H. Said, M. H. Upton, Young-June Kim, and Jeroen van den Brink. Longer-range lattice anisotropy strongly competing with spin-orbit interactions in pyrochlore iridates. *Phys. Rev. B*, 89:115111, Mar 2014.

[LCS+14] E. Lefrançois, L. C. Chapon, V. Simonet, P. Lejay, D. Khalyavin, S. Rayaprol, E. V. Sampathkumaran, R. Ballou, and D. T. Adroja. Magnetic order in the frustrated ising-like chain compound sr_3niiro_6. *Phys. Rev. B*, 90:014408, 2014.

[LKH+12] X. Liu, Vamshi M. Katukuri, L. Hozoi, Wei-Guo Yin, M. P. M. Dean, M. H. Upton, Jungho Kim, D. Casa, A. Said, T. Gog, T. F. Qi, G. Cao, A. M. Tsvelik, Jeroen van den Brink, and J. P. Hill. Testing the Validity of the Strong Spin-Orbit-Coupling Limit for Octahedrally Coordinated ?Iridate Compounds in a Model System Sr_3CuIrO_6. *Phys. Rev. Lett.*, 109:157401, 2012.

[LPMS+16] E. Lefrançois, A.-M. Pradipto, M. Moretti Sala, L. C. Chapon, V. Simonet, S. Picozzi, P. Lejay, S. Petit, and R. Ballou. Anisotropic interactions opposing magnetocrystalline anisotropy in Sr_3NiIrO_6. *Phys. Rev. B*, 93:224401, Jun 2016.

[MA78] Mamoru Mekata and Kimio Adachi. Magnetic structure of $CsCoCl_3$. *Journal of the Physical Society of Japan*, 44(3):806–812, 1978.

[Mek77] Mamoru Mekata. Antiferro-ferrimagnetic transition in triangular ising lattice. *Journal of the Physical Society of Japan*, 42(1):76–82, 1977.

[MIRS07] Niharika Mohapatra, Kartik K. Iyer, Sudhindra Rayaprol, and E. V. Sampathkumaran. Geometrically frustrated magnetic behavior of Sr_3NiRhO_6 and Sr_3NiPtO_6. *Phys. Rev. B*, 75:214422, Jun 2007.

[MSS+12] D. Mikhailova, B. Schwarz, A. Senyshyn, A. M. T. Bell, Y. Skourski, H. Ehrenberg, A. A. Tsirlin, S. Agrestini, M. Rotter, P. Reichel, J. M. Chen, Z. Hu, Z. M. Li, Z. F. Li, and L. H. Tjeng. Magnetic properties and crystal structure of Sr_3CoIrO_6 and Sr_3NiIrO_6. *Phys. Rev. B*, 86(13):134409, October 2012.

[NGzL94] T. N. Nguyen, D. M. Giaquinta, and H.-C. zur Loye. Synthesis of the New One-DimensionalCompound Sr_3NiPtO_6: Structure and Magnetic Properties. *Chem. Mater.*, 6(10):1642–1646, 1994.

[NKK+99] Seiji Niitaka, Hiroshi Kageyama, Masaki Kato, Kazuyoshi Yoshimura, and Koji Kosuge. Synthesis, Crystal Structure, and Magnetic Properties of New One-Dimensional Oxides Ca_3CoRhO_6 and Ca_3FeRhO_6. *J. Solid State Chem.*, 146:137 – 143, 1999.

[NzL95] T. N. Nguyen and H.-C. zur Loye. A Family of One-Dimensional Oxides: Sr_3MlrO_6 (M = Ni, Cu, Zn): Structure and Magnetic Properties. *J. Solid State Chem.*, 117(2):300–308, 1995.

[Ogu64] Takehiko Oguchi. Exchange Interactions in $Cu(NH_3)_4SO_4{\cdot}H_2O$. *Phys. Rev.*, 133:A1098–A1099, Feb 1964.

[OW14] X. Ou and H. Wu. Impact of spin-orbit coupling on the magnetism of Sr_3MIrO_6 (M = Ni, Co). *Sci. Rep.*, 4:4609, 2014.

[PLM+14] K. Prsa, M. Laver, M. Mansson, S. Guerrero, P. M Derlet, I. Zivkovic, H. T. Yi, L. Porcar, O. Zaharko, S. Balog, J. L Gavilano, J. Kohlbrecher, B. Roessli, C. Niedermayer, J. Sugiyama, C. Garcia, H. M Ronnow, C. Mudry, M. Kenzelmann, S. W. Cheong, and J. Mesot. Magnetic nano-fluctuations in a frustrated magnet. *ArXiv e-prints*, 2014.

[SFR+04] E. V. Sampathkumaran, N. Fujiwara, S. Rayaprol, P. K. Madhu, and Y. Uwatoko. Magnetic behavior of Co ions in the exotic spin-chain compound $Ca_3Co_2O_6$ from ^{59}Co NMR studies. *Phys. Rev. B*, 70:014437, Jul 2004.

[SIP75] D. J. Scalapino, Y. Imry, and P. Pincus. Generalized ginzburg-landau theory of pseudo-one-dimensional systems. *Phys. Rev. B*, 11:2042–2048, Mar 1975.

[SKSD10] Soumyajit Sarkar, Sudipta Kanungo, and T. Saha-Dasgupta. *Ab initio* study of low-dimensional quantum spin systems Sr_3NiPtO_6, Sr_3CuPtO_6, and Sr_3NiIrO_6. *Phys. Rev. B*, 82:235122, Dec 2010.

[SKT+14] J. Singleton, J. W. Kim, C. V. Topping, A. Hansen, E.-D. Mun, S. Ghannadzadeh, P. Goddard, X. Luo, Y. S. Oh, S.-W. Cheong, and V. S. Zapf. 55 Tesla coercive magnetic field in frustrated Sr_3NiIrO_6. *ArXiv e-prints*, 2014.

[TMH+05] K. Takubo, T. Mizokawa, S. Hirata, J.-Y. Son, A. Fujimori, D. Topwal, D. D. Sarma, S. Rayaprol, and E.-V. Sampathkumaran. Electronic structure of Ca_3CoXO_6 (X = Co, Rh, Ir) studied by x-ray photoemission spectroscopy. *Phys. Rev. B*, 71:073406, Feb 2005.

[TWA+16] S. Toth, W. Wu, D. T. Adroja, S. Rayaprol, and E. V. Sampathkumaran. Frustrated ising chains on the triangular lattice in sr_3niiro_6. *Phys. Rev. B*, 93:174422, May 2016.

[VL77] J. Villain and J. M Loveluck. Néel temperature of a low-dimensional antiferromagnet in a magnetic field. *J. Physique Lett.*, 38(2):77–80, Dec 1977.

[WAT+15] W. Wu, D. T. Adroja, S. Toth, S. Rayaprol, and E. V. Sampathkumaran. Giant gap in the magnon excitations of the quasi-1D chain compound Sr_3NiIrO_6. *ArXiv e-prints*, 2015.

[YLT+13] Wei-Guo Yin, X. Liu, A. M. Tsvelik, M. P. M. Dean, M. H. Upton, Jungho Kim, D. Casa, A. Said, T. Gog, T. F. Qi, G. Cao, and J. P. Hill. Ferromagnetic Exchange Anisotropy from Antiferromagnetic Superexchange in the Mixed $3d-5d$ Transition-Metal Compound Sr_3CuIrO_6. *Phys. Rev. Lett.*, 111:057202, 2013.

[YTH+05] C. Yasuda, S. Todo, K. Hukushima, F. Alet, M. Keller, M. Troyer, and H. Takayama. Néel temperature of quasi-low-dimensional heisenberg antiferromagnets. *Phys. Rev. Lett.*, 94:217201, Jun 2005.

[ZZJ+10] G. R. Zhang, X. L. Zhang, T. Jia, Z. Zeng, and H. Q. Lin. Intrachain antiferromagnetic interaction and mott state induced by spin-orbit coupling in Sr_3NiIrO_6. *J. Appl. Phys.*, 107(9), 2010.

R2Ir2O7

Chapter 4

The pyrochlore compounds

Contents

4.1 Introduction to the pyrochlore iridates

The pyrochlore compounds, $A_2B_2O_7$ (A=Y or rare-earth-element, B = transition metal), belong to a family of compounds which has been and is still widely studied since a few decades. Its peculiar structure, composed of two interpenetrated pyrochlore lattices (network of corner-sharing tetrahedra, see Fig. 4.1), is described by the $Fd\bar{3}m$ space group. It is one of the archetype structures in which a wide variety of magnetic frustration effects can be observed depending on the magnetocrystalline anisotropy and the nature of the magnetic interactions. A large variety of behaviors was observed among these compounds such as disordered phases: spin ices *e.g.* in $(Dy,Ho)_2Ti_2O_7$ [HBM+97, HBHC98, BG01], spin glasses *e.g.* in $Y_2Mo_2O_7$ [GSYR86] and spin liquids *e.g.* in $Tb_2Ti_2O_7$ [GDG+99, GGB+01] but also complex ordered phases: ordered spin ice in $Tb_2Sn_2O_7$ [BJB01, MHT+02, MARC+05] or order-by-disorder magnetic process in $Er_2Ti_2O_7$ [BWH69, SSR+99, CHH+03, PWLB07].

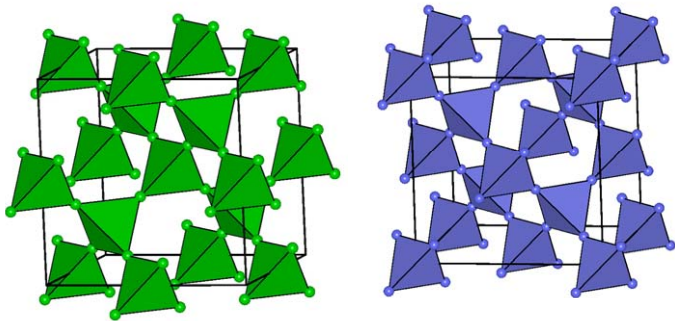

Figure 4.1 – *The A (left) and B (right) sublattices of the cubic pyrochlore materials made of corner sharing tetrahedra. Either or both sublattices can be magnetic.*

This family was initially studied with non magnetic transition metal ions (Ti, Sn), focusing on the rare-earth magnetism [BWH69, GSYR86, HBM+97, SSR+99, RDG+99]. Lately, pyrochlores where both elements are magnetic came under focus. Both sublattices being magnetic, novel behaviors are thus to be expected for these compounds.

In this context, the family of compounds with Iridium as transition metal element especially attracted a lot of attention. Ir being a 5*d* element, it presents a strong spin-orbit coupling as well as moderate electronic correlations in oxide solids compared to 3*d* and 4*d* counterparts. These quantities are then of the same order of magnitude, influencing both the electronic and magnetic properties (see Chapter 1). Moreover, the Ir^{4+} was shown to be close to a new entangled spin-orbitronic state characterized by an effective angular momentum $j_{\text{eff}} = 1/2$ when situated in an octahedral environment [KJM+08, KOK+09]. Strong dependence between the electronic and magnetic properties, the presence of unprecedented electronic phases with topological properties, or directional magnetic exchange interactions are thus expected as a result of this state.

Atoms	Wyckoff sites	Site symmetry	Coordinates
A	16*d*	. $\bar{3}$ *m*	(0, 0, 0)
B	16*b*	. $\bar{3}$ *m*	($1/2$, $1/2$, $1/2$)
O1	8*b*	$\bar{4}$ 3 *m*	($3/8$, $3/8$, $3/8$)
O2	48*f*	2 . *m m*	(x, $1/8$, $1/8$)

Table 4.1 – *Details of the symmetry and coordinates of the Wyckoff sites for $A_2B_2O_7$.*

It has also been predicted that the Ir 5*d* electrons, in the pyrochlore iridates, might stabilize unprecedented electronic phases like the Weyl semi-metal: semi-metal presenting electronic band touching points called Weyl points, at which the dispersion is linear [PB10, WTVS11, WKK12, WKCKB14]. The condition for this to occur is that the Ir sublattice orders in the so called "all-in/all-out" (AIAO) magnetic configuration (see Fig. 4.2), which is the only one preserving the cubic symmetry whilst breaking the time-reversal symmetry. Indeed it has been shown that Weyl points can exist only when these two conditions are met [ZWB12].

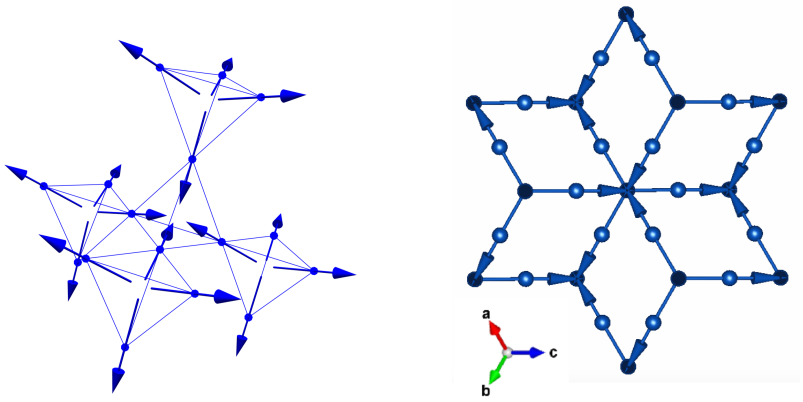

Figure 4.2 – *Sketch of the all-in/all-out magnetic configuration on the pyrochlore lattice from a perspective point of view (left) and along the* $\langle 111 \rangle$ *direction (right). This configuration corresponds to all spins pointing either toward or away from the center of the tetrahedra.*

The first studies of the $R_2Ir_2O_7$ series showed that almost all the members of this family exhibit a metal-to-insulator transition (MIT) when the temperature decreases (see Fig. 4.3) [TWH01, MWHT11]. Moreover, this MIT appears to coincide with a magnetic transition characterized by a ZFC-FC bifurcation of the magnetization. The high temperature electronic state and the MIT temperature T_{MI} both depend on the rare-earth element. It was argued from electronic structure calculations that the Ir^{4+} ions stabilizes the AIAO magnetic configuration [WTVS11]. However, the Ir order is difficult to probe directly, using usual neutron scattering experiments, due to the small value of its magnetic moment and its relatively strong neutron absorption ($\sigma_{abs} = 425$ barns for thermal neutrons).

In order to probe the Ir magnetic order in this family of compounds, we first started by investigating compounds with non magnetic R element. In this context, we chose to investigate the magnetic properties of the polycrystalline Yttrium based compound: $Y_2Ir_2O_7$. Note that, all measurements presented on the $R_2Ir_2O_7$ in this manuscript have been performed on polycrystalline samples. Part of this work has been published in [LSB+15].

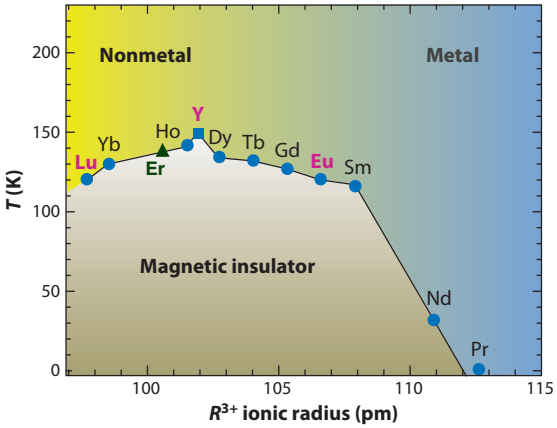

Figure 4.3 – *Phase diagram for the pyrochlore iridates $R_2Ir_2O_7$ based on transport and magnetism measurements (from [WKCKB14]). The R-elements that do not have a local magnetic moment are emphasized in bold magenta. The only non-lanthanide, R = Y, is denoted by a square. The Er compound denoted by the black triangle has been added to the original figure.*

4.2 $Y_2Ir_2O_7$

I will now discuss the results obtained on $Y_2Ir_2O_7$ by magnetization measurements performed on a QD MPMS® SQUID magnetometer.

The temperature dependence of the magnetic susceptibility M/H measured after a ZFC-FC procedure in 0.01 T is shown Fig. 4.4. Differences between the two curves are observed below 150 K, where a huge opening is present below 150 K. This difference is associated with the Ir magnetism as it is the only magnetic element in the material. It is interpreted as the polarization of a weak ferromagnetic component along the applied field. However, it has to be noted that such a difference is rather unexpected in the case of an AIAO magnetic order as it is an antiferromagnetic arrangement.

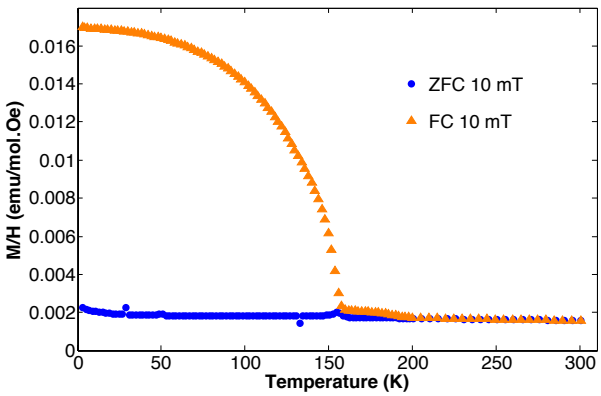

Figure 4.4 – *Temperature dependence of the magnetic susceptibility (M/H) measured after a ZFC (in blue) and a FC (in orange) procedure in 0.01* T.

The magnetic field dependence of the magnetization (see Fig. 4.5) shows a linear behavior for magnetic field up to 10 T at all temperatures. This indicates that the system is far away from its saturated magnetization. The presence of a very small opening of the hysteresis curve is observed at 2 K. Surprisingly, if the magnetization is measured after a cooling in a finite magnetic field, the magnetization is shifted towards higher values suggesting the presence of a field-induced ferromagnetic component.

A small curvature is observed for low magnetic field (see right part of Fig. 4.5). By measuring the magnetization of the empty sample holder we were able to conclude that this signal comes from the presence of magnetic impurities in the sample holder.

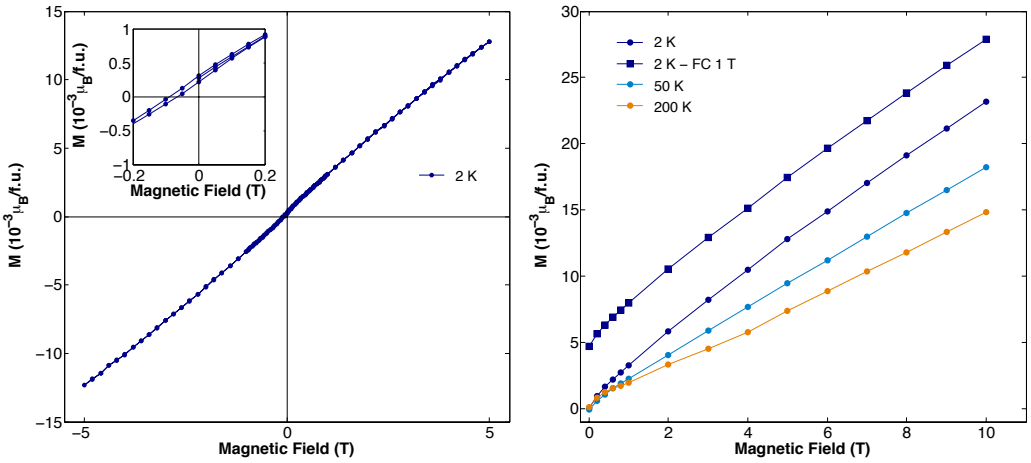

Figure 4.5 – *(left) Magnetic field dependence of the magnetization measured up to 5* T *at 2* K*. Inset: opening of the magnetic cycle measured at 2* K *in a zero field. (right) Magnetic field dependence of the magnetization measured up to 10* T *after a FC in 1* T *at 2* K *(dark blue squares) and after a ZFC (dots) at 2* K *(in dark blue) at 50* K *(in light blue) and at 200* K *(in orange).*

Neutron powder diffraction experiments were performed on this sample on the WISH diffractometer at the Target Station 2 at ISIS with P. Manuel and D. Khalyavin. No magnetic Bragg peaks that could reveal an Ir magnetic ordering were observed down to 2 K. This result is consistent with other neutron diffraction experiments [DDA+12], merely confirming that the Ir ordered magnetic moment is too weak to be measured by this technique.

μSR experiments have also been performed on $Y_2Ir_2O_7$ by Disseler *et al.* An Ir magnetic ordering was evidenced with a magnetic moment estimated to 0.15 μ_B/Ir^{4+} but no firm conclusions could be drawn on the Ir moment arrangement [DDA+12].

Similar experiments were performed on $Eu_2Ir_2O_7$ where the Eu^{3+} ions, being in a singlet state of angular momentum, are non magnetic. The magnetization measurements, neutron powder diffraction and μSR experiments show a behavior similar to the Y based compound with the presence of a ZFC-FC opening at 120 K [TWH01, MWN+07, MWHT11], the absence of additional Bragg peaks observed by neutron scattering at low temperature and well defined muon spin precession frequency [ZMM+11]. Moreover Resonant Elastic X-ray Scattering (REXS) measurements on a single crystal of $Eu_2Ir_2O_7$ evidenced the presence of magnetic intensity on top of a charge peak suggesting the presence of a magnetic order with a propagation vector $\mathbf{k}$ = (0, 0, 0) [SUA+13]. The observed magnetic peak is compatible with two configurations: the all-in/all-out order and a coplanar arrangement. The intensity of the magnetic peak being the same for the two arrangements, magnetic scattering alone could not allow to unambiguously determine the magnetic configuration.

As the investigation of the Ir magnetic order using compounds with non magnetic R element was inconclusive, we decided to study pyrochlore iridates with magnetic rare-earth elements. By studying compounds where both R and Ir are magnetic, we expect to probe the Ir order through its influence on the R sublattice. For that, we assume that the R ions do not interact down to very low temperature

(at least down to few K). This seems to be a fair assumption regarding the behavior of the pyrochlore compounds with non magnetic transition metal ion.

4.3 $Tb_2Ir_2O_7$

We choose to start with Terbium as it displays quite large magnetic moments (see Table 4.2). Besides, the Tb^{3+} local environment in $Tb_2Ir_2O_7$ is similar to the one in tin or titanium pyrochlore. Thus we made the assumption that the Tb single ion magnetocrystalline anisotropy is similar. This assumption of a similar magnetocrystalline anisotropy in those materials and in the iridates will be considered true also for all the other rare-earth ions. Therefore, Tb^{3+} is expected to present an easy-axis anisotropy along the local $\langle 111 \rangle$ cubic axis.

Tb^{3+}	Electronic configuration	S	L	J	$g_J J$ (μ_B)	Expected anisotropy	Lattice parameter (Å)
	$4f^8$	3	3	6	9	easy axis $\parallel \langle 111 \rangle$	10.252(2)

Table 4.2 – *Details of the electronic configuration and of the spin, angular and total angular momentum of the Tb^{3+} ions. The expected anisotropy of the Tb ions and the lattice parameter of the $Tb_2Ir_2O_7$ compounds are also given.*

I will first present the magnetization measurements performed on a QD SQUID magnetometers and a SQUID magnetometer equipped with a dilution fridge developed at Institut Néel, then the neutron powder diffraction experiment which allowed determining the Tb magnetic arrangement.

4.3.1 Magnetization measurements

Figure 4.6 shows the temperature dependence of the magnetic susceptibility M/H measured after ZFC and FC procedures in 0.01 T. Similarly to $Y_2Ir_2O_7$, a bifurcation between the two curves is observed around T_{MI} = 130 K. This bifurcation is consistent with the previous studies and is associated to the magnetic ordering of the Ir sublattice. Comparing these measurements to the non magnetic Y based compound, we note that both curves continue to increase below this bifurcation, the FC one lying above the ZFC. At lower temperature, the two curves cross, the ZFC curve increasing faster the the FC one. Finally around 6 K, a bump is observed in both cases.

The isothermal magnetization curve as function of the magnetic field are shown Fig. 4.7 for temperatures from 300 K to 80 mK. The high temperature curve shows a linear magnetic field dependence, characteristic of a paramagnetic system. As the temperature is decreased, a tendency towards saturation is observed although not yet reached for 8 T, the highest magnetic field applied at 80 mK (not shown here). For temperatures below 10 K, an inflection point is also observed in the magnetization around 1.8 T. This is characteristic of a metamagnetic process and could be related to the presence of the bump observed at 6 K in the magnetic susceptibility as it is no longer present at 10 K.

From magnetization measurements, we suspect that the Ir sublattice orders around $T_{MI} = 130$ K. The presence of additional features in the magnetic susceptibility at 6 K and in the magnetization curves below this temperature could indicate the presence of additional magnetic interactions, possibly the Tb-Tb interactions.

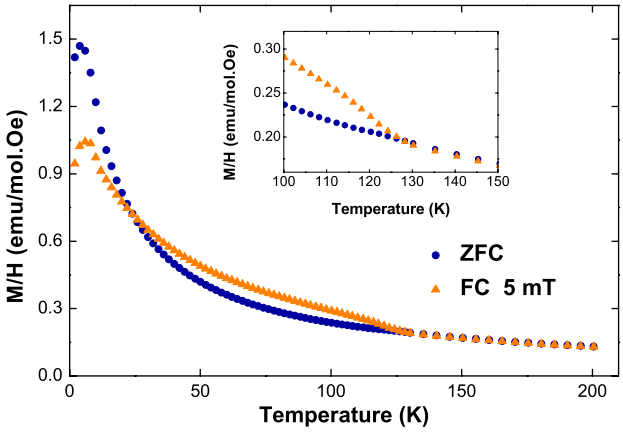

Figure 4.6 – *M/H versus T for $Tb_2Ir_2O_7$ measured after a ZFC (in blue) and a FC (in orange) procedure in 5 mT. Inset: zoom of the ZFC-FC opening happening around 130* K.

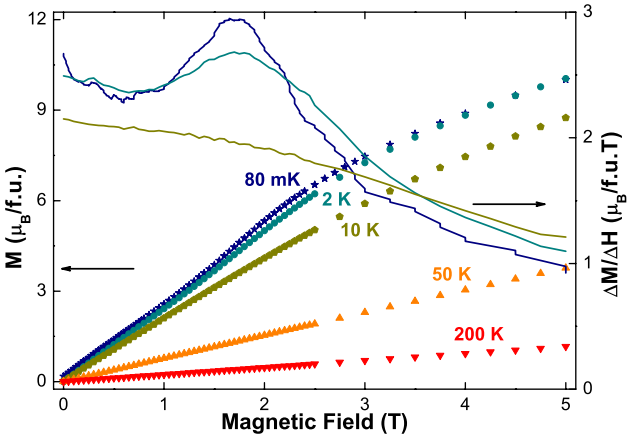

Figure 4.7 – *(left hand side) M versus H for $Tb_2Ir_2O_7$ measured at different temperatures. (right hand side) Derivative of the magnetization curve below 10* K *showing a maximum indicative of a metamagnetic process.*

4.3.2 Neutron Powder Diffraction

In order to determine the magnetic order in $Tb_2Ir_2O_7$, neutron powder diffraction experiments were performed on the WISH diffractometer at the Target Station 2 at the ISIS Facility with P. Manuel and D. Khalyavin.

Diffractograms were measured from 200 K (above T_{MI}) down to 2 K. At the time we performed the experiment, high quality polycrystalline samples were still challenging to obtain, thus the sample used for these measurements contains a non negligible quantity of Terbium oxide impurities (Tb_2O_3 and Tb_4O_7). These impurities present a magnetic order around 8 K, so in the following part, I will not show the measurements performed below 10 K since strong magnetic peaks associated to these impurities are present and difficult to refine.

Figure 4.8 shows the diffractometers measured at 200 and 10 K as well as the difference between these two measurements. The presence of additional magnetic Bragg peaks are observed on top of

the nuclear ones. These magnetic peaks are resolution limited indicating a 3D magnetic order and are indexed by a magnetic propagation vector **k** = (0,0,0).

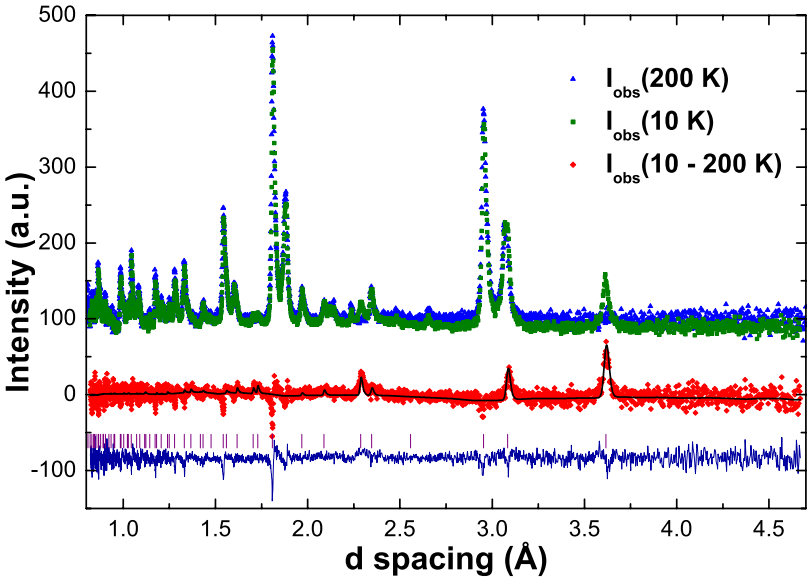

Figure 4.8 – *Neutron diffractograms recorded for $Tb_2Ir_2O_7$ at 10 K (in green) and 200 K (in blue). Difference between the 10 and 200 K diffractograms is shown in red and the black line represents the calculated intensity using the AIAO model for the Tb magnetic order.*

The possible magnetic structures compatible with the space group of this compound were determined from group theory and representation analysis [Ber68]. Four possible irreducible representations (IR) are obtained (see Table 4.3). Among these IR, τ_1 of dimension 1, is the one corresponding to the all-in/all-out magnetic configuration.

The Rietveld refinement of the neutron data shows that the AIAO magnetic structure is the only arrangement accounting correctly for the intensity of the magnetic Bragg peaks associated to the ordering of the Tb moments. We were able to refine only the Tb magnetic moment below 40 K and down to 2 K. The ordered magnetic moment is $M(Tb) = 4.9(1)\ \mu_B$ at 10 K. The magnetic moment of the Ir could not be refined because it is too weak for the experimental sensitivity. Nevertheless, as both Ir and Tb occupy sites of the same symmetry, they have to be described by the same irreducible representation assuming a second order phase transition from the shape of the peak observed by specific heat measurements [MWHT11]. Therefore, as the Tb sublattice orders in the AIAO magnetic order, from symmetry principles the Ir sublattice has to be ordered in this AIAO configuration as well.

Figure 4.9 shows the temperature dependence of the Tb^{3+} ordered magnetic moment. Its intensity starts to increase significantly below 40 K and does not follow a Brillouin function as it would be expected for a primary order parameter. A similar behavior is reported in the isostructural compound $Nd_2Ir_2O_7$ (see Fig. 4.10) [TMI+12], in which Nd^{3+} ions present an easy axis anisotropy along the $\langle 111 \rangle$ direction similarly to Tb^{3+} ions. The temperature evolution of M_{Tb} is rather indicative of a magnetization induced through a molecular field.

Under the hypothesis that the Ir sublattice is ordered below 130 K, we can then assume that this molecular field, denoted $\lambda \vec{M}_{Ir}$, results from the effective Tb-Ir magnetic coupling. To check this, we

Magnetic sites	Tb_1 $(\frac{1}{2}, \frac{1}{2}, \frac{1}{2})$	Tb_2 $(\frac{1}{4}, \frac{3}{4}, 1)$	Tb_3 $(\frac{3}{4}, 1, \frac{1}{4})$	Tb_4 $(1, \frac{1}{4}, \frac{3}{4})$
τ_1	$\begin{pmatrix} u \\ u \\ u \end{pmatrix}$	$\begin{pmatrix} -u \\ -u \\ u \end{pmatrix}$	$\begin{pmatrix} -u \\ u \\ -u \end{pmatrix}$	$\begin{pmatrix} u \\ -u \\ -u \end{pmatrix}$
τ_2	$\begin{pmatrix} u+\frac{1}{2}v \\ -\frac{1}{2}u+\frac{1}{2}v \\ -\frac{1}{2}u+v \end{pmatrix} + i\frac{\sqrt{3}}{2}\begin{pmatrix} v \\ -u-v \\ u \end{pmatrix}$	$\begin{pmatrix} -u-\frac{1}{2}v \\ \frac{1}{2}u-\frac{1}{2}v \\ -\frac{1}{2}u-v \end{pmatrix} + i\frac{\sqrt{3}}{2}\begin{pmatrix} -v \\ u+v \\ u \end{pmatrix}$	$\begin{pmatrix} -u-\frac{1}{2}v \\ -\frac{1}{2}u+\frac{1}{2}v \\ \frac{1}{2}u+v \end{pmatrix} + i\frac{\sqrt{3}}{2}\begin{pmatrix} -v \\ -u-v \\ -u \end{pmatrix}$	$\begin{pmatrix} u+\frac{1}{2}v \\ \frac{1}{2}u-\frac{1}{2}v \\ \frac{1}{2}u+v \end{pmatrix} + i\frac{\sqrt{3}}{2}\begin{pmatrix} v \\ u+v \\ -u \end{pmatrix}$
τ_3	$\begin{pmatrix} u-w \\ -u+v \\ -v+w \end{pmatrix}$	$\begin{pmatrix} -u-w \\ u+v \\ -v-w \end{pmatrix}$	$\begin{pmatrix} u+w \\ u-v \\ -v-w \end{pmatrix}$	$\begin{pmatrix} -u+w \\ -u-v \\ v+w \end{pmatrix}$
τ_4	$\begin{pmatrix} u+p+q \\ u+w+r \\ v+w+q \end{pmatrix}$	$\begin{pmatrix} -u+p+q \\ -u+w+r \\ v-w-q \end{pmatrix}$	$\begin{pmatrix} u+p-q \\ -u-w+r \\ v+w-q \end{pmatrix}$	$\begin{pmatrix} -u+p-q \\ u-w+r \\ v-w+q \end{pmatrix}$

Table 4.3 – *Magnetic configurations associated with the four irreducible representations (τ_1 to τ_4) of the group of the propagation vector* $\mathbf{k}$ *= (0, 0, 0). u, v, w, p, q and r are refinable parameters of the magnetic moment components.*

calculated the Tb^{3+} induced magnetic moment by first assuming that the temperature dependence of the Ir^{4+} magnetic moment follows a Brillouin function. Next, the Tb^{3+} magnetic moment can be calculated, knowing the crystalline electric field (CEF) excitation spectra. For that the following Hamiltonian was considered:

$$\mathcal{H}_{CEF} = A_2^0\,\mathbf{O}_2^0 + A_4^0\,\mathbf{O}_4^0 + A_4^3\,\mathbf{O}_4^3 + A_6^0\,\mathbf{O}_6^0 + A_6^3\,\mathbf{O}_6^3 + A_6^6\,\mathbf{O}_6^6$$

where O_n^m are the Stevens operators [Ste52, Hut64] and A_n^m are the adjustable CEF parameters. The A_n^m parameters are usually refined from inelastic neutron scattering (INS) measurements coupled with CEF calculations. At the time we performed this analysis, no INS data were available, therefore these parameters were estimated by assuming that the environment in $Tb_2Ir_2O_7$ is exactly the same as in $Nd_2Ir_2O_7$ (for which the CEF parameters were reported [WTM+11]). The CEF parameters were accordingly estimated as:

$$A_n^m(Tb) = \frac{A_n^m(Nd)}{\Theta_J(Nd)\langle r^n\rangle_{Nd}}\Theta_J(Tb)\langle r^n\rangle_{Tb},$$

where $\Theta_J(Tb) = \alpha_J, \beta_J, \gamma_J$ stands respectively for the Stevens reduced matrix elements associated with the Stevens operators O_2^m, O_4^m and O_6^m, $\langle r^n\rangle$ are radial integrals and $A_n^m(Nd)$ are the CEF parameters extracted provided in [WTM+11].

The Tb-Ir interaction is taken into account through the Zeeman contribution to the Hamiltonian:

$$\mathcal{H}_{Tb-Ir} = \lambda\vec{M}_{Ir}(T)g_J\mu_B\vec{J}$$

The Tb^{3+} magnetic moment is then computed as $\vec{M}_{Tb} = g_J\mu_B Tr(\vec{J}\exp(-\beta\mathcal{H}))$, where $\mathcal{H} = \mathcal{H}_{\text{CEF}} + \mathcal{H}_{Tb-Ir}$. This model accounts well for the observed slow increase of M_{Tb} below T_{MI} which accelerates on lowering the temperature without any sign of saturation (see Fig. 4.9). It allows to extract a value for the Ir^{4+} molecular field λM_{Ir}, found $\approx 3.0(5)$ T at 10 K.

Moreover, we can also look at the direction of the Ir molecular field λM_{Ir} at the Tb site. Left part of Fig. 4.11 shows a schematic representation considering a perfect AIAO magnetic arrangement of the

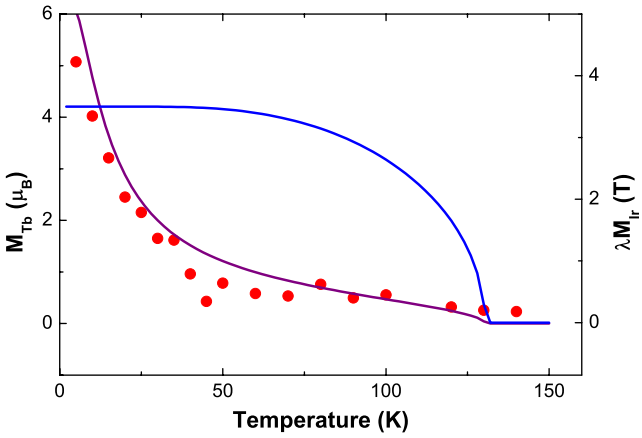

Figure 4.9 – *Temperature dependence of the square root of the* (2, 2, 0) *magnetic reflection intensity, corresponding to the most intense magnetic reflection (red dots). It is compared to the calculated* Tb^{3+} *ordered moment (purple line) induced by the molecular field* λM_{Ir} *generated by the* Ir^{4+} *magnetization whose temperature is assumed to follow a Brillouin function (blue line).*

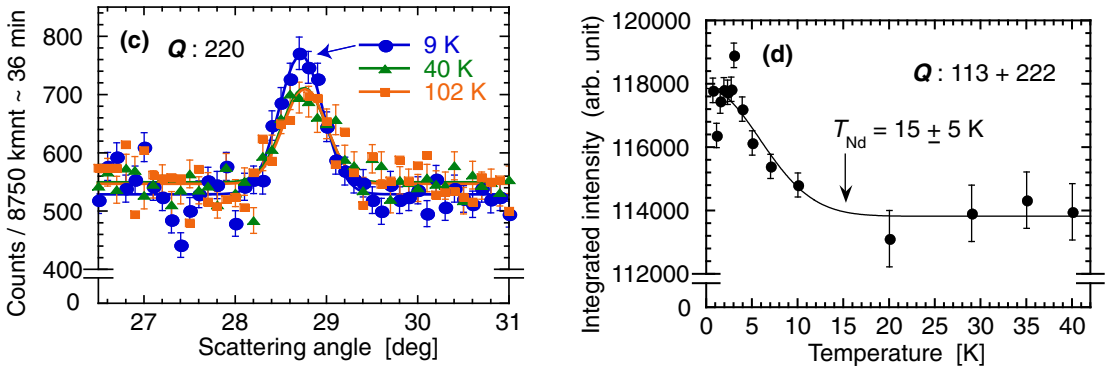

Figure 4.10 – *Measured neutron diffraction data for powder* $Nd_2Ir_2O_7$*. (Left) Bragg reflection lines measured around the (2, 2, 0) reciprocal lattice point at 9, 40, and 102* K*. (Right) Temperature dependence of summation of the integrated intensities of the (1, 1, 3) and (2, 2, 2) reflections. All the lines are a guide to the eye. From [TMI+12]*

Ir moment. The molecular field produced by the Ir first neighbor of one rare-earth ion is aligned along the ⟨111⟩ direction, which is the direction corresponding to the easy axis anisotropy in the Tb case. Thus, in $Tb_2Ir_2O_7$, the Tb magnetic ordering is induced through the Tb-Ir magnetic coupling and is in agreement with the Tb magnetocrystalline anisotropy.

A remaining unanswered issue is the presence of the ZFC-FC opening at the Ir magnetic ordering. This is not compatible with an AIAO antiferromagnetic structure and arises rather from intrinsic and/or extrinsic defects. These defects can be of various type such as the presence of a 180° magnetic domain walls [TTO+15] or the presence of non magnetic sites. Indeed, it has been argued that Ir^{5+}/Ir^{4+} substitution (Ir^{5+} ions being non magnetic) can exist in the pyrochlore iridates [ZWS+14]. Such defects will affect the direction of the molecular field on the rare-earth site as described in Fig.4.11. The resulting molecular field would then be slightly shifted from the ⟨111⟩ direction. The rare-earth magnetic moments affected by these defective molecular field could then be easily polarized by an

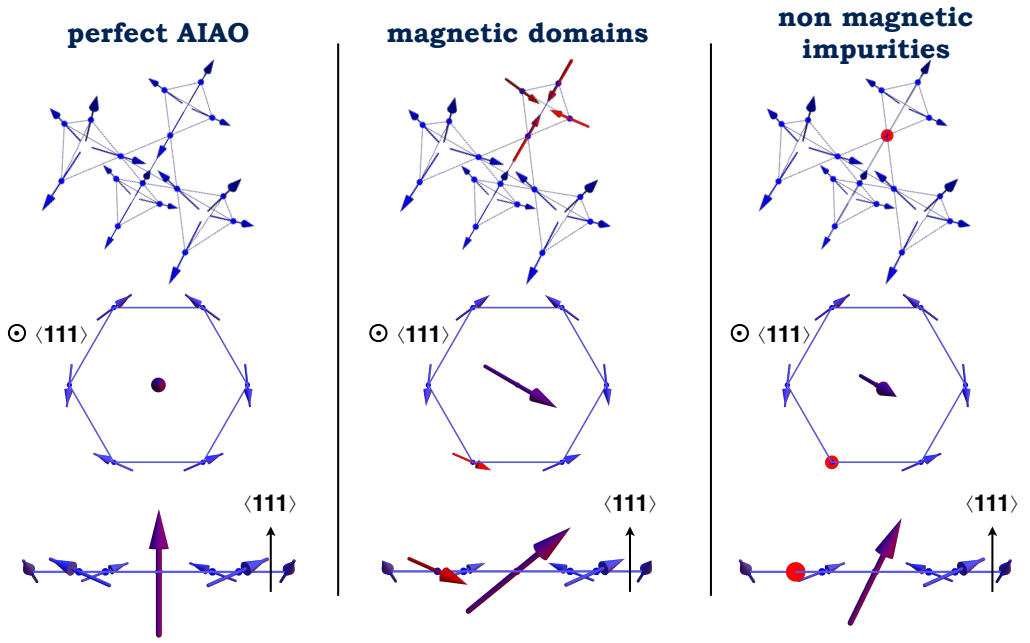

Figure 4.11 – *(top) AIAO magnetic configuration on the Ir pyrochlore sublattice for an ideal case (left) and taking into account the presence of defects (shown in red) such as magnetic domains (middle) or non magnetic impurities (right). (bottom) Magnetic moments on a hexagon of 6 Ir^{4+} ions in the AIAO configuration (blue and red arrows) yielding a molecular field at the central Tb^{3+} ions whose direction is represented by the purple arrow. In the perfect AIAO Ir order, the molecular field is along the ⟨111⟩ cubic direction. With the presence of defects, it is slightly shifted away from this direction by an angle of 54.7° for a magnetic domain and 29.5° for a non magnetic impurity.*

external magnetic field, leading to the ZFC-FC opening. The presence of less than 0.01% of magnetic impurities or domain walls would be indeed enough in order to see a ZFC-FC opening of this magnitude.

To summarize on $Tb_2Ir_2O_7$, we have indirectly proven that the Ir sublattice orders in the AIAO structure around 130 K. This magnetic ordering creates a molecular field whose direction is compatible with the Tb easy axis anisotropy, and induces the AIAO magnetic arrangement on the Tb sublattice seen by neutron diffraction. Some additional features are observed below 10 K in the magnetization measurements that are most probably indicative of the Tb-Tb interactions.

4.4 $Er_2Ir_2O_7$

In this part we focus on a pyrochlore with another rare-earth magnetic element: Erbium. From previous studies realized in Er pyrochlore compounds, the Er^{3+} is known to display an easy plane magnetocrystalline anisotropy perpendicular to the ⟨111⟩ direction. We will show that this change of anisotropy with respect to the Tb case leads to a drastic change on the rare-earth magnetism in the pyrochlore iridates.

I will first present the magnetization measurements performed on high-quality polycrystalline sample using similar tools than for the previous compounds. I will then present the results of neutron

Er^{3+}	Electronic configuration	S	L	J	$g_J J$ (μ_B)	Expected anisotropy	Lattice parameter (Å)
	$4f^{11}$	$3/2$	6	$15/2$	9	Easy plane $\perp \langle 111 \rangle$	10.16(2)

Table 4.4 – *Details of the electronic configuration and of the spin, angular and total angular momentum of the Er^{3+} ions. The expected anisotropy of the Er ions and the lattice parameter of the $Er_2Ir_2O_7$ compounds are also given.*

powder diffraction data performed down to 2 K on the WISH diffractometer at the ISIS Facility with P. Manuel and down to 50 mK on the D7 diffractometer using polarized neutron with XYZ polarization analysis at the Institut Laue-Langevin with G. Nilsen.

4.4.1 Magnetization measurements

Figure 4.12 (left part) shows the temperature dependence of the magnetic susceptibility M/H. A ZFC-FC difference is observed around T_{MI} =140 K which is associated to the Ir sublattice magnetic ordering. Below this temperature, the FC curve remains above the ZFC one and both increase down to 2 K without any sign of saturation.

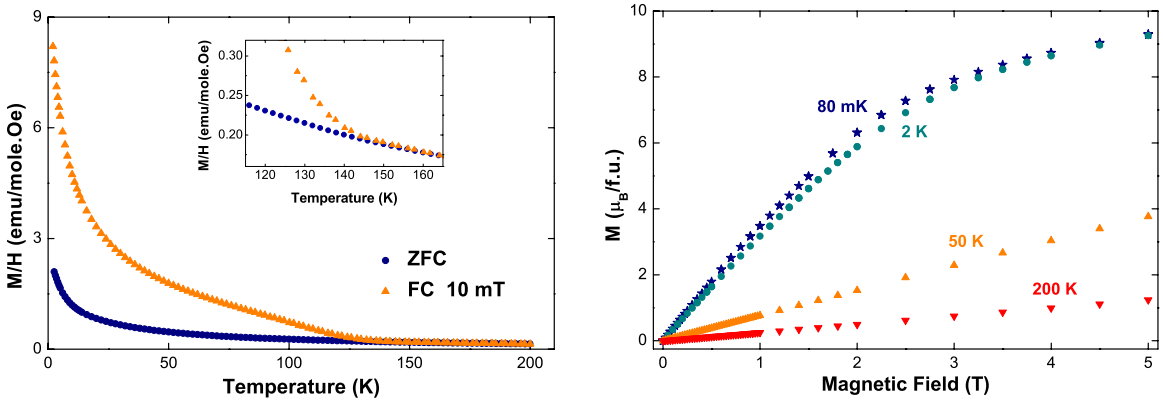

Figure 4.12 – *(left) M/H versus T for $Er_2Ir_2O_7$ measured after a ZFC (in blue) and a FC (in orange) procedure in 10 mT. Inset: zoom of the ZFC-FC opening happening around 145* K. *(right) M versus H for $Er_2Ir_2O_7$ measured at different temperatures.*

The magnetic field dependence of the magnetization is shown Fig. 4.12 (right part). Similarly to $Tb_2Ir_2O_7$, a tendency towards saturation is observed but not reached for the highest applied magnetic field of 8 T.

Magnetic susceptibility measurements were also performed at low temperature (see Fig. 4.13). An additional ZFC-FC difference is observed around 0.6 K and shifts towards higher temperature when the applied magnetic field is increased. This indicates the presence of some magnetic freezing in the system. During this ZFC-FC procedure, the magnetic field could only be applied below 4 K. Thus assuming that the Ir sublattice is ordered at this temperature, only thermomagnetic irreversibilities from the Er sublattice should be observed. This opening could then be explained by the presence of Er-Er magnetic interactions that come into play in this temperature range. Therefore the magnetization measurements on $Er_2Ir_2O_7$ indicate an Ir magnetic ordering at T_{MI} =140 K, as well as the possible presence of Er-Er correlations occurring around 0.6 K.

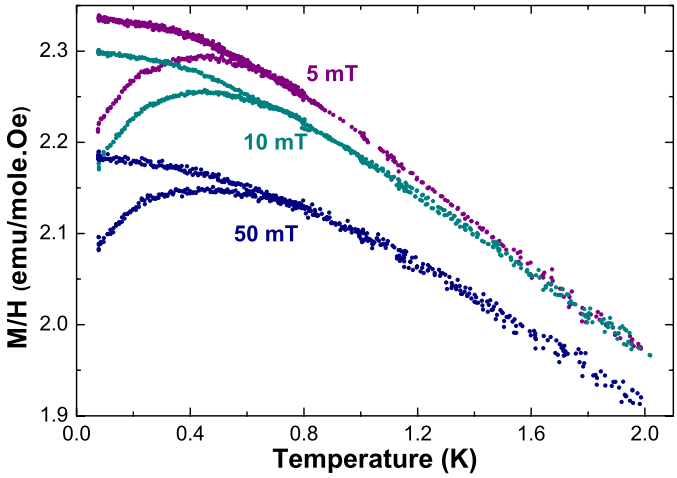

Figure 4.13 – *M/H versus T for $Er_2Ir_2O_7$ measured between 0.08 and 2 K after ZFC and FC in different magnetic fields, the magnetic field in the FC procedure is applied below 4 K.*

4.4.2 Neutron Powder Diffraction

Neutron powder diffraction experiments were performed in order to probe the Er magnetic order.

No magnetic Bragg peaks are observed down to 2 K on WISH, and down to 0.05 K (see Fig. 4.14) on D7 (incident neutron beam wavelength λ_i = 3.12 Å), indicating the absence of long range magnetic order in $Er_2Ir_2O_7$ at least for the Er sublattice. However, the existence of short range correlations, evidenced by the presence a large bump around Q = 1.15 $Å^{-1}$, is observed as the temperature is lowered. These correlations are likely related to Er-Er interactions.

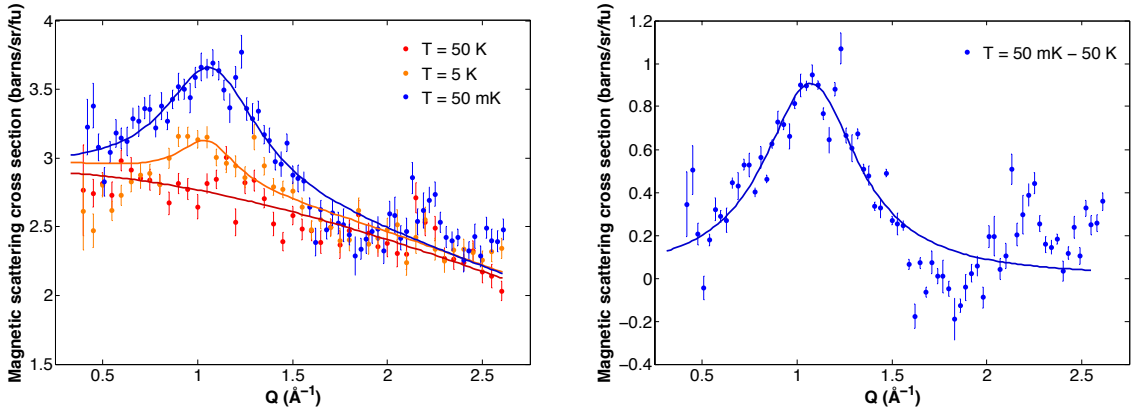

Figure 4.14 – *(right) Diffuse magnetic scattering cross section for $Er_2Ir_2O_7$ measured between 0.05 K and 50 K on D7 using XYZ polarization analysis. The lines are guide to the eye. (left) Diffuse magnetic scattering measured by neutron scattering at 0.05 K after subtraction of the high temperature reference data (T=50 K). Note that a small signal is also observed around 2.2 $Å^{-1}$. This corresponds to the position of a nuclear peak and is an artifact of the XYZ polarization analysis.*

The presence of similar spin pair correlations were previously reported in another pyrochlore compound: $Er_2Sn_2O_7$ (see Fig. 4.15) [SSW+11, GPL+13]. This compound presents only one magnetic ion: Er^{3+}. It does not show any long range magnetic ordering down to 100 mK but exhibits a freezing

around 200 mK observed by ZFC-FC magnetization measurements similarly to $Er_2Ir_2O_7$. The diffuse scattering at low temperature measured by neutron scattering is well reproduced considering the presence of short range correlations associated to special Palmer-Chalker spin configurations (see ψ_3 configuration in Fig. 4.15). This order is associated to a single representation authorized by symmetry for a $\mathbf{k}$ = (0, 0, 0) propagation vector and described by the τ_3 irreducible representation in Table 4.3 (it is called Γ_7 in [GPL+13]). The other magnetic configuration ψ_2 belongs to the τ_2 IR (Γ_5 in [GPL+13]) and corresponds to the magnetic order of the Er^{3+} magnetic moments in $Er_2Ti_2O_7$. Note that the Hamiltonians involving anisotropic exchange determined in $Er_2Ti_2O_7$ [SRG+12, BPM+13] and in $Er_2Sn_2O_7$ [GPL+13] allows to understand the different behaviors between these two compounds. In $Er_2Sn_2O_7$, a Palmer-Chalker magnetic order is predicted below ≈ 0.2 K [YBJS13]. Experimentally, only short range correlations are observed down to 0.1 K where it orders in the Palmer-Chalker configuration[1]. Due to the similarity with the diffuse scattering in $Er_2Sn_2O_7$, the behavior of $Er_2Ir_2O_7$ could thus also be explained by invoking Er-Er short-range correlations possibly corresponding to these Palmer-Chalker configurations. It remains puzzling that this compound orders at such a low temperature. The invoked reason is that the system is close to a quantum phase transition preventing its ordering [YBJS13] but it remains an open question whether this is the case of $Er_2Ir_2O_7$.

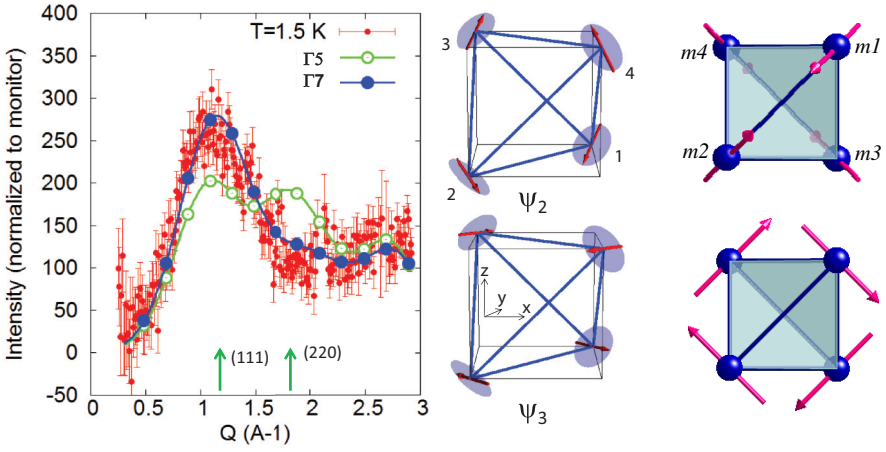

Figure 4.15 – *Left: Diffuse magnetic scattering measured on $Er_2Sn_2O_7$ by neutron scattering at 1.5 K. High temperature reference data (T=50 K) have been subtracted. The lines are the results of a fit assuming either the $\psi_2 - \Gamma_5$ (green open circles) or the $\psi_3 - \Gamma_7$ (blue solid circles) structure. Middle: Magnetic configurations ψ_2 and ψ_3. From [GPL+13]. Right: Visualization of the spin configuration in the (yz) plane from [PWLB07]*

The contrasting behavior between $Tb_2Ir_2O_7$ and $Er_2Ir_2O_7$ can finally be understood by considering the difference of magnetocrystalline anisotropy between the two rare-earth ions. In the case of Tb^{3+}, the easy axis anisotropy is compatible with the Ir molecular field which induces the AIAO Tb magnetic order. Assuming that the Ir sublattice displays the same ordering in $Er_2Ir_2O_7$, the Ir molecular field is in this case perpendicular to the easy plane anisotropy of the Er^{3+} ions. Thus, these two would compete, prohibiting any Er magnetic ordering until Er-Er interactions step in at low temperature. This also allows explaining the ZFC-FC difference observed for $Er_2Ir_2O_7$, considering the presence of defects. Indeed, by shifting the molecular field away from the $\langle 111 \rangle$ direction (see Fig. 4.11), it will allow the Er magnetic moment to be polarized along the perpendicular component of this molecular

[1] private discussion with E. Lhotel

field.

In summary, $Er_2Ir_2O_7$ exhibits magnetic ordering of the Ir sublattice around 140 K. The Er sublattice does not present any long range order down to 50 mK. However, the presence of a magnetic freezing and of short range correlations that might emerge from Palmer-Chalker configurations are observed at low temperature. These correlations are accountable to the Er local easy plane magnetism arising from Er-Er interactions.

Although $Er_2Ir_2O_7$ presents magnetic properties drastically different from $Tb_2Ir_2O_7$, both are compatible with an AIAO ordering of the Ir sublattice and can be explained by the change of magnetocrystalline anisotropy between the two rare-earth ions. This anisotropy will either compete against or be consistent with the direction of the Ir molecular field.

4.4.3 Symmetry analysis

In order to better understand the absence of magnetic ordering in $Er_2Ir_2O_7$ despite the Er-Ir coupling, it is relevant to determine which of these interactions are allowed by symmetry.

Each Rare-earth-Iridium pair is along a two-fold axis (see Fig. 4.16), thus the point group symmetry at the center of the pair is 2.

Figure 4.16 – *Sketch of two neighboring rare-earth and iridium ions with the symmetry elements.*

Taking into account the action of the 2-fold axis on symmetric $J = \begin{pmatrix} J_{xx} & J_{xy} & J_{xz} \\ J_{xy} & J_{yy} & J_{yz} \\ J_{xz} & J_{yz} & J_{zz} \end{pmatrix}$ and antisymmetric $\vec{D} = \begin{pmatrix} D_x \\ D_y \\ D_z \end{pmatrix}$ exchange interactions, the interaction tensor in the local basis $(\hat{\mathbf{x}}, \hat{\mathbf{y}}, \hat{\mathbf{z}})$, attached to the R-Ir pair (see Fig. 4.16), is written as:

$$J_{loc} = \begin{pmatrix} J_{xx} & 0 & 0 \\ 0 & J_{yy} & J_{yz}+D_x \\ 0 & J_{yz}-D_x & J_{zz} \end{pmatrix} \tag{4.1}$$

We can rewrite this tensor in the basis attached to the cubic unit cell $(\hat{\mathbf{i}}, \hat{\mathbf{j}}, \hat{\mathbf{k}})$:

$$J_{cub} = \frac{1}{6} \begin{pmatrix} J_2 & J_4+3\sqrt{2}D & J_4+3\sqrt{2}D \\ J_4-3\sqrt{2}D & J_1 & J_3 \\ J_4-3\sqrt{2}D & J_3 & J_1 \end{pmatrix}, \tag{4.2}$$

with

$$\begin{cases} J_1 &= 3J_{xx} + J_{yy} + 2J_{zz} - 2\sqrt{2}J_{yz} \\ J_2 &= 4J_{yy} + 2J_{zz} + 4\sqrt{2}J_{yz} \\ J_3 &= -3J_{xx} + J_{yy} + 2J_{zz} - 2\sqrt{2}J_{yz} \\ J_4 &= -2J_{yy} + 2J_{zz} + \sqrt{2}J_{yz} \end{cases}$$

Considering one rare-earth ion, its nearest neighbors are six iridium forming a hexagon (see

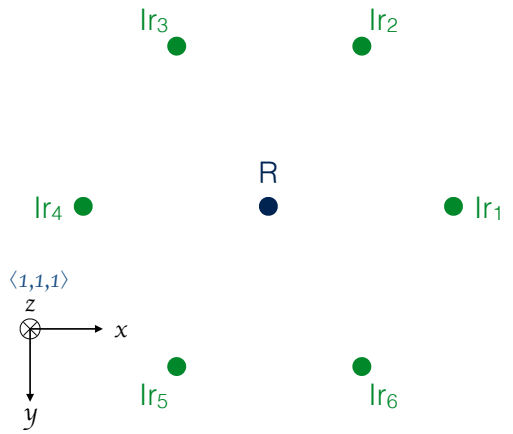

Figure 4.17 – *Sketch of one rare-earth ion surrounded by its first nearest neighbors: six iridium ions arranged on a hexagon.*

Fig. 4.17). Assuming that the interaction between R and one first neighbor Ir is described by J_{cub}, the interactions with the five other first neighbors Ir can be deduced by symmetry.

When summing all the R-Ir contributions over the six Ir neighbors, all exchange terms cancel out in the Hamiltonian, i.e. $\sum_i \vec{S}_R \cdot J_{R-Ir_i} \cdot \vec{S}_{Ir_i} = 0$ for an in-plane R magnetic moment. Therefore there cannot be any energy gain through the R-Ir magnetic coupling that could favor the system energy for rare-earth ion with a perfect easy plane anisotropy.

Up to now, we have established that an AIAO order of the Ir sublattice is compatible with the magnetic behavior of the rare earth sublattice in the Nd, Tb and Er compounds. We can assume that the other pyrochlore iridate compounds display the same Ir AIAO magnetic order. In order to check this assumption we have then studied other pyrochlore iridates considering rare-earth with different magnetocrystalline anisotropy:

- easy axis anisotropy along the ⟨111⟩ direction: Ho and Dy. A behavior similar to the Tb- or Nd-based compounds is expected resulting in an AIAO induced magnetic ordering of the rare-earth sublattice due to Ir molecular field.
- easy plane anisotropy perpendicular to the ⟨111⟩ direction: Yb. No long range magnetic order is expected similarly to the Er-based compound, down to the temperature at which rare-earth−rare-earth interactions come into play.
- isotropic rare-earth: Gd, with zero orbital magnetic moment at a first order. As the Gd^{3+} magnetic moments do not display any preferred orientation, they should be easily polarized by the Ir molecular field leading to an induced AIAO magnetic order of the rare-earth sublattice.

4.5 $R_2Ir_2O_7$ (R = Ho, Dy, Yb, Gd)

In this section, I will present the study of the magnetic properties of these compounds, starting with the magnetization measurements performed on commercial QD SQUID magnetometers between 2 and 200 K. Then I will present the neutron powder diffraction experiments which were performed on two diffractometers at the Institut Laue-Langevin. The D1B diffractometer (coll. C. Colin) was used for rare-earths with a small absorption cross section for thermal neutrons (wavelength of the incoming

neutron beam $\lambda = 2.52$ Å). This is the case for Ho, Yb and isotopic ^{160}Gd. For the other rare-earths (Dy and natural Gd), the measurements were performed on the D4c hot neutron diffractometer (coll. H. Fisher) with incoming neutron wavelength $\lambda = 0.5$ Å, at which the absorption cross sections of these two rare-earths are strongly reduced.

R^{3+}	Electronic configuration	S	L	J	$g_J J$ (μ_B)	Expected anisotropy	Lattice parameter (Å)
Ho^{3+}	$4f^{10}$	2	6	8	10	Easy-axis $\parallel \langle 111 \rangle$	10.1859(2)
Dy^{3+}	$4f^{9}$	$5/2$	5	$15/2$	10	Easy-axis $\parallel \langle 111 \rangle$	10.2309(5)
Yb^{3+}	$4f^{13}$	$1/2$	3	$7/2$	4	Easy-plane $\perp \langle 111 \rangle$	10.1025(2)
Gd^{3+}	$4f^{7}$	$7/2$	0	$7/2$	7	Isotropic	10.281(3)

Table 4.5 – *Details of the electronic configuration and of the spin, angular and total angular momentum of the Ho^{3+}, Dy^{3+}, Yb^{3+} and Gd^{3+} ions. The expected anisotropy of the rare-earth ions and the cubic lattice parameter of the $R_2Ir_2O_7$ compounds are also given.*

4.5.1 Magnetization measurements

Figures 4.19 to 4.21 show the magnetization measurements of the (Dy, Ho, Yb, Gd)$_2$Ir$_2$O$_7$ compounds: temperature dependence of the magnetic susceptibility M/H and field dependence of the magnetization.

All of them display similar magnetic susceptibility measurements: a ZFC-FC difference is observed at respectively, 120, 140, 145 and 120 K for the Ho-, Dy-, Yb- and Gd-based compounds that is indicative of the Ir sublattice magnetic ordering. Below this temperature, both curves increase down to 2 K without any sign of saturation, the FC curve remaining above the ZFC one. This is also consistent with measurements previously reported by Matsuhira *et al.* [MWHT11]. A difference between the different compounds is observed in the amplitude of the ZFC-FC opening: while it is hardly visible for the Ho, Dy and Gd compounds, the Yb one exhibits a much larger difference. This observation is consistent with the previous measurements: indeed for the Tb compound the opening was also smaller compared to the one for the easy plane Er compound. This could be explained by the difference of magnetocrystalline anisotropy: rare-earth with an easy plane anisotropy cannot be polarized by the Ir molecular field and are then more easily polarized by an external magnetic field. Note that measurements of the $Dy_2Ir_2O_7$ on a polycrystalline sample have previously been described in the literature [MWH$^+$11]. The reported magnetic susceptibility differs from what we observe. A slight ZFC-FC difference is first observed below 134 K similarly to our compound. Then, on cooling, both the ZFC and FC susceptibilities display a broad maximum at 4.5 K that is absent in our measurements.

Concerning the $M(H)$ measurements for $Ho_2Ir_2O_7$ the magnetization shows a tendency to saturation at high magnetic field and at the lowest temperature (2 K) with a magnetization of 9.8 μ_B/f.u. at 5 T (see right part of Fig. 4.18). This is about half the value expected for the saturated moment of the Ho^{3+} ions, namely 20 μ_B/f.u. since each free Ho^{3+} ions display a magnetic moment of 10 μ_B (see Table 4.5).

Looking at the magnetization of $Dy_2Ir_2O_7$ (right part of Fig. 4.19), a 8.2 μ_B/f.u. magnetization plateau is reached at 5 T and 2 K. The Dy^{3+} free ions display a similar magnetic moment to the Ho^{3+}

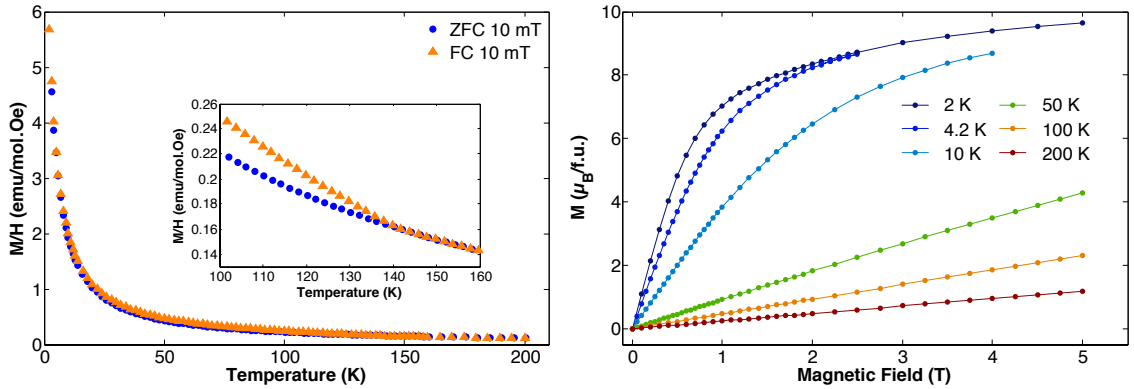

Figure 4.18 – *(left) M/H versus T for $Ho_2Ir_2O_7$ measured after a ZFC (in blue) and a FC (in orange) procedure in 0.01* T. *Inset: zoom of the ZFC-FC opening happening around 140* K. *M versus H for $Ho_2Ir_2O_7$ measured at different temperatures.*

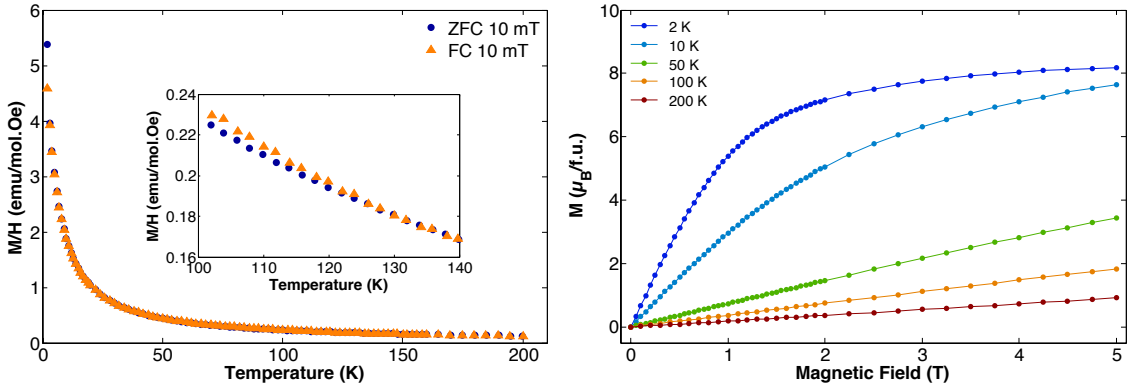

Figure 4.19 – *(left) M/H versus T for $Dy_2Ir_2O_7$ measured after a ZFC (in blue) and a FC (in orange) procedure in 0.01* T. *Inset: zoom of the ZFC-FC opening happening around 120* K. *(right) M versus H for $Dy_2Ir_2O_7$ measured at different temperatures.*

ones, although a saturated magnetization around 20 μ_B/f.u. is also expected.

Similarly, $Yb_2Ir_2O_7$ seems to approach a magnetization plateau of 3.5 μ_B/f.u. at 2 K but not yet reached at 5 T. The expected saturated magnetization is 6 μ_B/f.u. in this case as Yb^{3+} ions in their doublet ground state display a magnetic moment of 3 μ_B in the titanate and stannate pyrochlores [HBF+01, YDdRB+13].

These three compounds (Ho, Dy and Yb) exhibit a magnetization plateau at almost half the value of the expected saturated magnetization and a linear behavior of the magnetization with the applied magnetic field from 50 K up to room temperature. This magnetization plateau was actually expected in the case of the Ho and Dy. Indeed it has been calculated for antiferromagnetic Ising spins on a pyrochlore lattice by Harris *et al.* [HBHC98] due to the strong easy axis anisotropy preventing the magnetic moments to get aligned with the magnetic field. Therefore the measured magnetization corresponds to the projection of the ordered magnetic moments in the plane containing the magnetic field direction. The magnetization plateau at less than half the expected saturated moment is also observed in $Yb_2Ir_2O_7$ although the Yb ions present an easy-plane anisotropy and translates the fact that the Yb ion is not purely easy plane. It has also been observed in $Yb_2Ti_2O_7$ [LGL+14].

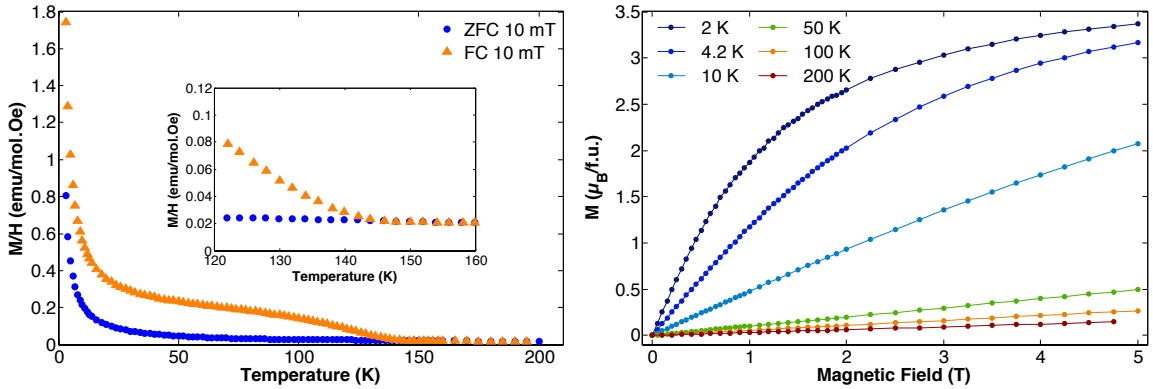

Figure 4.20 – *(left) M/H versus T for $Yb_2Ir_2O_7$ measured after a ZFC (in blue) and a FC (in orange) procedure in 0.01* T. *Inset: zoom of the ZFC-FC opening happening around 145* K. *(right) M versus H for $Yb_2Ir_2O_7$ measured at different temperatures.*

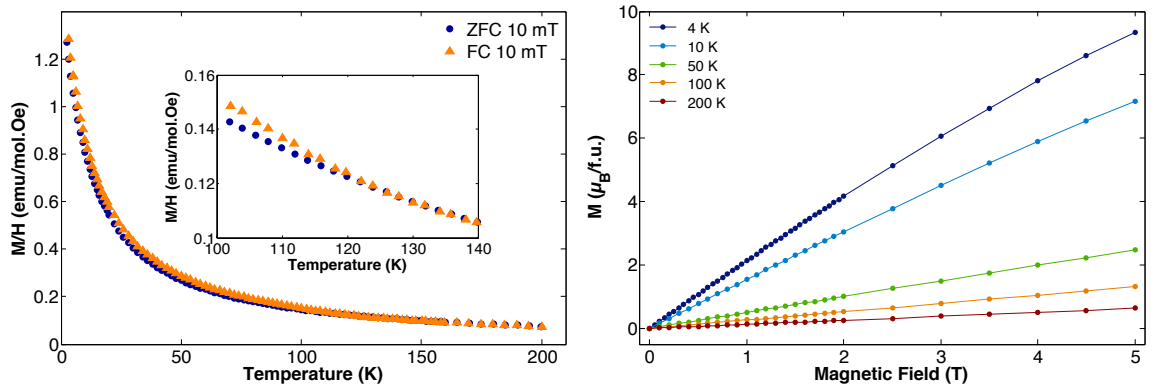

Figure 4.21 – *(left) M/H versus T for $Gd_2Ir_2O_7$ measured after a ZFC (in blue) and a FC (in orange) procedure in 0.01* T. *Inset: zoom of the ZFC-FC opening happening around 120* K. *(right) M versus H for $Gd_2Ir_2O_7$ measured at different temperatures.*

$Gd_2Ir_2O_7$ shows a slightly different behavior. The magnetization is still increasing with a quasi constant slope at 5 T and 2 K, indicating that the saturated magnetization will be reached for a much higher magnetic field (see Fig. 4.21). Besides, the Gd saturated magnetic moment is 7 μ_B and we can expect a maximum of 14 μ_B/f.u for the saturated magnetization of $Gd_2Ir_2O_7$. Thus there is no sign of a magnetization plateau around half the saturated magnetization as observed for the 3 previous compounds in agreement with the expected isotropy of the Gd ion.

4.5.2 Neutron Powder Diffraction

Neutron powder diffraction experiments have been performed on the Ho-, Dy-, Yb- and Gd-based compounds in order to probe the rare-earth magnetic structure and therefore confirm indirectly the AIAO Ir magnetic order from the Ir−rare-earth coupling.

The Ho compound was measured on the D1B diffractometer. Diffractograms were recorded every 1 K from 3 K to 200 K. Figure 4.22 shows the temperature dependence of the diffractograms. Additional Bragg peaks are observed below 50 K and are indexable with a **k** = (0, 0, 0) propagation vector.

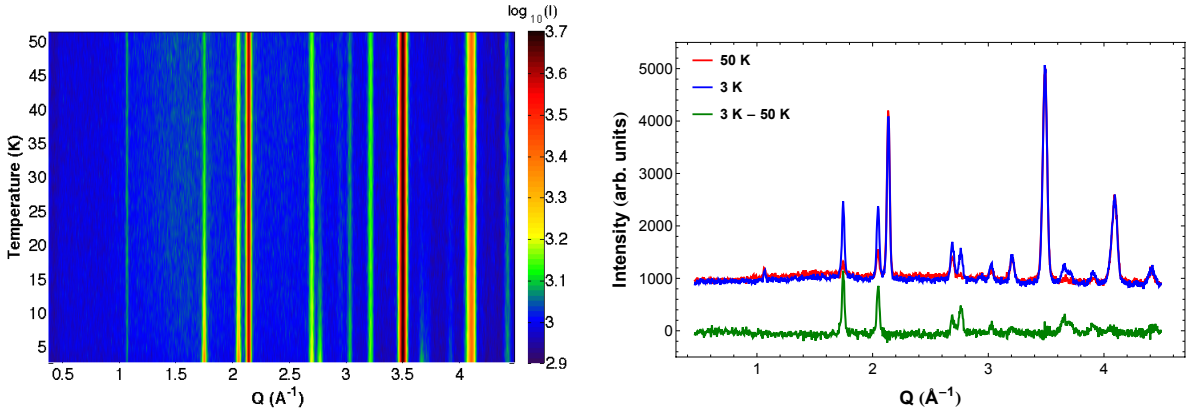

Figure 4.22 – *(left) Thermodiffractogram recorded for $Ho_2Ir_2O_7$ between 3 and 50* K*. (right) Neutron diffractograms recorded at 1.5 (blue line) and 50* K *(red line). The difference between the 1.5* K *and 50* K *data is show in green.*

Similarly to $Tb_2Ir_2O_7$, the irreducible representation allowing us to refined the data corresponds to an AIAO magnetic configuration of the Ho sublattice, as expected considering the magnetocrystalline anisotropy of the Ho^{3+} ions. Moreover, the temperature evolution of the refined Ho magnetic moment (see Fig. 4.23) indicates that its ordering is induced in the same way than the Tb one. At 1.5 K, a magnetic moment of 5.03(3) μ_B is refined.

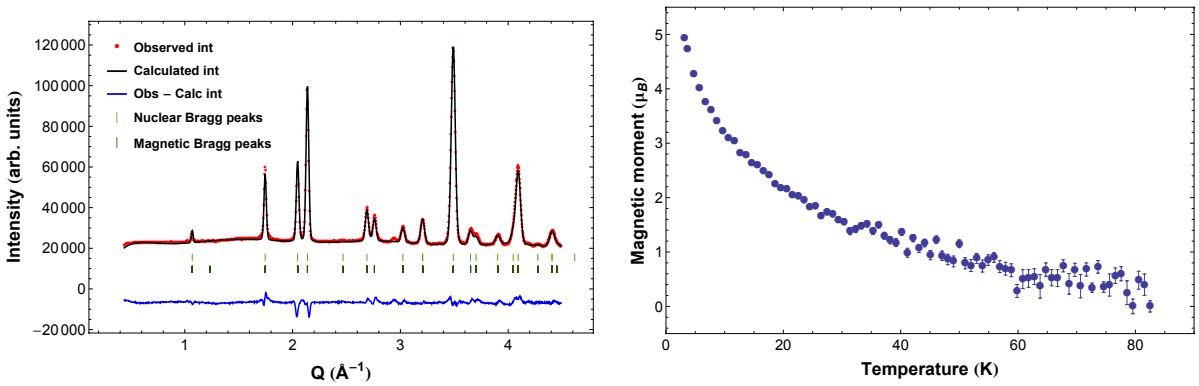

Figure 4.23 – *(left) Neutron diffractogram recorded for $Ho_2Ir_2O_7$ at 3* K *(red dots). The black line represents the calculated intensity using the AIAO model for the Ho magnetic order. (right) Temperature evolution of the refined Ho^{3+} magnetic moment using the AIAO model.*

For $Dy_2Ir_2O_7$, the D4c diffractometer was used to perform the experiment. Diffractograms were recorded between 3 K and room temperature. In the same way than the Ho and Tb pyrochlore compounds, additional Bragg peaks are observed at low temperature (see Fig. 4.24), corresponding to an AIAO magnetic order of the Dy moments. The refinement of the 3 K data gives a Dy magnetic moment of 5.60(3) μ_B.

These two compounds, presenting rare-earth with an easy axis magnetocrystalline anisotropy, display an induced AIAO magnetic order on the rare-earth sublattice, similarly to $Tb_2Ir_2O_7$. These first two results are so far consistent with the assumption of an AIAO Ir order in the whole pyrochlore iridates family.

We then studied the $Yb_2Ir_2O_7$ compound, in which the Yb^{3+} ion is expected to present an easy

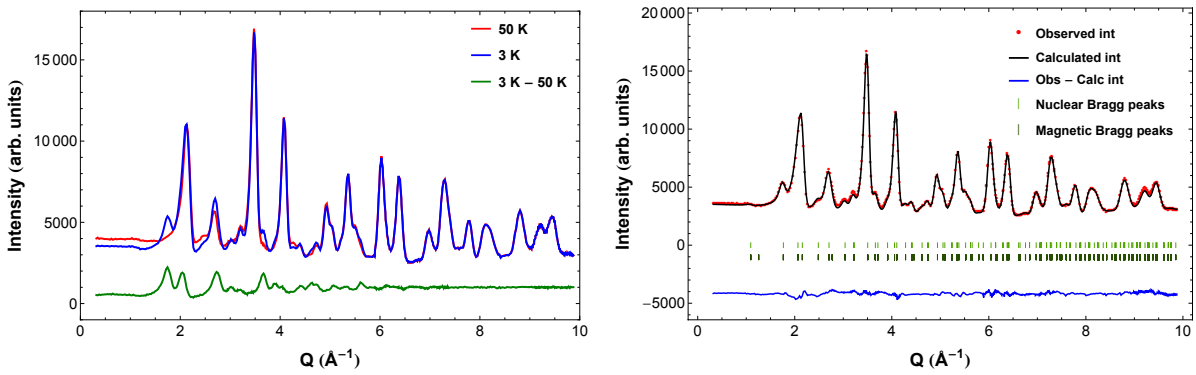

Figure 4.24 – *(left) Neutron diffractograms recorded for $Dy_2Ir_2O_7$ at 3 (blue line) and 50* K *(red line). The difference between the 3* K *and 50* K *data is shown in green. (right) Neutron diffractogram recorded at 3* K *(red dots) and calculated intensity (black line) using the AIAO model for the Dy magnetic order.*

plane anisotropy. Figure 4.25 shows the diffractograms recorded at 1.5, 50 and 200 K as well as the difference between the low temperature and the 50 K diffractograms. No additional intensity is observed as the temperature is lowered indicating the absence of long range order of the Yb sublattice. The small peaks observed in the 1.5 - 50 K difference around 2.2, 3.5 and 4.2 Å^{-1} are due to the different Debye-Waller terms in the nuclear scattering cross section. This result is consistent with what we found in $Er_2Ir_2O_7$ and with an Ir AIAO configuration in $Yb_2Ir_2O_7$ as well.

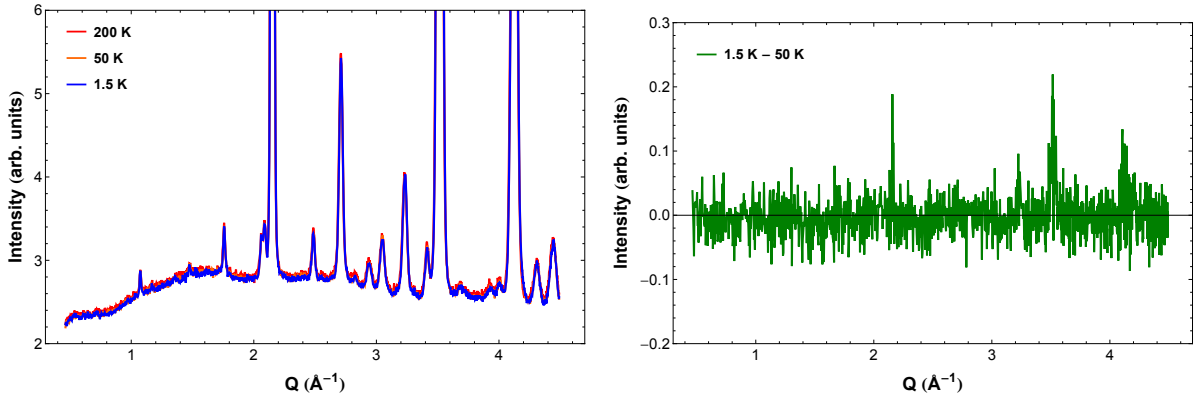

Figure 4.25 – *(left) Neutron diffratograms recorded for $Yb_2Ir_2O_7$ at 1.5 (blue), 50 (orange) and 200* K *(red). (right) Difference between the 1.5 and 50* K *data.*

Last, the magnetic order of the Gd sublattice in $Gd_2Ir_2O_7$ was studied similarly to the previous compounds. The neutron powder diffraction measurements were first performed on a natural Gd-based compound using the D4c diffractometer considering the huge absorption cross section of Gd for thermal neutrons (see Table 4.6).

Figure 4.26 shows the diffractograms recorded between 3 K and 200 K. Additional intensity is observed as the temperature is lowered indicating that the Gd magnetic moments order. Looking at the difference between the low temperature and 50 K (see Fig. 4.27) magnetic Bragg peaks are observed for wavevector transfer $\mathbf{Q} > 1.5$ Å^{-1} at the same positions than for the Tb, Ho and Dy-based pyrochlores, indicating a possible AIAO magnetic order of the Gd sublattice. To our surprise a broader peak is also observed in the lower $\mathbf{Q}$ region, for $\mathbf{Q} \approx 1.15$ Å^{-1}. This signal rises at the same temperature as the

Neutron absorption cross section	Thermal neutrons $\lambda = 1.8$ Å	Cold neutrons $\lambda = 0.5$ Å
natural Gd	49700	500
^{160}Gd	0.77	0.21

Table 4.6 – *Neutron absorption cross section of the natural and isotopic Gd element for the wavelengths used on D1B and D4c.*

magnetic Bragg peaks but is not accounted for by the AIAO model.

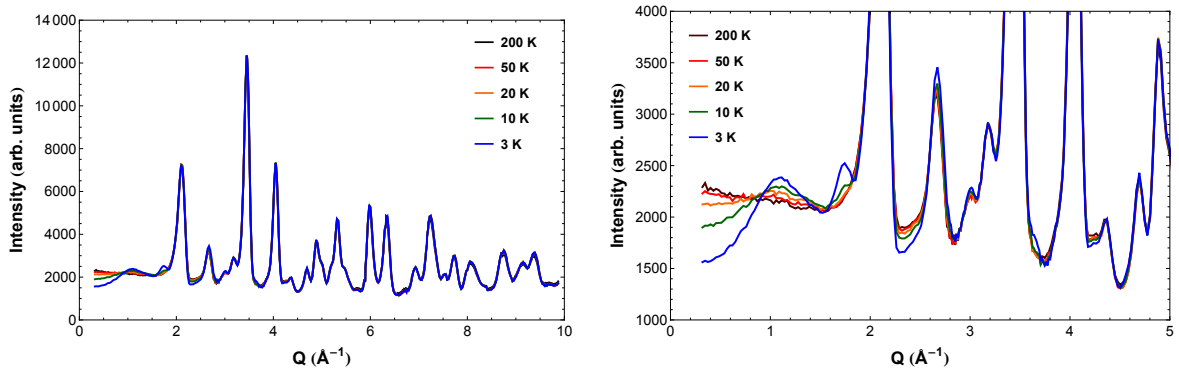

Figure 4.26 – *(left) Neutron diffractograms recorded for $Gd_2Ir_2O_7$ between 3 K and 50 K on D4c. (right) Zoom of the diffractograms for* **Q** *< 5 Å.*

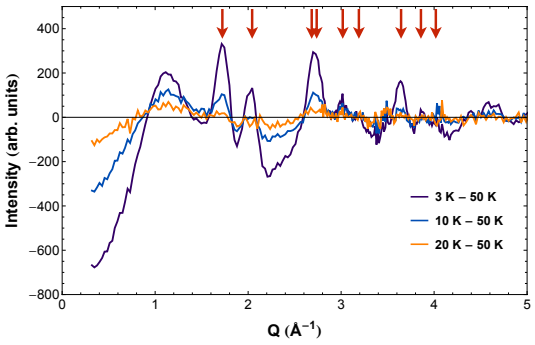

Figure 4.27 – *Difference between the diffractograms recorded at 3, 10 and 20 K and the diffractogram recorded at 50 K on D4c for $Gd_2Ir_2O_7$. The arrows indicate the position of the expected Bragg peaks for an AIAO arrangement of the Gd magnetic moments.*

Having synthesized a small amount of isotopic $^{160}Gd_2Ir_2O_7$, we performed an additional neutron powder diffraction experiment using the D1B diffractometer which has a better **Q** resolution. Left part of figure 4.28 shows the difference between the diffractograms recorded at 3 K and 50 K for the isotopic compound. First, the same magnetic Bragg peaks are observed at the same position in both diffractograms. These magnetic peaks are refined using an AIAO magnetic order, leading to a value of 4.2 μ_B at low temperature for the ordered Gd magnetic moment (see right part of Fig. 4.28). As the Gd^{3+} magnetic moment is assumed to be isotropic in first approximation, this AIAO order was expected and is another proof of the AIAO order of the Ir sublattice in this family.

The better resolution of D1B also allows us to interpret the additional signal observed at $\mathbf{Q} \approx 1.15$ Å^{-1}. This signal is very broad in $\mathbf{Q}$, and is indicative of the presence of short range correlations in $Gd_2Ir_2O_7$.

We have to note that these correlations appear at the same temperature as the AIAO magnetic Bragg peaks. It is rather surprising to observe the coexistence of both a long range order and short range correlations rising at the same temperature. Moreover, the short range correlations look similar to those observed in the Er compound, which presents an easy plane of anisotropy perpendicular to the direction of the Ir molecular field. A priori similar behaviors between $Er_2Ir_2O_7$ and $Gd_2Ir_2O_7$ were not expected since Gd^{3+} ion is assumed magnetically isotropic.

However, we have to take into account that the isotropic nature of the Gd^{3+} ions is only true to a first order since the first excited state is at an energy of 4 eV ($\approx 46.4 \times 10^3$ K) [Wyb66]. A study of the $Gd_2Ti_2O_7$ and $Gd_2Sn_2O_7$ pyrochlore compounds showed that the Gd^{3+} ions are actually slightly anisotropic with an easy plane anisotropy perpendicular to the $\langle 111 \rangle$ direction. Using a simplified model taking into account nearest-neighbor exchange and a staggered planar anisotropy, an anisotropy constant of 0.223 K and 0.140 K for $Gd_2Ti_2O_7$ and $Gd_2Sn_2O_7$ respectively was determined[GZS+07]. Thus, it is not excluded that the small Gd anisotropy could lead to this coexistence of phases. One last point to be noted is that in $Er_2Ir_2O_7$, short range correlations are observed only at very low temperature as they are due to the Er-Er interactions which are quite small, while in $Gd_2Ir_2O_7$ they appear at the same temperature than the long range order. Therefore it may be related in some way to the Gd-Ir interactions rather than to the Gd-Gd interactions.

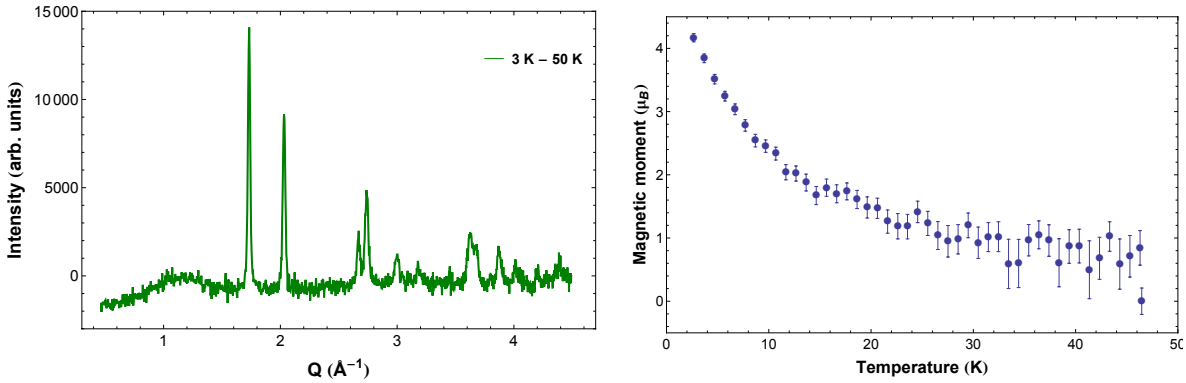

Figure 4.28 – *(left) Difference between the diffractograms recorded at 3 and 50 K on D1B. (right) Temperature evolution of the refined Gd^{3+} magnetic moment using the AIAO model.*

In order to get better insight on the magnetic correlations, one can also perform magnetic Pair Distribution Function (mPDF) analysis [FYB14]. mPDF is obtained experimentally by Fourier transforming the magnetic scattering intensity from the neutron powder diffractograms. mPDF reveals local magnetic correlations directly in real space. Besides, the mPDF technique does not differentiate between diffuse and Bragg scattering, so it also provides sensitivity to both short- and long-range magnetic order. This will give positive (resp. negative) peaks at distance corresponding to spin pair separation for ferromagnetic-like (resp. antiferromagnetic-like) correlations in the direction perpendicular to the spin pair bond.

mPDF analysis was performed for both $Dy_2Ir_2O_7$ and $Gd_2Ir_2O_7$ using the difference between the 3 K and 50 K diffractograms recorded on D4c. The Dy compound, perfectly ordered in the AIAO configuration, is used as a reference for comparison with the Gd compound (see Fig. 4.29). The Fourier

transform was performed on the data for **Q** from 0 to 10 $Å^{-1}$, corresponding to the **Q** range which gives the best data in the real space. The low r region ($r < 2$ Å), is not relevant to the physics of the system since it is greatly dependent on the size of the **Q** region chosen to perform the Fourier transform.

A difference is observed between the two compounds at a distance $r \approx 3.6$ Å. This distance corresponds to the distance between two nearest R or Ir neighbors but also to nearest R-Ir neighbors (distance denoted d_1 in the sketch in Fig. 4.29). However, considering that we are looking at the spin pair correlation function and that the Ir magnetic moment is smaller than 0.1 μ_B, we have $\langle \vec{S}(R) \cdot \vec{S}(R) \rangle > \langle \vec{S}(R) \cdot \vec{S}(Ir) \rangle \gg \langle \vec{S}(Ir) \cdot \vec{S}(Ir) \rangle$. Therefore it can be safely assumed that we are mostly sensitive to the R-R or R-Ir spin pair correlations, and that there is a change in these correlations between the Dy and Gd compounds.

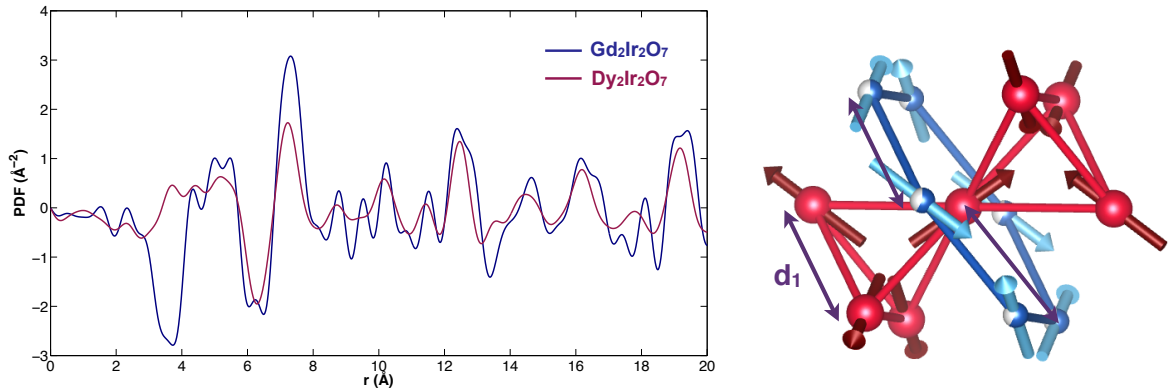

Figure 4.29 – *(left) mPDF of $Dy_2Ir_2O_7$ (purple) and $Gd_2Ir_2O_7$ (blue) obtained by Fourier transforming the experimental magnetic scattered intensity. (right) Sketch of a central R^{3+} ions (central red dot) with its 6 nearest neighbor Ir^{4+} (in blue) and R^{3+} ions (in red). The arrows represent the Gd and Ir magnetic moments arranged in the AIAO magnetic configuration.*

We then tried to find models accounting for the magnetic behavior of the two compounds and performed mDF analysis of the calculated magnetic scattered intensity using these models.

For $Dy_2Ir_2O_7$, a simple AIAO magnetic configuration has been considered giving a good agreement between the experimental and calculated mPDF (see left part of Fig. 4.30).

For $Gd_2Ir_2O_7$, we used a model taking into account both an AIAO long range order and magnetic short range correlations. Monte Carlo calculations were performed considering the Gd sublattice alone with easy plane magnetic anisotropy for the Gd magnetic moments and antiferromagnetic Gd-Gd nearest-neighbor interactions. From these calculations, we extracted the spin configuration and calculated the magnetic scattered intensity that would yield neutron powder diffraction. We then used the Fullprof Suite program in order to calculate the scattered magnetic intensity for an AIAO magnetic order of the Gd sublattice. Finally, the mPDF analysis was performed on the weighted sum of these two calculated scattered intensities. Using this phenomenological model, a very good agreement is obtained between the experimental and calculated mPDF (see right part of Fig. 4.30), indicating that this is the right lead in order to understand the physics of $Gd_2Ir_2O_7$. However, the origin of this different behavior for the Gd pyrochlore is still unknown at this stage, especially since, as noted above, due to their temperature range, the spin correlations cannot be a priori explained by Gd-Gd interactions.

In this section, $R_2Ir_2O_7$ compounds with rare-earth displaying various anisotropies were studied.

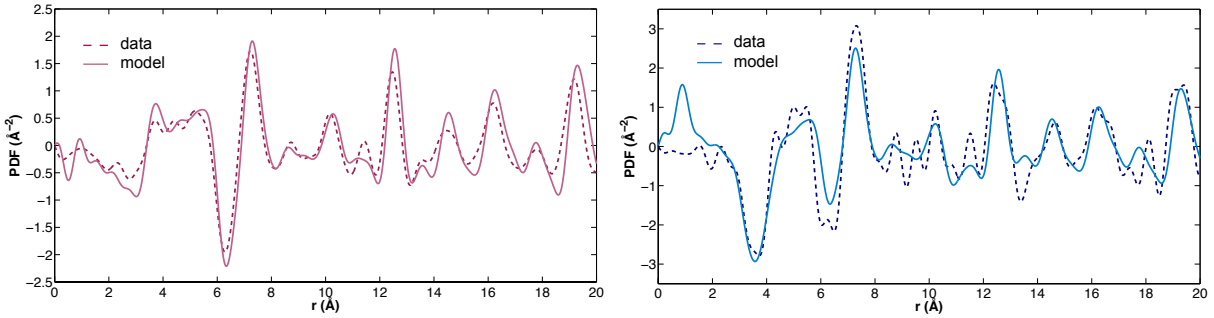

Figure 4.30 – *mPDF of $Dy_2Ir_2O_7$ (left) and $Gd_2Ir_2O_7$ (right) obtained by Fourier transforming the experimental magnetic scattered intensity (plain lines) and the calculated magnetic scattered intensity using models described in the text (dotted lines).*

From the magnetization measurements, we have found that the Ir sublattice orders between 120 and 150 K depending on the considered compound. From the neutron powder diffraction experiments we were able to probe the magnetic order of the rare-earth, which allowed to highlight a systematic behavior depending on the rare-earth magnetocrystalline anisotropy. Besides, all these behaviors are compatible with an all-in/all-out magnetic order of the Ir sublattice: rare-earth ions with easy axis anisotropy display an AIAO induced magnetic order as the Ir molecular field is consistent with their anisotropy while it competes against the easy plane anisotropy for the other rare-earth ions, which thus remain magnetically disordered.

Only the Gd-based compound shows a more complex behavior with the coexistence of long range and short range correlations. This is so far interpreted as the expression of the small easy plane anisotropy of the Gd^{3+} ions which seems to affect the Gd-Gd spin-pair correlations.

4.6 Inelastic Neutron Scattering

Having determined the magnetic structure of the $R_2Ir_2O_7$, it is also interesting to look at the excitation spectra of these compounds. This will give insight on two main physical properties: the crystal electric field (CEF) levels giving information about the magnetocrystalline anisotropy of the rare-earth elements and the possible collective magnetic excitations.

To study the excitation spectra of the $R_2Ir_2O_7$ compounds, inelastic neutron scattering (INS) experiments have been performed with J. Ollivier and B. Fåk on three different instruments at the Institut Laue Langevin: IN5, IN6 and IN4. These are three time-of-flight spectrometers (see Chap. 2 for details) working with various wavelengths. This allows probing low-energy excitations with a good energy-resolution together with high-energy excitations (up to 150 meV).

A wavelength $\lambda = 5.1$ Å was used on the IN6 spectrometer with an energy-resolution $\Delta E \approx 0.07$ meV. This gives access to excitations up to 3 meV on the Stokes side (neutron energy loss side). On IN5, an incoming neutron beam with a wavelength $\lambda = 4.8$ Å was used in order to probe the very-low energy excitations (up to 2.5 meV on the Stokes side) with an energy resolution $\Delta E \approx 0.1$ meV. Finally, on IN4, we used several wavelengths [from 0.74 Å ($E_{max} = 135$ meV and $\Delta E \approx 16$ meV) to 2.44 Å ($E_{max} = 12$ meV and $\Delta E \approx 1$ meV)] in order to probe different energy regions.

In this section, I will focus on the results obtained for three compounds: $Tb_2Ir_2O_7$, $Er_2Ir_2O_7$ and

$Gd_2Ir_2O_7$. INS experiments have also been performed on the other compounds (with R = Ho, Dy, Yb), however the data analysis is still ongoing.

Besides the phonon signals, all of these compounds exhibit a few well defined excitations that can be easily interpreted as magnetic excitations from the evolution of their scattering intensity which decreases with the modulus of the wave vector transfer $|\mathbf{Q}|$. It roughly scales as the square of the magnetic form factor of the $4f$ electrons of the R^{3+} ions. Their dispersion is very small and is only observed for some of the low energy levels. This suggests that they mainly account for transitions between single ion energy levels of $4f$ electrons of individual R^{3+} ions splitted by the CEF. Their collective nature arising from the R-Ir and R-R exchange, manifests itself in their weak dispersion and can be considered only in a second stage of a quantitative analysis.

4.6.1 Experimental data

4.6.1.1 $Tb_2Ir_2O_7$

Figures 4.31 to 4.33 show the scattering function S(**Q**, ω) measured for $Tb_2Ir_2O_7$ between 2 and 300 K on IN4 (λ_i = 1.2 Å) and IN5 (λ_i = 4.8 Å).

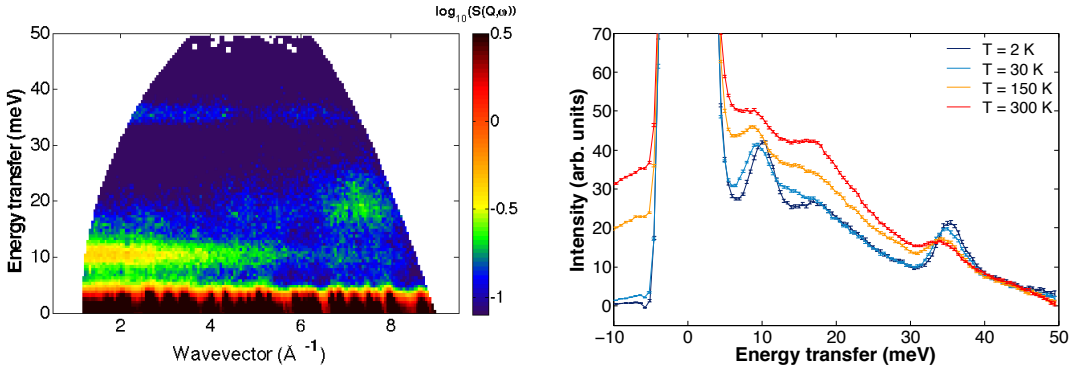

Figure 4.31 – *Inelastic neutron scattering intensity for $Tb_2Ir_2O_7$ at 2 K (left) and intensity summed over Q for temperature between 2 and 300 K (right) measured on IN4.*

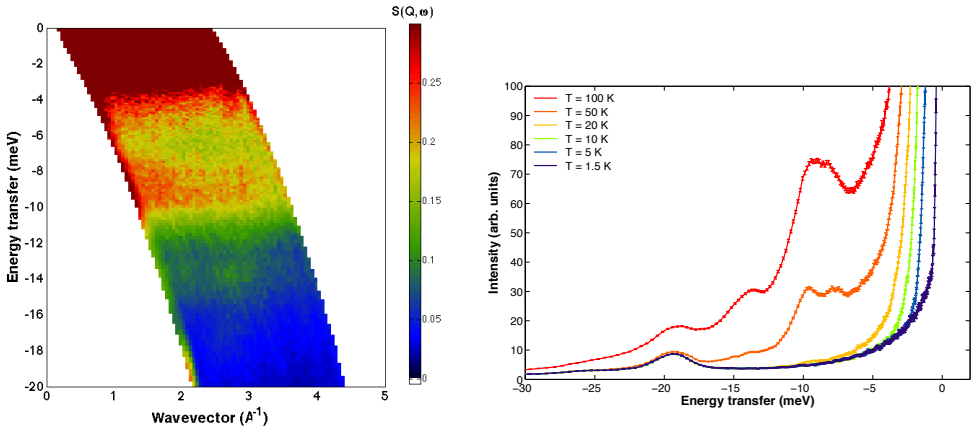

Figure 4.32 – *Inelastic neutron scattering intensity for $Tb_2Ir_2O_7$ at 100 K (left) and intensity summed over Q for temperature between 1.5 and 100 K (right) measured on IN5.*

At low temperature, several magnetic excitations are observed at 0.4, 1.5, 10, 14 and 35 meV. The

last four excitations are interpreted as transitions between CEF levels as their energies are close to the one observed for similar Tb based pyrochlore compounds: $Tb_2Ti_2O_7$ and $Tb_2Sn_2O_7$ (see Table 4.7) [RPI+16, ZFH+14].

We can also note that at 35 meV, in addition to the CEF level transition there is also the presence of a nuclear signal that is most visible for high value of Q. When integrating the data over the entire Q range, both the intensity of the magnetic and nuclear signals are summed. Moreover as the temperature increases the intensity of the nuclear signal is increased significantly.

Level (meV)	E_1	E_2	E_3	E_4
$Tb_2Ir_2O_7$ (this work)	1.5	10	14	35
$Tb_2Ti_2O_7$ [RPI+16]	1.4	10.2	16.7	42
$Tb_2Sn_2O_7$ [ZFH+14]	1.28	10.55	15.8	34

Table 4.7 – *Energies of the first excited levels reported for $Tb_2Ir_2O_7$ and for different Tb-based pyrochlore compounds for comparison (I only show the most recent results for these two compounds).*

As the temperature increases, several modifications in the INS spectra are observed: the intensity of the lowest CEF transition at 1.5 meV is strongly reduced. This is explained by the fact that the population of the corresponding excited state increases at the expense of the ground state with increasing temperature. Therefore the intensity associated to the transition from the ground state to this level decreases and transitions from this excited level are now allowed. This is shown in Figure 4.32 where an additional excitation is observed around 8 meV corresponding to a transition from the 1.5 to the 10 meV level.

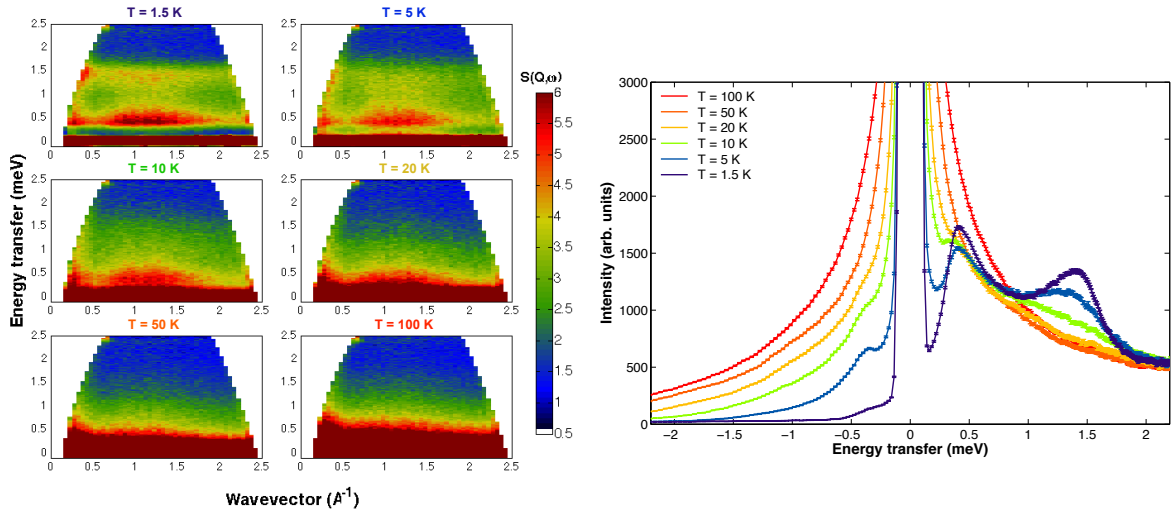

Figure 4.33 – *Inelastic neutron scattering intensity measured for $Tb_2Ir_2O_7$ on IN5 as function of Q and the energy (left) and summed over Q (right) between 1.5 and 100* K.

Concerning the low energy excitation observed at 0.4 meV (see Fig. 4.33), we believe that it corresponds to a splitting of the ground state doublet induced by the Tb-Ir magnetic coupling. At 1.5 K, this excitation is well separated from the ground state and shows non negligible amplitude dispersion along Q, with a maximum of intensity around Q = 1.2 Å^{-1}. When the temperature increases, this excitation merges with the quasi-elastic signal. In addition, the dispersion of this level could be inherited from the dispersion of the Ir magnetic excitation that we do not see in the experiment.

It should be noted however that the ground state doublet is non Kramers. Since the first excited doublet (also non Kramers) is close in energy and the molecular field is large enough to mix these two doublets, the splitting can be attributed to the exchange field. Otherwise it would not be observed by neutron scattering. In $Tb_2Ti_2O_7$ [GGB+01, MBH07] and $Tb_2Sn_2O_7$ [PBM+12] this would have been the case since the molecular field is much weaker. Yet similar splittings were observed in these compounds which has led to propose possible quadrupolar interactions and coupling with vibrations. These are not totally excluded in our Ir-based compounds as well.

4.6.1.2 $Er_2Ir_2O_7$

Figure 4.34 shows the inelastic neutron scattered intensity S(**Q**, ω) recorded for $Er_2Ir_2O_7$ at 1.6 K on IN4 for incoming neutron beam with wavelength of 0.74, 0.9 and 1.6 Å, allowing to probe excitations up to 135, 90 and 27 meV respectively. The INS intensity S(**Q**, ω) recorded on IN6 is shown Figure 4.35.

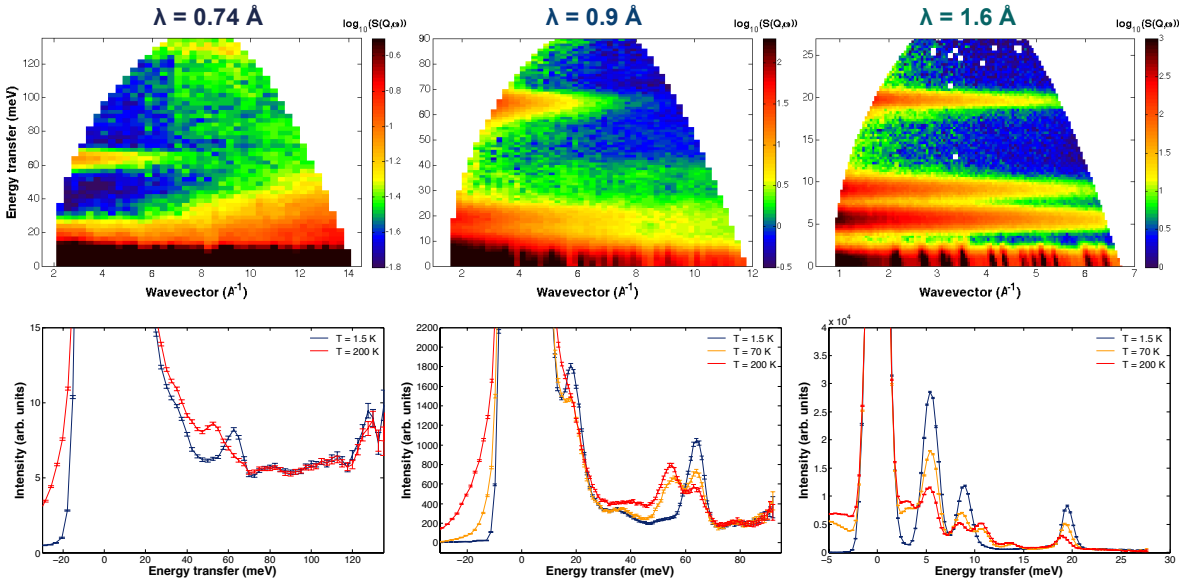

Figure 4.34 – *Inelastic neutron scattering intensity for $Er_2Ir_2O_7$ at 1.5 K (top) and intensity summed over Q for temperature between 1.5 and 200 K (bottom) measured on IN4 for three different wavelengths: 0.74 Å (left), 0.9 Å (middle) and 1.6 Å (right).*

Level (meV)	E_1	E_2	E_3	E_4
$Er_2Ir_2O_7$ (this work)	5.5	9	19.5	64
$Er_2Ti_2O_7$ [CHH+03]	6.3	7.3		
$Er_2Sn_2O_7$ [GPL+13]	5.1	7.6	17.2	

Table 4.8 – *Energies of the first excited levels reported for $Er_2Ir_2O_7$ and for different Er-based pyrochlore compounds for comparison (I only show the most recent results for these two compounds).*

Several excitations can be observed with their energies listed Table 4.8. They are associated to CEF level transitions in the system.

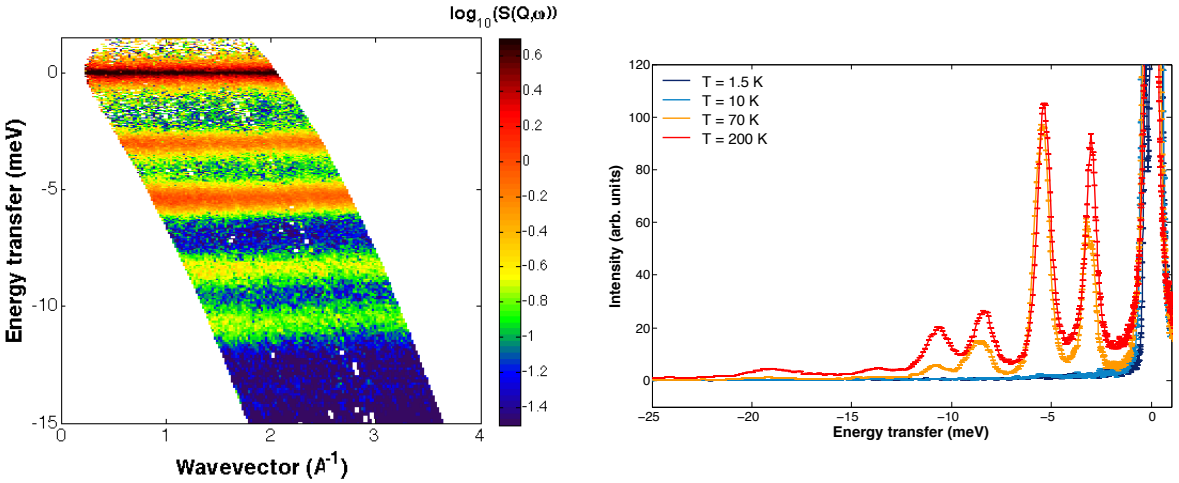

Figure 4.35 – *Inelastic neutron scattering intensity for $Er_2Ir_2O_7$ at 200 K (left) and intensity summed over Q for temperatures between 1.5 and 200 K (right) measured on IN6.*

As the temperature is increased, transitions from the first excited levels are also allowed and can be observed (see Figs. 4.34 and 4.35). In particular excitations are observed at 3, 10.5, 55 meV, corresponding to E_2-E_1, E_3-E_2 and E_4-E_2 respectively.

Finally looking at the low energy part of the INS intensity, an additional excitation is observed at 0.35 meV (see Fig. 4.36). This excitation appears as the temperature is lowered and thus could be explained by the splitting of the doublet ground state CEF level due to the Ir molecular field similarly to the Tb compound which is possible if the anisotropy is not perfectly easy plane. The excitation shows also a strong dispersion along Q with a shape differing slightly from the one in the $Tb_2Ir_2O_7$.

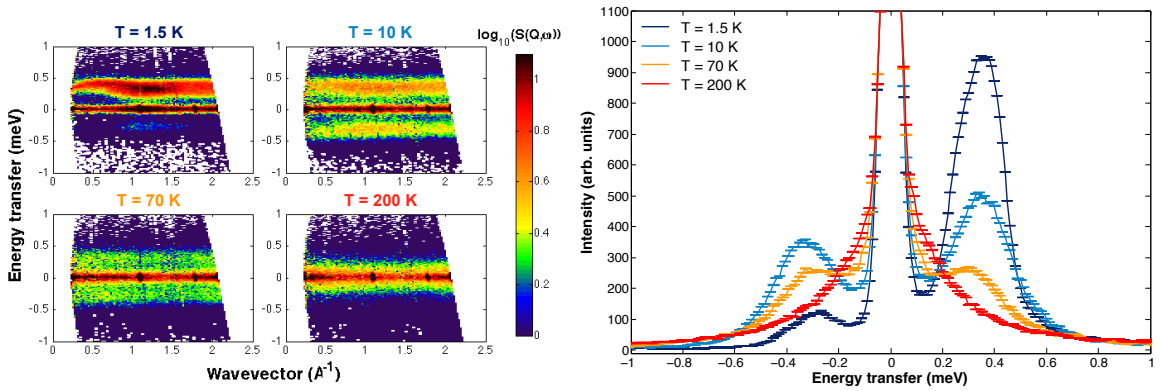

Figure 4.36 – *Inelastic neutron scattering intensity measured for $Er_2Ir_2O_7$ on IN6 as function of Q and the energy (left) and summed over Q (right) between 1.5 and 200 K.*

4.6.1.3 $Gd_2Ir_2O_7$

Finally, INS experiments were performed on $Gd_2Ir_2O_7$ similarly to the previous compounds. As the Gd^{3+} ions are supposed to display a quenched orbital moment, the $4f$ levels should be degenerated and thus no CEF excitations are expected. However, magnetic excitations arising from the coupling between the Gd and the Ir ions are possible and thus low energy excitations similar to the one observed

for $(Er,Tb)_2Ir_2O_7$ could be observed.

Figures 4.37 shows the INS intensity S(**Q**, ω) recorded on IN4 at 1.5 K for incoming neutron beam with wavelength of 0.9, 1.2 and 2.44 Å. No magnetic excitations are observed up to 90 meV as expected.

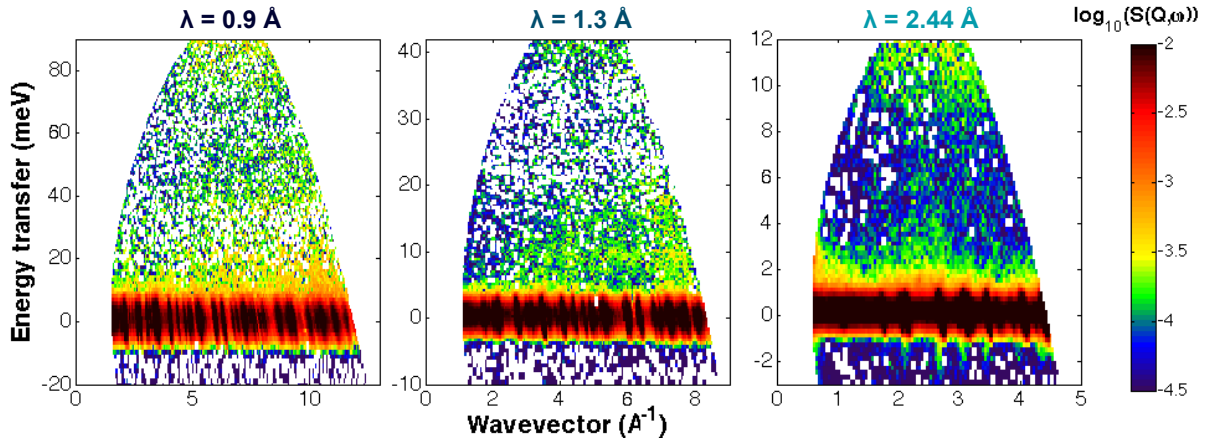

Figure 4.37 – *Inelastic neutron scattering intensity for $Gd_2Ir_2O_7$ at 1.5 K measured on IN4 for three different wavelengths: 0.9 Å (left), 1.3 Å (middle) and 2.44 Å (right).*

However looking at the low energy part of the INS intensity that was recorded on IN6, a magnetic excitation is observed around 0.3 meV. This excitation appears below 150 K and displays a strong modulation in Q that is similar to the one observed for $Er_2Ir_2O_7$. Therefore this excitation is associated to the influence of the Ir molecular field on the $4f$ levels of the Gd^{3+} ions. Besides, the strong similitude with the Er compound, reinforces the assumption that the Gd ions might display a small XY anisotropy.

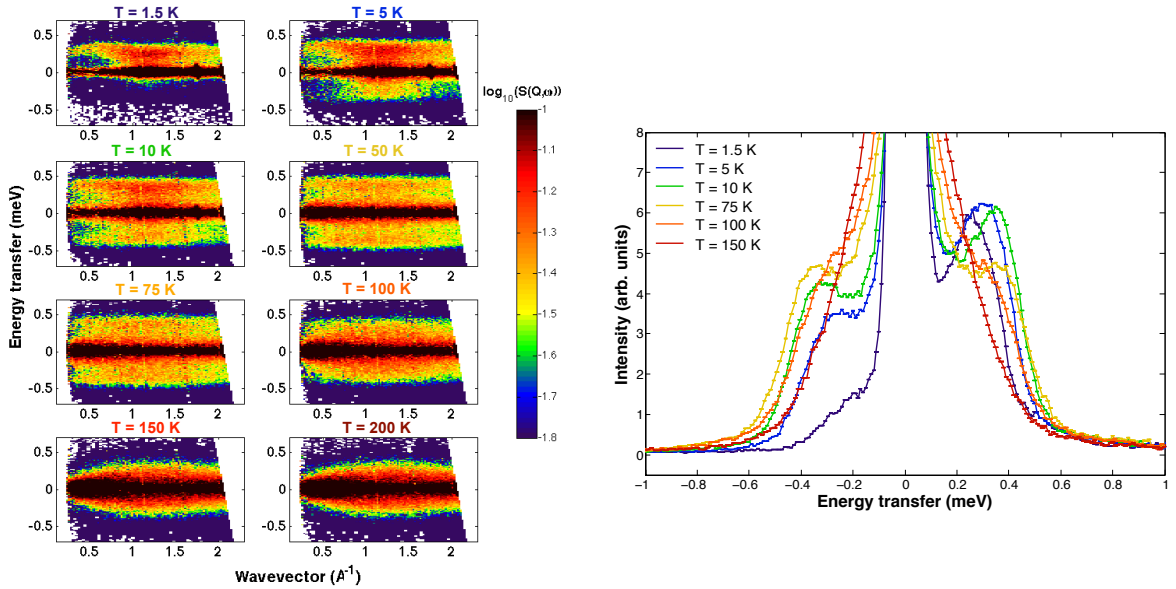

Figure 4.38 – *Inelastic neutron scattering intensity measured for $Gd_2Ir_2O_7$ on IN6 as function of Q and the energy (left) and summed over Q (right) between 1.5 and 200 K.*

Having determined the CEF levels for the different rare-earth elements, a fit of the INS intensity

can be performed in order to determine the nature of the ground state which will give more insight into the anisotropy of the rare-earth.

4.6.2 CEF analysis

The CEF Hamiltonian for the f electrons in the D_{3d} ($\bar{3}m$) point group symmetry of the 16d site occupied by the R^{3+} ions in the $R_2Ir_2O_7$ crystal can be expressed as:

$$\mathcal{H}_{\text{CEF}} = B_2^0\ \mathbf{C}_2^0 + B_4^0\ \mathbf{C}_4^0 + B_4^3\ (\mathbf{C}_4^3 - \mathbf{C}_4^{-3}) + B_6^0\ \mathbf{C}_6^0 + B_6^3\ (\mathbf{C}_6^3 - \mathbf{C}_6^{-3}) + B_6^6\ (\mathbf{C}_6^6 + \mathbf{C}_6^{-6}), \tag{4.3}$$

when the quantization axis is chosen along the local 3-fold axis. The $\mathbf{C}_k^q$ stand for Wybourne operators that, in a spatial rotation, transform like the spherical harmonics Y_k^q. The B_k^q are real parameters to be determined from the experimental data. If only the ground multiplet $|f^n \alpha LSJM\rangle$ ($M = -J, -J+1, \cdots, J$) of the selected R^{3+} ion is considered, and only in that case, then the CEF Hamiltonian is often formulated in the literature using the Stevens operators $\mathbf{O}_k^q$ [Ste52, Hut64]. Note that this notation is the one used in Section 4.3 for the estimation of the Ir molecular field in $Tb_2Ir_2O_7$ using the CEF parameters determined by Sagayama *et al.* in the Nd based compounds. The details for the conversion between the two formalisms are given in Appendix F.

The CEF parameters B_k^q are extracted from the experimentally recorded INS spectra by first diagonalizing the CEF Hamiltonian $\mathcal{H}_{\text{CEF}}$ on the ground multiplet $|f^n \alpha LSJM\rangle$ of the selected R^{3+} ion. Then the orientation averaged scattering function is computed from the obtained eigenvalues E_n and eigenstates $|n\rangle$:

$$S(|\mathbf{Q}|,\omega) = f(|\mathbf{Q}|)^2 \sum_{n,m} \frac{e^{-E_n/k_BT}}{Z}\ \frac{2}{3}\ |\ \langle n|\vec{J}|m\rangle\ |^2\ \mathcal{R}(\omega - E_{n\to m}) \tag{4.4}$$

where $Z = \sum_n e^{-E_n/k_BT}$ is the partition function, $E_{n\to m} = E_m - E_n$ the transition energy from the state $|n\rangle$ to the state $|m\rangle$ and $\mathcal{R}(\omega)$ the convolution of the Dirac δ function with an instrumental resolution function. The collective nature of the excitations being ignored at this stage, $S(|\mathbf{Q}|,\omega)$ depends on the wavevector transfer $\mathbf{Q}$ only through the magnetic form factor $f(|\mathbf{Q}|)$. Within the ground multiplet $|f^n \alpha LSJM\rangle$ of the selected R^{3+} ion, this form factor can be computed in the dipole approximation as $f(|\mathbf{Q}|) = \langle j_0(|\mathbf{Q}|)\rangle + (g_L/g_J)\ \langle j_2(|\mathbf{Q}|)\rangle$ where $\langle j_K(|\mathbf{Q}|)\rangle = \int_0^\infty r^2 R_{4f}(r) j_K(r|\mathbf{Q}|)dr$ are K-Bessel transforms of the f-electron radial wavefunction $R_{4f}(r)$, $g_L = \frac{1}{2} + \frac{L(L+1)-S(S+1)}{2J(J+1)}$ and $g_J = \frac{3}{2} + \frac{S(S+1)-L(L+1)}{2J(J+1)}$. These quantities computed at once for each rare-earth ions are tabulated in [ACL+06].

The fits were performed by reverse Monte Carlo with Metropolis sampling and simulated annealing in the paramagnetic phase above the Ir magnetic ordering. At low temperature the effects of the Ir-R exchange interactions were taken into account by merely adding to the CEF hamiltonian a Zeeman contribution involving a molecular field. The CEF program used for this analysis was written by R. Ballou.

From the CEF parameters, the anisotropic Landé factor ($g_\perp$ and $g_\parallel$) can also be calculated by adding a Zeeman contribution :

$$\mathcal{H} = \mathcal{H}_{\text{CEF}} + g_\alpha \mu_B\ H \cdot S_\alpha \tag{4.5}$$

where μ_B is the Bohr magneton and $\alpha = \perp$ or $\parallel$. Then g_α is extracted from the energy of the first excited state ($g_\alpha = {}^{E_1}/_{\mu_B\ H}$). These parameters give an indication of the anisotropy of the system:

– ${}^{g_\perp}/_{g_\parallel} = 1$ for an isotropic anisotropy,

– $g_\perp/g_\parallel > 1$ for an easy plane anisotropy,

– $g_\perp/g_\parallel < 1$ for an easy axis anisotropy.

4.6.2.1 $Er_2Ir_2O_7$

$Er_2Ir_2O_7$ is the compound for which the most CEF levels are observed, therefore this put more constraints onto the CEF parameters and a fit of good quality was obtained (see Fig. 4.39). The CEF parameters used for the fit are shown in Table 4.9. The fit was optimized using the data recorded at 200 K and for an incoming wavelength λ_i = 1.6 Å explaining the fact that the intensities are not matching perfectly for the data recorded for λ_i = 0.9 Å, although the energies of the calculated CEF levels agree well with the experimental ones.

The CEF parameters are close to the ones found for $Er_2Ti_2O_7$ and $Er_2Sn_2O_7$ [CGM+09, GPL+13]. The Landé factors have also been calculated and we found $g_\perp$ = 7.3 and $g_\parallel$ = 0.99 leading to $g_\perp/g_\parallel$ = 7.37. This indicates that the system presents an easy plane anisotropy, although comparing this value with the ones for $Er_2Ti_2O_7$ and $Er_2Sn_2O_7$, we can see that the easy plane anisotropy for $Er_2Ir_2O_7$ is stronger than for $Er_2Ti_2O_7$ but is weaker compared to $Er_2Sn_2O_7$.

	CEF parameters (K)						Anisotropic Landé factor		
	B_{20}	B_{40}	B_{43}	B_{60}	B_{63}	B_{66}	$g_\perp$	$g_\parallel$	$g_\perp/g_\parallel$
$Er_2Ir_2O_7$ (this work)	495	3390	958	782	-671	1285	7.3	0.99	7.37
$Er_2Ti_2O_7$ [CGM+09]	616	2 850	795	858	-493	980	6.8	2.62	2.6
$Er_2Sn_2O_7$ [GPL+13]	656	3 010	755	738	-653	990	7.52	0.054	139

Table 4.9 – *CEF parameters given in the Wybourne formalism (in K) for $Er_2Ir_2O_7$, $Er_2Ti_2O_7$ (from ref. [CGM+09]) and $Er_2Sn_2O_7$ (from ref. [GPL+13]).*

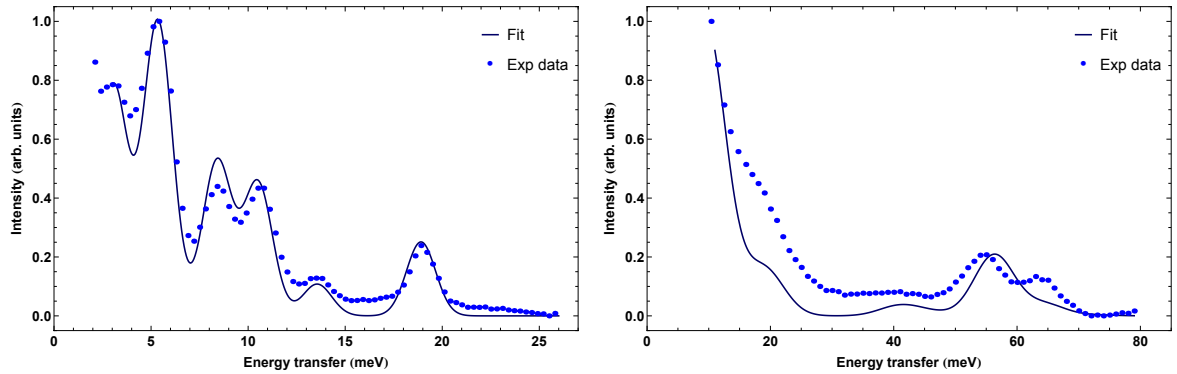

Figure 4.39 – *Experimental INS intensity measured for $Er_2Ir_2O_7$ at 200 K on IN4 with incoming neutron of wavelengths λ_i = 1.6 Å and λ_i = 0.9 Å. The plain lines correspond to the calculated INS intensity for $Er_2Ir_2O_7$ using the CEF parameters detailed in the Table 4.9.*

Having determined the CEF parameters, we added a Zeeman contribution to take into account the Ir molecular field and try to estimate its amplitude in order to reproduce the observed splitting of the ground state leading to a magnetic excitation around 0.35 meV. For $Er_2Ir_2O_7$, this leads to a Ir molecular field of about 2 T.

4.6.2.2 $Tb_2Ir_2O_7$

For $Tb_2Ir_2O_7$, the fitting of the summed intensity was not as straightforward compared to $Er_2Ir_2O_7$ mainly due to the presence of a strong nuclear signal which modifies the intensity of the observed excitations. In order to minimize the contribution of the nuclear signal, we performed the fit using the intensity summed over a reduced Q-range (between 1.25 and 4.25 $Å^{-1}$) and using the data recorded at low temperature as the nuclear signal is weaker than for the higher temperatures.

However, working with the low temperature data implies to take into account the presence of the Ir molecular field. To reduce the number of fitting parameters, we thus decided to use the value of 2 T determined for $Er_2Ir_2O_7$ for the Ir molecular field .

	CEF parameters (K)						Anisotropic Landé factor		
	B_{20}	B_{40}	B_{43}	B_{60}	B_{63}	B_{66}	$g_\perp$	$g_\parallel$	$g_\perp/g_\parallel$
$Tb_2Ir_2O_7$ (this work)	811	3353	958	875	-875	1113	0.066	2.74	0.024
$Tb_2Ti_2O_7$ [RPI+16]	649	3597	1323	750	-977	1497	0.090	7.45	0.012
$Tb_2Sn_2O_7$ [MBH07]	454	2620	837	-433	-328	1296	0.044	11.16	0.0039

Table 4.10 – *CEF parameters given in the Wybourne formalism (in K) for $Tb_2Ir_2O_7$, $Tb_2Ti_2O_7$ (from ref. [RPI+16]) and $Tb_2Sn_2O_7$ (from ref. [MBH07]).*

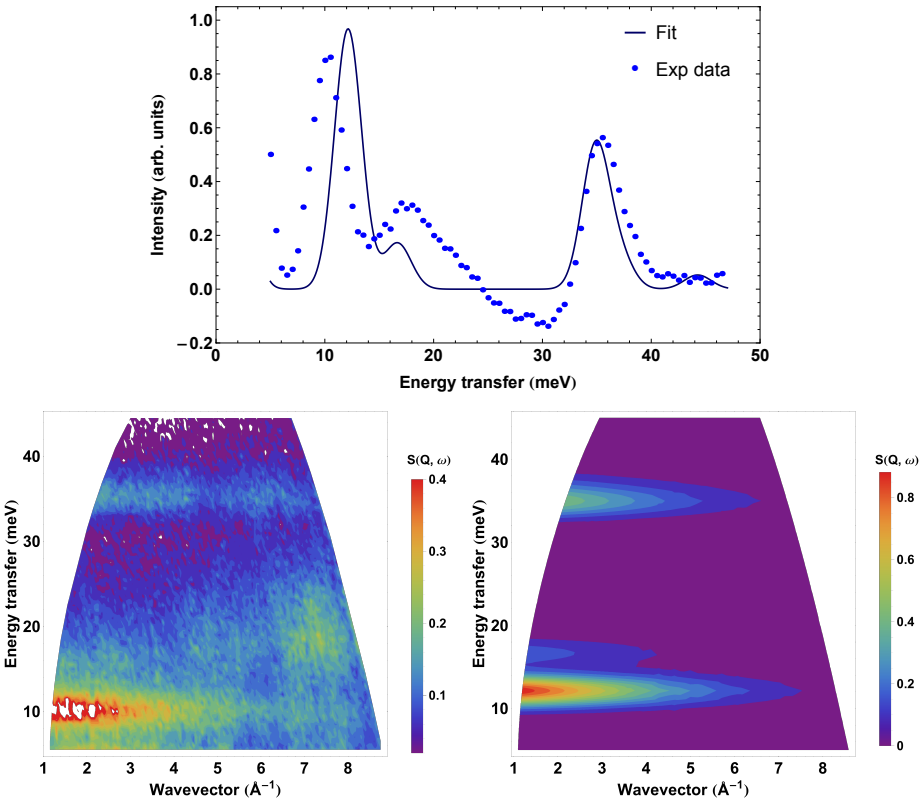

Figure 4.40 – *(Top)Experimental INS intensity measured for $Tb_2Ir_2O_7$ at 2 K on IN4 with incoming neutron of wavelength λ_i = 1.2 Å. The plain line correspond to the calculated INS intensity for $Tb_2Ir_2O_7$ using the CEF parameters detailed in the Table 4.10. (Bottom) Experimental (left) and calculated (right) INS intensity S(Q, ω).*

As the data are not of good quality mainly due to the population of the magnetic signals contaminated by nuclear contributions, the fit does not reproduce perfectly the experimental data and could be largely improved. Besides, the determined parameters are rather different than the ones determined in section 4.3 which were calculated by scaling those from the Nd^{3+} ions.

Note that the value of the Ir molecular field, that we used for refining the Tb CEF parameters, is slightly reduced compared to 3 T calculated previously. Another estimation should be done using these CEF parameters. Nevertheless, these two values are of the same order of magnitude so it does not affect the interpretation of the physics of the system.

4.6.2.3 $Gd_2Ir_2O_7$

For $Gd_2Ir_2O_7$ the effects of CEF might be ignored since the $4f$ electronic shell of Gd^{3+} ion is half-filled, but this would be legitimate only in the Russel-Saunders approximation according to which the $4f$ electrons in Gd^{3+} are in the purely spin ground octet ${}^8S_{7/2}$ ($S = 7/2, L = 0, J = 7/2$). As a matter of fact, a small admixture exists with multiplets of non zero orbital moments $|{}^6P_{7/2}\rangle$ ($S = 7/2, L = 1, J = 7/2$), $|{}^6D_{7/2}\rangle$ ($S = 5/2, L = 2, J = 7/2$), $\cdots$. Due to the hierarchy of the interactions, the in-shell electron-electron correlations being larger than the spin-orbit coupling, themselves larger than the CEF, the mixing is fairly independent of the host crystals and the spin octet states rather write:

$$|\Psi\rangle = s\,|{}^8S_{7/2}\rangle + p\,|{}^6P_{7/2}\rangle + d\,|{}^6D_{7/2}\rangle + \cdots \tag{4.6}$$

with $s = 0.9866$, $p = 0.162$, $d = -0.0123$, $\cdots$ [Wyb66].

The matrix element $\sum_{kq} B_k^q \langle \Psi M|\mathbf{C}_k^q|\Psi M'\rangle$ of the CEF Hamiltonian $\mathcal{H}_{\text{CEF}} = \sum_{kq} B_k^q \mathbf{C}_k^q$ between the states $|\Psi M\rangle$ can be computed from those of the Wybourne operators, $\mathbf{C}_k^q$, on the multiplet states $|f^n \alpha SLJM\rangle$, which are given by [Wyb65]. More details are given in Appendix G.

It results that the CEF Hamiltonian can simply be expressed as:

$$\mathcal{H}_{\text{CEF}} = -\frac{4\sqrt{5}}{315} pdB_2^0 \mathbf{C}_2^0 \approx 0.56 \times 10^{-4} B_2^0 \mathbf{C}_2^0, \tag{4.7}$$

where $\mathbf{C}_2^0 = 3\mathbf{J}_z^2 - J(J+1)\mathbf{I}$ is a Wybourne operator acting on the spin octet ${}^8S_{7/2}$ with an effective CEF parameter given by $-\frac{4\sqrt{5}}{315} pdB_2^0$.

If the environment is exactly the same as in $Er_2Ir_2O_7$, then B_2^0 is estimated to 52 meV which gives an effective CEF parameter of about 3×10^{-3} meV. It has been argued that this provides only an order of magnitude and that a number of other contributions of similar magnitude and even a little larger emerge from high order of perturbations involving spin orbit interactions with excited states, configuration mixing interactions or else relativistic and correlated CEF effects [Wyb66]. Assuming that the Gd-Ir and Er-Ir exchange interactions are of the same order of magnitude, *i.e.* characterized by an Ir molecular field of about 2 T at low temperature, the spin gap of $0.35 - 0.40$ meV found out in the $Gd_2Ir_2O_7$ INS spectra can be reproduced when the effective CEF parameter is in the order of 15×10^{-3} meV. Its positive value suggests a local easy plane anisotropy.

With INS experiments and CEF analysis, we thus determined the CEF parameters for $Tb_2Ir_2O_7$ and $Er_2Ir_2O_7$. From these parameters, we were also able to estimate the amplitude of the Ir molecular field which is shown to split the CEF ground state level. The estimated value is consistent between the three

studied compounds. In order to go further in the analysis we would need to fit the dispersion of this additional magnetic contribution by taking into account collective excitations.

4.7 Monte Carlo Calculations

In order to better understand the different ingredients involved in the physics of the $R_2Ir_2O_7$ family, especially $Er_2Ir_2O_7$ and $Gd_2Ir_2O_7$ with easy-plane anisotropy, Monte Carlo calculations were performed. There are three different exchange interactions to take into account for this family: the Ir-Ir interactions which produce the ordering of the Ir sublattice in the AIAO magnetic configuration, the Ir-R interactions which lead to an induced AIAO magnetic order for easy axis rare-earths or which compete against the easy-plane anisotropy of the rare-earths. These two interactions occur at a "high" temperature, corresponding to T_{MI}, for most of the pyrochlore iridates. The last interactions are the R-R interactions which occur at low temperature, in the (sub)Kelvin range.

First, the expression of the magnetic exchange interactions has to be found, beginning by analyzing the symmetry of this interaction which will constraint the authorized terms in the expression of the interaction tensor. The symmetry analysis is described in the two sections following the details of the Monte Carlo calculations.

For the calculations, I have first worked with each sublattice independently in order to fix some of the parameters, then both sublattices were considered simultaneously with an additional magnetic exchange coupling. The Monte Carlo calculations have been performed using a program written by L. Chapon (freely available at `https://forge.epn-campus.eu/svn/difmag/`).

4.7.1 Details on the Monte Carlo calculations

Monte Carlo calculations are performed using a conventional Metropolis algorithm, cooling the system from high temperature (100 K for the Er sublattice alone, 600 K for the Ir sublattice alone and the two coupled sublattices) to low temperature. The temperature is decreased exponentially by 5% each time. At each temperature step, 10^4 spin flips per spin are conducted for equilibration, then the spins configuration can be extracted. From the spins configuration, neutron powder diffractogram can be calculated in order to see the evolution of the magnetic ordering. Supercells of respectively 8x8x8 (8192 spins) and 6x6x6 (6912 spins) have been used for the sublattices alone and coupled respectively.

4.7.2 Definition of the different interactions

4.7.2.1 Rare earth-rare earth & Iridium-Iridum interactions

For the rare-earth and iridium sublattices, identical pairs are along a 2-fold axis and there are two perpendicular mirrors that contain the 2-fold axis. Thus the point group symmetry at the center of the pair is $mm2$ (see Fig. 4.41).

Taking into account the action of the 2-fold axis and of the 2 mirrors on symmetric $J = \begin{pmatrix} J_{xx} & J_{xy} & J_{xz} \\ J_{xy} & J_{yy} & J_{yz} \\ J_{xz} & J_{yz} & J_{zz} \end{pmatrix}$ and antisymmetric $\vec{D} = \begin{pmatrix} D_x \\ D_y \\ D_z \end{pmatrix}$ exchange interactions, the interaction tensor in the local basis $((\hat{\mathbf{x}}, \hat{\mathbf{y}}, \hat{\mathbf{z}})$, attached to the R-R or Ir-Ir pair, see Fig. 4.41) writes:

$$J_{loc} = \begin{pmatrix} J_{xx} & 0 & -D \\ 0 & J_{yy} & 0 \\ D & 0 & J_{zz} \end{pmatrix} \tag{4.8}$$

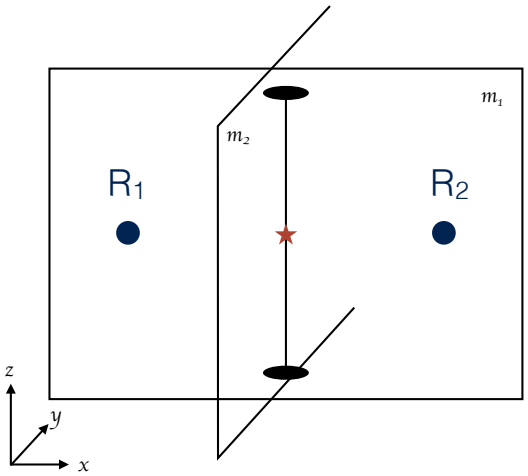

Figure 4.41 – *Sketch of two neighboring rare-earth ions with the symmetry elements. The local basis* $(\hat{\mathbf{x}}, \hat{\mathbf{y}}, \hat{\mathbf{z}})$ *is the basis attached to the R-R pair.*

We can rewrite this tensor in the basis attached to the cubic unit cell $(\hat{\mathbf{i}}, \hat{\mathbf{j}}, \hat{\mathbf{k}})$ (see Fig. 4.42):

$$J_{cub} = \begin{pmatrix} J_1 & J_3 & -J_4 \\ J_3 & J_1 & -J_4 \\ J_4 & J_4 & J_2 \end{pmatrix}, \quad \text{with} \quad \begin{cases} J_1 &= \frac{J_{xx}+J_{yy}}{2} \\ J_2 &= \frac{J_{xx}-J_{yy}}{2} \\ J_3 &= -\frac{D}{\sqrt{2}} \\ J_4 &= J_{zz} \end{cases} \tag{4.9}$$

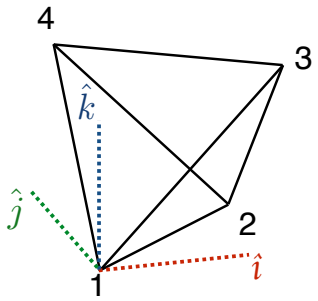

Figure 4.42 – *Sketch of one of the tetrahedra in the cubic basis* $(\hat{\mathbf{i}}, \hat{\mathbf{j}}, \hat{\mathbf{k}})$.

Considering one tetrahedron as sketched in Figure 4.42, the expression of J_{cub}, given in Eq. 4.9, corresponds to J_{1-2}. The other interactions among this single tetrahedron can be easily deduced by applying the correct transformation:

$$\begin{cases} J_{1-3} &= Rot_{\{1,1,1\}}\left[-\frac{2\pi}{3}\right] \cdot J_{12} \cdot {}^t Rot_{\{1,1,1\}}\left[-\frac{2\pi}{3}\right] \\ J_{1-4} &= Rot_{\{1,1,1\}}\left[\frac{2\pi}{3}\right] \cdot J_{12} \cdot {}^t Rot_{\{1,1,1\}}\left[\frac{2\pi}{3}\right] \\ J_{2-3} &= Rot_{\{-1,-1,1\}}\left[\frac{2\pi}{3}\right] \cdot Rot_{\{0,0,1\}}[\pi] \cdot J_{12} \cdot {}^t(Rot_{\{0,0,1\}}[\pi] \cdot Rot_{\{-1,-1,1\}}\left[\frac{2\pi}{3}\right]) \\ J_{2-4} &= Rot_{\{-1,-1,1\}}\left[-\frac{2\pi}{3}\right] \cdot Rot_{\{0,0,1\}}[\pi] \cdot J_{12} \cdot {}^t(Rot_{\{0,0,1\}}[\pi] \cdot Rot_{\{-1,-1,1\}}\left[-\frac{2\pi}{3}\right]) \\ J_{4-3} &= Rot_{\{1,-1,-1\}}\left[-\frac{2\pi}{3}\right] Rot_{\{1,0,0\}}[\pi] \cdot J_{14} \cdot {}^t(Rot_{\{1,0,0\}}[\pi] \cdot Rot_{\{1,-1,-1\}}\left[-\frac{2\pi}{3}\right]) \end{cases}$$

The rare-earth sublattice is composed of 4 equivalent tetrahedra (labelled 1, 2, 3 and 4 in Fig. 4.43).

The interactions among these tetrahedra are the same. There are another set of 4 equivalent tetrahedra (5, 6, 7 and 8), for which the interactions are deduced from the first set of interactions by symmetry.

For example J_{1-11} is related to J_{1-2} through the inversion center at the position of R_1. We can then deduced all the rare-earth interactions inside the unit cell.

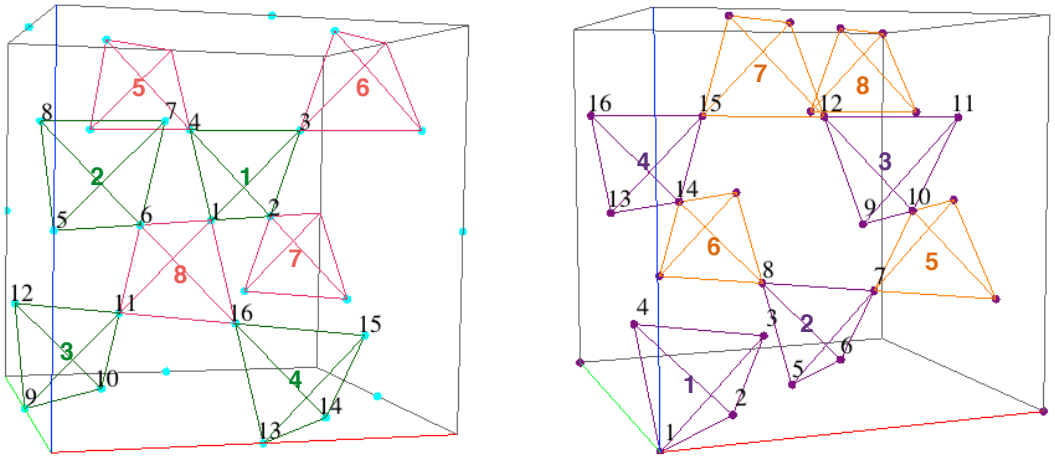

Figure 4.43 – *Representation of the rare-earth (left) and iridium (right) sublattices in the cubic basis* $(\hat{\mathbf{i}}, \hat{\mathbf{j}}, \hat{\mathbf{k}})$. *The equivalent tetrahedra are represented in the same color.*

4.7.2.2 Rare earth-Iridium interactions

The symmetry analysis for the R-Ir interaction is detailed section 4.4. I recall that the exchange tensor writes:

$$J_{cub} = \frac{1}{6}\begin{pmatrix} J_2 & J_4+3\sqrt{2}D & J_4+3\sqrt{2}D \\ J_4-3\sqrt{2}D & J_1 & J_3 \\ J_4-3\sqrt{2}D & J_3 & J_1 \end{pmatrix} \tag{4.10}$$

with

$$\begin{cases} J_1 &= 3J_{xx} + J_{yy} + 2J_{zz} - 2\sqrt{2}J_{yz} \\ J_2 &= 4J_{yy} + 2J_{zz} + 4\sqrt{2}J_{yz} \\ J_3 &= -3J_{xx} + J_{yy} + 2J_{zz} - 2\sqrt{2}J_{yz} \\ J_4 &= -2J_{yy} + 2J_{zz} + \sqrt{2}J_{yz} \end{cases}$$

4.7.3 Results of the Monte Carlo calculations

4.7.3.1 Calculations with the Iridium sublattice

For the iridium sublattice, only DM interaction is considered, as it allows stabilizing an AIAO order alone. The DM interaction is expressed by:

$$D_{1-2} = \begin{pmatrix} -D \\ D \\ 0 \end{pmatrix},$$

where D is fixed to 70 K, value for which the Ir sublattice orders around 130 K, temperature which corresponds to T_{MI}. The ordering temperature is deduced from the calculated specific heat, in which a peak is observed at the transition as it is a second order transition (see Fig. 4.44). In the calculated

neutron powder diffractograms, magnetic peaks corresponding to an AIAO arrangement of the Ir magnetic moments are observed from 100 K down to the lowest temperature.

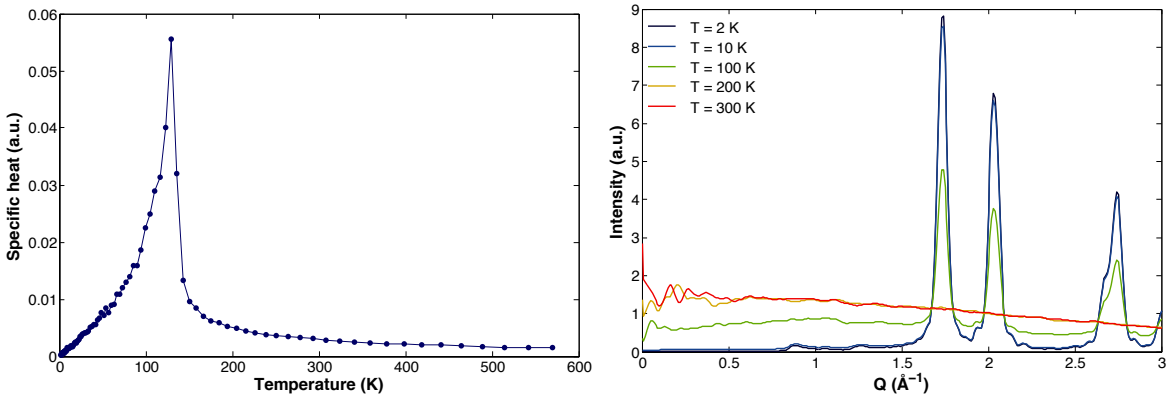

Figure 4.44 – *Specific heat (left) and temperature evolution of the neutron powder diffraction (right) calculated from the Monte Carlo simulation on the Ir sublattice.*

4.7.3.2 Calculations with the rare-earth sublattice

For the rare-earth interactions, the considered Hamiltonian is the following (from [GPL+13]) :

$$\mathcal{H} = \sum_{\langle ij \rangle} \Big[J_{zz} S_i^z S_j^z - J_\pm (S_i^+ S_j^- + S_i^- S_j^+) + J_{\pm\pm} [\gamma_{ij} S_i^+ S_j^+ + \gamma_{ij}^* S_i^- S_j^-] + J_{z\pm} [S_i^z (\zeta_{ij} S_j^+ + \zeta_{ij}^* S_j^-) + i \leftrightarrow j] \Big] \quad (4.11)$$

where S_i^μ denote components of the spins in the local pyrochlore bases and γ_{ij} and ζ_{ij} consist of unimodular complex numbers with $\zeta_{ij} = -\gamma_{ij}^*$ [RSGB11]. The exchange parameters (J_{zz}, $J_\pm$, $J_{\pm\pm}$ and $J_{z\pm}$) are linked to the parameters defined in subsection 4.7.2.1 by the following relationships :

$$\begin{cases} J_{zz} &= -\frac{1}{3}(2J_1 - J_2 + 2(J_3 + 2J_4)) \\ J_\pm &= \frac{1}{6}(2J_1 - J_2 - J_3 - 2J_4) \\ J_{\pm\pm} &= \frac{1}{6}(J_1 + J_2 + 2J_3 + 2J_4) \\ J_{z\pm} &= \frac{1}{3\sqrt{2}}(J_1 + J_2 + J_3 - J_4) \end{cases} \equiv \begin{cases} J_1 &= \frac{1}{3\sqrt{2}}(4\sqrt{2}J_\pm + 2\sqrt{2}J_{\pm\pm} + 4J_{z\pm} - \sqrt{2}J_z z) \\ J_2 &= \frac{1}{3}(-4J_\pm + 4J_{\pm\pm} + 4\sqrt{2}J_{z\pm} + J_{zz}) \\ J_3 &= -\frac{1}{3}(2J_\pm + 4J_{\pm\pm} - 2\sqrt{2}J_{z\pm} + J_{zz}) \\ J_4 &= -\frac{1}{3}(2J_\pm - 2J_{\pm\pm} + \sqrt{2}J_{z\pm} + J_{zz}) \end{cases}$$

The exchange interactions include the anisotropic Landé factors ($g_\parallel$ and $g_\perp$) [GPL+13] and thus take into account the anisotropy of the rare-earth ground state doublet [Cur07, RSGB11].

For the Monte Carlo calculations, I have used the exchange parameters determined for the compound $Er_2Sn_2O_7$ as it displays similarities with $Er_2Ir_2O_7$, although the Er^{3+} ions magnetocrystalline anisotropy is weaker for $Er_2Ir_2O_7$. Indeed $Er_2Sn_2O_7$ does not order before 100 mK, despite the fact that it displays a freezing around 200 mK and Palmer-Chalker short range correlations, similar to what is observed in $Er_2Ir_2O_7$.

The fitted exchange parameters are the following :

$$\begin{cases} J_{\pm\pm} &= 7.4 \\ J_{\pm} &= 1.35 \\ J_{zz} &= 0 \\ J_{z\pm} &= 0.025 \end{cases} (10^{-2}\text{ meV}) \rightarrow \begin{cases} J_1 &= 6.76 \\ J_2 &= 8.11 \\ J_3 &= -10.74 \\ J_4 &= 4.02 \end{cases} (10^{-2}\text{ meV}) \equiv \begin{cases} J_1 &= 0.784 \\ J_2 &= 0.942 \\ J_3 &= -1.247 \\ J_4 &= 0.467 \end{cases} (\text{K})$$

Using these parameters, short range correlations are observed down to 0.77 K with the presence of a large bump around 1.15 Å^{-1}. At this temperature, the system orders magnetically as it can be seen from the peak in the specific heat and from the observed magnetic Bragg peaks (see Fig. 4.45). The magnetic order from the calculations is found to be the Palmer-Chalker state (see details in section 4.4) as it can be observed by analyzing the spin configuration extracted from the Monte-Carlo calculations. The real system does not show any long range ordering. We recall however that the Monte Carlo simulations are classical calculations which do not take into account quantum fluctuations or instabilities which may prevent the ordering of the real system.

The computed short range correlations around 1.15 Å^{-1} are consistent with the physics of both $Er_2Sn_2O_7$ and $Er_2Ir_2O_7$.

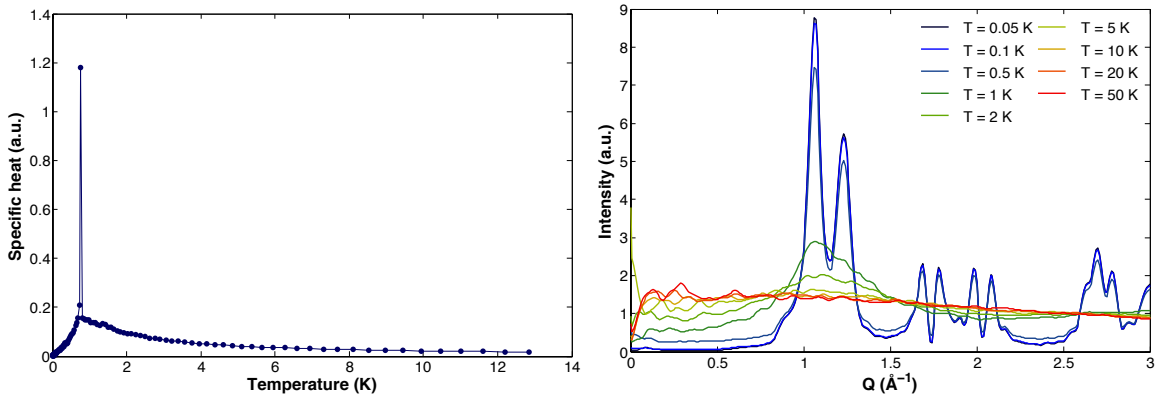

Figure 4.45 – *Specific heat (left) and temperature evolution of the neutron powder diffraction (right) calculated from the Monte Carlo simulation on the Er sublattice.*

4.7.3.3 Calculations on $R_2Ir_2O_7$.

Finally, calculations have been performed on the entire system taking into account the two sublattices with their interactions and also an additional interaction between the Ir and R ions. To begin with, an isotropic interaction is used between only the R and Ir nearest neighbors. This is not a realistic representation of the effective R-Ir interaction as it has no reason to be isotropic and the exchange tensor is allowed to have non zero off-diagonal components (see Eq. 4.10).

Figure 4.46 shows the neutron powder diffractograms, for the entire system (left part) and the R sublattice alone (right part), calculated from the spin configurations extracted from the Monte Carlo calculations at different temperatures and for different values of the R-Ir isotropic interactions.

It is interesting to note that, for small values of the R-Ir interaction (between 1 and 3 K), both a large bump around 1.15 Å^{-1} indicative of Palmer-Chalker interactions and magnetic Bragg peaks associated

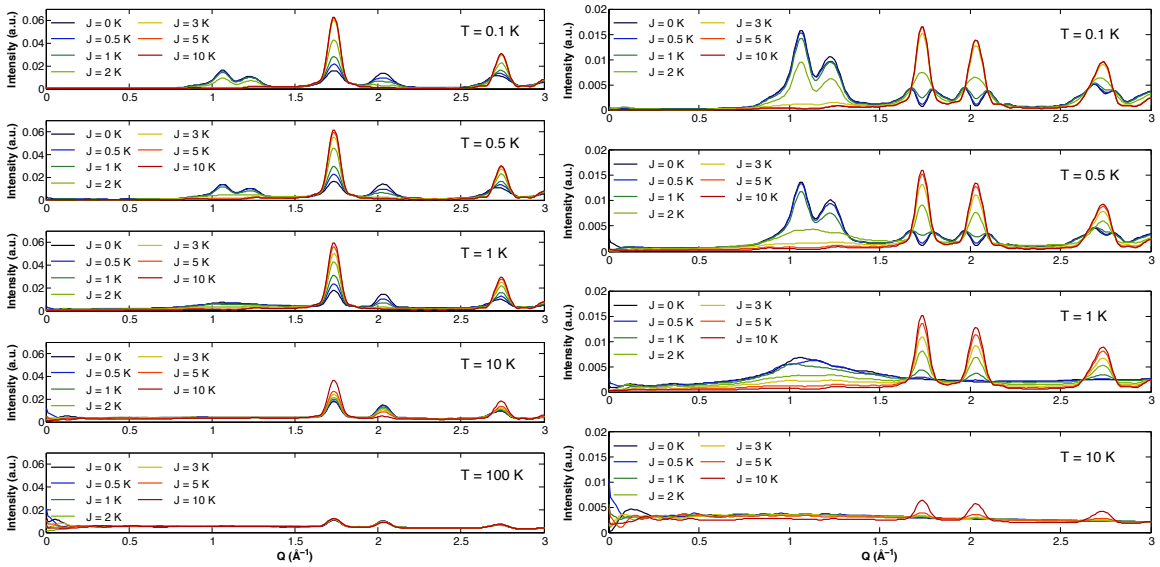

Figure 4.46 – *Evolution of the neutron powder diffractograms obtained from the Monte Carlo calculations for $R_2Ir_2O_7$ (left) and for the R sublattice alone (right) for different values of the R-Ir exchange interaction and for several temperatures.*

to an AIAO magnetic order are observed on the R sublattice (see right part of Fig. 4.46 and Fig. 4.47). For higher values of this coupling, the R sublattice orders in the AIAO magnetic configuration similarly to the Ir sublattice. This could give new insight into the physics of $Gd_2Ir_2O_7$ and $Er_2Ir_2O_7$ as it looks similar to what have been experimentally observed by neutron powder diffraction.

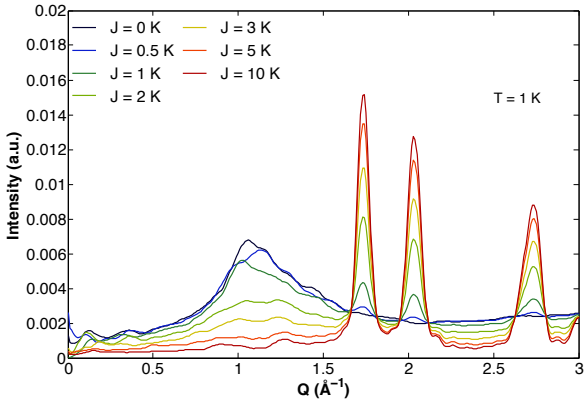

Figure 4.47 – *Evolution of the neutron powder diffraction calculated from the Monte Carlo calculations for the R sublattice alone for different values of the R-Ir exchange term at 1* K.

However, the Gd^{3+} ions magnetocrystalline anisotropy if any, should not be as large as for the Er^{3+} ions in $Er_2Sn_2O_7$. Therefore more calculations have be done using a different R-R exchange tensor before concluding. It becomes obvious from these calculations, that some anisotropic terms need to be included to describe the physics of $Gd_2Ir_2O_7$. One possible explanation could be that the anisotropy comes from the R-Ir interactions rather that from the Gd^{3+} ions. However this would imply that the Ir magnetic moments are not perfectly aligned along the $\langle 111 \rangle$ direction.

Moreover, the R-Ir interactions are assumed to be stronger than the R-R interactions so it would be interesting to perform calculations without R-R interactions in a first step considering anisotropic R-Ir exchange tensor contrary to what have been performed so far.

4.8 Conclusion and perspectives

In this chapter, we studied several pyrochlore iridates with various rare-earth elements, magnetic or not and displaying different magnetocrystalline anisotropy: easy axis anisotropy for the Tb, Ho and Dy, easy plane anisotropy for the Er and Yb and weak anisotropy for the Gd.

We first started by studying the non magnetic rare-earth based compound: $Y_2Ir_2O_7$. A signature of the Ir magnetic ordering is observed with the presence of a ZFC-FC opening in the magnetic susceptibility. However it remains very difficult to have an unambiguous evidence of the Ir magnetic order using microscopic probes such as neutron scattering, muon spectroscopy or synchrotron X-rays scattering.

For the other studied compounds with magnetic rare-earths, we do not get a direct evidence of the Ir magnetic order. However we found that their magnetic behaviors fully agree with an all-in/all-out Ir magnetic order. Indeed, with this magnetic configuration, the Ir nearest neighbors of a rare-earth site produce a molecular field whose direction is along the $\langle 111 \rangle$ local direction at this site. Therefore the Ir molecular field is either consistent with or competes against the R^{3+} ions magnetocrystalline anisotropy.

For easy axis anisotropic rare-earth elements (Tb, Ho and Dy), the Ir molecular field forces the R sublattice to order in the same all-in/all-out magnetic configuration. This is deduced experimentally from the temperature evolution of the ordered R magnetic moment which does not follow a Brillouin function as it should if it was the primary order parameter of a second order magnetic transition. Signature of R-R interactions are also observed at lower temperatures for these compounds. For example in $Tb_2Ir_2O_7$, a metamagnetic transition is observed below 10 K in the magnetization measurements but the magnetic order remains AIAO.

In the case of easy plane magnetocrystalline anisotropy of the rare-earth elements (Er and Yb), the Ir molecular field competes with the R^{3+} anisotropy and we showed that neither symmetric nor antisymmetric exchange interactions allow to gain energy for an ideal easy plane anisotropy, leading to an absence of magnetic order until the lowest temperatures where the R-R interactions needs to be accounted for. In the case of $Er_2Ir_2O_7$, an additional magnetic irreversibility is observed at 600 mK, interpreted as a magnetic freezing of the Er magnetism. Moreover, short range correlations have also been observed at low temperature in the magnetic diffuse scattering. Its analysis suggests that the Er sublattice presents Palmer-Chalker short range correlations similarly to $Er_2Sn_2O_7$.

Finally we also studied $Gd_2Ir_2O_7$, that was assumed to be isotropic and thus supposed to simply stabilize an induced all-in/all-out magnetic order due to the Ir molecular field. However this last compound revealed unexpected and puzzling features. Indeed the coexistence of both an all-in/all-out long range order and Palmer-Chalker short range correlations are observed by neutron powder diffraction. The two phases seem to appear at the same temperature and coexist down to 2 K. This behavior is not fully understood at the moment but could come from a slightly easy-plane anisotropic behavior of the Gd^{3+} ions.

We also studied the inelastic spectra by TOF INS experiments of all these compounds. These measurements allowed to observe the CEF level transitions and thus in principle to determine the CEF parameters and accurate magnetocrystalline anisotropy.

We have carried out such analysis for three of the $R_2Ir_2O_7$ compounds (Tb, Er, Gd)$_2Ir_2O_7$. In all cases, an additional magnetic level slightly dispersing is observed at low temperature and low energy. It has been interpreted as resulting from the Ir molecular field which splits the CEF ground state of the R^{3+} ions. Besides the dispersion of this signal could be the indirect signature of the Ir collective excitations or of the R-R interactions.

The study of these compounds revealed a systematic behavior depending on the rare-earth magnetocrystalline anisotropy but is far from being complete as some of the temperature behaviors remain unexplained at the moment.

Low temperature neutron scattering measurements have not yet been performed for $Yb_2Ir_2O_7$, but are planned and could reveal short range correlations similarly to $Er_2Ir_2O_7$ or show evidence of ferromagnetic correlations such as $Yb_2Ti_2O_7$ [GER+04].

Concerning $Gd_2Ir_2O_7$, neutron powder diffraction using a dilution fridge are planned in order to see if both the long range order and short range correlations phases remain down to very low temperature or if one disappears in favor of the other.

Finally, the Monte Carlo calculations need to be continued and will give great insights for understanding the remarkable behavior of $Er_2Ir_2O_7$ and $Gd_2Ir_2O_7$.

New magnetization measurements have also been performed on $Dy_2Ir_2O_7$ and $Ho_2Ir_2O_7$ using a dilution fridge to probe the low temperature magnetic properties. These two compounds seem to exhibit slow spin dynamics at low temperature evidenced by the presence of a peak in the AC magnetic susceptibility. Moreover, the low temperature magnetization curves present a step before the saturation plateau. The dynamics and the step are usual signatures of a spin-ice phase which is observed in the Ho and Dy titanates due to effective ferromagnetic R-R interactions. These are very preliminary results, which still need to be analyzed in order to obtain a consistent interpretation.

Bibliography

[ACL+06] I. S. Anderson, J. M. Carpenter, G. Lander, R. Pynn, J. M. Rowe, O. Schärpf, V. F. Sears, and B. T. M. Willis. *International Tables for Crystallography, ch 4.4: Neutron techniques*, volume C. 2006.

[Ber68] E. F. Bertaut. Representation analysis of magnetic structures. *Acta Crystallogr., Sect. A:*, 24:217, 1968.

[BG01] Steven T. Bramwell and Michel J. P. Gingras. Spin ice state in frustrated magnetic pyrochlore materials. *Science*, 294(5546):1495–1501, 2001.

[BJB01] V Bondah-Jagalu and S T Bramwell. Magnetic susceptibility study of the heavy rare-earth stannate pyrochlores. *Can. J. Phys.*, 79(11-12):1381–1385, 2001.

[BPM+13] P Bonville, S Petit, I Mirebeau, J Robert, E Lhotel, and C Paulsen. Magnetization process in $Er_2Ti_2O_7$ at very low temperature. *Journal of Physics: Condensed Matter*, 25(27):275601, 2013.

[BWH69] H.W.J. Blöte, R.F. Wielinga, and W.J. Huiskamp. Heat-capacity measurements on rare-earth double oxides $R_2M_2O_7$. *Physica*, 43(4):549 – 568, 1969.

[CGM+09] H. Cao, A. Gukasov, I. Mirebeau, P. Bonville, C. Decorse, and G. Dhalenne. Ising versus XY Anisotropy in Frustrated $R_2Ti_2O_7$ Compounds as "Seen" by Polarized Neutrons. *Phys. Rev. Lett.*, 103:056402, Jul 2009.

[CHH+03] J. D. M. Champion, M. J. Harris, P. C. W. Holdsworth, A. S. Wills, G. Balakrishnan, S. T. Bramwell, E. Čižmár, T. Fennell, J. S. Gardner, J. Lago, D. F. McMorrow, M. Orendáč, A. Orendáčová, D. McK. Paul, R. I. Smith, M. T. F. Telling, and A. Wildes. $Er_2Ti_2O_7$: Evidence of quantum order by disorder in a frustrated antiferromagnet. *Phys. Rev. B*, 68:020401, Jul 2003.

[Cur07] S. H. Curnoe. Quantum spin configurations in $tb_2ti_2o_7$. *Phys. Rev. B*, 75:212404, Jun 2007.

[DDA+12] S. M. Disseler, Chetan Dhital, A. Amato, S. R. Giblin, Clarina de la Cruz, Stephen D. Wilson, and M. J. Graf. Magnetic order in the pyrochlore iridates $A_2Ir_2O_7$ (A = Y, Yb). *Phys. Rev. B*, 86:014428, Jul 2012.

[FYB14] Benjamin A. Frandsen, Xiaohao Yang, and Simon J. L. Billinge. Magnetic pair distribution function analysis of local magnetic correlations. *Acta Crystallographica Section A*, 70(1):3–11, Jan 2014.

[GDG+99] J. S. Gardner, S. R. Dunsiger, B. D. Gaulin, M. J. P. Gingras, J. E. Greedan, R. F. Kiefl, M. D. Lumsden, W. A. MacFarlane, N. P. Raju, J. E. Sonier, I. Swainson, and Z. Tun. Cooperative Paramagnetism in the Geometrically Frustrated Pyrochlore Antiferromagnet $Tb_2Ti_2O_7$. *Phys. Rev. Lett.*, 82:1012–1015, Feb 1999.

[GER+04] J. S. Gardner, G. Ehlers, N. Rosov, R. W. Erwin, and C. Petrovic. Spin-spin correlations in $yb_2ti_2o_7$: A polarized neutron scattering study. *Phys. Rev. B*, 70:180404, Nov 2004.

[GGB+01] J. S. Gardner, B. D. Gaulin, A. J. Berlinsky, P. Waldron, S. R. Dunsiger, N. P. Raju, and J. E. Greedan. Neutron scattering studies of the cooperative paramagnet pyrochlore $tb_2ti_2o_7$. *Phys. Rev. B*, 64:224416, Nov 2001.

[GPL+13] Solene Guitteny, Sylvain Petit, Elsa Lhotel, Julien Robert, Pierre Bonville, Anne Forget, and Isabelle Mirebeau. Palmer-Chalker correlations in the XY pyrochlore antiferromagnet $Er_2Sn_2O_7$. *Phys. Rev. B*, 88:134408, Oct 2013.

[GSYR86] J.E. Greedan, M. Sato, Xu Yan, and F.S. Razavi. Spin-glass-like behavior in $Y_2Mo_2O_7$, a concentrated, crystalline system with negligible apparent disorder. *Solid State Communications*, 59(12):895 – 897, 1986.

[GZS+07] V N Glazkov, M Zhitomirsky, A I Smirnov, C Marin, J-P Sanchez, A Forget, D Colson, and P Bonville. Single-ion anisotropy and transverse magnetization in the frustrated gadolinium pyrochlores. *Journal of Physics: Condensed Matter*, 19(14):145271, 2007.

[HBF+01] J A Hodges, P Bonville, A Forget, M Rams, K KrÃşlas, and G Dhalenne. The crystal field and exchange interactions in $Yb_2Ti_2O_7$. *Journal of Physics: Condensed Matter*, 13(41):9301, 2001.

[HBHC98] M. J. Harris, S. T. Bramwell, P. C. W. Holdsworth, and J. D. M. Champion. Liquid-gas critical behavior in a frustrated pyrochlore ferromagnet. *Phys. Rev. Lett.*, 81:4496–4499, Nov 1998.

[HBM+97] M. J. Harris, S. T. Bramwell, D. F. McMorrow, T. Zeiske, and K. W. Godfrey. Geometrical Frustration in the Ferromagnetic Pyrochlore $Ho_2Ti_2O_7$. *Phys. Rev. Lett.*, 79:2554–2557, Sep 1997.

[Hut64] M.T. Hutchings. Point-charge calculations of energy levels of magnetic ions in crystalline electric fields. volume 16 of *Solid State Physics*, pages 227 – 273. Academic Press, 1964.

[KJM+08] B. J. Kim, Hosub Jin, S. J. Moon, J.-Y. Kim, B.-G. Park, C. S. Leem, Jaejun Yu, T. W. Noh, C. Kim, S.-J. Oh, J.-H. Park, V. Durairaj, G. Cao, and E. Rotenberg. Novel $J_{\text{eff}} = 1/2$ Mott State Induced by Relativistic Spin-Orbit Coupling in Sr_2IrO_4. *Phys. Rev. Lett.*, 101:076402, 2008.

[KOK+09] B. J. Kim, H. Ohsumi, T. Komesu, S. Sakai, T. Morita, H. Takagi, and T. Arima. Phase-Sensitive Observation of a Spin-Orbital Mott State in Sr_2IrO_4. *Science*, 323(5919):1329–1332, 2009.

[LGL+14] E. Lhotel, S. R. Giblin, M. R. Lees, G. Balakrishnan, L. J. Chang, and Y. Yasui. First-order magnetic transition in $Yb_2Ti_2O_7$. *Phys. Rev. B*, 89:224419, Jun 2014.

[LSB+15] E. Lefrançois, V. Simonet, R. Ballou, E. Lhotel, A. Hadj-Azzem, S. Kodjikian, P. Lejay, P. Manuel, D. Khalyavin, and L. C. Chapon. Anisotropy-tuned magnetic order in pyrochlore iridates. *Phys. Rev. Lett.*, 114:247202, Jun 2015.

[MARC+05] I. Mirebeau, A. Apetrei, J. Rodríguez-Carvajal, P. Bonville, A. Forget, D. Colson, V. Glazkov, J. P. Sanchez, O. Isnard, and E. Suard. Ordered Spin Ice State and Magnetic Fluctuations in $Tb_2Sn_2O_7$. *Phys. Rev. Lett.*, 94:246402, Jun 2005.

[MBH07] I. Mirebeau, P. Bonville, and M. Hennion. Magnetic excitations in $Tb_2Sn_2O_7$ and $Tb_2Ti_2O_7$ as measured by inelastic neutron scattering. *Phys. Rev. B*, 76:184436, Nov 2007.

[MHT+02] Kazuyuki Matsuhira, Yukio Hinatsu, Kenichi Tenya, Hiroshi Amitsuka, and Toshiro Sakakibara. Low-Temperature Magnetic Properties of Pyrochlore Stannates. *J. Phys. Soc. Jpn*, 71(6):1576–1582, 2002.

[MWH+11] Kazuyuki Matsuhira, Makoto Wakeshima, Yukio Hinatsu, Chihiro Sekine, Carley Paulsen, Toshiro Sakakibara, and Seishi Takagi. Slow dynamics of Dy pyrochlore oxides $Dy_2Sn_2O_7$ and $Dy_2Ir_2O_7$. *J. of Phys: Conf. Series*, 320(1):012050, 2011.

[MWHT11] Kazuyuki Matsuhira, Makoto Wakeshima, Yukio Hinatsu, and Seishi Takagi. Metal-Insulator Transitions in Pyrochlore Oxides $Ln_2Ir_2O_7$. *J. Phys. Soc. Jpn*, 80(9):094701, 2011.

[MWN+07] Kazuyuki Matsuhira, Makoto Wakeshima, Ryo Nakanishi, Takaaki Yamada, Akira Nakamura, Wataru Kawano, Seishi Takagi, and Yukio Hinatsu. Metal-Insulator Transition in Pyrochlore Iridates $Ln_2Ir_2O_7$ (Ln = Nd, Sm, and Eu). *Journal of the Physical Society of Japan*, 76(4):043706, 2007.

[PB10] Dmytro Pesin and Leon Balents. Mott physics and band topology in materials with strong spin-orbit interaction. *Nature Physics*, 6:376–381, 2010.

[PBM+12] Sylvain Petit, Pierre Bonville, Isabelle Mirebeau, Hannu Mutka, and Julien Robert. Spin dynamics in the ordered spin ice $Tb_2Sn_2O_7$. *Phys. Rev. B*, 85:054428, Feb 2012.

[PWLB07] A Poole, A S Wills, and E Lelièvre-Berna. Magnetic ordering in the xy pyrochlore antiferromagnet $er_2ti_2o_7$: a spherical neutron polarimetry study. *Journal of Physics: Condensed Matter*, 19(45):452201, 2007.

[RDG+99] N. P. Raju, M. Dion, M. J. P. Gingras, T. E. Mason, and J. E. Greedan. Transition to long-range magnetic order in the highly frustrated insulating pyrochlore antiferromagnet $Gd_2Ti_2O_7$. *Phys. Rev. B*, 59:14489–14498, Jun 1999.

[RPI+16] M Ruminy, E Pomjakushina, K Iida, K Kamazawa, D. Adroja, U Stuhr, and T Fennell. Crystal field parameters of the rare earth pyrochlores $R_2Ti_2O_7$ (R = Tb, Dy, Ho). *ArXiv e-prints*, May 2016.

[RSGB11] Kate A. Ross, Lucile Savary, Bruce D. Gaulin, and Leon Balents. Quantum excitations in quantum spin ice. *Phys. Rev. X*, 1:021002, Oct 2011.

[SRG+12] Lucile Savary, Kate A. Ross, Bruce D. Gaulin, Jacob P. C. Ruff, and Leon Balents. Order by Quantum Disorder in $Er_2Ti_2\mathbf{O}_7$. *Phys. Rev. Lett.*, 109:167201, Oct 2012.

[SSR+99] R. Siddharthan, B. S. Shastry, A. P. Ramirez, A. Hayashi, R. J. Cava, and S. Rosenkranz. Ising pyrochlore magnets: Low-temperature properties, "ice rules," and beyond. *Phys. Rev. Lett.*, 83:1854–1857, Aug 1999.

[SSW+11] P M Sarte, H J Silverstein, B T K Van Wyk, J S Gardner, Y Qiu, H D Zhou, and C R Wiebe. Absence of long-range magnetic ordering in the pyrochlore compound $Er_2Sn_2O_7$. *J. Phys. Condens. Matter*, 23(38):382201, 2011.

[Ste52] K W H Stevens. Matrix elements and operator equivalents connected with the magnetic properties of rare earth ions. *Proceedings of the Physical Society. Section A*, 65(3):209, 1952.

[SUA+13] H. Sagayama, D. Uematsu, T. Arima, K. Sugimoto, J. J. Ishikawa, E. O'Farrell, and S. Nakatsuji. Determination of long-range all-in-all-out ordering of Ir^{4+} moments in a pyrochlore iridate $Eu_2Ir_2O_7$ by resonant x-ray diffraction. *Phys. Rev. B*, 87:100403, Mar 2013.

[TMI+12] Keisuke Tomiyasu, Kazuyuki Matsuhira, Kazuaki Iwasa, Masanori Watahiki, Seishi Takagi, Makoto Wakeshima, Yukio Hinatsu, Makoto Yokoyama, Kenji Ohoyama, and Kazuyoshi Yamada. Emergence of Magnetic Long-range Order in Frustrated Pyrochlore $Nd_2Ir_2O_7$ with Metal-Insulator Transition. *J. Phys. Soc. Jpn*, 81(3):034709, 2012.

[TTO+15] Samuel Tardif, Soshi Takeshita, Hiroyuki Ohsumi, Jun-ichi Yamaura, Daisuke Okuyama, Zenji Hiroi, Masaki Takata, and Taka-hisa Arima. All-In−All-Out Magnetic Domains: X-Ray Diffraction Imaging and Magnetic Field Control. *Phys. Rev. Lett.*, 114:147205, Apr 2015.

[TWH01] Nobuyuki Taira, Makoto Wakeshima, and Yukio Hinatsu. Magnetic properties of iridium pyrochlores $R_2Ir_2O_7$ (R = Y, Sm, Eu and Lu). *Journal of Physics: Condensed Matter*, 13(23):5527, 2001.

[WKCKB14] William Witczak-Krempa, Gang Chen, Yong Baek Kim, and Leon Balents. Correlated quantum phenomena in the strong spin-orbit regime. *Annu. Rev. Condens. Matter Phys.*, 5(1):57–82, 2014.

[WKK12] William Witczak-Krempa and Yong Baek Kim. Topological and magnetic phases of interacting electrons in the pyrochlore iridates. *Phys. Rev. B*, 85:045124, 2012.

[WTM+11] M Watahiki, K Tomiyasu, K Matsuhira, K Iwasa, M Yokoyama, S Takagi, M Wakeshima, and Y Hinatsu. Crystalline electric field study in the pyrochlore $Nd_2Ir_2O_7$ with metal-insulator transition. *Journal of Physics: Conference Series*, 320(1):012080, 2011.

[WTVS11] Xiangang Wan, Ari M. Turner, Ashvin Vishwanath, and Sergey Y. Savrasov. Topological semimetal and fermi-arc surface states in the electronic structure of pyrochlore iridates. *Phys. Rev. B*, 83:205101, May 2011.

[Wyb65] B. G. Wybourne. Spectroscopic properties of rare earth. pages 164–165. Interscience Publishers, 1965.

[Wyb66] B. G. Wybourne. Energy levels of trivalent gadolinium and ionic contributions to the ground-state splitting. *Phys. Rev.*, 148:317–327, Aug 1966.

[YBJS13] H. Yan, O. Benton, L. D. C. Jaubert, and N. Shannon. Living on the edge : ground-state selection in quantum spin-ice pyrochlores. *ArXiv e-prints*, November 2013.

[YDdRB+13] A. Yaouanc, P. Dalmas de Réotier, P. Bonville, J. A. Hodges, V. Glazkov, L. Keller, V. Sikolenko, M. Bartkowiak, A. Amato, C. Baines, P. J. C. King, P. C. M. Gubbens, and A. Forget. Dynamical Splayed Ferromagnetic Ground State in the Quantum Spin Ice $Yb_2Sn_2\mathbf{O}_7$. *Phys. Rev. Lett.*, 110:127207, Mar 2013.

[ZFH+14] J. Zhang, K. Fritsch, Z. Hao, B. V. Bagheri, M. J. P. Gingras, G. E. Granroth, P. Jiramongkolchai, R. J. Cava, and B. D. Gaulin. Neutron spectroscopic study of crystal field excitations in $Tb_2Ti_2O_7$ and $Tb_2Sn_2O_7$. *Phys. Rev. B*, 89:134410, Apr 2014.

[ZMM+11] Songrui Zhao, J. M. Mackie, D. E. MacLaughlin, O. O. Bernal, J. J. Ishikawa, Y. Ohta, and S. Nakatsuji. Magnetic transition, long-range order, and moment fluctuations in the pyrochlore iridate $Eu_2Ir_2O_7$. *Phys. Rev. B*, 83:180402, May 2011.

[ZWB12] A. A. Zyuzin, Si Wu, and A. A. Burkov. Weyl semimetal with broken time reversal and inversion symmetries. *Phys. Rev. B*, 85:165110, Apr 2012.

[ZWS+14] W. K. Zhu, M. Wang, B. Seradjeh, Fengyuan Yang, and S. X. Zhang. Enhanced weak ferromagnetism and conductivity in hole-doped pyrochlore iridate $Y_2Ir_2O_7$. *Phys. Rev. B*, 90:054419, Aug 2014.

General conclusion

In this thesis, I have focused on two families of 5*d* transition metal oxides which both present two different magnetic elements and crystalline structures that are prone to magnetic frustration, leading to a wealth of novel behaviors.

In the chain compounds of formula Sr_3NiMO_6 (with M = Pt, Ir), we have first studied the magnetic behavior of Sr_3NiPtO_6, in order to isolate the magnetic behavior of the Ni ion, in particular its large anisotropy. This study has then allowed to better understand the physics of Sr_3NiIrO_6, where the non magnetic Pt ions are replaced by the magnetic Ir ions.

In the pyrochlore iridates, $R_2Ir_2O_7$ with R a rare-earth element, several compounds of the family have been studied including rare-earths displaying different magnetocrystalline anisotropy: easy axis, easy plane or isotropic. This allowed to get a quantitative understanding of the magnetic behavior of the rare-earth sublattice depending on its anisotropy but also, importantly, of the Ir magnetic properties and its coupling with the rare-earth.

Concerning the chain compounds, we first studied Sr_3NiPtO_6. The physics of this system is by itself of interest. It is found to stabilize the so-called large-*D* phase, associated with the large easy-plane anisotropy of the Ni ions. This phase was unambiguously confirmed using polarized neutron scattering experiment, which demonstrated the non magnetic nature of the ground state.

Substituting the non magnetic Pt ions by magnetic Ir ions changes drastically the observed magnetic behavior. In Sr_3NiIrO_6, the Ni easy plane anisotropy is overcome, around 200 K, by the highly anisotropic Ni-Ir intrachain exchange interactions. This has been shown by the analysis of the spin-waves and is attributed to the spin-orbit entangled state of the Ir^{4+} ion due to its strong spin-orbit coupling. These interactions lead to a magnetic order where the magnetic moments are confined along the chain direction. A change of the magnetic structure is observed at 17 K, possibly from a partially disordered antiferromagnetic structure to an amplitude modulated antiferromagnetic structure. This transition goes along with the appearance of a weak ferromagnetic component in the chain direction leading to a huge coercive field and a mysterious loss of the in-plane correlations of the magnetic arrangement.

Our results open interesting perspectives. For instance, comparing our magnetic Hamiltonian to the one of a recent numerical study of a mixed-spin XXZ chain with single-ion anisotropy, it is found that, in the parameter space of exchange and single-ion anisotropies, Sr_3NiIrO_6 lies close to the boundary separating the observed ordered Ising ferrimagnetic phase from a disordered XY phase (see Fig. 1) [L. Qiang *et al.*, Int J. Mod. Phys. B **29**, 150070 (2015)]. The transition between these two phases could be achieved in Sr_3NiIrO_6 by applying uniaxial pressure along the chain direction in order to change the strength of the trigonal distortion. Although experimentally demanding, this might thus allow us to probe unexplored regions of XXZ-mixed spin chains phase diagram and quantum phase transitions.

Among the pyrochlore compounds $R_2Ir_2O_7$, we have been studying those with the rare-earth el-

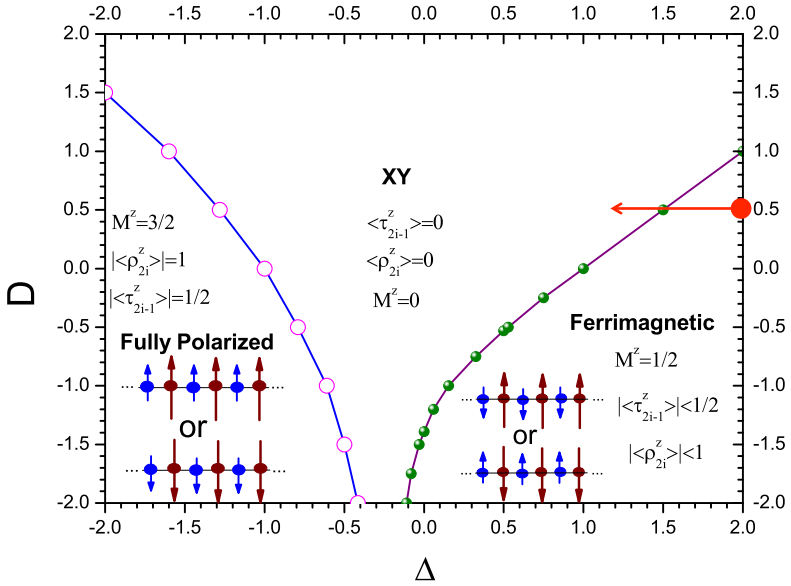

Figure 1 – *Schematic phase diagram of the spin-1/2 - spin 1 mixed-spin XXZ chain with single-ion anisotropy D and exchange anisotropy* $\Delta = J_{zz}/J_{xx}$. *The red dot shows the position of* Sr_3NiIrO_6 *in the phase diagram. Adapted from [L. Qiang et al., Int J. Mod. Phys. B* **29**, *150070 (2015)].*

ements R = Y, Gd, Tb, Dy, Ho, Er and Yb. These rare-earths present various magnetocrystalline anisotropy which allows to perform a comparative study in this family.

Using neutron scattering experiments, only the rare-earth magnetism can be probed, because the Ir ions display weak magnetic moments. Nevertheless, probing the rare-earth behavior has proven to provide great insights on the Ir magnetism. One of our main result is that, in all the studied compounds, the rare-earth magnetism is always compatible with an all-in/all-out (AIAO) magnetic order for the Ir sublattice. This order is the only one consistent with the exotic electronic phases, such as Weyl semi-metal, suspected to exist in the pyrochlore iridates as a consequence of the strong SOC of the Ir ions.

The all-in/all-out order occurs at relatively high temperature concomitantly with the SOC induced metal-insulator transition. It creates a molecular field acting on the rare-earth pyrochlore sublattice, parallel to the local $\langle 111 \rangle$ direction at the rare-earth sites. This is of utmost importance as it allows to probe the magnetic properties of the rare-earth sublattice when it is submitted to a well defined local molecular field. Rare-earths presenting an anisotropy with an easy axis parallel to this direction are polarized in an AIAO magnetic configuration as the Ir molecular field direction is consistent with the anisotropy. On the contrary, for rare-earths with an easy plane anisotropy perpendicular to the $\langle 111 \rangle$ direction, the molecular field competes against it and prevents any magnetic ordering of the rare-earth sublattice. As a transverse field to the local magnetic moment, it might in particular amplify the quantum fluctuations.

Among all compounds of the series, the must unexpected behavior was observed in $Gd_2Ir_2O_7$. Assuming that the Gd ions are isotropic, an induced AIAO arrangement of the Gd magnetic moment was indeed expected. As a matter of fact, not only magnetic Bragg peaks associated with an AIAO long range order but also short range correlations were observed simultaneously that recall the diffuse scattering observed for $Er_2Ir_2O_7$. These short range correlations could then be associated to some weak easy plane anisotropy of the Gd ions, which is indeed found from our crystalline electric field analysis, although it differs from that of $Er_2Ir_2O_7$ by several orders of magnitude. The understanding of this

strange behavior is open.

More insights to the Ir magnetism has been given by the analysis of the inelastic neutron scattering experiments which has to be completed to all the investigated rare-earths. The modulation of the low energy levels observed at low temperature are signatures of the R-R and/or R-Ir interactions. In the second case, this will give indirect information on the Ir spin dynamics.

Moreover, we have started to study the very low temperature magnetic properties of these compounds, when the rare-earth−rare-earth interactions become relevant and can compete with the Ir molecular field to possibly reveal new magnetic behaviors. For example, in $Ho_2Ir_2O_7$, the Ho sublattice is first induced in an AIAO antiferromagnetic arrangement. However, in the stannate and titanate Ho pyrochlores, the Ho-Ho effective interactions are ferromagnetic, so similar interactions could also be at play in $Ho_2Ir_2O_7$ and compete with the AIAO field-induced order. As a matter of fact, recent low temperature DC and AC magnetization measurements performed on $Ho_2Ir_2O_7$ show interesting spin dynamics that could be reminiscent of a low temperature reentrant spin ice physics (see Fig. 2, coll V. Cathleen and E. Lhotel).

This is clearly a strong incentive to systematically investigate the very low temperature phases of all the members of the series recalling that we have with these compounds the unique opportunity to investigate geometric frustration under a multi axial molecular field.

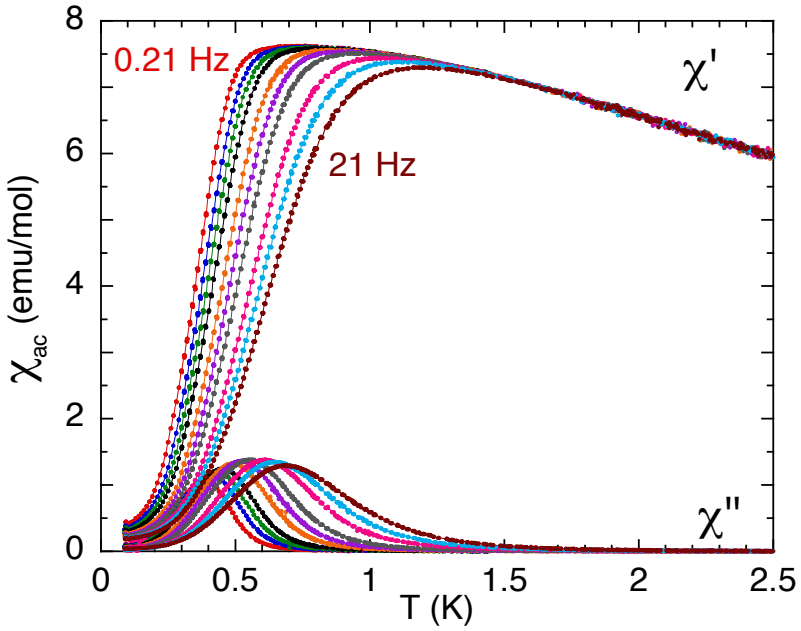

Figure 2 – *Temperature dependence of the in-phase (χ′ - top) and out-of-phase (χ″ - bottom) magnetization measured at different frequencies for $Ho_2Ir_2O_7$.*

Appendix A

Hexagonal and rhombohedral settings of trigonal space groups.

All trigonal crystals with rhombohedral lattices can be represented as an equivalent hexagonal system; there is a choice of using a hexagonal or a rhombohedral setting.

The hexagonal setting is in fact a supercell with 3 irreducible rhombohedral units.

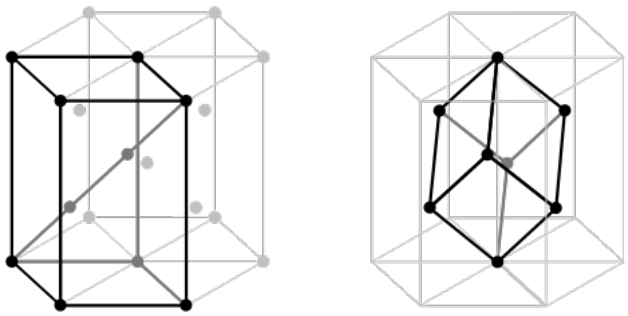

Figure A.1 – *Trigonal lattice sketch with the hexagonal (left) and rhombohedral (right) representation.*

The rhombohedral lattice vectors are expressed in the hexagonal ones by:

$$\begin{cases} a_R &= \frac{a_H+b_H+c_H}{3} \\ b_R &= \frac{2a_H+b_H+c_H}{3} \\ c_R &= \frac{-a_H-2b_H+c_H}{3} \end{cases}$$

And the hexagonal vectors are expressed in the rhombohedral ones using:

$$\begin{cases} a_H = -a_R + b_R \\ b_H = a_R c_R \\ c_H = a_R + b_R + c_R \end{cases}$$

If the hexagonal unit cell is given by (in Cartesian coordinates):

$$a_H = \frac{a}{2}\begin{pmatrix} 1 \\ -\sqrt{3} \\ 0 \end{pmatrix},\ b_H = \frac{a}{2}\begin{pmatrix} 1 \\ \sqrt{3} \\ 0 \end{pmatrix}\ \&\ c_H = c\begin{pmatrix} 0 \\ 0 \\ 1 \end{pmatrix},$$

with a and c being the corresponding hexagonal lattice constants, we obtain the Rhombohedral unit cell in Cartesian coordinates:

$$a_R = \frac{1}{3}\begin{pmatrix} 0 \\ a\sqrt{3} \\ c \end{pmatrix},\ b_R = \frac{1}{3}\begin{pmatrix} a3/2 \\ -a\sqrt{3}/2 \\ c \end{pmatrix}\ \&\ c_R = \frac{1}{3}\begin{pmatrix} -a3/2 \\ -a\sqrt{3}/2 \\ c \end{pmatrix},$$

Appendix B

Fits of the **Q** scans from the REXS experiment

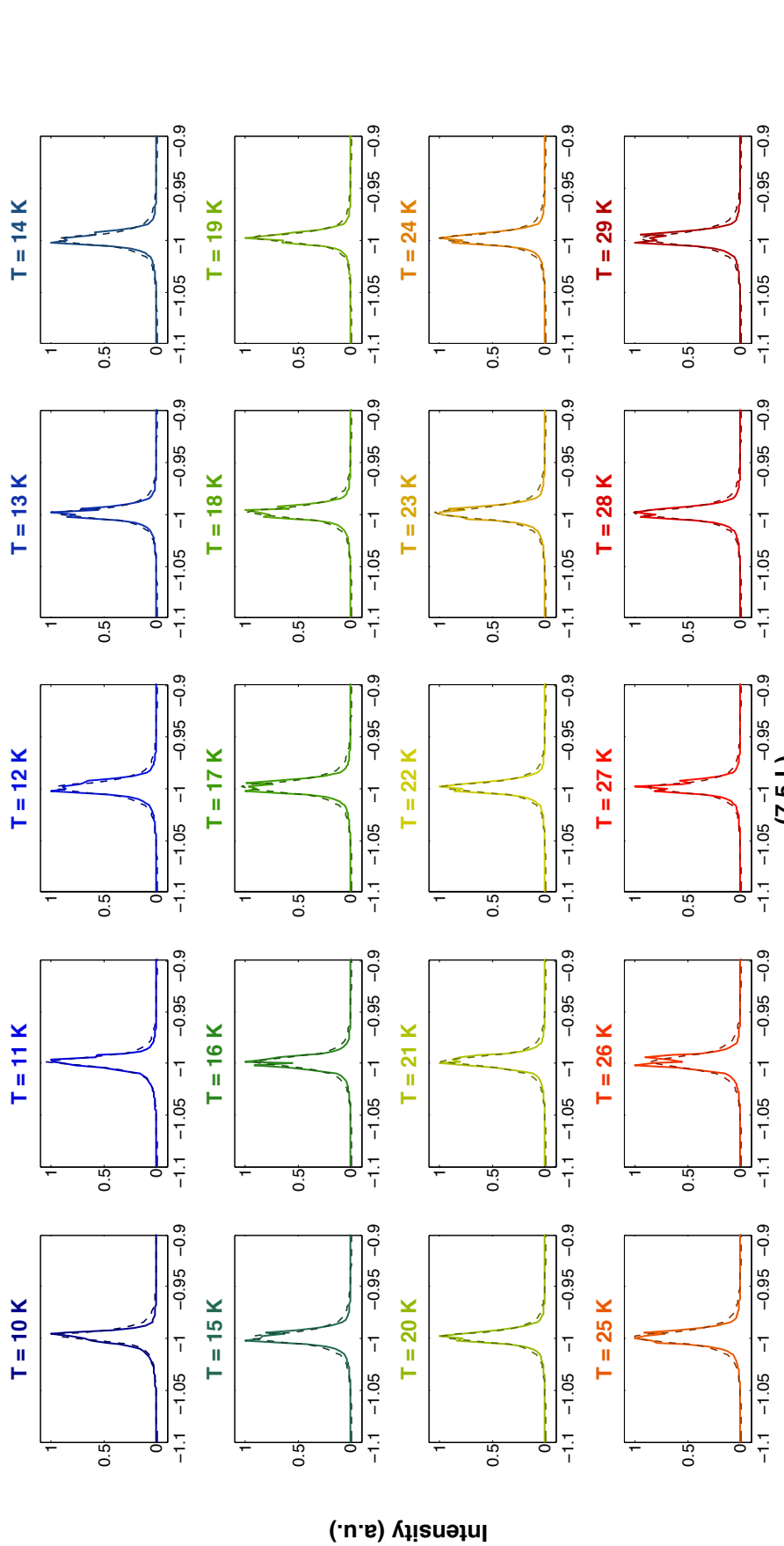

Figure B.1 – *Temperature evolution of the (7 5 L) scans for the charge peak (7 5 0). Data are shown by the plain lines and fits by the dashed lines.*

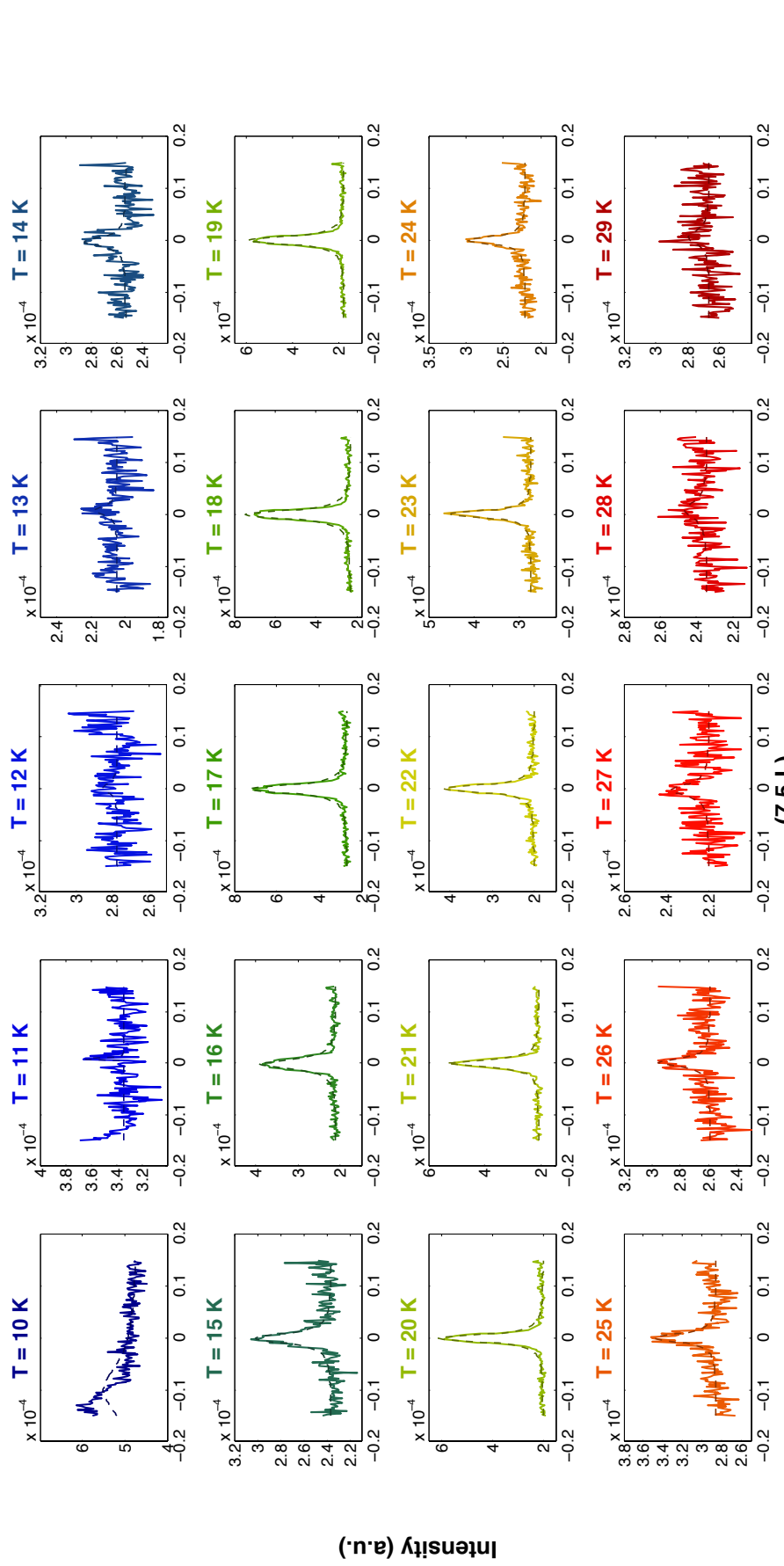

Figure B.2 – *Temperature evolution of the (7 5 L) scans for the magnetic peak (7 5 -1). Data are shown by the plain lines and fits by the dashed lines.*

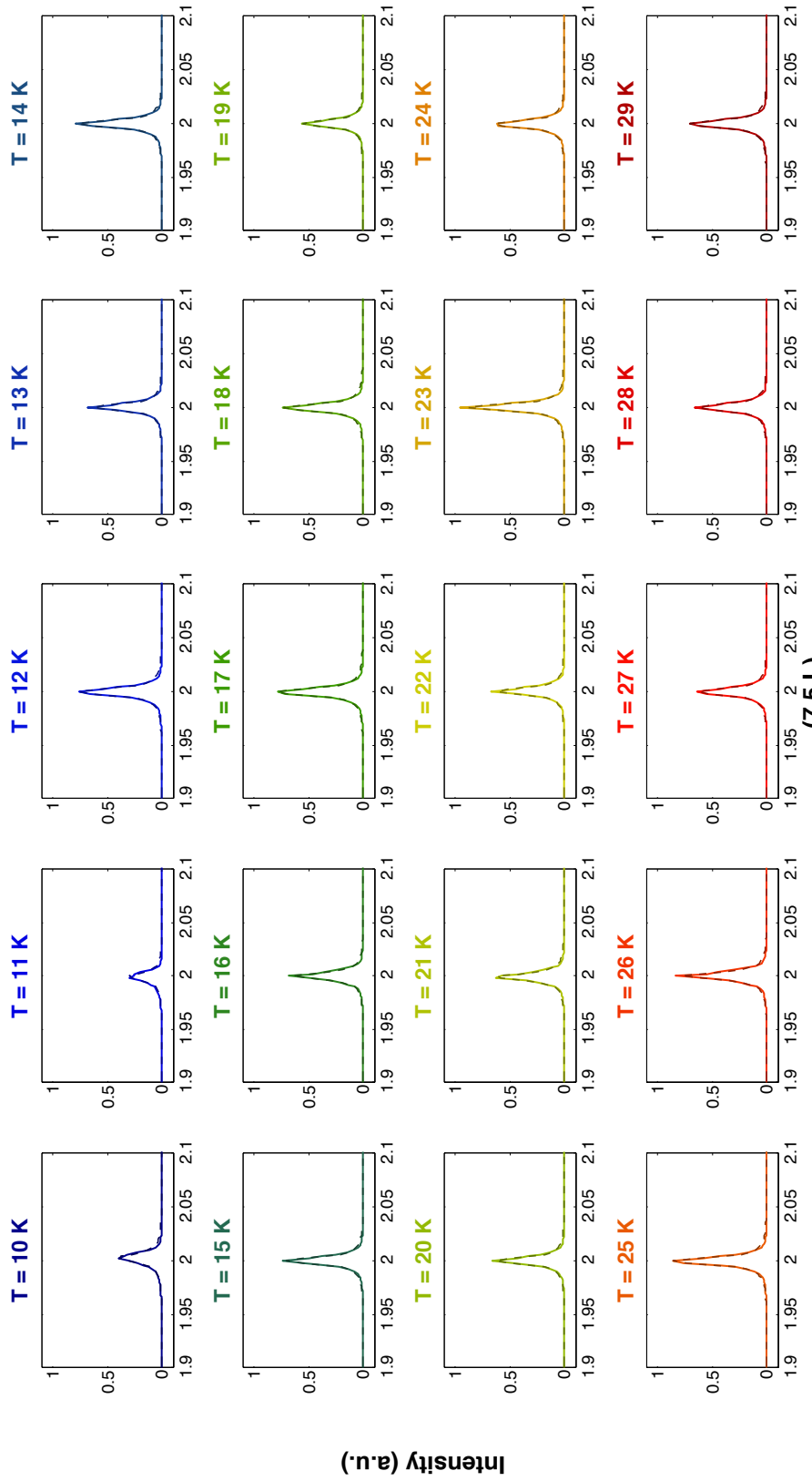

Figure B.3 – *Temperature evolution of the (7 5 L) scans for the charge peak (7 5 2). Data are shown by the plain lines and fits by the dashed lines.*

Appendix C

Fits of the **Q** scans from the RIXS experiment

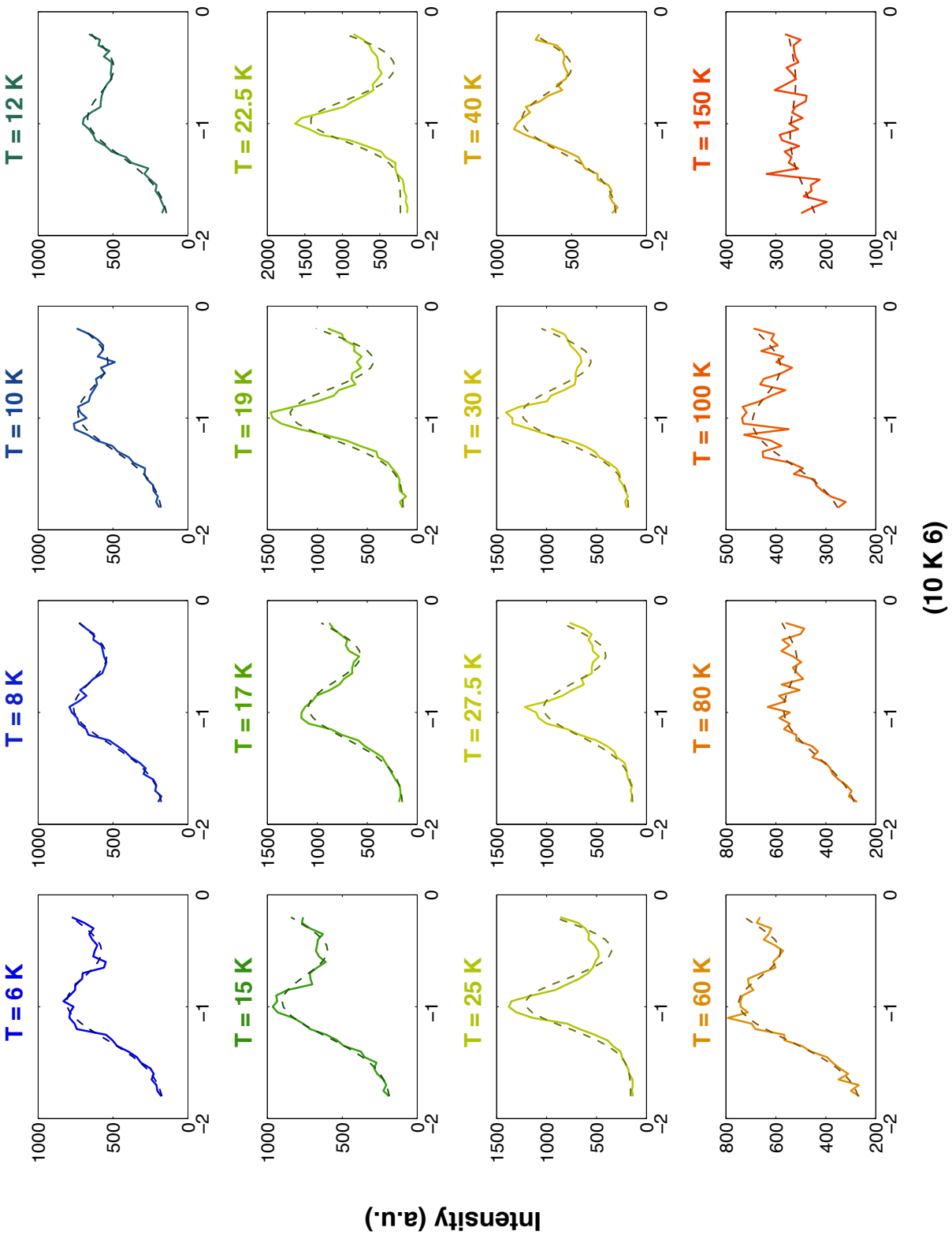

Figure C.1 – *Temperature evolution of the (10 K 6) scans. Data are shown by the plain lines and fits by the dashed lines.*

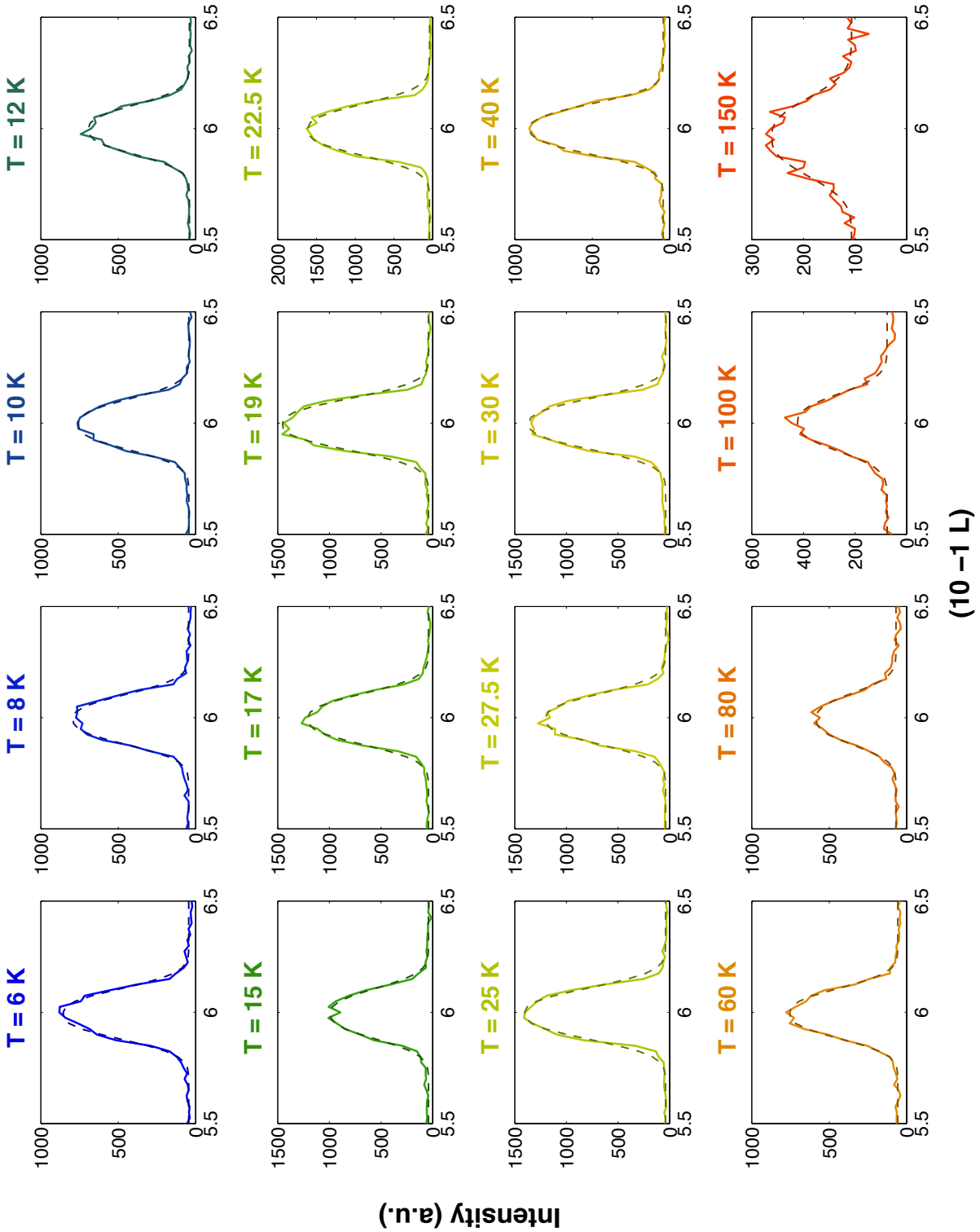

Figure C.2 – *Temperature evolution of the (10 -1 L) scans. Data are shown by the plain lines and fits by the dashed lines.*

Appendix D

Possibility to observe single magnons in Sr_3NiIrO_6 by RIXS

We checked that single magnon excitations in Sr_3NiIrO_6 can effectively be detected by RIXS. The RIXS scattering intensity is given by the Kramers-Heisenberg formula [T. Åberg and B. Crasemann in *X-ray Anomalous (Resonance) Scattering: Theory and Experiment*, edited by FK. Fisher G. Materlik and C. Sparks (Elsevier, Amsterdam, 1994)] and is proportional to the matrix elements of the polarization dependent dipole operator $C_\epsilon = \epsilon\vec{r}$ as:

$$I_{\hbar\omega\to\hbar\omega'} \propto |\langle 5d_f|C_{\epsilon'}|3p_{\frac{3}{2}}\rangle\langle 3p_{\frac{3}{2}}|C_\epsilon|5d_i\rangle|^2, \tag{D.1}$$

where $5d_i$ and $5d_f$ stand for the initial and final d states and $3p_{\frac{3}{2}}$ for the intermediate states. Using the dipole matrix reported in [F. M. F. de Groot, P. Kuiper, and G. A. Sawatzky, Phys. Rev. B **57**, 14584 (1998).], we can compute the matrix elements displayed in Eq. D.1 for the different possible intermediate $3p_{\frac{3}{2}}$ states. They are gathered in Table I for initial and final d states in the ground level with respect to $\bar{d}$-d excitations, *i.e.* $|0,\uparrow\rangle$ and $|0,\downarrow\rangle$ states defined as:

$$\begin{cases} |0,\uparrow\rangle = \frac{ic|a_{1g},\uparrow\rangle + i|e_g'^{+},\downarrow\rangle + |e_g'^{-},\downarrow\rangle}{\sqrt{c^2+2}} \\ |0,\downarrow\rangle = \frac{c|a_{1g},\downarrow\rangle - |e_g'^{+},\uparrow\rangle - i|e_g'^{-},\uparrow\rangle}{\sqrt{c^2+2}} \end{cases}, \tag{D.2}$$

the parameter c depending on the the ratio between the amplitude of the trigonal distortion and the spin-orbit coupling Δ/λ. All of them are not null thereby implying that single magnons with spin deviations in the ground level do contribute to the scattering.

	$\|\frac{3}{2},\pm\frac{3}{2}\rangle$	$\|\frac{3}{2},\pm\frac{1}{2}\rangle$
$\|0,\uparrow\rangle \rightleftharpoons \|0,\downarrow\rangle$	$\frac{i2\sqrt{2}c}{2+c^2}$	$-\frac{i\sqrt{2}(2+5c+2c^2)}{3(2+c^2)}$

Table D.1 – *Computed* $\langle 0,\uparrow(\downarrow)|C_{\epsilon'}|3p_{\frac{3}{2}}\rangle\langle 3p_{\frac{3}{2}}|C_\epsilon|0,\downarrow(\uparrow)\rangle$ *quantities for the different* $3p_{\frac{3}{2}}$ *states.*

Appendix E

Symmetry analysis of the Ni-Ir interactions.

All the bilinear contribution to the exchange interactions between a pair of moments can be deduced from the appropriate symmetry analysis. In Sr_3NiIrO_6, each Nickel-Iridium pair is along a three-fold axis (see Fig. E.1), thus the point group symmetry at the center of the pair is 3.

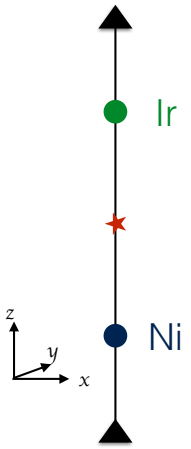

Figure E.1 – *Sketch of two neighboring nickel and iridium ions with the symmetry elements.*

The 3-fold axis does not change the positions but acts on the spins orientations in the following way:

$$\begin{pmatrix} S_x \\ S_y \\ S_z \end{pmatrix} \rightarrow \begin{pmatrix} -\frac{1}{2}S_x - \frac{\sqrt{3}}{2}S_y \\ \frac{\sqrt{3}}{2}S_x - \frac{1}{2}S_y \\ S_z \end{pmatrix}$$

Thus the 3-fold axis imposes the following conditions for :

– symmetric exchange tensor $J = \begin{pmatrix} J_{xx} & J_{xy} & J_{xz} \\ J_{xy} & J_{yy} & J_{yz} \\ J_{xz} & J_{yz} & J_{zz} \end{pmatrix}$, $J_{xx} = J_{yy}$ and $J_{xy} = J_{yz} = J_{xz} = 0$

– antisymmetric exchange $\vec{D} = \begin{pmatrix} D_x \\ D_y \\ D_z \end{pmatrix}$, $D_x = D_y = 0$

The interaction tensor in the local basis $((\hat{\mathbf{x}}, \hat{\mathbf{y}}, \hat{\mathbf{z}})$, attached to the Ni-Ir pair, see Fig. E.1) then writes:

$$J_{loc} = \begin{pmatrix} J_{xx} & D_z & 0 \\ -D_z & J_{xx} & 0 \\ 0 & 0 & J_{zz} \end{pmatrix} \tag{E.1}$$

Appendix F

Conversion between Wybourne and Stevens CEF parameters

The CEF Hamiltonian for the f electrons in the D_{3d} ($\bar{3}m$) point group symmetry of the 16d site that the R^{3+} ions occupy in the $R_2Ir_2O_7$ crystal writes

$$\begin{aligned}\mathcal{H}_{\text{CEF}} &= B_2^0\,\mathbf{C}_2^0 + B_4^0\,\mathbf{C}_4^0 + B_4^3\,(\mathbf{C}_4^3 - \mathbf{C}_4^{-3}) + \\ &+ B_6^0\,\mathbf{C}_6^0 + B_6^3\,(\mathbf{C}_6^3 - \mathbf{C}_6^{-3}) + B_6^6\,(\mathbf{C}_6^6 + \mathbf{C}_6^{-6})\end{aligned} \tag{F.1}$$

when the quantisation axis is chosen along the local 3-fold axis. The $\mathbf{C}_k^q$ stand for Wybourne operators, that in a spatial rotation, transform like the spherical harmonics Y_k^q. The B_k^q are real parameters to be determined from the experimental data. If only the ground multiplet $|f^n \alpha LSJM\rangle$ ($M = -J, -J+1, \cdots, J$) of the selected R^{3+} ion is considered, and only in that case, then the CEF Hamiltonian is often formulated in the literature using the Stevens operators $\mathbf{O}_k^q$ [Ste52, Hut64]. It then writes:

$$\mathcal{H}_{\text{CEF}} = A_2^0\,\mathbf{O}_2^0 + A_4^0\,\mathbf{O}_4^0 + A_4^3\,\mathbf{O}_4^3 + A_6^0\,\mathbf{O}_6^0 + A_6^3\,\mathbf{O}_6^3 + A_6^6\,\mathbf{O}_6^6 \tag{F.2}$$

with $A_2^0 = \alpha_J \frac{1}{2} B_2^0$, $A_4^0 = \beta_J \frac{1}{8} B_4^0$, $A_4^3 = \beta_J \frac{\sqrt{35}}{2} B_4^3$, $A_6^0 = \gamma_J \frac{1}{16} B_6^0$, $A_6^3 = \gamma_J \frac{\sqrt{105}}{8} B_6^3$ and $A_6^6 = \gamma_J \frac{\sqrt{231}}{16} B_6^6$. The Stevens coefficients α_J, β_J and γ_J depend only on the ground multiplet $|f^n \alpha LSJM\rangle$ of the selected R^{3+} ion and have been tabulated [Hut64]. The required Stevens operators can be computed as

$$\mathbf{O}_2^0 = 3\mathbf{J}_z^2 - \mathbf{X} \qquad (\mathbf{X} = J(J+1)\mathbf{I})$$

$$\mathbf{O}_4^0 = 35\mathbf{J}_z^4 - (30\mathbf{X} - 25\mathbf{I})\mathbf{J}_z^2 + 3\mathbf{X}^2 - 6\mathbf{X}$$

$$\mathbf{O}_4^3 = \frac{1}{4}[\mathbf{J}_z(\mathbf{J}_+^3 + \mathbf{J}_-^3) + (\mathbf{J}_+^3 + \mathbf{J}_-^3)\mathbf{J}_z]$$

$$\mathbf{O}_6^0 = 231\mathbf{J}_z^6 - (315\mathbf{X} - 735\mathbf{I})\mathbf{J}_z^4 + (105\mathbf{X}^2 - 525\mathbf{X} + 294\mathbf{I})\mathbf{J}_z^2 +$$
$$+(-5\mathbf{X}^3 + 40\mathbf{X}^2 - 60\mathbf{X})$$

$$\mathbf{O}_6^3 = \frac{1}{4}[\{11\mathbf{J}_z^3 - (3\mathbf{X} + 59\mathbf{I})\mathbf{J}_z\}(\mathbf{J}_+^3 + \mathbf{J}_-^3) + (\mathbf{J}_+^3 + \mathbf{J}_-^3)\{11\mathbf{J}_z^3 - (3\mathbf{X} + 59\mathbf{I})\mathbf{J}_z\}]$$

$$\mathbf{O}_6^6 = \frac{1}{2}[\mathbf{J}_+^6 + \mathbf{J}_-^6]$$

where $(-\mathbf{J}_+/\sqrt{2}, \mathbf{J}_z, \mathbf{J}_-/\sqrt{2})$ are the spherical components of the angular momentum $\vec{\mathbf{J}}$ vector and $\mathbf{I}$ the unit operator, i.e. the $(2J+1)-$dimensional unit matrix.

Bibliography

[Hut64] M. T. Hutchings. Point-charge calculations of energy levels of magnetic ions in crystalline electric fields. volume 16 of *Solid State Physics*, pages 227 – 273. Academic Press, 1964.

[Ste52] K W H Stevens. Matrix elements and operator equivalents connected with the magnetic properties of rare earth ions. *Proceedings of the Physical Society. Section A*, 65(3):209, 1952.

Appendix G

Details for the CEF analysis for $Gd_2Ir_2O_7$

The effects of CEF in $Gd_2Ir_2O_7$ might be ignored since the $4f$ electronic shell of Gd^{3+} ion is half-filled, but this would be legitimate only in the Russel-Saunders approximation according to which the $4f$ electrons in Gd^{3+} are in the purely spin ground octet ${}^8S_{7/2}$ ($S = 7/2, L = 0, J = 7/2$). As a matter of fact, a small admixture exists with multiplets of non zero orbital moments $|{}^6P_{7/2}\rangle$ ($S = 7/2, L = 1, J = 7/2$), $|{}^6D_{7/2}\rangle$ ($S = 5/2, L = 2, J = 7/2$), $\cdots$. Due to the hierarchy of the interactions, the in-shell electron-electron correlations being larger than the spin-orbit coupling, themselves larger than the CEF, the mixing is fairly independent of the host crystals and the states rather write:

$$|\Psi\rangle = s\,|{}^8S_{7/2}\rangle + p\,|{}^6P_{7/2}\rangle + d\,|{}^6D_{7/2}\rangle + \cdots \tag{G.1}$$

with $s = 0.9866$, $p = 0.162$, $d = -0.0123$, $\cdots$ [Wyb66].

The matrix element $\sum_{kq} B_k^q \langle \Psi M|\mathbf{C}_k^q|\Psi M'\rangle$ of the CEF Hamiltonian $\mathcal{H}_{\text{CEF}} = \sum_{kq} B_k^q \mathbf{C}_k^q$ between the states $|\Psi M\rangle$ can be computed from those of the Wybourne operators, $\mathbf{C}_k^q$, on the multiplet states $|f^n \alpha SLJM\rangle$, which are given by [Wyb65] :

$$\begin{aligned}\langle f^n \alpha SLJM|\mathbf{C}_k^q|f^n \alpha' SL'J'M'\rangle = (-1)^{J-M} \begin{pmatrix} J & k & J' \\ -M & q & M' \end{pmatrix} \times \\ (-)^{S+L+J'+k} \left[(2J+1)(2J'+1)\right]^{1/2} \begin{Bmatrix} J & J' & k \\ L' & L & S \end{Bmatrix} \times \\ (-7) \begin{pmatrix} 3 & k & 3 \\ 0 & 0 & 0 \end{pmatrix} \times \left(f^n \alpha SL||\mathbf{U}^{(k)}||f^n \alpha' SL'\right)\end{aligned} \tag{G.2}$$

where $(:::)$ and $\{:::\}$ stand for 3j-symbols and 6j-symbols and the reduced matrix elements of the so-called unit tensor operators $\mathbf{U}^{(k)}$ have been tabulated by Nielson and Koster [Nie63].

If the states $|\Psi\rangle$ are composed only of the states $|{}^8S_{7/2}\rangle$, $|{}^6P_{7/2}\rangle$ and $|{}^6D_{7/2}\rangle$ then the only involved non zero reduced matrix element are $({}^6P\,||\mathbf{U}^{(2)}||\,{}^6D) = \sqrt{3/14} = -({}^6D\,||\mathbf{U}^{(2)}||\,{}^6P)$. It follows that:

$$\sum_{kq} B_k^q \langle \Psi M|\mathbf{C}_k^q|\Psi M'\rangle = -\frac{4\sqrt{5}}{315} p d B_2^0 \langle M|\mathbf{C}_2^0|M'\rangle,$$

which means that only the quadrupolar component of the expansion of the CEF potential over the

spherical harmonics will induce a spliting of the ground octet and that this effect can be accounted for by means of a Wybourne operator $\mathbf{C}_2^0 = 3\mathbf{J}_z^2 - J(J+1)\mathbf{I}$ operating on the spin octet ${}^8S_{7/2}$ with an effective CEF parameter given by $-\frac{4\sqrt{5}}{315}pdB_2^0$, namely

$$\mathcal{H}_{\text{CEF}} = -\frac{4\sqrt{5}}{315}pdB_2^0\mathbf{C}_2^0 \approx 0.56 \times 10^{-4}B_2^0\mathbf{C}_2^0$$

Bibliography

[Hut64] M. T. Hutchings. Point-charge calculations of energy levels of magnetic ions in crystalline electric fields. volume 16 of *Solid State Physics*, pages 227 – 273. Academic Press, 1964.

[Ste52] K W H Stevens. Matrix elements and operator equivalents connected with the magnetic properties of rare earth ions. *Proceedings of the Physical Society. Section A*, 65(3):209, 1952.

[Nie63] C. W. Nielson. Spectroscopic Coefficients for the p^n, d^n, And f^n Configurations Cambridge, Mass.: M. I. T. Press, 1963.

[Wyb65] B. G. Wybourne. Spectroscopic properties of rare earth. pages 164–165. Interscience Publishers, 1965.

[Wyb66] B. G. Wybourne. Energy levels of trivalent gadolinium and ionic contributions to the ground-state splitting. *Phys. Rev.*, 148:317–327, Aug 1966.

Résumé :

Cette thèse porte sur l'étude d'oxydes d'iridium dont le fort couplage spin-orbite est susceptible de générer de nouvelles phases électroniques et magnétiques. Deux familles de composés ont été considérées : $Sr_3NiM'O_6$, à chaines de spins mixtes arrangées sur réseau triangulaire, et $R_2Ir_2O_7$, à réseaux pyrochlores interpénétrés de spins. Ils ont été synthétisés sous forme polycristalline et pour certains sous forme monocristalline puis étudiés macroscopiquement par mesure d'aimantation. Ils ont ensuite été sondés microscopiquement par diffusion de neutrons et de rayons X. Nos mesures montrent que dans les composés à chaînes de spins Sr_3NiPtO_6 et Sr_3NiIrO_6, les ions Ni^{2+} présentent une très forte anisotropie magnétocristalline planaire perpendiculaire à l'axe des chaînes. Nous démontrons que ceci stabilise dans Sr_3NiPtO_6 une phase non magnétique dite "large-D". Cette anisotropie se manifeste dans Sr_3NiIrO_6 à haute température. Ce composé s'ordonne cependant à basse température dans une structure magnétique avec les moments alignés le long de l'axe des chaînes. Nous expliquons ce changement d'anisotropie comme étant dû à la présence des ions Ir^{4+} dont le couplage spin-orbite produit une forte anisotropie des interactions Ni-Ir qui confinent les moments magnétiques le long des chaînes. Concernant les pyrochlores iridates $R_2Ir_2O_7$, les mesures d'aimantation et de diffraction de neutron sont cohérents avec un ordre "all-in/all-out" des moments magnétiques des ions Ir^{4+}, révélé indirectement via le comportement du sous-réseau des terres rares R. Cet ordre est le seul compatible avec la phase semi-métal de Weyl prédite comme résultant du fort couplage spin-orbite. Le comportement du sous-réseau de terre rare R dépend de l'anisotropie magnétocrystalline des ions R^{3+}. Les ions à anisotropie uniaxiale locale sont polarisés par le champ moléculaire produit par l'ordre de l'iridium dont la direction coïncide avec l'axe d'anisotropie. Les ions à anisotropie locale planaire perpendiculaire à cette direction ne présentent pas d'ordre magnétique induit par celui de l'iridium. A plus basse température, les interactions entre terres rares génèrent des comportements magnétiques plus complexes.

Summary :

This thesis focuses on the study of iridium oxides, in particular on the consequences of the strong spin-orbit coupling of the iridium. Two families of compounds have been investigated : $Sr_3NiM'O_6$, with mixed spin chains arranged on a triangular lattice, and $R_2Ir_2O_7$ with interpenetrated pyrochlores networks of spins. Polycrystalline samples have been synthesized and in some instances single crystals were successfully grown. They were investigated macroscopically by magnetization measurements and probed microscopically by neutron and synchrotron X-ray scattering experiments. Our measurements showed that in the spin chain compounds Sr_3NiPtO_6 and Sr_3NiIrO_6, the Ni^{2+} ions show a strong easy plane magnetocrystalline anisotropy, perpendicular to the chain axis. This stabilizes in Sr_3NiPtO_6 the so-called "large-D" non-magnetic phase. The planar anisotropy comes out in Sr_3NiIrO_6 at high temperature. The compound however orders at low temperature in a magnetic configuration with all the magnetic moments confined along the chain axis. We explain this change of anisotropy as due to the Ir^{4+} ions whose spin-orbit coupling produces a strong anisotropy of the intra-chain Ni-Ir magnetic interactions overwhelming the single-ion Ni^{2+} anisotropy. Concerning the pyrochlore iridates $R_2Ir_2O_7$, magnetization measurements and neutron powder diffraction experiments are consistent with an "all-in/all-out" magnetic ordering of the Ir magnetic moments, revealed indirectly through the magnetic behavior of the rare-earth sublattice. This ordering is the only one consistent with a Weyl semi-metal phase predicted to arise from the spin-orbit coupling. The magnetic behavior of the rare-earth sublattice depends on the rare earth magnetocrystalline anisotropy. The ions with local uniaxial anisotropy are polarized by the Ir molecular field, whose direction coincides with the anisotropy axis. The ions with local planar anisotropy perpendicular to this direction show no iridium induced long-range magnetic ordering. At lower temperature, rare-earth interactions generate more complex magnetic behaviors.